Micro-Electro-Mechanical Actuators Using Confined Polymers

Gih-Keong Lau

Micro-Electro-Mechanical Actuators Using Confined Polymers

PROEFSCHRIFT

ter verkrijging van de graad van doctor
aan de Technische Universiteit Delft,
op gezag van de Rector Magnificus Prof. dr. ir. J. T. Fokkema,
voorzitter van het College voor Promoties,
in het openbaar te verdedigen op woensdag 5 december 2007 om 10:00 uur
door

Gih-Keong Lau

Master of Engineering,
Nanyang Technological University, Singapore
geboren te Muar, Maleisië.

Dit proefschrift is goedgekeurd door de promotoren:

Prof. dr. ir. A. van Keulen
Prof. dr. P. M. Sarro

Dr. ir. J. F. L. Goosen, toegevoegd promotor

Samenstelling promotiecommissie:

Rector Magnificus	Technische Universiteit Delft, voorzitter
Prof. dr. ir. A. van Keulen	Technische Universiteit Delft, promotor
Prof. dr. P. M. Sarro	Technische Universiteit Delft, promotor
Dr. ir. J. F. L. Goosen	Technische Universiteit Delft, toegevoegd promotor
Prof. dr. P. J. French	Technische Universiteit Delft
Prof. dr. M. C. Elwenspoek	Universiteit Twente
Prof. dr. D. Reynaerts	Katholieke Universiteit Leuven, België
Prof. dr. S. M. Spearing	University of Southampton, UK

ISBN 978-90-9022531-9

Author email: g.k.lau@tudelft.nl or gihkeong@gmail.com

In memory of my father

To my mother and brothers

To Sin-Yee

Summary

This thesis presents research efforts and results of miniaturizing polymeric 'artificial muscles' for micro-electro-mechanical systems (MEMS). The polymers considered for micro-actuation include dielectric elastomers and thermally expandable polymers. These polymers are insulating and relatively compliant. Electrodes, heat conductor or heater are integrated into them to enable electric activation. However, the electrodes or heater are so stiff that they restrain actuation of the polymers. To effectively exploit the polymers for the miniaturized actuators, confinement effects on the polymers need to be clarified and taken into account in the mechanical design of the embedded electrodes or heaters.

Confinement effects on compliant polymers are studied using both theoretical and numerical models. The confinement is found to suppress stress-induced actuation of dielectric elastomers, but it boosts strain-induced actuation of thermal expandable polymers. These understandings lead to various designs of electrode or heater for polymeric actuators. For example, dielectric elastomer micro-actuators have a design with an array of discrete and short electrodes, whereas polymeric thermal micro-actuators have a design with a meandering heat conductor.

Theoretical and numerical studies on the designs suggest that the constrained thermal expansion delivers more powerful actuation than the constrained dielectric elastomer does. In addition, fabrication of the micro-actuators using a thermally expandable polymer is more successful than that using a dielectric elastomer. As a result, a later stage of the present research focuses mainly on the micro-actuators based on thermally expandable polymers.

The present research has developed a new class of polymer thermal micro-actuators with embedded heat conductors (or skeletons, in the other words). This actuator design features an adequate actuation strain, a large actuation stress, high work energy density and improved heat transfer. It outperforms many other thermal actuator designs based on either pure polymers or silicon. Therefore, the present thermal actuator could be a promising option to drive many micro-electro-mechanical systems.

Various layout designs of heaters and skeletons are developed for thermally expandable polymers. These include meandering skeletons of symmetric, asymmetric

and V- shapes. Polymer actuators with the different skeleton layout could deliver varying characteristics of motion and force . The generated motion can be rectilinear, curvilinear, in-plane or out-of-plane.

Besides introduction of novel designs, the present research has also presented comprehensive modeling for a polymeric thermal actuator with a symmetric skeleton. The modeling covers thermo-mechanical and electro-thermal aspects. A finite-width plane-strain model is developed for a polymer strip bonded between rigid interfaces. In addition, a one-dimensional electro-thermal model is developed for a polymeric actuator with the embedded skeleton of a symmetric meandered layout. These models lay the foundations for subsequent analysis in the material selection and design optimization.

Analysis based on the models shows that a polymer strip with a bond width 5 times the strip thickness could attain 95% the maximum strain enhancement for the infinite bond width. In addition, an embedded heat-conductive skeleton improves heat transfer to polymer. Therefore, the actuator design can be compact and have a fast thermal response. In addition, an exercise of material selection suggest that epoxy and nylon are good and powerful as expansion materials while most metals and silicon are suitable as skeletons. Design optimization shows that a 20-30% volume fraction of skeleton can in fact maximizes the actuation strain and work density of the polymer actuators.

Experimental characterization shows that the polymeric micro-actuators with the embedded skeleton can produce a large motion at a low driving voltage and a reasonably low temperature. In addition, the micro-actuators show powerful polymeric expansion. For example, a V-shape SU-8 micro-actuator of 1 mm long could produce an actuation force as much as about a tenth of a Newton below 200 °C. On the other hand, cure shrinkage happens above a temperature above 220 °C for SU-8 and consequently break the V-shape silicon skeleton, which is clamped at both ends. These observations show that the polymeric actuation is very powerful but can be catastrophic.

The thesis has presented design, theory, analysis, and characterizations for a new class of polymeric thermal actuators with embedded skeletons. The work confirms that the confined thermally expandable polymers are effective for actuation. These polymeric micro-actuators have potential for a wide range of applications.

Samenvatting

In dit proefschrift worden de onderzoeksdoeleinden en resultaten gepresenteerd over het miniaturiseren van uit polymeren vervaardigde "kunstspieren" voor het gebruik in micro elektromechanische systemen (MEMS). De voor microactuatie beschouwde polymeren omvatten diëlektrische elastomeren en thermische expanderende polymeren. Deze polymeren zijn isolatoren en zijn relatief flexibel. Elektroden, warmtegeleiders en verwarmingselementen worden geïntegreerd om directe elektrische aansturing mogelijk te maken. Deze elementen zijn echter dusdanig stijf, dat zijn vervorming van de polymeeractuator beletten. Om de eigenschappen van deze polymeren effectief te gebruiken in geminiaturiseerde actuatoren, is het nodig om de invloed op de flexibiliteit te doorgronden, met in acht nemen van het mechanische ontwerp van de geïntegreerde elektroden of verwarmingselementen.

Het effect van inklemmen van de flexibele polymeren wordt bestudeerd met behulp van zowel analytische als numerieke modellen. De inklemming onderdrukt de spannings-geïnduceerde actuatie, zoals in de diëlektrische elastomeer actuator. In de rek-geïnduceerde actuatie, zoals in de thermisch expanderende actuator, kan inklemming het effect versterken. Dit inzicht leidt tot verschillende ontwerpen van elektroden of verwarmingselementen voor polymeeractuatoren. Eén van deze ontwerpen bestaat uit rijen discrete en korte elektroden voor diëlektrische elastomeer micro-actuatoren en een ander ontwerp bestaat uit een gevouwen warmtegeleider voor thermische polymeer micro-actuator.

Analytische en numerieke studies van de ontwerpen suggereert dat de ingeklemde thermische expansie krachtiger actuatie levert dan de diëlektrische elastomeren. Fabricage methoden voor beiden typen polymeer actuatoren zijn ontwikkeld, gebruik makend van technieken voor geïntegreerde systemen zoals fotolithografie en etstechnieken. Dit bleek het meest succesvol voor de thermisch expansie actuatoren, en met het ook op deze bevindingen richt het tweede deel van dit onderzoek zich grotendeels op thermische polymeeractuatoren.

Het onderzoek heeft geleid tot een nieuwe klasse van thermische polymeer microactuatoren met geïntegreerde warmtegeleiders (met andere woorden: het geraamte). Dit actuator ontwerp heeft als eigenschappen: aanzienlijke actuatorrek, een grote actuatiespanning, hoge energiedichtheid en een verbeterde warmtegeleid-

ing. De prestaties zijn beter dan de meeste andere thermische actuatoren gebaseerd op uitsluitend polymeren of silicium. Dit maakt deze thermische actuator een veelbelovende optie voor toepassing in veel micro-elektromechanische systemen.

Verschillende geometrien van de verwarmingselementen en het geraamtes zijn ontworpen voor de thermisch expanderende polymeren. Deze omvatten meanderende symmetrische, asymmetrische en V-vormige structuren. De verschillende geraamten zorgen voor verschillende krachten en bewegingen. Deze gegenereerde beweging kan lineair, gekromd, in het vlak of uit het vlak zijn.

Naast de introductie van de nieuwe ontwerpen, wordt ook uitvoerig het modelleren van de thermische polymeeractuator met geïntegreerd symmetrisch geraamte gepresenteerd. Het modelleren omvat thermisch-mechanische en elektromechanische aspecten. Een eindige breedte in het veld rek model is afgeleid voor een strip van gelaagde polymeren tussen twee starre raakvlakken. Ook is een één dimensionaal elektrisch-thermisch model ontwikkeld voor een polymeeractuator met een symmetrische structuur voor het ingebedde geraamte. Deze modellen leggen de basis voor de analyse van het materiaal en de ontwerpoptimalisatie.

Analyse gebaseerd op de modellen laat zien dan een binding van vijf maal de dikte van de strook van de gebonden polymeer 95% verbetering kan bereiken voor een oneindige breedte. Warmtetransport van en naar de polymeer is ook effectiever door het warmtegeleidende geraamte. Hierdoor kan de actuator compact ontworpen worden met een snellere thermische responsie. Bovendien suggereert een studie naar mogelijke materialen dat epoxy en nylon goede en krachtige materialen voor expansie zijn, terwijl de geraamten het beste vervaardigd kunnen worden van de meeste metalen of silicium. Ontwerpoptimalisatie laat zien dat 20 tot 30 procent van het volume nodig is voor het geraamte voor het maximaliseren van de actuator rek en energiedichtheid van de polymeeractuatoren.

Experimentele karakterisatie laat zien dat de polymeer micro-actuatoren met het ingebedde geraamte een grote verplaatsing kunnen bewerkstelligen bij een laag aanstuurvoltage en een redelijk lage temperatuur. Bovendien laten de microactuatoren een krachtige expansie zien. Bijvoorbeeld; een V-vormige SU-8 microactuator die niet langer is dan 1 millimeter kan een kracht produceren van enkele tienden van Newtons beneden de 200 graden Celsius. Hierbij dient te worden opgemerkt dan krimp door verglazing optreed boven de 220 graden voor SU-8, wat breuk veroorzaakt in het geraamte van de V-vormige actuator die aan twee kanten is ingeklemd. Deze bevindingen laten zien dat de polymeer activering erg krachtig is maar tegelijk catastrofaal kan zijn.

Dit proefschrift presenteerde het ontwerp, theorie, analyse en karakterisering van een nieuwe klasse van thermische polymeeractuator met ingebed geraamte. Het onderzoek bevestigt dat de ingeklemde thermisch expanderende polymeren effectief zijn voor actuatie doeleinden. Deze polymeer microactuatoren zijn veelbelovend voor een breed scala aan toepassingen.

Contents

Chapter 1

Introduction

Actuators are devices that generates force and motion. Examples of actuator include electric motors, ultrasonic motor, bimetals, and piezoelectric switches. They have been miniaturized and integrated into micro-electronic systems to provide added functions of sensing and actuation. The miniaturization and integration lead to the micro-electro-mechanical systems (MEMS). The micro-actuators are found in many applications. For example, the micro-actuators are deployed to drive the scanning mirror array for a digital light processor or to inject ink droplets for an inkjet printer. The actuators operate on various principles, which can be electrostatic, electromagnetic, electrostrictive, piezoelectric, electrothermal, or involve a phase change [142]. They can be made of various materials.

Recently, new polymeric materials have been developed and adopted for application in artificial muscles [11, 98]. The new materials feature a large actuation strain and a high work density. However, they are subjected to respective limitations. For example, dielectric elastomer actuators require a prohibitively high driving voltage of a few thousand volts; whereas, liquid crystalline elastomers show a slow thermal response. To address this issues, this work is motivated to miniaturize the new materials together with embedded electrodes or heaters.

1.1 Polymer Actuators

Polymers are widely used as engineering materials, both in macroscopic and microscopic systems [96]. In microsystems, they are used as structural materials for micro-channels (e.g. polydimethlysiloxane (PDMS)), conducting materials for electrodes (e.g. polyaniline), sacrificial materials for release (e.g. polystyrene), sensing materials (e.g. polyvinylidene fluoride (PVDF)), or actuation materials. In the present study, polymers are used as actuation materials.

The actuation mechanisms vary among polymeric materials [98, 118]. The present discussion focuses on dry and solid-state polymers. For example, compliant dielectric elastomers are actuated under Maxwell stress which is induced by electric charges due to an applied electric field; electrostrictive polymers undergo crystalline

or semi-crystalline re-orientation under an applied electric field; liquid crystalline elastomers undergo phase change, as well as, volumetric change in response to temperature change. These actuation materials are applicable to deliver large strains and high work energies (see Table 1.1). More details on them are referred to a review by Madden *et al.* [98].

These actuation polymers have been incorporated in prototypes of macroscopic actuator. However, they require high driving voltages or currents in the macroscopic settings. For example, a 25-50 μm thick layer of dielectric elastomer actuator generally requires driving voltages of several thousand volts. This issue can be addressed with miniaturization. For example, the dielectric elastomeric and electrostrictive polymeric actuators only need several tens of volt for effective actuation if they are made sub-micron thin layers.

In addition, scaling down improves dynamic bandwidth of actuators. In the case of dielectric elastomers and piezoelectric polymers, reduced inertia at the microscopic scale attributes to bandwidth enhancement [118]. In the case of thermally responsive liquid crystal elastomers (LCE), a reduced heat path at the microscopic scale contributes to a quick thermal response because the characteristic thermal time constant is inversely proportional to the square of thickness. For example, it is possible to achieve a characteristic thermal time constant of 100 μs using a 1 μm thick LCE film [98].

There are many incentives to scale down these polymeric actuators. In addition, it is rewarding to introduce these polymeric materials to MEMS. Their adoption in MEMS will bring advanced performance which could hardly be delivered by the traditional actuation materials, such as piezoelectric materials or silicon. For example, a dielectric elastomer actuator can produce an adequately large rotation angle to drive optical mirrors [74]. In addition, elastomers can undergo a large strain without brittle fracture. These characteristics make polymeric materials reliable and robust for deployment in a rugged environment.

1.2 Challenges to Miniaturization

Electro-active polymers have been extensively studied in the material aspects. [11, 74, 98, 116, 118, 136, 151]. However, they are less investigated in the aspect of miniaturization and micro-fabrication. Micro-fabrication of compliant electro-active polymers remains relatively primitive. They can be deposited readily as thin film by solution casting [124, 158]. However, most of them cannot be patterned using photolithography. Moreover, they are difficult to etch or remove cleanly and neatly [124]. Micro-machining of electro-active polymers remains challenging, in contrary to the ease of processing the photoresists developed for microelectronic micro-fabrication. Therefore, innovation in the micro-machining techniques for electro-active polymers is very sought after.

Some electro-active polymers can be shaped into microstructures using the meth-

Table 1.1 Comparison of actuation polymers [98]

Performance Specification	Units	Acrylate Elastomer VHB	Electro-strictive Polymer	Liquid Crystal Elastomer
Driving temperature rise	°C	-	-	80-100
Maximum driving field	V/μm	125-440	13 -150	-
Maximum strain	%	10-100	3.5 - 7	19-45
Range of stress	MPa	1.6 - 7.7	20 - 45	0.45
Range of work density	kJ/m^3	150 - 3400	320 - 1000	3-56
Electro-mechanical coupling factor	%	25 90	10 - 40	<10
Dynamic bandwidth	kHz	10 - 50	100 - 10	1-10
Young's modulus	MPa	1.0 - 3.0	400-1200	0.06-4

ods of solution casting and micro-molding. However, not all active polymers are able to retain activeness when micro-machined. Some maintain the activeness but with performance deterioration. For example, the PVDF thin film prepared by solution casting can poorly obtain permanent dipole polarization, as compared to the extruded thin sheet, which are stretched and poled at elevated temperature [11]. In addition, total work energy stored in polymeric thin films decreases due to miniaturization. This effect may compromise the benefits brought by thinning the polymeric films. Multi-layer stacking for energy accumulation may alleviate the issue, but in turn, requires many process steps [84, 126].

Only a smaller class of active polymers are available for micro-actuation. In this context, some dielectric elastomers and thermal expandable polymers listed in Tables 1.2 and 1.3 are found suitable for micro-actuation. They are highlighted because they can be micro-fabricated with relative ease and they do not need to be stretched to retain the actuation capability. In addition, they can be obtained commercially without additional chemical modification.

Although the selected polymers are not the best actuation materials in terms of strains and stresses, their work energy density remains higher than conventional actuation materials. For example, polyurethane [116, 136, 166] exhibits a very large electrostrictive strain, approximately more than two times higher than that of PVDF, whereas silicone rubber can undergoes a large strain and sustain a very high electric field (see Table 1.2). On the other hand, thermally expandable polymers exhibit an adequate actuation strain and a large actuation stress (see Table 1.3). For example, SU-8 epoxy in particularly could deliver a maximum thermal stress of 92 MPa, which is far greater than the actuation stress obtained from the dielectric elastomers.

The polymeric materials mentioned above are electrically and thermally insulating. To enable electric activation, conductive electrodes or heaters are required to be integrated with them. However, there exists certain complexity in integrating and miniaturizing electrodes or heaters using metals or conducting polymers. For

Table 1.2 Electro-mechanical properties of some dielectric elastomers [116, 136]

Performance Specification	Units	Polyurethane Deerfield PT6100S	Silicone Dow Corning Sylgard 186	Silicone Nusil CF19-2186
Maximum driving field	V/μm	160	144	235
Maximum strain	%	11	32	32
Maximum stress	MPa	1.6	0.51	1.36
Maximum work density	kJ/m^3	87	82	220
Electro-mechanical coupling factor	(%)	21	54	54
Dielectric constant (1 kHz)	1	7.0	2.8	2.8
Young's modulus	MPa	17	0.7	1.0

Table 1.3 Thermo-mechanical properties of some polymers

Performance Specification	Units	Polyurethane Dow Pellethane [32]	Silicone, Dow Corning Sylgard 184 [31]	Epoxy Microchem SU-8 [37, 107]
Maximum temperature	°C	182-210	200	230
Maximum thermal strain	%	3.1	5.6	3.07
Maximum thermal stress	MPa	0.13	0.056	92.25
Maximum work density	kJ/m^3	1.98	1.57	1416
Thermal conductivity	W/m/K	0.2-0.35	0.17	0.2
Thermal expansion coefficient	ppm/K	168	320	50-150
Young's modulus	MPa	4.1	0.75 - 1.0	3.0-5.2 $\times 10^3$

example, a conducting polymer such as polyaniline [139] has inadequate electrical conductivity, whereas the compliant electrodes containing carbon particles and elastomeric binder cannot be made thinner than the size of carbon particles [126]. In addition, there is poor adhesion between thin metallic electrodes and the compliant electro-active polymers that undergo a large strain [116]. These issues may hinder successful miniaturization of electro-active polymers for micro-actuation application.

In addition, mechanical effect of the integrated electrodes or heater may dominate the actuation performance of a sub-micron thin polymeric material. For example, compliant dielectric elastomers have limited actuation when they are constrained by metallic thin films of significant stiffness [13,139]. Similarly, electrostrictive polymers produce less actuation strain when bonded to metal plates [119, 152]. In contrast, surface confinement of thermally expandable polymer does not inhibit its volumetric expansion. Instead, the volumetric expansion is directed perpendicular to the confined surfaces. For example, Wu *et al.* [157] reported a large transverse thermal expansion of polyimide adhesive in between memory stack or printed wire boards. The constrained thermal expansion of adhesive is unintended

in the stacking, and it has not been exploited for the actuator application.

1.3 Motivation

The discussion above suggests that miniaturization of actuation polymers brings many benefits, such as a low driving potential, and a faster response time. Electrodes or heaters are required to enable electrical activation of polymeric materials. However, miniaturization makes the actuation polymers subject to more pronounced confinement by the relatively stiff electrode or heater. The electrodes or heaters, as thin as a few sub-microns, can impose significant mechanical restraint on the polymers of a few microns thick and render them ineffective actuation. Furthermore, miniaturization may compromise the capability of the polymer actuators to deliver adequate work energy.

The conflicting consequences of miniaturization make it difficult to exploit and design the polymeric actuators. To untangle the puzzles of the conflicting consequences, the present research will first investigate confinement effects of stiff electrodes or heaters on the compliant actuation polymers. Subsequently, understanding on the confinement effects are used to guide mechanical design of the embedded electrodes or heaters. Ultimately, the electrode or heater designs will be tailored to actuation mechanism of each polymer to garner the effective actuation. The polymers which are constrained by electrodes or heaters are hereby termed as 'confined polymers'.

1.4 Scope

Present research aims at developing powerful micro-actuators based on the confined polymers. The present thesis will explores various design concepts of polymeric actuators with embedded electrodes or heaters, in order to garner the synergy of composite integration. Feasibility of micromachining the electrodes, heaters and actuation polymers, and their integration will be investigated. Interaction between the design and fabrication techniques will hopefully resolve some issues inherent to multi-layer polymeric actuators.

Actuator design is specific to and dependent on the actuation principles, as well as, materials. Two major actuation principles are exploited, namely charge induced stress or Maxwell stress actuation, and thermal expansion. This leads to two major design directions. The design for stress-induced dielectric elastomers consist of short and discrete electrode plates wired up by shallow interconnects of high flexibility. The design for strain-induced thermally expandable polymers consists of a wide, full-height and continuous skeleton for stiffness reinforcement.

The present scope focuses on design concepts, theory, modeling, and fabrication feasibility of the mentioned polymeric actuation principles. These efforts lay the

foundations of miniaturizing electric-activated polymeric actuators. The research is carried out at the Department of Precision and Microsystems Engineering (PME) and in close collaboration with the Laboratory of Electronic Components, Materials and Technology (ECTM), Delft University of Technology. A PhD collaborator at the ECTM group assisted in silicon micro-fabrication technology and applied the developed polymeric actuators to drive micro-grippers, which are capable to manipulate small particles.

1.5 Thesis Organization

The presented thesis is organized into two parts. The First Part (Chapters 2 and 3) describes the design and feasibility study of dielectric elastomeric micro-actuators with embedded electrode microstructures, whereas the Second Part deals with the design, analysis, characterization, and optimization of thermally expandable polymeric micro-actuators with embedded silicon skeletons. These chapters are mainly based on some published papers and prepared manuscripts. They may therefore overlap partially in terms of a few common contents or figures.

Chapter 2 studies dielectric elastomer actuators with embedded electrodes. The elastomer is squeezed electrostatically to generate strain. The electrodes present surface confinement to the compliant elastomer, and consequently suppress the generated strain. The confinement effects will be investigated using a model of an elastomeric parallel-plate capacitor. The analysis suggests that the stress-induced strain decreases with the electrode width of the elastomeric capacitor. The dielectric elastomer actuation is electromechanically stable even up to the breakdown voltage, and it therefore may not incur to pull-in instability. Based on the insight gained from the capacitor model, discrete electrode array is designed to decrease the confinement effects. The elastomer actuator design features a higher actuation force and a lower stiffness, as compared to the air-gap electrostatic comb actuator with silicon flexures. In addition, they are resistant to shock and dust blockage.

Chapter 3 presents surveys and experiment the fabrication methods to realize dielectric elastomer actuators with embedded electrodes. The embedded electrodes has a two-level microstructure of discrete electrodes and thin continuous interconnects. The electrode design allows actuation of the compliant elastomer. Relevant fabrication methods are experimentally tested to make the two-level electrodes. In addition, methods for processing and micro-patterning dielectric elastomers are also investigated.

The Second Part studied thermal micro-actuator designs which integrate a silicon skeleton in a thick polymeric block. In Chapter 4 to 8, the focus is mainly on a symmetric meandering silicon skeleton. Subsequently, other skeleton designs are also explored. Chapter 9 deals with a design with an asymmetric silicon skeleton, whereas Chapter 10 present a design with a V-shape silicon skeleton.

Chapter 4 introduces a design concept to enhance linear thermal expansion

using a bonded polymer. The actuator design consists of a symmetric meandering silicon skeleton and polymer filling in the gaps of the skeleton. Confinement by the interfaces with silicon skeleton directs polymeric expansion in the actuation direction and leads to the strain enhancement. Theoretical and numerical models show that this composite actuator can deliver high actuation stress at a strain as much as the unconstrained polymer alone.

Chapter 5 studies thermo-elastic responses of a polymeric layer, which is bonded between two rigid plates. Closed-form solutions of the thermally induced strain and stress are obtained using the 'mean pressure' method. The analytical model is validated with finite element models. The closed-form solution and parametric study show that the apparent thermal expansion increases at an decreasing rate with respect to the aspect ratio of the bonded polymeric layer. In addition, the study determines the finite confinement width at or above which strain enhancement is achieved to a large extent.

Chapter 6 presents numerical and theoretical models to evaluate electro-thermal responses of a polymeric actuator with an embedded skeleton. The skeleton is made of silicon and has a symmetric meandering layout. An electro-thermal model for the actuator is obtained by straightening the meandering heat conduction path with appropriate assumptions. It predicts successfully the temperature distribution of actuator under resistive heating. In addition, the actuation stroke is analytical determined using the thermo-mechanical equation derived in Chapter 5. The analysis shows that the polymeric actuator with the embedded skeleton can deliver highly planar and rectilinear motion and exhibits improved heat transfer, as well as, a fast time response.

Chapter 7 presents strategies of material selection for building a powerful polymeric actuator with an embedded skeleton. The study surveys various component materials in terms of their thermal characteristics and themo-elastic actuation capabilities. The study shows the possibly optimum combinations of polymer and skeleton materials to improve various design criteria, such as apparent coefficient of thermal expansion, stiffness, effective actuation stress and work density. Furthermore, the study shows that Poissons ratio and bulk modulus of polymer are important to the actuator performance.

Chapter 8 presents design optimization of a polymeric actuator with an embedded skeleton. The optimization tunes volume fractions of the polymer and skeleton materials to optimize the overall actuator performance without perturbing the overall geometry. In addition to the volume fraction of polymer, the bond width, layer thickness, and aspect ratio of polymer component are identified as important design parameters. In addition, the path length and layout of skeleton component also affect the actuator performance.

After a few preceding chapters on the actuator design with a symmetric skeleton, another two chapters will present the designs with other skeleton layouts, which result in different motion characteristics.

Chapter 9 presents a polymeric thermal bender that embeds an asymmetric skeleton. The asymmetric skeleton consists a meandering segment and a straight segment, which are connected at the tip. Polymeric filling is mainly located in the meandering segment and contributes to longitudinal expansion that bends the actuator towards the straight segment. This configuration is very different from a typical asymmetric actuator made of a single material. It features a large bending motion, and a large lateral force at a low driving voltage.

Chapter 10 presents a polymeric micro-actuator design that embodies a V-shape meandering silicon skeleton in a SU-8 epoxy block. The comparison with a V-shape silicon thermal actuator shows that the present actuator design out-performs its counterpart in many aspects: a large apex motion and a large apex force, at a lower temperature rise and a lower input power. The large improvement in thermal actuation is a result of using the confined epoxy. In additin, a parametric study shows that a narrow design for the V-shape meandering skeleton could achieve a large apex motion, as good as a wide design.

All successful embodiments show benefits using the confined polymers for effective thermal actuation. In the final chapter, concluding remarks are provided. In addition, future work and research directions are projected.

PART 1

Actuators Using Dielectric Elastomers

Chapter 2

Dielectric Elastomer Actuator with Embedded Electrodes

This chapter [1] presents a novel design of actuated elastomers using rigid, vertical standing electrodes. The electrodes are designed to have a small width, small gap and large depth in order to produce a large electrostatic force at a moderate voltage. The short and discrete electrode design reduces its constraining effect on soft elastomers. This novel design embodies lateral stacking to accumulate small strain into an adequate displacement for micro-actuation. Analytical and numerical analyses are performed to evaluate the force-displacement characteristics of the elastomer actuators. It is shown that actuation of the novel design is not limited by the electrostatic pull-in instability. The actuator is capable of traveling a large range at a high electric field. A theoretical benchmark comparison with a conventional air-gap electrostatic comb drive indicates that the new elastomer actuator promises large flexibility, large attraction force, and robustness against shock and dust blockage.

2.1 Introduction

Electrostatically squeezed elastomers have recently been used to produce large strain for robotic applications [118]. A basic elastomer actuator is an elastomeric capacitor, with two layers of soft electrodes sandwiching a soft dielectric elastomer. When charged, the soft electrodes attract each other, simultaneously squeezing and stretching the soft dielectric layer. A typical layer of the dielectric elastomer is 25 - 50 μm thick. It requires a very high driving voltage in the order of several kilovolts to produce adequate Maxwell stress, as well as to produce the large strain. However, it consumes no current at the static operation. Dielectric elastomer actuators can produce strain and stress in a range comparable to natural muscles [118].

Macroscopic-size elastomer actuators have been successfully used for large-strain actuation. This inspires efforts to scale them down. The main motivation for their miniaturisation is to generate a high electric field at a moderate driving voltage across a small gap. Multi-layer stacking of thin films has been demonstrated for this purpose [126]. The materials used for making soft electrodes usually contain

[1] This chapter is based on a paper published in the Journal of Micromech. Microeng. [84]

rigid conductive particles and volatile binders, for example carbon grease or silver-loaded gels [118, 126]. The conductive particles have a size of several microns and the size limits the minimal thickness of the soft electrode. In addition the volatile binders degrade over time, causing the conductive particles to loosen off or the soft electrodes to delaminate. Therefore, these constituent materials for the compliant electrodes may not be suitable for the device miniaturization. Furthermore, these materials are not compatible with IC fabrication processes. Some work has been done to construct stiffer electrodes using compatible materials. For example, Benslimane *et al.* [13] used a silver layer of 0.11 μm on a silicone elastomer of 50 μm and Pimpin *et al.* [119] used slit electrodes of gold to reduce the constraining effect of the stiffer electrodes.

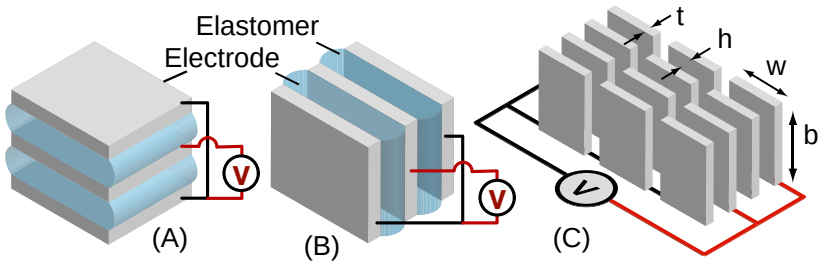

Fig. 2.1 Schematic view of (a) layer stacking; (b) lateral stacking (on a hidden substrate beneath); (c) vertical standing electrodes for many lateral stacking

In principle, miniaturisation of the electrostatically squeezed elastomers is expected similar performance to air-gap electrostatic actuators or multi-layer actuators. However, physical properties of the soft elastomers do not allow them to be miniaturized into those conventional designs if they are to work efficiently. The soft elastomers are incompressible. They have higher dielectric constants, and are therefore capable of generating higher electrostatic forces than air-gap electrostatic actuators at the same driving electric field. But, they are softer and cannot be patterned as tall structures on their own. For example, a silicone rubber has a dielectric constant of 2.6 and a Young's modulus of 1 MPa; and polyurethane elastomer has a dielectric constant of 7.0 and a Young's modulus of 17 MPa [116]. Miniaturization of multi-layer stacked designs is possible, but this is time consuming to deposit layer by layer (Fig. 2.1a). Also, it is difficult to make reliable interconnects across the very thin layers. If no stacking is used, a single thin layer itself is too weak to do useful work. These difficulties with existing designs motivate the search for a new elastomeric actuator design, which exploits the specific physical properties of the soft elastomer and suits the miniaturization using IC fabrication process.

2.2 Actuator Design

We propose a novel design using vertical standing electrodes for actuating elastomer fillings (Fig. 2.1b). The electrodes (Fig. 2.1c) are designed to have small width (w), large height (b), small thickness (t), and be placed at small gap intervals (h). A typical design of the electrodes is 6-9 μm long, 25 μm tall and 3 μm wide, with gaps of 2-3 μm. The electrodes are wired up through 1-2 μm thick comb-like compliant interconnects. The gaps between the standing electrodes are filled up with soft elastomers. The electrodes are charged using alternating voltage polarity so that two neighboring electrodes are squeezing the intermediate filling, which will change in thickness and will bulge over the electrode edges. The new design uses short and discrete pieces of rigid electrodes to reduce the constraining effect on the elastomer during actuation. This makes the present design different from the existing elastomeric actuators with layers of soft electrodes (Fig. 2.1a).

The new actuator is basically a lateral stack of many elastomer-filled capacitors with vertical electrodes standing side by side. The stack can be designed with various electrode layouts, promising possibilities of both in-plane and out-of-plane motion generation. Conceptually, three major fabrication steps can make a functional device using the proposed design, namely a deep etching or electroplating step to build the electrode array, a step to fill the gap with liquid prepolymer and a third step of device release. Since the electrode array can be built in a single fabrication step, the present design is supposed to involve less fabrication steps than for the multi-layer design.

2.3 Linear theory

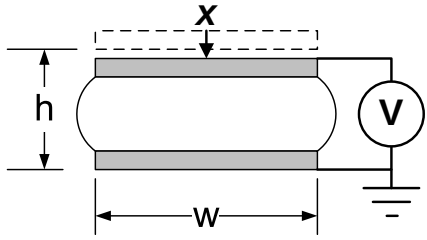

Fig. 2.2 A schematic view of an elastomer capacitor

The design concept of the actuated elastomers with rigid electrodes has been presented in the preceding section. Here, we will evaluate the displacement characteristic and actuation limit of the design using a theoretical analysis. A simple model of elastomer-filled capacitor (see Fig. 2.2) is used for the analysis with the following assumptions: 1) The electrodes are rigid and infinitely deep (refer to di-

mension b). 2) Interconnects among the electrodes have negligible stiffness. 3) The elastomer is bonded perfectly to the rigid electrodes, with no slipping at interfaces. 4) The elastomer is also infinitely deep. 5) The elastomer is incompressible in volume but able to undergo shape change [118]. 6) The elastomer is non-conducting. 7) The elastomer is subjected to a uniform electric field with a negligible fringe field. 8) The elastomer is passive and not electrostrictive.

The model of the elastomer-filled capacitor (Fig. 2.2) resembles the geometry of a rubber block bonded to rigid plates. Hence, the effective stiffness of the capacitor can be approximated with the formula of the bonded rubber undergoing a small displacement [44]. The bonded rubber exhibits higher compressive stiffness than a free rubber block because additional hydrostatic pressure is developed over the bonded and constrained surfaces. This can be represented by a higher effective Young's modulus. The effective modulus E_c of the bonded block is related to the intrinsic modulus E and a shape factor or an aspect ratio, which is defined as the dimension of the bonded surface (i.e. the plate width w) over the dimension of the free surface (i.e. rubber height h) [44]:

$$E_c = \frac{E}{3}\left(4 + \left(\frac{w}{h}\right)^2\right) \tag{2.1}$$

The compressive stiffness of the bonded rubber block is thus

$$k_c = \frac{E_c A}{h} = \frac{EA}{3h}\left(4 + \left(\frac{w}{h}\right)^2\right) \tag{2.2}$$

where A is area of the electrode plate.

If a voltage V is applied across the elastomer filling between the rigid electrode plates, an electrostatic force F_e develops:

$$F_e = \frac{1}{2}\left(\frac{\epsilon A}{h^2}\right)V^2 \tag{2.3}$$

where ϵ is the permittivity of the dielectric elastomer. This electrostatic force will compress the elastomer.

The normal displacement h of the compressed rubber block is obtained by dividing the electrostatic force by the effective elastomer stiffness:

$$\Delta h = \frac{F_e}{k_c} = \frac{3\epsilon V^2}{2Eh\left(4 + (w/h)^2\right)} \tag{2.4}$$

The strain e_c induced to the rubber block is thus the displacement divided by the elastomer height:

$$e_c = \frac{\Delta h}{h} = \frac{3\epsilon V^2}{2E\left(4h^2 + w^2\right)} \tag{2.5}$$

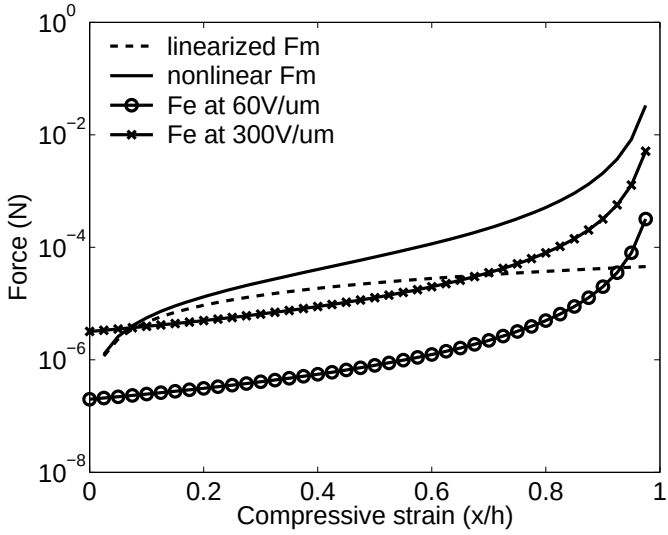

Fig. 2.3 Mechanical and electrostatic forces for an elastomer capacitor with following parameters: an initial gap (h) of 2 μm, an electrode width (w) of 5 μm, unit depth (b) of 1 μm, Young's modulus (E) of 1 MPa, and dielectric constant of 2.5

2.4 Non-Linear theory

The elastomer films with soft electrodes are prone to electro-mechanical instability when activated at a very high electric field. A large compressive stress is induced at the high field and it may go beyond the stress level above which the film can structural withstand. Above this stress level, the film locally contracts rapidly, leading to film thinning and ultimately electrical breakdown and shorting [116]. This electro-mechanical instability is also named as the pull-in instability. Since the unstable elastomer film is subjected to a large-strain contraction, a nonlinear analysis is needed to study the phenomenon of pull-in instability.

The linear stiffness of a bonded rubber was given in Eq. 2.2 based on the small-displacement assumption. When the rubber block is compressed further, the decreasing thickness of the block results in an increase in its shape factor. Integrating the incremental force as derived from Eq. 2.2 , Lindley [94] arrived at the nonlinear spring force F_m for the perfectly bonded rubber undergoing a large compressive displacement x:

$$F_m = EA\left\{\frac{4}{3}\ln\left(\frac{h}{h-x}\right)+\frac{2}{3}\left(\frac{w}{h}\right)^2\left[\left(\frac{h}{h-x}\right)^2-1\right]\right\} \tag{2.6}$$

When the nonlinear electrostatic force is in balance with the nonlinear mechanical spring force, the equilibrium displacement of the squeezed elastomers can be determined. For example, Fig. 2.3 shows that the upper plate of a 5μm-wide, 2μm thick elastomer-filled capacitor slightly displaces under electrostatic attraction of

120 V - 600 V. The nonlinear analysis estimates smaller displacements than the linear analysis does. This yields an equilibrium displacement of 8.3 nm at 120 V, and 221.5 nm at 600 V. However, the linear analysis yields the equilibrium displacement of 8.6 nm at 120 V and 292.8 nm at 600 V, which are 4.2% and 32.2% higher than the respective nonlinear estimations. However, this example shows that the induced strain is small at a moderate driving voltage. For example, the electrically induced strain at 120 V is only 0.4% and the error between nonlinear and linear estimations is just 4.2%. Therefore, it is found that the linear analysis is good enough for the small-displacement estimation.

If the deformed elastomer is compressed further to a thickness much smaller than that at the equilibrium state, the nonlinear mechanical spring force is increasing tremendously with the closing gap. The mechanical spring force is observed to be always larger than the electrostatic attraction force (Fig. 2.3). It tends to restore the over deformed elastomer back to its equilibrium state. However, a linear analysis using a constant initial stiffness leads to a wrong finding that an electrostatic force exceeds a linearized mechanical spring force at a large compressive displacement off the equilibrium position.

2.4.1 *Pull-in Analysis*

The example in Fig. 2.3 illustrates that the elastomer filled parallel-plate capacitor may undergo a large deformation without electrical pull-in instability. Here, we will formally investigate the stability issue using the idealized model of the capacitor and an analysis method similar to that for an air-gap parallel-plate electrostatic actuator [128]. It is assumed that the lower plate of the elastomer-filled capacitor is stationary and the upper plate is movable under the electrostatic attractive force. As the electrostatic force attracts the upper plate, a nonlinear mechanical force induced by the squeezed elastomer will resist the upper plate in opposite direction to the electrostatic force until the two forces balance out. If the upper plate is perturbed from the equilibrium position, it is a question whether the upper plate returns to the equilibrium position.

As the gap between the parallel plates closes under an electrostatic force, the upper plate travels at a compressive displacement x. The net compressive force F_{net} on the upper plate is the sum of electrostatic force F_e and the nonlinear mechanical spring force F_m (from Eq. 2.6) as below:

$$\begin{aligned} F_{net} &= F_e - F_m \\ &= \frac{1}{2}\frac{\epsilon A V^2}{(h-x)^2} - EA\left\{\frac{4}{3}\ln\left(\frac{h}{h-x}\right) + \frac{2}{3}\left(\frac{w}{h}\right)^2\left[\left(\frac{h}{h-x}\right)^2 - 1\right]\right\} \end{aligned} \quad (2.7)$$

The net force is zero at equilibrium position. If the upper plate is perturbed from the equilibrium position, the small change in the net force determines whether the upper plate will be restored back to the equilibrium position. The small change

in the net force resulting from the small perturbation displacement can be written as

$$\delta F_{net} = \frac{\partial F_{net}}{\partial x}\delta x \tag{2.8}$$

The first derivative of the net force is

$$\frac{\partial F_{net}}{\partial x} = \frac{\varepsilon A V^2}{(h-x)^3} - EA\left\{\frac{4}{3}\left(\frac{1}{h-x}\right) + \frac{4}{3}w^2\left(\frac{1}{h-x}\right)^3\right\} \tag{2.9}$$

Replacing the electrostatic force with the mechanical force at the equilibrium position, the first derivative of the net force becomes:

$$\frac{\partial F_{net}}{\partial x} = \frac{4}{3}EA\left(\frac{1}{h-x}\right)\left\{2\ln\left(\frac{h}{h-x}\right) - \left(\frac{w}{h}\right)^2 - 1\right\} \tag{2.10}$$

The stability characteristic of the actuator depends on the sign of the first derivative. If the first derivative is positive, the perturbation force is in the same direction as the perturbation displacement; thus it may lead to the collapse of the upper plate onto the bottom one. However, if the first derivative is negative, the perturbation force is opposite to the direction of the perturbation displacement, and it is capable to restore the upper plate to the equilibrium position.

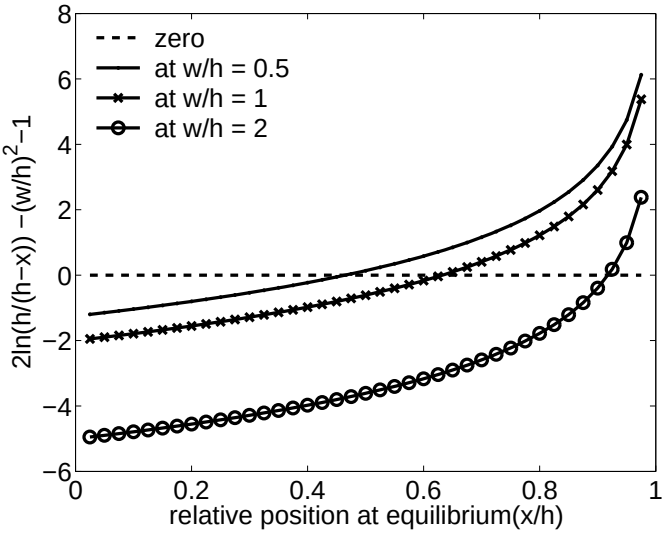

Fig. 2.4 A normalized function that determines the sign of the first derivative of net force with respect to the relative position at equilibrium

The upper plate can move at most through the gap between the electrode plates before touching the bottom. In other words, the compressive displacement x is always smaller than the initial gap h. The remaining gap $(h-x)$ is always positive.

Therefore, the sign of the first derivative is solely dependent on the normalized terms in the brace of Eq. 2.10 . At the point where the derivative is zero, the bonded elastomer actuator is about to become unstable under the electrostatic attractive forces. The zero-crossing point is the point at which the electromechanical pull-in sets on. Therefore , it is the maximum displacement that the elastomer-filled capacitor can achieve. Fig 2.4 shows a function of the normalized term with respect to the equilibrium position. The normalized function crosses zero at different equilibrium positions, depending on the aspect ratio w/h. The wider the electrode is, the larger the zero-crossing position is. For example, an actuator with electrodes of a low aspect ratio (at 0.5) undergoes a pull-in at 46% of the initial gap; whereas an actuator with electrodes of a moderate aspect ratio (at 2.0) undergoes a pull-in at 92% of the initial gap.

A typical design of the elastomer-filled actuator has electrodes of the aspect ratio greater or equal to 2. At the aspect ratio of 2 and a gap of 2 μm, the pull-in is expected to happen at 92 % strain and at a prohibitive high voltage of 983 V. The pull-in field is 491 V/μm, which is far greater than the field strength of most dielectric elastomers. For example, Nusil CF19-2186 silcone rubber has a field strength of 235 V/μm, Dow Corning Sylgard 186 silicone rubber has field strength of 144 V/μm, and Dow Corning HS3 silicone rubber has field strength of 72 V/μm [116]. It is concluded that the dielectric elastomers may fail first because of the electrical breakdown, rather than the electromechanical pull-in that occurs at a much higher electric field. It implies that the electromechanical pull-in instability is not a limiting factor to the actuation performance of the rigidly bonded elastomer capacitor. Instead, other factors may be limiting the maximum achievable strain of the elastomer capacitor, for examples, the breakdown voltage and the bond strength over the electrode/elastomer interfaces.

2.5 Linear Analysis for Stacked Design

The linear and nonlinear analyses above show that the elastomer capacitor deforms slightly under the electrostatic forces at operating voltages. If the actuator is to operate under a moderate voltage of 120V, a linear analysis should be sufficient to approximate the displacement characteristics of the elastomer capacitor. The linear analysis can also be extended to stacked actuators, which assemble many units of the basic elastomer capacitor.

2.5.1 *Normal Stack*

Stacking many elastomer capacitors in series can accumulate the small displacement of each unit into a larger overall displacement. In this analysis, we use a stacked model comprising of n identical capacitors, which have rigid electrode plates of thickness t and an elastomer film of thickness h. It is assumed that the plate thick-

ness is comparable to the elastomer thickness, but the plate is rigid and undergoes negligible deformation under electrostatic force. The effective strain e for the serial-stacked actuator is obtained by dividing the sum of displacements over the total thickness of the stack:

$$e = \frac{n\Delta h + 0}{nh + (n+1)t} = \left(\frac{nh}{nh + (n+1)t}\right) e_c \tag{2.11}$$

where n is the number of rubber blocks and $n + 1$ is the number of rigid plates

The effective strain depends very much on design parameters of an individual capacitor, in particularly, the gap and the width. The influences of these parameters are shown in Eqs. 2.2 and 2.4. The electrostatic forces increase with the decreasing gap or with the increasing width. On the other hand, the effective stiffness of the bonded elastomers is related to the gap and the width in conflicting trends. It decreases with the increasing gap or with the decreasing width. Therefore, there may exist an optimum combination of the design parameters that maximize the electrostatic force while minimizing the effective stiffness.

The series stacking can accumulate small strain into a larger total displacement. However, it does not help accumulate electrostatic forces. The forces generated in the elastomer are independent of the series stacking. They are solely determined by the electrostatic field, the electrode area, and the dielectric constant regardless of the Young's modulus of the dielectric elastomer. Instead, the forces can be accumulated through parallel stacking, which increases the total electrode area.

2.5.2 *Lateral Bimorphs*

A lateral bimorph is formed by bonding two stacks of elastomers actuators side by side (Fig. 2.5a). The two stacks are structurally connected in parallel but electrically separated. The combined structure of the two-bonded stacks bends laterally when one of the two stacks is electrically charged while the other is kept passive. The combined structure behaves like a piezoelectric bimorph, and it can transform normal compressive strains into a lateral displacement. We will therefore refer to it as an 'elastomer bimorph'. The elastomer bimorph is relatively soft and weak to move against an external load. This distinguishes it from the relatively stiffer piezoelectric bimorph. As the elastomer bimorph operates on a similar actuation mechanism like a piezoelectric bimorph, its displacement characteristics can thus be estimated using a similar analysis method for thermal bimetals [145].

It is assumed that the bimorph consists of an active stack of cross-sectional width W_1 and an inactive stack of cross-sectional width W_2. Each stack may consist of parallel electrodes of smaller widths, which influence the effective Young's modulus of elastomers according to Eq. 2.1 . Without loss of generality, we can assume that each stack consists of a series of capacitors with effective modulus computed from the actual electrode widths, which may be smaller than the full cross-sectional widths. The active and the passive stacks have respective effective flexural rigidities

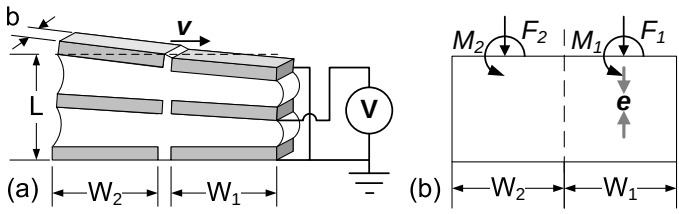

Fig. 2.5 A schematic view of an elastomer bimorph (a) showing dimensions (3-D); (b) showing forces and moments (2-D)

and cross-section areas, i.e. E_1I_1 and A_1, and E_2I2 and A_2. When the bimorph bends under an induced strain in the active stack, forces and moments are developed and applied to both the active and the inactive stacks as F_1, M_1 and F_2, M_2 respectively (Fig. 2.5b). The induced strain e is as calculated from Eq. 2.11 for a stack of capacitors undergoing normal compression. Since the deformation occurs under the induced strain, the cross section of the bimorph should have zero total force and zero total moment such that

$$F_1 + F_2 = 0 \tag{2.12}$$

$$M_1 + M_2 - \frac{1}{2}F_1W_1 + \frac{1}{2}F_2W_2 = 0 \tag{2.13}$$

Along the longitudinal interface between the two stacks, the interfacial strains calculated from both stacks are equal. The strains are a sum of axial strain, bending strain and induced strain:

$$\frac{F_1}{E_1A_1} + \frac{W_1M_1}{2E_1I_1} + e = \frac{F_2}{E_2A_2} - \frac{W_2M_2}{2E_2I_2} \tag{2.14}$$

Substituting Eq. 2.12 into Eq. 2.13 gives axial forces in term of moments

$$M_1 + M_2 - \frac{1}{2}F_1W_1 + \frac{1}{2}F_2W_2 = 0 \tag{2.15}$$

or

$$F_1 = -F_2 = \frac{2\,(M_1 + M_2)}{(W_1 + W_2)}$$

The moments are related to the radius of curvature such that

$$M_1 = \frac{E_1I_1}{R} \qquad M_2 = \frac{E_2I_2}{R} \tag{2.16}$$

Substituting Eq. 2.15 and Eq. 2.16 into Eq. 2.14, we have the curvature as

$$\frac{1}{R} = -e\left[2\left(\frac{1}{E_1A_1} + \frac{1}{E_2A_2}\right)\left(\frac{E_1I_1 + E_2I_2}{W_1 + W_2}\right) + \left(\frac{W_1 + W_2}{2}\right)\right]^{-1} \tag{2.17}$$

If the two stacks are of the same cross-sectional area A, the same cross-sectional width W, moment of inertia I and thickness, and the same modulus E under the small-strain assumption, Eq. 2.17 can be simplified as:

$$\frac{1}{R} = -e\left[2\left(\frac{2}{EA}\right)\left(\frac{EI}{W}\right) + W\right]^{-1} = \frac{-e}{W + 4I/AW} \tag{2.18}$$

Assuming the bimorph has a rectangular cross-section and has an electrode width W of several microns, i.e. much smaller than the length, the moment of inertia of that cross-section is determined as $I = bW3/12$ and the cross-section area is $A = bW$. Substituting these geometrical parameters into Eq. 2.18, we have a simplified expression:

$$\frac{1}{R} = \frac{-3e}{4W} \tag{2.19}$$

A lateral displacement for a clamped-free bimorph of length L is thus obtained as:

$$v = \frac{L^2}{2R} = \frac{-3eL^2}{8W} \tag{2.20}$$

It is concluded that the lateral displacement at the tip of the elastomer bimorph is proportional linearly to the induced strain but inversely proportional to the sectional width. The lateral displacement at the tip is amplified such that it is $3L/8W$ time larger than the total compressive displacement of the active stack, i.e. eL.

2.6 Validation

The analytical calculation in the preceding section provides insight into displacement characteristics of an ideal elastomer capacitor or stacks of the capacitors. The analysis shows that constraining effects increase with wider electrodes and narrower elastomer filling. It also describes the basic relationships among electromechanical actuation strain, material properties and geometric parameters of the elastomer capacitors. However, the analysis neglects the effect of the electric fringe field. It does not fully account for the influence of boundary conditions on the incompressible elastomers. In addition, it may not be able to predict more sophisticated geometry of the inserted rigid electrodes of varying shapes.

The nonlinear analysis shows that the elastomer-filled parallel-plate actuator undergoes small strain at the operating range of driving voltage. The analysis also shows that it can be driven at a very high voltage to achieve a larger strain, but it may be prone to failure caused by the electrical break down at the high field. Since this type of actuator operates in the range of small strain, the actuator performance can well be simulated using a linear finite element analysis, which is capable of modelling more sophisticated geometry than analytical models do. In the finite element analysis, it is assumed that: 1) Both the electrodes and elastomer filling have infinite depth. 2) The elastomer is perfectly bonded to the stiff electrode. 3) Interconnects

between the electrodes have negligible stiffness. 4) The elastomer is only subjected to electrostatic force, without electrostriction effect. 5) The elastomer undergoes small displacements.

These assumptions are identical to those for the linear analytical model. However, they differ in the facts that: 1) The stiff electrodes are slightly deformable. 2) Lateral stretching of elastomers is slightly restrained by neighbouring units. 3) Constraining effects of boundary conditions are included. 4) Electric fringe field is taken into account.

The simulation is done using a commercial finite element package, ANSYS [2]. The finite element model of the elastomer actuators consists of structural elements, electric elements, and infinite electric elements. The structural elements (PLANE82) are used to model displacement fields of electrodes and elastomers. The electric elements (PLANE121) are used to model electric pontential fields in dielectric elastomers and surrounding air, whereas the infinite electric elements (INFIN110) are used to model an open boundary of a 2-D unbounded electric field. These elements are 2-D 8-node quadrilateral elements.

Sequentially coupled analyses are performed to simulate the static electromechanical behaviour of an elastomer capacitor and an elastomeric bimorph. The first analysis computes the electric potential field, together with Maxwell stress tensor [115], over a domain outside the electrodes of fixed potential. The second analysis computes the displacement field of the whole domain including both stiff electrodes and soft dielectric elastomers under the loads of the computed Maxwell stress. The analyses can be iterated for more converged and accurate electromechanical results, but a single iteration suffices for small-strain response of the present examples.

Two examples are modelled: an elastomer capacitor and an elastomer bimorph. They consist of silicon electrodes, a filling of PDMS (poly-dimethyl-siloxane, also termed silicone rubber), and surrounding of air. Physical properties of these materials are listed in Table 2.6 [34, 116]. Their geometrical dimensions are listed in Table 2.6.

Fig. 2.6a shows the deformed finite element model of the elastomer capacitor. The bottom electrode of the capacitor model is fixed, while its top electrode is free to move under an electrostatic potential of 120 V. Fig. 2.7a shows that the displacement of the top electrodes is decreasing with the increasing width of electrodes, at a 2-μm gap. Both analytical and finite element models predict the same trend of displacement. The numerical prediction is slightly higher than the analytical prediction at electrode widths larger than 2 μm. However, the discrepancy worsens at widths smaller than the gap. This can be explained by the fact that the analytical model neglects the fringe field, which contributes to larger electrostatic forces at the small electrode widths.

Fig. 2.6b shows the deformed finite element model of the elastomer bimorph. The bimorph consists of two stacks of elastomer capacitors. Structurally, one end of

Table 2.1 Physical properties of materials

Physical Properties	Silicon [34]	PDMS [116]
Young's modulus	165 GPa	1.0 MPa
Poisson's ratio	0.22	0.49
Dielectric constant	-	2.5

the bimorph is fixed while the rest is free to move. Electrically, one of the two stacks is activated at 120 V whereas the other is kept passive. Fig. 2.7b shows that the lateral tip displacement of the bimorph is decreasing with the increasing electrode width. In this example, the analytical results agree well with the finite element result over most range of the electrode width, except at electrode widths smaller than the 2-μm gap. For the electrode with less than 2-μm width, the analytical result becomes much larger than the finite element results. The discrepancy arises because the analytical model over-estimates the obtainable lateral bending by assuming that both the active and the passive stacks share the same displacement at the interface and neglecting a possible slip across the physical interface between the two stacks. The inter-stack interface is connected through a strip of 2 μm wide elastomer filling. The soft interface filling may shear and rotate. Thus, the compression in the active stack may not be able to transmit to the passive stack as effectively as in the analytical assumption, resulting in the smaller lateral tip displacement as predicted by the finite element model when the interface deformation manifests at small electrode widths.

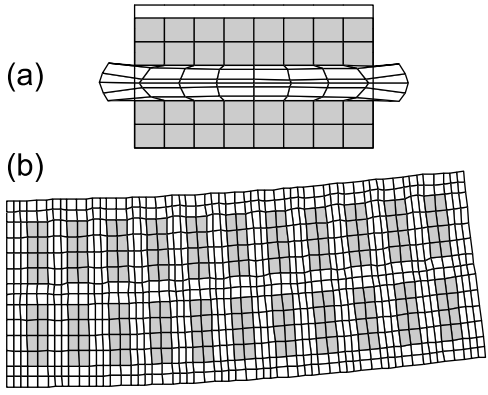

Fig. 2.6 Deformed finite element models in exaggerated scale: (A) an elastomer capacitor; (B) an elastomer bimorph

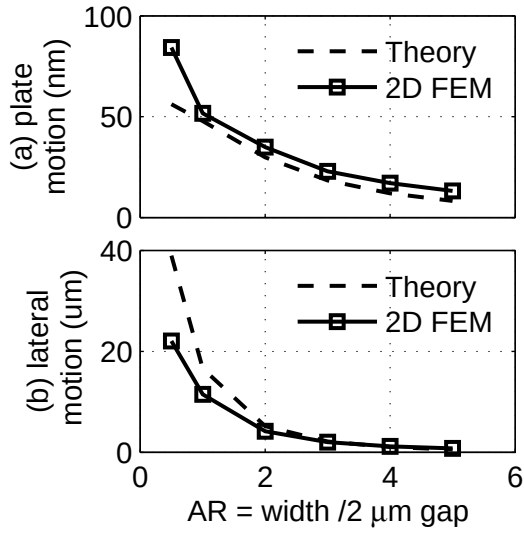

Fig. 2.7 Motions versus aspect ratio of electrode (width/gap) for (A) an elastomer capacitor; (B) an elastomer bimorph

Table 2.2 Geometrical dimensions

Specification	Dimensions
Electrode thickness	2 μm
Electrode length	1 - 10 μm
Gap between electrodes	2 μm
Spacing between stack	2 μm
Stack number	20
Stack length	86 μm

2.7 Benchmarking

The proposed elastomer actuators are driven by electrostatic forces, like air-gap electrostatic actuators. However, the elastomer actuators differ from the latter in that their electrodes of opposite voltage polarity are all embedded structurally in the deformable elastomers. In other words, there are no stator electrodes. The electrostatic forces among these electrodes cancel out each other while squeezing the elastomers. This means that the actuation forces and the resulting strain are distributed over the stacked elastomers and electrodes. In contrast, movable electrodes for the typical air-gap electrostatic actuators are supported by suspension flexures and they are structurally disconnected from the stator electrodes. Electrostatic forces are accumulated to deform the suspensions of lumped flexibility through the movable electrodes.

Table 2.3 Dimensions for bimorphs

Specification	Dimensions
Electrode thickness	2 μm
Electrode length	5 μm
Gap between electrodes	2 μm
Spacing between stack	2 μm
Electrodes across stack	4
Electrodes along stack	16

Table 2.4 Dimensions for comb drives

Specification	Dimensions
Suspension Length	70 μm
Suspension Width	2 μm
Finger thickness	2 μm
Finger length	5 μm
Gap between fingers	2 μm
Number of fingers	18

It is interesting to compare the actuation performances of both types of electrostatic actuators. The comparison also serves to gain additional insight into the potential of the new elastomer actuators. We choose to compare an actuated elastomer bimorph with a lateral comb drive (Fig. 2.8). Both actuators perform the same function of moving a shuttle laterally. They are designed to occupy roughly the same footprint, and to have the same electrode thickness and gap width. However, their configuration differs. The elastomer bimorph consists of four elastomer stacks on each side of the moving shuttle. Capacitors in the stacks are made of PDMS and silicon electrodes. Thus, the elastomer stacks are inherently flexible in

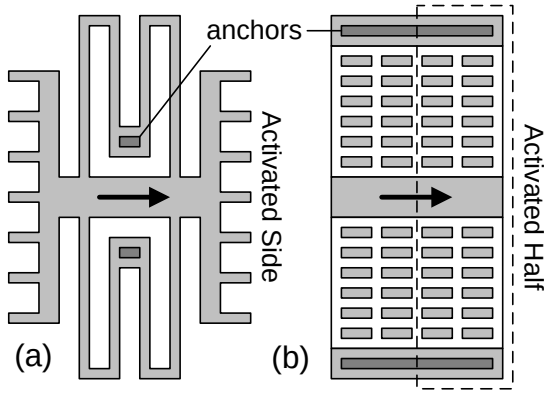

Fig. 2.8 Schematic view of (a) lateral comb drive and (b) lateral bimorph

Table 2.5 Performances of lateral actuators

Specifications	Lateral comb	Elastomer bimorph
Area (μm×μm)	38×138	30×140
Lateral stroke @ 120V (μm)	0.12	0.23
Lateral frequency (kHz)	234.15	48.93
Lateral stiffness kx (μN/μm)	12.30	0.28
Vertical stiffness ky (μN/μm)	377.79	6.19
Cross-axis sensitivity (ky/kx)	30.71	22
Electric strength (V/μm) [113, 116]	72.5-176	72-235
Driving capacitance (fF)	2.150	4.815
Maximum electric energy density (kJ/m^3)	4.3-25.4	11.9-126.6

the lateral direction. On the other hand, the comb drive is equipped with a pair of bent flexural suspensions on each side of the shuttle. The flexures are made of stiff silicon. They have to be designed to be long and thin to achieve the required lateral flexibility. The geometrical dimensions of both actuators are listed in Tables 2.7 and 2.7 respectively.

Two-dimensional (2D) finite element analyses are performed for both actuators based on the assumptions described in the preceding section. Although the plane strain assumption is used for modeling the high-aspect-ratio actuators, a unit thickness of 1 μm is used in the 2D modelling for computing stiffness and frequencies. The stiffness per unit thickness is convenient for performance comparison. The simulation shows that the elastomer actuator produces a larger lateral stroke at 0.23 μm at a driving voltage of 120 V. A higher lateral flexibility and a higher generated force in the elastomer actuator attributes to the larger displacement. The comb drive moves less under the same driving voltage. However, it has much higher stiffness and lateral resonant frequencies. The detailed simulation results are listed in Table 2.7.

The evaluation shows that the elastomer actuator has very low stiffness per unit thickness: a lateral stiffness is 0.28 N/m and a vertical stiffness is 6.19 N/m. Such a low vertical stiffness is disastrous for an air-gap lateral comb drive because it causes side instability [88], where the movable combs risk moving vertically and touching the stator comb of opposite voltage polarity. However, it is not a problem to the elastomer bimorph whose electrodes are completely cushioned by dielectric elastomers and protected from the electromechanical instability. The low stiffness over the small footprint may be desired for some applications, which cannot be satisfied by the stiff and intricate silicon suspensions for the comb drive. However, if a higher stiffness is desired, the elastomer bimorph has some room for performance tuning by stiffening the elastomer with longer rigid electrodes or narrower gaps.

Since the elastomer actuator is made of soft dielectrics of higher dielectric constants, it could produce higher electrostatic forces than the air-gap electrostatic actuators do when subjected to the same electric field. In addition, some soft dielectric elastomers may have higher dielectric strength than the air. The actuator

made of these elastomers may therefore operate at a higher driving voltage and is capable of storing a higher maximum electric energy given the same volume. The electric energy density depends on the actuator geometry, the dielectric strength and the dielectric constant [113, 116]. The present evaluation shows the elastomer bimorph stores higher electric energy density in the range between 11.8 and 126.6 kJ/m^3. However, the air-gap comb drives in this example stores less electric energy density, in the range between 4.3 and 25.4 kJ/m^3.

The two-dimensional analysis is done using a 2-D simplified model without considering interconnect stiffness. It might give a higher displacement estimate than an actual elastomer actuator with interconnects. But, the simplified evaluation defines an upper bound on the displacement characteristics, which the elastomer actuator of high aspect ratio can achieve. The elastomer actuator is deemed robust despite its low stiffness. This is because it is better protected against dust blockage and better damped with elastomer filling. The air-gap electrostatic comb drive does not fare well in these respects. The discussion above has shown advantages and disadvantages of the elastomer actuators.

2.8 Conclusions

We have evaluated the feasibility of electrically actuating elastomers with rigid electrodes for producing micro-motion. The evaluation by analytical and numerical methods shows that the elastomers bonded to the rigid electrodes are stiffened and deform less under an electrostatic force than free elastomers. However, lateral stacking of electrodes, which is introduced in the new design, accumulates small strain into adequate micro-motion. It is also shown that the pull-in instability is not a limiting factor to the actuation range of the bonded elastomer actuators. It is shown that miniaturization of dielectric elastomer actuators with small electrode gaps promises to generate large electrical force and adequate strain at moderate voltages.

The proposed new actuation concept promises a variety of designs and wide range of performance. In particular, the vertically standing electrodes can be designed in various layouts and various ways of stacking, in order to produce either in-plane or out-of-plane motion. The design of the short and discrete electrodes is not only useful for actuating soft electro-passive elastomers, but is also effective in reducing the constraining effect on electrostrictive polymers of higher stiffness. Further works are in progress to realize the new designs of squeezed elastomer actuator.

Chapter 3

Fabrication Methods

This chapter presents a survey and attempts on fabrication methods to make a dielectric elastomer actuator. The actuator design consists of elastomer encapsulant and a two-level microstructure of electrodes and interconnects. The electrode and interconnect geometry affects the actuator performance to a large extent. Two fabrication methods are surveyed and tested to make the multi-level electrodes, namely electro-deposition of copper and deep etching of silicon. In addition, we survey polymer processing methods and evaluate micro-manufacturability of a few dielectric elastomers. We tested trenching filling with liquid pre-polymers. The preliminary tests indicate that it remains challenging to use the present micro-fabrication methods to realize the miniaturized dielectric elastomer actuator with embedded electrodes and interconnects.

3.1 Introduction

Many designs of dielectric elastomer actuators start from a planar structure, which consists of a layer of dielectric elastomer and two layers of compliant electrodes that sandwich the dielectric layer [98,118]. The planar configuration can be built up and becomes more sophisticated by rolling it into a tube, stacking it into multiple layers, or mounting it onto a frame. Despite the variety of final shapes, the initial fabrication steps for the planar structure remain the same. The fabrication steps are based on film deposition methods; for example, spin coating of a liquid pre-polymer, spraying coating of conductive ink, brushing of carbon grease, or sputtering or thermal evaporation of metallic films. The film depositions result in planar structures, which remain largely parallel with respect to the substrate plane.

In the present work, we propose a design of dielectric elastomer actuator with an embedded two-level microstructure of electrodes and interconnects (see Fig. 3.1). The interconnects are thin and they remain planar with respect to the substrate plane, but the electrodes are standing vertically with respect to the plane. The electrodes have a high aspect ratio and they are closely packed with small gaps between each other. The actuation polymeric material fills the gaps and encapsulates

the overall structures of interconnects and electrodes. They contribute to either the electrostriction or the shape change under electric activation. The present actuator design has a more complex geometry of electrodes than the thin-film capacitor, and it is therefore more difficult to fabricate. The fabrication steps are proposed to first form a multi-level microstructure of electrodes and interconnects and then to fill the trenches between electrodes with a polymer.

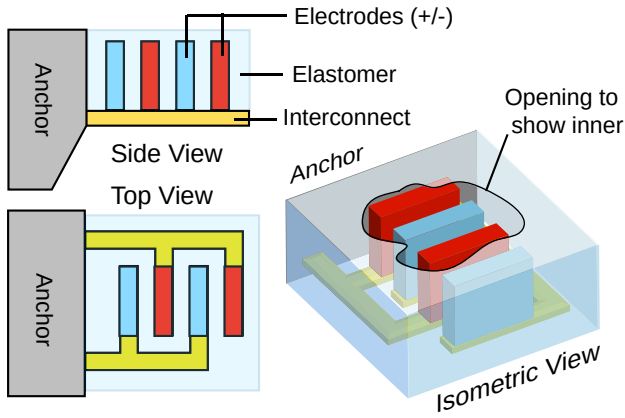

Fig. 3.1 A schematic drawing showing a dielectric elastomer actuator with embedded electrodes and interconnects

3.2 Multi-level Electrodes

The two-level microstructure of electrodes and interconnects serves for both electrical activation and structural reinforcement. The structural reinforcement should be minimized to allow actuation of the soft dielectric elastomer. Therefore, the preferred design consists of an array of discrete electrodes and shallow comb-like interconnects as shown in Fig. 3.2. The array of discrete electrodes and elastomer filling form an array of dielectric elastomer capacitors. Electric capacitance of the capacitors should be maximize to increase actuation stress at a lower voltage. With these design concerns in mind, the preferred embodiment of the electrodes have a small spacing (say 3 μm wide) and a large electrode area at an adequate height (say 30 μm high). The discrete electrodes preferably have a short width (say 6 μm wide). On the other hand, the interconnects should be made as thin as possible (say 1 μm thick) in order to decreases the in-plane stiffness that resist the in-plane actuation of the capacitors. Otherwise, a finite thickness of the interconnects may cause out-of-plane motion to the actuator due to geometry asymmetry across the thickness [77]. Hopefully, the preferred embodiment could exploit the compliant elastomer for effective actuation.

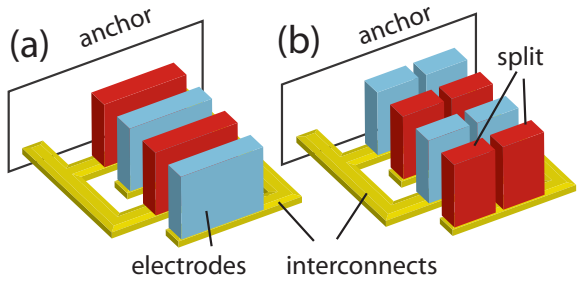

Fig. 3.2 Electrode designs: (a) wide electrodes that severely restrict the actuation of soft elastomer; (b) discrete and short electrodes that decreases the confinement effect on the soft elastomer

3.3 Fabrication Methods

In this section, we survey fabrication methods for the dielectric elastomer actuator with embedded electrodes. The fabrication methods can be divided with respect to the components, namely the electrodes, interconnects and dielectric elastomer. The requirements for the component fabrication are varying. The electrodes require a fabrication capability to form trenches with a small gap but a large depth, i.e. a high aspect ratio. The thin-film interconnects need to have good contact with electrodes and to maintain structural flexibility. On the other hand, the elastomer has to be placed in the narrow and deep trenches between electrodes and patterned at the desired area. In addition, a very important fabrication step is to release the elastomer actuator from the substrate and the surrounding cavity. Otherwise, an unreleased elastomer actuator may hardly move under the Maxwell stress even though it is compliant.

The sections start with a survey of polymer processing, followed by a survey of electrode fabrication. The section on polymeric processing introduces the basic concept of producing patterns using photosensitive and non-photosensitive polymers. The subsequent section deals with forming of multi-level electrodes using copper plating and silicon bulk micromachining. In the subsequent section, experiments are carried out to fabricate multi-level electrodes and perform polymeric filling. In the test of electroplating, the focus will be on producing polymeric mold of high aspect ratio. In the test of deep silicon etching, the attention goes to the alignment of two-level masks and etch depth uniformity for deep trenches. Finally, the trench filling with liquid polymeric pre-polymer will be discussed.

3.4 Survey on Polymer Processing

Not all polymers are responsive to electric activation. Polymers that are responsive to electric activation are called electro-active polymers. Most electro-active polymers can be deposited by spin casting when they are in solution form. However, they are not photo-patternable. This makes their patterning difficult using micro-fabrication methods. In addition, micro-fabrication methods exclude the use of a pre-stretching step, which is required to achieve electro-activeness for some polymers, such as 3M VHB dielectric acrylics [73] and poly-vinylidene fluoride (PVDF) [98]. Therefore, development of micro-fabrication methods for the electro-active polymer is important to ensure successful miniaturization.

3.4.1 *Photo-sensitive Polymers*

Photoresists are light-sensitive materials used in photolithography and photoengraving to form a patterned coating on a surface. They are mixtures of solvent, polymeric resin, and either photoactive dissolution inhibitor or photoactive cross-linking agent. The content of photo-sensitive chemical determines the mechanisms of photo-active reaction, which are discussed subsequently. The photo-resists are initially in a liquid form. They can be deposited on a wafer by spin coating. Afterwards, they are partly hardened into a solid form by solvent removal at a pre-baking step, before being exposed to UV light through an opaque mask [96, 102, 129].

Upon UV exposure, photo-chemical reactions locally change the properties of the photoresist, in particular their solubility in the development solvent. There are two different consequences depending on the chemical composition of photoresists.

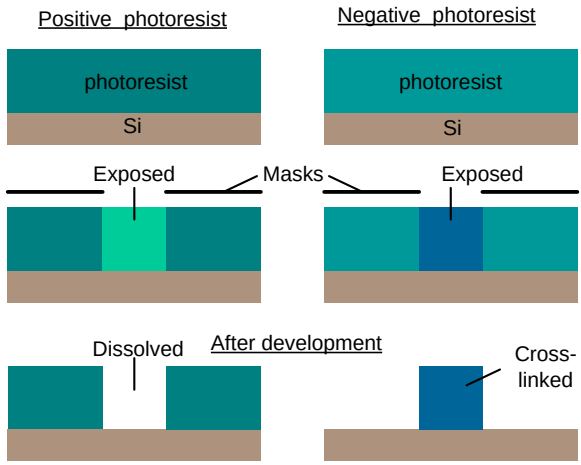

Fig. 3.3 Processing steps to perform optical lithography using (a) positive photoresist and (b) negative photoresist [96, 102, 129]

The photoresist containing the dissolution inhibitor becomes more soluble because the exposure causes scission to the inhibitor [68]. Development of this photoresist produces an image identical to that of the mask (see Fig. 3.3a). This kind of photoresist is therefore called positive resist. An example of such a polymer is Novolac resist (phenol formaldehyde polymer) like AZ9260 [146]. On the other hand, the photoresist containing the cross-linking agent becomes less soluble because the exposure initiates cross-linking. Development of this photoresist produces an inverse image to the mask (see Fig. 3.3b). This kind of photoresist is therefore called a negative photoresist. An example is the photosensitive epoxy SU-8 [132].

3.4.2 *Non-photosensitive polymers*

Several methods are available to pattern non-photosensitive polymers. However, only two of them are discussed here for their relevancy to electro-active polymers. The first method is based on the image transfer by etching a polymer. The second method is based on micro-molding of a polymer.

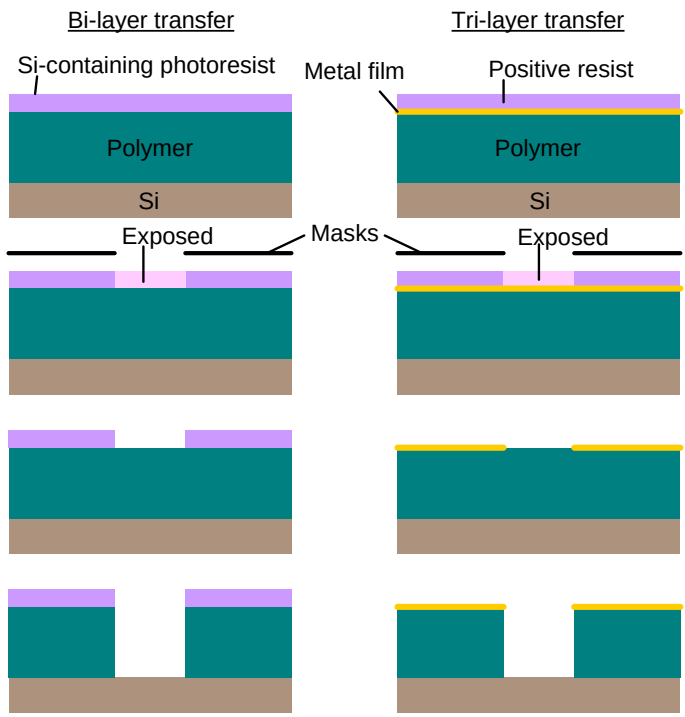

Fig. 3.4 Image transfer using polymeric etching: (a) bi-layer scheme using a photoresist mask [68]; (b) tri-layer scheme using a metal mask [164]

3.4.2.1 *Image Transfer Using Polymer Etching*

A typical scheme to transfer image to a polymeric layer involves the following steps (see Fig. 3.4a). Firstly, a hard-baked polymeric layer is covered selectively with a masking or imaging layer. The masking layer can be a plasma-resistant photoresist, an oxide film or a metal film. The masking layer is resistant against a subsequent etching step. Secondly, transfer etching is performed to remove the polymeric region which is not masked. This results in patterns in the polymeric layer. An example is the bi-layer lithography , which uses silicon-containing polymer as a hard mask against oxygen plasma to protect the underlying hard-baked Novolac resin (see Fig. 3.4a) [68, 100]. In another example where the mask layer is not photo-patternable, more fabrication steps are required to pattern a silicon-oxide mask using dry etching through a preceding imaging mask of photoresist (see Fig. 3.4b) [60, 87].

Removal of polymeric layers can be done using both wet or dry processing. Wet processing involves dissolution of the polymer in a solvent. Although not an etching process, this is commonly referred to as 'wet etching' of polymers. For ease of use, this terminology will be used in this thesis. For example, polyvinyliden fluoride trifluoroethylene (PVDF/TrFE) copolymers are 'wet etched' using methyl ethyl ketone (2-butonanone), while polyurethane dissolves in tetrahydrofuran [139, 153]. Dry etching of polymers is also quite common. Polymers such as Novolak photoresist, polyimide and acrylics (PMMA) can generally be etched using O_2 and CF_4 plasmas [138]. Wet and dry etching of polymers is usually isotropic. They result in an undercut and rounded etch profile, which differs from the masking geometry. As a result, the etched polymer patterns have neither a high resolution nor a high aspect ratio.

To accomplish a high-aspect-ratio polymeric pattern and a vertical profile (Fig. 3.5), an anisotropic etching method is needed. Two possible anisotropic etching methods have been reported. The first method is cryogenic etching. For example, oxygen plasma is successfully used to form trenches of high aspect ratio in a Novolak layer maintained at a cryogenic temperature ($-100°$) [61, 164]. The sidewall of the

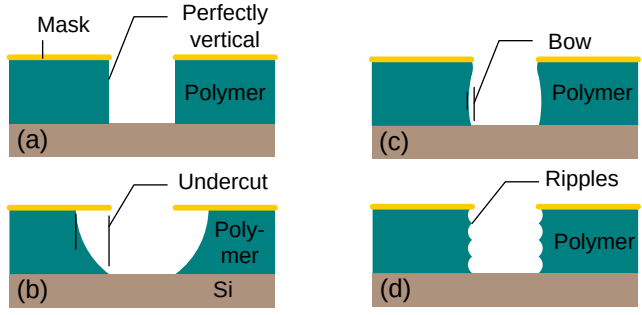

Fig. 3.5 Etch profile of the unmasked region of a polymeric layer: (a) perfect vertical profile; (b) rounded profile with undercut; (c) profile with bows [61, 138]; (c) profile with ripples [164]

etch trench is almost vertical with little bow (see Fig. 3.5c). Another method to achieve deep etching is based on the Bosch process, which switches plasma chemistry for etching and passivation. For example, Zahn *et al.* [164] alternates supplies of O_2 and C_4F_8 for reactive ion etching and passivating of a test polymer layer of polymethyl-methacrylate (PMMA). The Bosch-like process causes a rippling etch profile to the sidewall of the etched trench (see Fig. 3.5d). Principle of the Bosch process is discussed in a subsequent section on deep silicon etching.

However, etching of some polymers are difficult. A particular difficult example is the cured silicon-containing polymer, such as polydimethylsiloxane (PDMS) [124]. This explained why it is sometimes use a hard mask. Wet etching of PDMS using chemical solvent is reported, but it is slow [43] and not easy to control. The mechanisms of 'wet etching' the cured PDMS involve the scission of chemical bonds and the physical cleavage due to swelling. A swollen piece of the PDMS may result in lifting off the substrate, sooner than the slow chemical 'scission. However, a lightly etched and swollen piece of the PDMS may remain on the wafer or trapped in the recess of the mold. Dry etching of PDMS using O_2 and CF_4 plasmas has a etch rate of 0.3 μm/min and it requires high power (270W) [3]. However, it is impractical to dry etch a 30-50 μm thick PDMS layer because of large power consumption and a long etch time. In addition, the dry etching renders the etched PDMS layer rough surfaces and poor line edges (e.g. 10 μm roughness for a channel of a 70 μm deep step [43]). Therefore, it is not expected to produce high-resolution PDMS features.

3.4.2.2 *Micro-molding*

In view of the difficulty in dry etching polymers, other methods based on the molding process are considered (see Fig. 3.6). The molding process is simple and fast [70]. It uses a photoresist layer or a metal stencil with recessed patterns, as a mold. The liquid pre-polymer is then poured over the mold. Consequently, a blanket of the pre-polymer liquid covers everywhere on the mold, filling the recess patterns. When cured, the polymeric blanket forms a stamp that replicates the recess patterns of the mold, like the replicate molding of soft lithography [158]. However, if discrete patterns are desired, the top excess of the blanket must be removed and leveled.

There are three common methods to remove and level the top polymer excess.

The first method is similar to stencil printing (see Fig. 3.6a). It uses a traversing blade in contact with the top surface of the mold to mechanically remove the excess of liquid prepolymer [124]. After this step, there remains a residual film of prepolymer, which covers the mold like the blanket but thinner. The remaining polymer is then thermally cured. The thin residue film is later removed by mechanical grinding, which also appears in the second method. Upon removal of the photoresist mold using acetone, the polymeric patterns remain.

The second method uses mechanical polishing (see Fig. 3.6b) to remove the excess of the cured polymer. The micropolishing particles, under the load of a rotating grinding disk, remove the top excess of the cured polymer. The grinding

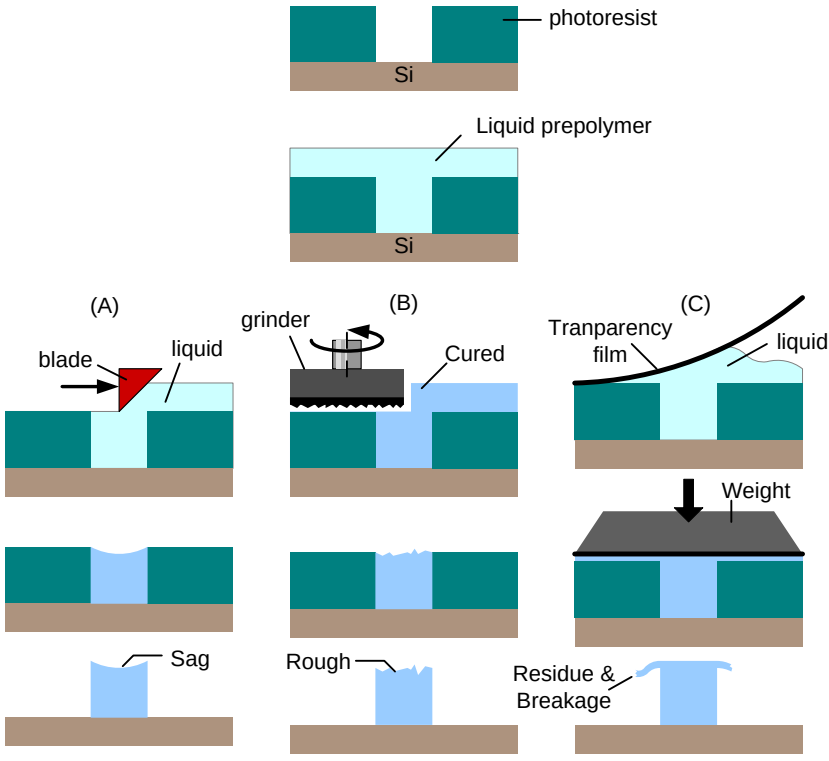

Fig. 3.6 Micro-molding methods for non-photo-sensitive polymers, using three different schemes to remove the top excess of the polymeric coating: (a) blade wiping [124]; (b) grinding [124]; (c) weight pressure [70].

and polishing process decreases the thickness of the remaining cured polymer and planarized the top surface, which may not be flat initially. However, the resulting top surface of the cured polymer is not smooth. It generally suffers from scratches after the grinding steps. The grinding and polishing process can continue until totally removing the excess. Therefore, there are no residues of cured polymer left on the top. Upon mold removal, the polymer patterns are revealed.

The third method to remove the top excess is based on compression molding (see Fig. 3.6c). It uses a clamp or a weight to squeeze out the top excess of the liquid prepolymer. To facilitate release, a transparency film (e.g. Mylar film) is spaced between the weight and the top of the photoresist mold. Two handling methods can minimize the trapped air between the interfaces. The first method brings gently the transparency into contact with the wet prepolymer from one side to the other. The second method uses a roller to press the transparency from one side to the other and push away the excess liquid pre-polymer [19]. A thin residue may remain between the interfaces of the transparency film and the top of the mold. It decreases in thickness with an increase in weight. Afterward, the prepolymer beneath the film

Table 3.1 Processability of Polymers

Concerns	Silicone rubber (Sylgard 184 [31])	Polyurethane elastomer (Pellethane 2103-80 [32])	Acrylic rubber (VHB 4910 [52, 73])	Photosensitive Epoxy (SU-8 [107])
Type of polymer	Thermoset	Thermoplast	Thermoplast	Thermoset
Initial form	Viscous liquid	Solid pellets	Solid tape	Liquid
Deposition methods	Liquid cast	Solution cast or hot melt	Tape adhesion	Liquid cast
Type of curing	Thermal	No	No	UV
Photo-patternability	No	No	No	Yes
Solubility in acetone	Poor	Moderate	Good	Poor
Solvent for the cured polymer [26, 31, 32, 52, 107]	TBAF[a] in THF[b]	THF[b]	cyclohexane, xylene	hot NMP[c]
Dry plasma etchants	O_2/CF_4 plasma (slow)	O_2 plasma (moderate)	O_2 plasma (fast)	O_2 plasma (slow)
Stencil for micro-molding	Any resist	Hard stencil	Hard stencil	Any resist
Micro-patternability	Moderate	Low	Low	High
Electroactiveness	Yes	Yes	Yes	No
Need for pre-stretching	No	No	Yes	No

[a]TBAF - Tetrabutyl-ammonium fluoride [43]. [b]THF - Tetrahydro-furan [139, 153]. [c]NMP - N-Methyl Pyrrolidinone [107]

is cured thermally. Finally, the film is removed to release the cured polymer in the recesses. A grinding step may be necessary to remove the residue.

3.4.3 *Polymer Processability*

The previous section has presented and discussed the background of the possible micro-fabrication methods for polymers. With this background information, it is now possible to evaluate the feasibility of miniaturizing some electro-active polymers, such as silicone rubber, polyurethane elastomers, acrylic rubber and epoxy. Table 3.1 summarizes all aspects of the micro-fabrication process for the selected polymers and elastomers. The important aspects include the initial form, methods of deposition, removal and micro-patterning. Some polymers exist in a liquid form while some are solid but soluble in a solvent. The polymer-containing solution can be deposited by spin casting with ease. The cast polymer solution may need baking to remove solvents or to initiate curing before they become a solid form.

In generally, it is rather difficult to pattern polymer coatings, which are not photo-sensitive. Micro-molding together with etching could form patterns to some electro-active polymers. A pre-requisite for micro-molding is that the elastomeric

solution or melt to be cast onto the mold must not react or dissolve the mold, which is usually another polymer, namely a photoresist. Wet etching of the electro-active polymers may swell and dissolute the electro-active polymers, especially the thermoplastics. Dry etching could literally 'burn away' the electro-active polymers. But these etching methods do not result in very precise dimensional control. In addition, some thermoset polymers are difficult to remove. For example, etching of the cured silicone rubber is slow using tetrabutyl-ammonium fluoride and tetrahydrofuran. Removal of the silicone rubber with 99% sulfuric acid is swift but uncontrollable. In short, micro-patterning of the silicone rubber and electro-active elastomers remains difficult. On the other hand, it is relatively easy to process the photo-patternable polymers, such as SU-8 epoxy.

3.5 Survey on Multi-level Microstructures

Most MEMS designs have planar structures with respect to the silicon substrate. For example, a MEMS switch is basiscally a thin-film capacitor with an air gap between the films, whereas an electrostatic actuator is bascially a planar capacitor with in-plane gaps. Both the capacitive sensor and electrostatic actuator require small gaps and large area to improve the sensing capacitance and actuation force respectively. Given the limited footprint, the room for improvement is small using the planar design. To overcome this, a two-and-half dimensional (2.5D) design is used to exploit the space perpendicular to the wafer plane. For example, high-aspect-ratio lateral comb drives are designed to increase the electrode area in the same footprint [60, 147]. The 2.5D structures are basically deep structures of a single level, and they can be realized using deep silicon etching or metal plating in a deep resist mold.

Three-dimensional (3D) multi-level microstructures are found in microelectronic and MEMS devices. In the area of microelectronics, the interconnects are the on-chip wiring that serves to carry signals and power among electronic components and interfaces of different levels [135]. The multi-level interconnects are nowadays made of copper using electro-deposition and planarization methods (the 'so called' copper damascene process). In the area of MEMS, demands for 3D microstructures arise when vertical comb design is developed to produce out-of-plane motion to drive a gimbaled torsional mirror [161]. The vertical comb design consists of two electrode levels, i.e. top and bottom levels. Fabrication of the two-level vertical comb can be done by stacking patterned silicon wafers or multi-steps patterning of a SOI wafer [28, 76, 160]. Challenges to the multi-level fabrication lie in the alignment of patterns at different levels and uniformity of each level.

The design for dielectric elastomer actuators requires high-aspect-ratio electrodes and shallow interconnects. This two-level microstructure of electrodes and interconnects can be made using metals or silicon. Therefore, they can be built using the micro-fabrication methods discussed above, namely the the electro-deposition

of metals and deep etching of silicon. The basic principles and overview of these fabrication methods are presented below.

3.5.1 *Electro-Deposition*

Electrodeposition, or electroplating, is an electrochemical process in which metal ions in a solution are deposited onto a cathode substrate. Growth rate of the plated metal depends on current, whereas the thickness uniformity depends on uniformity of current density [129]. The first step of electro-plating on a silicon wafer is to cover the surface with metal seed, which serves as a cathode for electro-deposition. Patterns of thick metal can be formed by electro-deposition on a selective area using through-mask plating, or by the more complicated damascene process [1].

Through-mask plating (see Fig. 3.7a) covers the seed layer using a patterned mask of insulating material, such as photoresist. Electroplating occurs only in the open region of the mask where the seed layer is exposed. The mask for the electro-deposition acts like a stencil mold and it should be thicker than the intended thickness of the deposited metal. Upon completion of the electroplating, the resist mask is removed, leaving the deposited metal patterns. Through-mask plating is suitable for making a single level micro-structure of considerable height. This technology has been used to fabricate lateral electrostatic comb drives, thin-film recording heads and solder bumps.

The damascene plating (see Fig. 3.7b) involves deposition of the metal seed, such

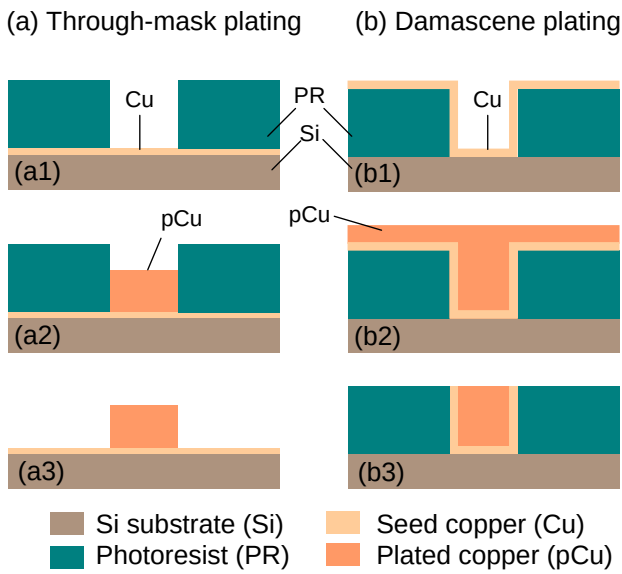

Fig. 3.7 Methods for copper electrode deposition [1]: (a) through-mask plating; (b) damascene plating .

as copper, over a patterned insulating structure, such as polyimide, which remains in the subsequent step. The electroplating deposits copper over the entire surface, including the vias extending through the insulating layer. Afterwards, the excess metal covering the top of the insulating layer is removed by a planarization step of chemical-mechanical polishing. Repeating the same process steps, subsequent layers of copper and polyimide can be deposited. The damascene copper electroplating technology has been used to form multi-level interconnects.

3.5.2 *Deep Silicon Etching*

Deep reactive ion etching (DRIE) is capable of forming high-aspect-ratio trenches in silicon with almost vertical sidewalls. The 'Bosch' process is one of the most popular methods used in DRIE. Anisotropic etching of silicon using this process is achieved by alternating plasma chemistries between silicon etching and sidewall passivation. SF_6 plasma is used for reactive-ion etching, whereas C_4F_8 plasma is used for polymer deposition. During etching, the polymer coating is sputtered away from the bottom of the etched trench, but remains on the sidewall. The remaining polymer coating protects the side wall from being etched in SF_6. When the polymer protection is exhausted, the plasma chemistry is switched to deposit the polymeric passivation layer before another cycle of etching is repeated [129].

Many variation of fabrication methods were developed to make a multi-level silicon microstructure, in particularly the vertical comb drives [28,76,160]. The major fabrication steps are similar, involving deep silicon etching of selective exposed areas, alignment of masks on multiple levels, and possible bonding of the etched levels if they are etched from separate wafers. Two examples of fabrication methods are used to illustrate the method of alignment [75,112]. Both fabrication methods start with a silicon-on-insulator (SOI) wafer, comprising of a top silicon device layer, a bottom silicon holder layer, and a silicon oxide spacing layer between the silicon layers (see Fig. 3.8).

The first method (see Fig. 3.8a) uses two oxide masks, one on the front side and the other on the back side of the SOI wafer [75]. Critical alignment is required for the two masks, which are separated at a distance of the wafer thickness. The front mask defines the layout of the top electrode in the top device layer, whereas the back mask defines the layout of the bottom electrode in the bottom holder layer. After that, deep silicon etching is performed on both sides to form the top and bottom electrodes. The etching stops on the insulator layer. After removal of the insulator layer, the formed top and bottom electrodes are spaced at the insulator thickness with no overlapping with height. Alignment of the aforementioned masks is important and affects the minimal gap spacing in the top and bottom layouts of electrodes. Misalignment and overlaps of the top and bottom electrodes may make the vertical comb inoperable.

In the second method (see Fig 8b), three masks are used. The two masks,

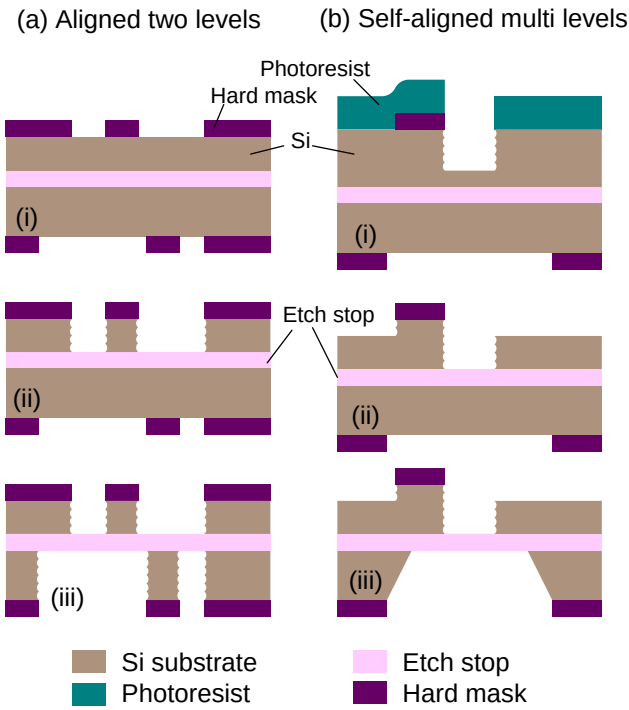

Fig. 3.8 Methods to form multi-level structures using deep silicon etching: (a) aligning mask on the front and rear sides of the wafer [75]; (b) self-aligning of two masks on the front side and crude aligning on the rear side [112].

defining the top and bottom electrodes, are both patterned on the front side and allow easy alignment [112]. The third mask on the rear side defines the release cavity and does not require a very accurate alignment with respect to the two front masks. The two front masks are made of two different materials, for example, silicon oxide and photoresist. They are patterned before the front side deep silicon etching. The first etching step, using both the resist and oxide masks, form trenches at an initial depth. Afterwards, the resist mask is removed, leaving only the oxide mask on the front side and exposing partial areas which were previously masked. The second etching step of the front side with only the oxide mask yields etched silicon structures of two heights. The shallow structures may overlap with height of the tall structures. In the last etching step, the rear cavity is formed and the insulator layer is etched to release the structures on the front.

3.6 Experiments

After surveying the state of the arts of micro-fabrication methods, we will attempt relevant methods to build the embedded electrodes for the dielectric elastomer actuators. The embedded electrode design consist of two levels, one level for vertical electrodes with intended height of 30 μm and the other level for thin interconnects with intended height of 1 μm. The height difference between the two levels is huge. The dimension control of the shallow interconnects is critical to ensure electric connectivity and structural flexibility. In addition, the spacing gaps for the electrodes should be small to enable dielectric actuation at a low driving voltage. Therefore, methods capable of producing high-aspect ratio microstructure are chosen, namely the through-mask copper plating and the self-aligned multilevel deep silicon etching. Subsequently, tests are conducted to fill the trenches between electrodes with polymers.

3.6.1 *Copper Plating*

The method of through-mask copper plating is modified in order to make the two-level copper electrodes/interconnects (see Fig. 3.9). Firstly, a 1-2 μm thick layer of titanium is sputtered. Then, a 1 μm thick seed layer of copper sputtered. Thirdly, the copper seed is patterned into comb shapes using wet etching. The patterned copper serves as a seed layer for plating and physically as the interconnects in the actuator design. Each of the comb-shape interconnects is structurally disconnected from another, but they are electrically connected through the titanium layer. In this way, a circuit completes for current flow and enable electroplating on top of the interconnects. A high-aspect-ratio mold is needed to shape the plated copper as vertical electrodes.

The high-aspect ratio mold is made of AZ9260 photoresist (thicker than 20 μm).

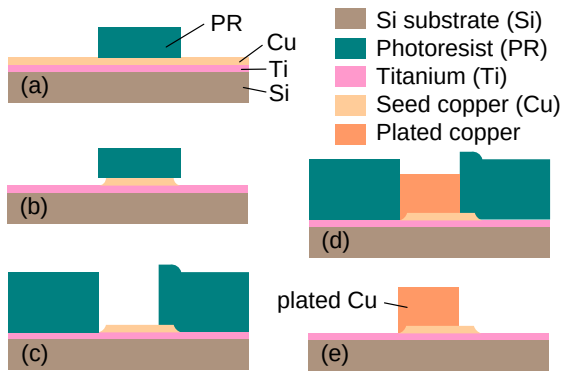

Fig. 3.9 Fabrication steps for two level copper electrode/interconnect microstructure using patterned seed and through-mask plating

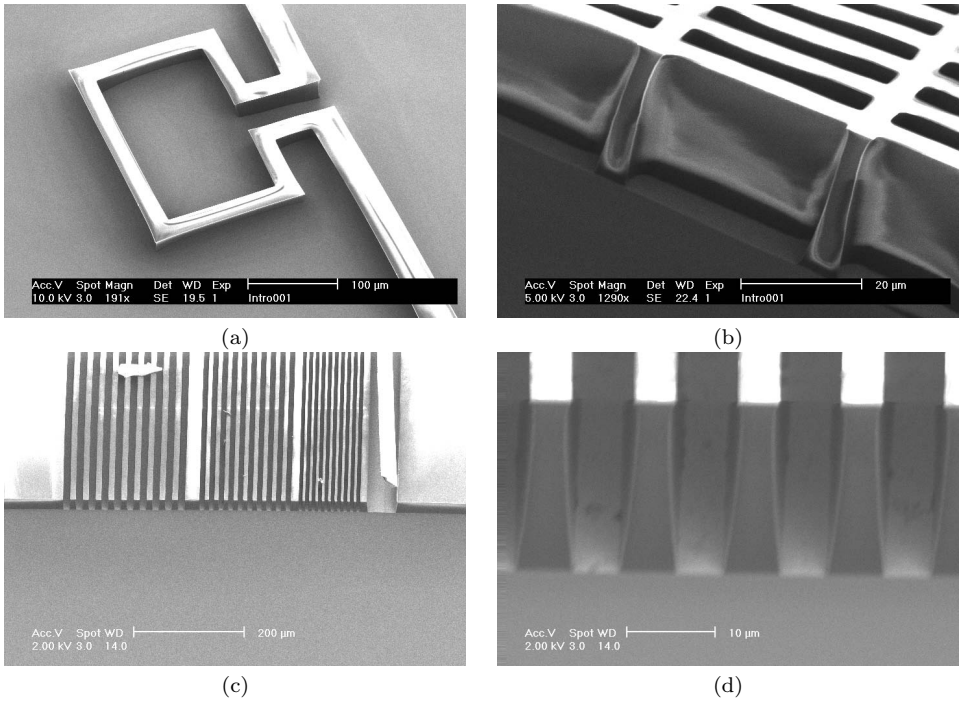

Fig. 3.10 Scanning electron micrographs of the high-aspect-ratio photoresist (AZ9260) molds: (a) a mold for interlocking cavities; (b) discrete trenches of regular sizes; (c) photoresist line patterns for dimension inspection; (d) zoomed view on the section of the line patterns with an intended pitch of 6 μm

The deposition of the thick photoresist is different from a conventional process step for a thin photoresist. The basic method is adapted after Yoon *et al.*'s method [162] using the local equipments at DIMES. Extra care and steps are taken to ensure successful deposition and development of the ultrathick resist. For example, exhaust and exit holes in the cover and bowl of the spin coater are completely sealed to prevent air flow from disturbing the surface of the wet photoresist. First step of the processes is a static dispense of 4ml AZ9260 photoresist on a 4-inch wafer. Then a single spin step at 1000 rpm for 4-10 seconds is performed to spread the photoresist evenly over the wafer. The high speed ensures good thickness uniformity while the short time is used to maintain a large thickness. The spun photoresist is then left to settle and reflow for 10 minutes in a space free from air disturbance.

Afterwards, the spun resist is subjected to a long pre-bake at 90 °C for 2 hours, with a ramp-up time of half an hour. The extended pre-bake is conducted so as to conform to the present clean-room regulation. However, the extended prebake removes solvent in the ultrathick photoresist to remove solvent and moisture as well. A re-hydration step is required to ensure successful photosensitive chemical reaction in the thick resist. In the re-hydration step, the photoresist is left in the

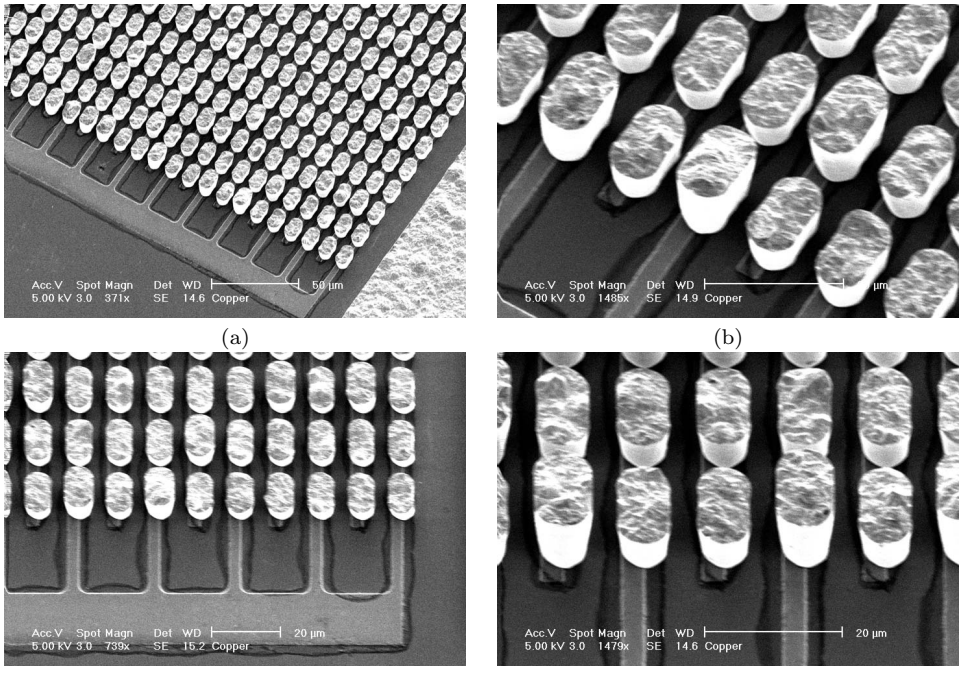

Fig. 3.11 Scanning electron micrographs showing the plated copper columns on etched copper lines: (a) perspective view at an angle; (b) a closer perspective view at an angle; (c) a perspective view at 90 °; (d) a closer perspective view at 90° . The height variation of the plated columns are shown

open air for overnight to absorb moisture. Afterwards, the rehydrated photoresist is exposed to UV light for 150 seconds at a dose per time of 10 W/cm^2. The exposed photoresist is immersed in a bath of the developer solution (AZ400K/water 1:4) without agitation. The bath is refreshed after 40 minutes of photoresist immersion. The development is complete after a total immersion time of 60 minutes. The developed photoresist mold is spun dried and left overnight. Post baking is avoided because it may thermally distort the mold. A short oxygen plasma treatment (200W for 2 minutes) is performed to ensure the plating solution can wet on the surface of the photoresist mold.

The present process recipe yields a high-aspect-ratio photoresist mold as shown in the scanning electron micrograph of samples. Fig. 3.10 shows a sample resist mold of 25 μm high having various patterns. Fig. 3.10d shows an angled view of 25-μm high photoresist columns having 6-μm spacing and 6-μm feature size. In other words, an aspect ratio of 4 is obtained for the resist mold using the present recipe.

A sample of 30-40 μm thick photoresist mold (not shown) is prepared for copper electroplating. Through-mask plating with the mold is performed in a copper plat-

ing bath, having a similar setup to the IBM paddle cell. An optimum current of 30 mA is supplied to achieve uniform growth at an anticipated rate 2 μm/minutes to minimize surface roughness [72,110]. Completion of the plating process is supposed to yield discrete copper columns on top of the comb-shape interconnects (see Fig. 3.11).

Fig. 3.11a shows that the wet etching of the copper interconnects causes undercuts and produces narrower lines than that designed. In the first attempt of copper plating without the oxygen plasma treatment, copper is deposited in some trenches of the photoresist mold, but not in other trenches. This issue arises because the plating solution does not wet those trenches. The wetting issue is resolved by a surface treatment with oxygen plasma. After the surface treatment, a second remedial plating step succeeds in depositing copper in the previously empty trenches of the same mold. These two plating steps, with partial plating in the first step, result in a height difference among the plated copper columns (see Fig. 3.11b-d). After removal of the photoresist mold, the copper columns remain on the wafer. The remaining columns are shown to have rounded corners, which differ in shape from the sharp corners in the mask. The geometry deviation may likely be attributed to the imperfect lithography.

Despite the geometry deviation, the fabricated copper microstructures suggest that the intended two-level microstructure of copper can be realized using the through-mask electro-deposition method on a patterned seed layer. Further experiments are required to release the copper structures from the substrate and maintain its structural integrity.

3.6.2 *Deep Silicon Etching*

Deep silicon etching can produce a two-level silicon microstructure of electrodes and interconnects. The adopted process method is the same as to make a self-aligned multi-level microstructure, as discussed above. Two masks are aligned on the front side using photoresist and silicon oxide. Two etching steps are required to produce the two-level structures of vertical electrodes and shallow interconnects. Using both masks, the first etching defines a shallow step between the floors of trenches and the top of the comb-shape interconnects. Using only the oxide mask, the second etching deepens the trenches, together with the step.

Experiments using the present equipment (ADIXEN) show that deep etching of silicon results in severely non-uniform etch depth. This is because the etch rate depends to a large extent on the sizes of the trench opening [102]. Fig. 3.12a-b shows a perspective view of a cluster of silicon columns next to cavities on the two sides. The cavity with a large opening is etched deeper than the cluster of silicon columns with a small opening. This yields a large difference in the floor height between the small trenches and the large cavity (see Fig 12b). In addition, it is observed that the cluster also have a non-uniform etch depth although the cluster

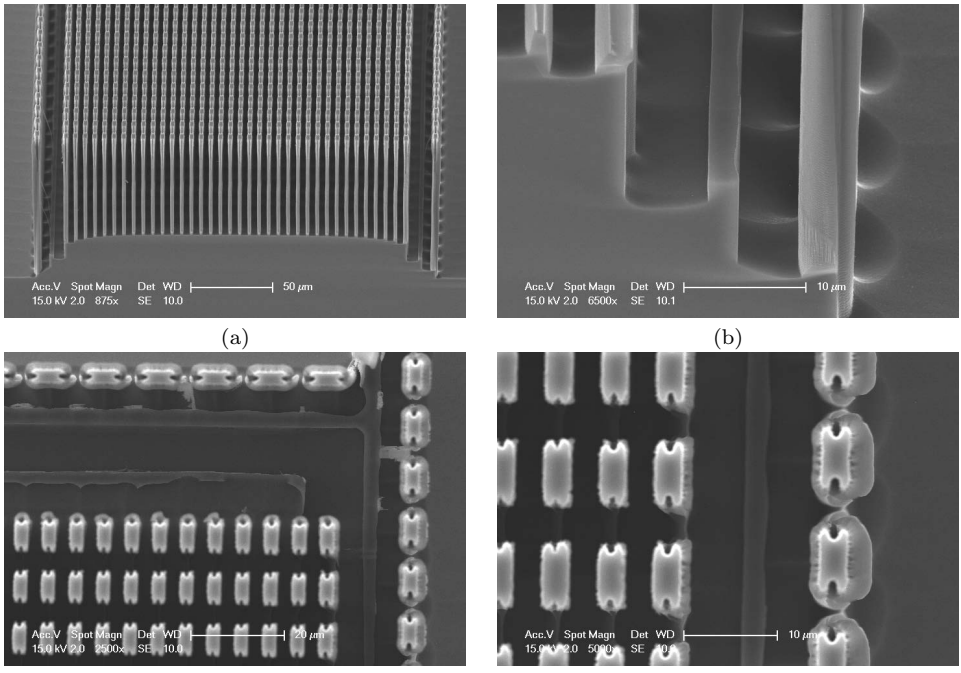

Fig. 3.12 Scanning electron micrographs showing the silicon pillars and shallow silhouette of interconnect patterns on the floors of the etched trenches: (a) perspective view showing the variation in etch depths in the cluster of silicon pillars and two big cavities; (b) a closer perspective view showing large variation in etch depths next to shallow line for interconnect pattern; (c) a top view of a cluster of silicon pillars and a shallow interconnect line on the etched floor; (d) a closer top view.

has regular and equal openings. The etch depth at the middle of the cluster is smaller than that on the boundary with the cavity. This suggests that the reactive plasma and chemicals happen to diffuse laterally from the cavity to the middle of the cluster.

Top view of the etched silicon (see Fig. 3.12c-d) shows that shallow interconnect patterns remains as a step on the etched floor. The remaining patterns no longer form a continuous line. Some are even gone completely as a result of the uncontrollable lateral etching on the etched floor. In addition, the top of the remaining interconnects is lower than the floor of the trenches in the cluster of silicon columns. The varying etch depth makes it impossible to produce a two-level microstructure of electrodes and interconnects. In addition, it makes backside etching impractical to release the desired two-level microstructures while keeping the interconnects intact. As a result, the experiment using deep silicon etching is discontinued.

Table 3.2 Viscosity of various materials

Liquid Materials	Viscosity (mPas)
Water (at 20 °C)	1.00
Xylene [10]	0.61
AZ9260 [26]	520
PDMS base (Sylgard 184) [31]	5500
PDMS mixed (Sylgard 184) [31]	4000
PDMS fluid (Dow 200 Fluid)	50-1000
SU-8 (Microchem) [107]	8.4-1500

3.6.3 *Trench Filling*

As the actuation media, elastomer materials must fill the trenches between the vertical electrodes. The trenches have small widths, as narrow as a few tenths of a micron, but they has large depths, ranging from several tens to a hundred microns. The combination of a submicron width and a hundred-micron depth are especially desired for large electrostatic force generation at a low driving voltage. But, the narrower and the deeper these trenches are, the more difficult it is to fill the trenches with liquid elastomer resin of considerable viscosity. In addition, there might also be problems in wetting the bottom of the deep trenches, or in plasma treating the bottom floors. For reference, Table 3.2 lists the viscosities of various liquids, including those pre-polymeric resins.

3.6.3.1 *PDMS*

Poly-dimethyl-siloxane (PDMS) elastomer is a common structural material to build micro-channels for micro-fluidics. One of the popular brand name for PDMS is Sylgard 184 from Dow Corning. Sylgard 184 PDMS elastomer are sold as two parts, i.e. clear liquid base resin and liquid cross-linking agent. The two parts are mixed and thermally cured to form a crosslinked elastomer in a solid form. The mixed PDMS is less viscous than the base resin, while both the mixture and base are thicker than water (see Table 3.2). The mixed PDMS decreases in viscosity when diluted with a solvent such as xylene. However, when xylene evaporates at room temperature, pores are left in the cured elastomer of PDMS and make it structurally weaker.

In the literature, PDMS is usually used to fill shallow or wide trenches. PDMS has been filled into 20 μm wide trenches for pattern transfer [72]. However, the present applications for elastomer actuators aims at filling even narrower trenches, as narrow as some submicrons. As an initial attempt, filling is tried in 0.5- to 2-μm wide and about 10-μm deep trenches . The filling process consists of the following steps: 1) flooding the wafer with liquid PDMS pre-polymer (10:1:1 of PDMS/crosslinker/xylene); 2) removing trapped air in the pre-polymer liquid and purging the trapped air in the trenches using a low vacuum; 3) spinning off the

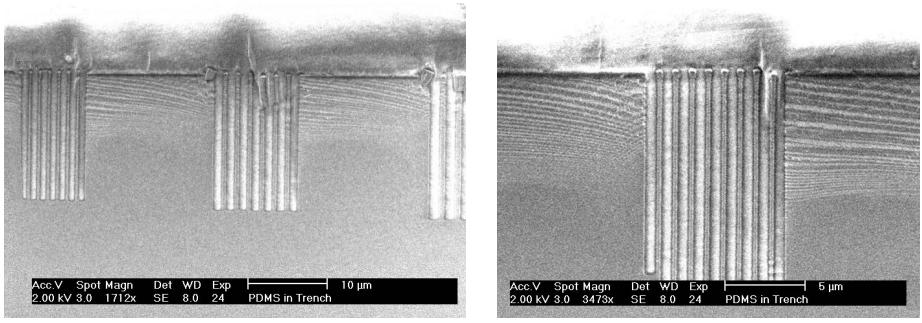

(a) (b)

Fig. 3.13 Scanning electron micrographs showing perfect filling of cured PDMS in various-sized trenches in a silicon wafer: (a) filling in trenches of three different widths; (b) filling in submicron wide trenches

excess of liquid pre-polymer using a spin coater; 4) curing the pre-polymer into a solid form at 90 °C for 1 hour. The vacuum-assisted process managed to fill PDMS into the trenches of a high aspect ratio without any trapped air. To illustrate this, Fig. 3.13 shows that trenches of half micron wide and twelve microns deep, at an aspect ratio of 25, are completely filled up with PDMS. The filling result is very encouraging.

3.6.3.2 *SU-8*

SU-8 is a high contrast, epoxy based photoresist. SU-8 consists of a solid resin, a solvent and a photosensitive cross-linking agent. It has viscosity ranging between 7.5 cSt to 1500 cSt, depending on the solid content. It can be spin coated to form a thick film and be patterned to form high-aspect ratio features. It is structurally strong, chemically and thermally stable. It has been widely used in micromachining as a structural material, for example, a master for mold replication.

SU-8 is a dielectric polymer of high rigidity. It has a dielectric constant of 3.2 at 10 MHz and it has a Young's modulus of 3 GPa. It is rather brittle as compared the elastomeric materials. For these reasons, the SU-8 epoxy is not an obvious choice of material to build a dielectric actuator. However, it is very suitable for microfabrication, in particularly for its ability to be optically patterned. As mentioned before, SU-8 epoxy is usually viscous and this presents a problem with respect to successful filling. An experiment of SU-8 filling is attempted to give an answer to this question.

To ensure successful filling, a SU-8 photoresist with a very low viscosity is adopted in the experiment. The adopted SU-8 has a product name of SU-8 2002. It has a viscosity of 7.5 cSt, containing 29 % solid resin in a solvent of gamma butyrolactone or cyclopentanone. SU-8 2002 is usually used to form 2-3 microns thick layer by spin coating. In the present test, we used it to fill trenches with a small width, i.e 3 micron. The process steps are as follow: 1) SU-8 2002 photoresist in a

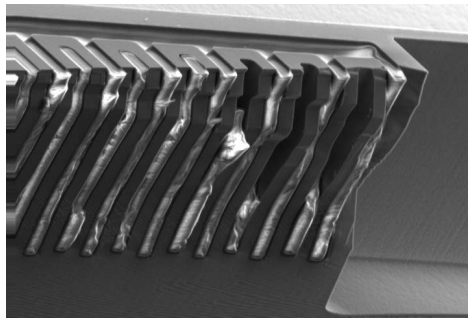

Fig. 3.14 Scanning electron micrographs showing perfect filling of cured SU-8 in 3-μm trenches in silicon wafer

liquid form is poured over a wafer with patterns of deep trenches. 2) The wet SU-8 blanket is left covering the wafer for 10 minutes to ensure that the liquid SU-8 fills into the trenches. 3) The top excess of the SU-8 blanket is thinned by a slow-speed spinning (300 rpm for 1 minute), before a soft baking to remove the solvent. Edge beads of SU-8 are formed at the rim of the wafer after the spin coating. They are removed using a chemical edge bead removal. Afterwards, a baking step is conducted to dry the the wet edges. Removal of the edge beads could ensure good contact with a photo-mask during the contact-mode exposure. After a UV exposure, the resist is developed in a bath of PGMEA (propylene glycol methyl ether acetate). The remained SU-8 patterns can further be cured with a hard bake.

Fig. 3.14 shows that the complete filling of 3-μm wide and 40-μm deep trenches is possible using the SU-8 2002 photoresist. It is observed that the SU-8 2002 does not cover the top of the vertical silicon structures. Absence of the top SU-8 coating may be due to the poor adhesion and wettability of SU-8 on the substrate (in this case silicon with native oxide) or aluminum film.

3.7 Conclusion

We proposed using a two-level microstructure of high electrodes and shallow interconnects to enable effective actuation of dielectric elastomers. The microstructure forms a backbone of the miniaturized dielectric elastomer actuators. Methods to fabricate the two-level electrode/interconnect microstructures were studied and some experiments were done. Preliminary tests suggest through-mask plating on a patterned seed is a suitable method for this microstructure. Deep silicon etching failed to produce two-level microstructure because of non-uniform etch depth, which is dependent on opening sizes of the mask.

In addition, processing of the actuation elastomer or polymers has been tested. Silicone rubber and photo-patternable epoxy filled successfully the sub-micron wide trenches. However, micro-patterning of elastomers remains difficult. A preliminary

test using a photoresist mold did not succeed in lifting off the cured PDMS residue that covers the mold everywhere. In addition, it is difficult to wet etch the cured PDMS. Etching of PDMS is very slow in TBAF/NMP etchant, but excessively fast and uncontrollable in 99% sulfuric acid. The unsuccessful micro-patterning of elastomers significantly hinders the attempt to miniaturize the dielectric elastomer actuators.

PART 2

Actuators Using Thermally Expandable Polymers

Chapter 4

Polymeric Thermal Actuator with Embedded Skeleton

A powerful and effective design of a polymeric thermal micro-actuator is presented in this chapter [1]. The design has SU-8 epoxy layers filled and bonded in a meandering silicon (Si) microstructure. The silicon microstructure reinforces the SU-8 layers by lateral restraint. It also improves the transverse thermal expansion coefficient and heat transfer for the bonded SU-8 layers. A theoretical model shows that the proposed SU-8/Si composite can deliver an actuation stress of 1.30 MPa/K, which is approximately 2.7 times higher than the unconstrained SU-8 layer, while delivering an approximately equal thermal strain.

4.1 Introduction

Thermal actuators feature relatively high actuation stress or strain. However, they have shortcomings in terms of high power consumption and high operating temperatures [8, 121]. To a large extent, their performance depends on the selected thermal expansion materials [64]. For example, silicon and metals with high moduli of elasticity produce high actuation stresses, but polymers with high thermal expansion coefficients (CTE) deliver relatively high actuation strains. According to Ashby [5], the linear CTE (α) is almost inversely proportional to the Young's modulus (E). This means that compliant but high-CTE polymers may not be ideal for generating large actuation stress and strain simultaneously. Owing to their electrical and thermal insulating properties, most polymers requires integrated heaters to enable electrical activation [8, 111]. The heaters are normally made of surface metallic films, and may induce non-uniform heating across the polymeric thickness. This may inevitably cause out-of-plane bending to the polymeric layers.

[1] This chapter is based on a paper published in the Appl. Phys. Lett. [83]

4.2 Actuator Design

In this chapter, we present a design of polymeric thermal actuators to accomplish enhanced in-plane actuation. This design combines multiple materials for effective thermal actuation. It consists of an aluminum film heater, a silicon (Si) microstructure, and polymeric epoxy (SU-8) encapsulant (see Fig. 4.1). The silicon microstructure is meandering in shape and has a high aspect ratio. Its gaps and surrounding areas are filled and encapsulated with SU-8 epoxy, whereas its top is covered with the aluminum (Al) heater. The Si 'skeleton' serves to conduct heat and to reinforce the SU-8 encapsulant; the Al line is responsible for resistive heating; whereas, the SU-8 epoxy serves to expand and open the spacing of the Si 'skeleton'.

The proposed design has been fabricated using bulk micromachining of silicon and casting of SU-8-2002 polymer [82]. Testing shows that a 530-μm long sample device (consisting of a 0.675-μm thick Al film and a 50-μm high Si microstructure) delivers a 2.5% in-plane longitudinal strain at 2 V, while consuming less than 27 mW (see Fig. 4.1(b)), and shows no noticeable out-of-plane motion. The actuation using this composite design is efficient. This motivates investigation into its potential actuation capabilities. The normal activation of the actuator design by resistive heating causes an unknown and non-uniform temperature distribution. This may obscure the influences of thermoelastic properties on the actuation capability. Therefore, external uniform heating is adopted in the theoretical and experimental evaluations below to exclude this effect and accurately control the temperature.

4.3 Theory

The confined SU-8 filling in the meandering silicon microstructure is similar in configuration to a polymeric layer sandwiched between two silicon layers in a composite stack (see Fig. 4.1(a)). The silicon layers reinforce the polymeric layer by the lateral restraint on the bond interface. As a result, the volumetric expansion of the polymer layer is concentrated perpendicular to the bond interface, with little lateral bulging at the free edges. The phenomenon of directionally enhanced thermal strain was observed as an unintended effect in a stacked memory cube with adhesive layers [55]. In this work, we exploit the effect for enhancing electro-thermal actuation.

A laminar model is developed to evaluate performance of a representative unit cell, which consists of three infinitely wide layers (Si/SU-8/Si). The material properties are assumed linear and isotropic [157], well below the polymeric glass transition temperature (T_g) or below the silicon melting temperature (T_m). Flexibility coupling between the bonded polymer and silicon layers is considered in the constitutive equations:

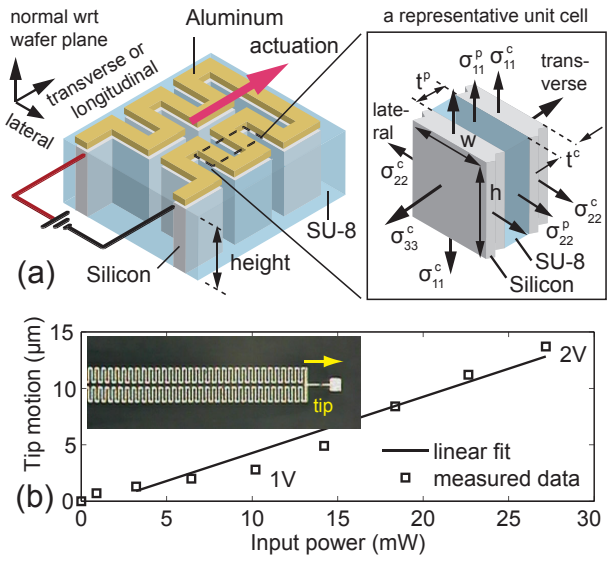

Fig. 4.1 (a) A schematic drawing of the proposed polymeric thermal actuator, consisting of a symmetrically meandering silicon (Si) microstructure, SU-8 encapsulant and an aluminum (Al) heater, together with a representative unit cell of three layers (Si/SU-8/Si); (b) The measured tip displacement for a sample device ($h = 50$ μm, $t^c = 3$ μm, and $t^p = 3\mu$m, $w = 28\mu$m) as a function of input power when electrically activated by the aluminum heater (0.675 m thick)

$$
\begin{aligned}
e^p_{ij} &= \frac{1+\upsilon^p}{E^p}\sigma^p_{ij} - \frac{\nu^p}{E^p}\sigma^p_{kk}\delta_{ij} + \alpha^p \Delta T \delta_{ij} \\
e^c_{ij} &= \frac{1+\nu^c}{E^c}\sigma^c_{ij} - \frac{\nu^c}{E^c}\sigma^c_{kk}\delta_{ij} + \alpha^c \Delta T \delta_{ij}
\end{aligned}
\tag{4.1}
$$

where e_{ij} is the strain tensor; σ_{ij} is the stress tensor; δ_{ij} is the Kronecker delta. Summation convention is used for repeated indices [125]. Referring to Fig. 4.1(a), indices 11 and 22 denote the lateral directions ($\parallel$) parallel to the layer sidewalls, whereas index 33 denotes the transverse direction ($\perp$). Both the lateral and transverse directions are parallel to the wafer plane. The superscripts p and c denote polymeric and conductive silicon layers respectively. The symbols E and ν denote the Young's moduli and Poisson's ratio respectively.

In each layer, transverse thermal strains are assumed uniform under a uniform temperature rise ΔT and zero external loading. Lateral strains are common at the interface between the layers. The lateral force summation is zero, but the internal lateral stresses in the layers are non-zero due to the CTE mismatch. In the transverse direction, the apparent CTE for the constrained polymer layer increases, but that for the silicon layers decreases. The transverse CTEs for the bonded layers are derived below, in which $\gamma = t^p E^p / t^c E^c$:

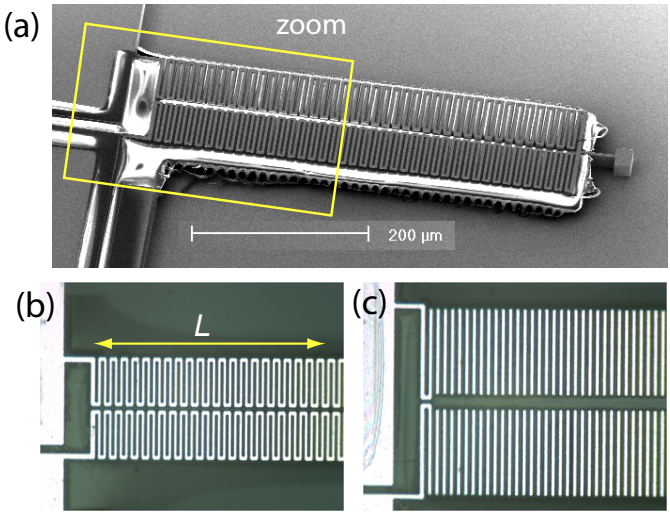

Fig. 4.2 Microscopic images showing full and partial views of the micro-machined devices: (a) a scanning electron micrograph of a sample device still residing on silicon substrate ($h = 50$ μm, $t^c = 3$ μm, and $t^p = 3$ μm); (b) an optical image of a polymeric actuator with 53-μm wide (w) meandering silicon microstructure; (c) an optical image of a polymeric actuator with 103-μm wide (w) parallel plates.

$$\alpha_{\perp}^{p} = \frac{e_{33}^{p}}{\Delta T} = \alpha^{p} + \frac{2\upsilon^{p}(\alpha^{p} - \alpha^{c})}{1 - \nu^{p} + \gamma(1 - \nu^{c})}$$
$$\alpha_{\perp}^{c} = \frac{e_{33}^{c}}{\Delta T} = \alpha^{c} - \frac{2\nu^{c}(\alpha^{p} - \alpha^{c})}{(1 - \nu^{c}) + \gamma^{-1}(1 - \nu^{p})} \tag{4.2}$$

The apparent transverse thermal expansion coefficient of the three-layer model is a sum of the component coefficients in Eq. (2): $\alpha_{\perp} = (1-\phi)\alpha_{\perp}^{c} + \phi\alpha_{\perp}^{p}$, in which $\phi = t^p/(t^p + t^c)$ is the volume fraction of the polymer component. In the limiting case where γ=0, α^c=0, the apparent polymeric CTE becomes $\alpha^p = (1+\nu^p)/(1-\nu^p)$.

Owing to the lateral restraint of the stiff silicon layers, the bonded polymer layer undergoes less transverse strain when loaded transversely. The enhanced stiffness is derived by solving Eq. (1) with ΔT =0 and nonzero transverse stresses $\sigma_{33}^{p} = \sigma_{33}^{c} \neq 0$, and using the same assumptions of lateral force equilibrium and displacement compatibility as above. The apparent transverse modulus ($E_{\perp}$) for the composite stack is derived as : $E_{\perp}^{-1} = (1-\phi)(E_{\perp}^{c})^{-1} + \phi(E_{\perp}^{p})^{-1}$, in which the Young's modulus for the constrained polymer ($E_{\perp}^{p}$) and that for the constrained conductors ($E_{\perp}^{c}$) are given below,

$$\frac{1}{E_{\perp}^{p}} = \frac{e_{33}^{p}}{\sigma_{33}^{p}} = \frac{1}{E^{p}}\left[1 - \frac{2\upsilon^{p}(\upsilon^{p} - \eta\upsilon^{c})}{1 - \upsilon^{p} + \gamma\,(1 - \upsilon^{c})}\right]$$
$$\frac{1}{E_{\perp}^{c}} = \frac{e_{33}^{c}}{\sigma_{33}^{c}} = \frac{1}{E^{c}}\left[1 + \frac{2\gamma\upsilon^{c}(\upsilon^{p} - \eta\upsilon^{c})}{1 - \upsilon^{p} + \gamma\,(1 - \upsilon^{c})}\right] \tag{4.3}$$

where $\eta = E^p/E^c$.

Furthermore, the embedded silicon microstructure improves heat transfer to the insulating polymers. The transverse thermal conductivity ($k_\perp$) and the lateral ($k_\parallel$) for the polymeric composite stack are derived below:

$$\frac{1}{k_\perp} = \phi\frac{1}{k_1} + (1-\phi)\,\frac{1}{k_2}$$
$$k_\parallel = \phi k_1 + (1-\phi)\,k_2 \tag{4.4}$$

4.4 Actuation Capability

Table 4.1 compares the derived properties for the 50/50 % Si/SU-8 composite design (i.e. at ϕ= 0.5) with those for the base materials, like silicon, epoxy, and aluminum [36,37,92,156]. It is shown that the composite design has tremendous improvement in the actuation capability. The constrained CTE for SU-8 epoxy is estimated to double, resulting in an apparent composite CTE equal to the unconstrained SU-8 CTE. In addition, the composite produces more than double the actuation stress per Kelvin ($E_\perp\alpha_\perp$) as compared to those of silicon or epoxy. The actuation stress at $\Delta T > 10$ °C easily exceeds those generated by electro-active polymers at several kilovolts [117,165]. Furthermore, the actuation energy density per squared Kelvin ($E_\perp\alpha_\perp^2/2$) is more than four times higher than that of aluminum, which is known for its high CTE among metals [69]. The transverse thermal conductivity doubles, and the lateral conductivity becomes even better, reaching a half of the silicon conductivity. Hence, heat transfer across the thick polymer layers in the composite is greatly enhanced.

In the present composite design, the constituent polymer is fully constrained in the high-aspect-ratio meandering microstructure. Therefore, the bonded polymeric layers exhibit bulk properties. Without the constraint, a free SU-8 layer, expanding in all directions, does not deliver as much concentrated work as the constrained layer does. A bulk SU-8 sample under hydrostatic compression is reported to have a higher Young's modulus and CTE than a planar film sample under directional stretching. For example, the bulk has a volumetric CTE of 452-ppm/K, while the linear in-plane CTE of the thin film ranges between 87 - 102 ppm/K [36, 37]. Moreover, the bulk modulus is 5.88 GPa, while the thin-film in-plane modulus is 3.2 GPa [36,37]. This polymeric composite design well exploits the bulk SU-8 properties by layered confinement for unidirectional actuation.

Table 4.1 Comparison of thermal expandable materials

	Units	Al [92]	Si [92, 156]	SU-8 [36, 37]	50-50% SU-8/Si
Young's modulus (E)	GPa	69	130	3.2	8.89 $\perp$
Poisson's ratio (ν)	1	0.35	0.28	0.33	-
Linear CTE (α)	10^{-6}/K	23.1	2.6	150.7	146.2
Thermal conductivity (k)	W/m/K	237	148	0.2	0.4/74.1$\parallel$
Maximum temperature	°C	660 (T_m)	1414 (T_m)	238 (T_g)	238
Actuation stress ($E\alpha$)	MPa/K	1.59	0.35	0.48	1.30
Energy density ($\frac{1}{2}E\alpha^2$)	J/m^3/K^2	18.41	0.48	36.32	95.04

4.5 Testing

To measure the apparent transverse CTE of the composite, a 4-inch wafer with released micro-machined composite actuators is placed on a temperature controllable hot plate. It is heated up to the desired steady-state temperature, which is measured with a thermocouple. In-plane dimension changes, i.e. $\Delta L/L$, of the devices are measured by comparing the focused images at an elevated temperature (155 $\pm$ 5 °C) with those at the room temperature (25 °C). Fig. 4.2 shows examples of optical microscope images (model: Keyence VHX).

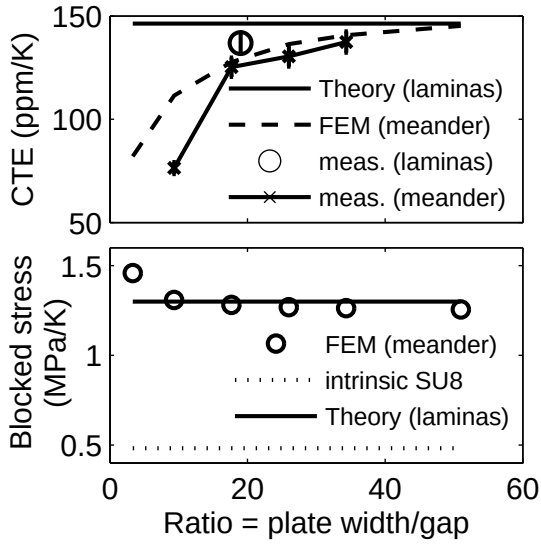

Fig. 4.3 Trends of the apparent transverse CTE (*top*) and the blocked transverse stress (*bottom*) with respect to the aspect ratio of the layer width to the spacing between the layers, for two polymeric composite designs: (i) embedded with parallel silicon plates or (ii) embedded with meandering silicon microstructures

Fig. 4.3 shows that the transverse dimensional change increases with the width of the silicon meandering microstructures. This is attributed partly to the enhancement in constrained thermal expansion and partly to the reduced influence of the horseshoe bends of the meandering silicon microstructures. The measured CTE agrees in trend with that simulated using a 3-D finite element (FE) model. The FE analysis is performed using ANSYS. At a large layer width, the simulated and measured CTEs approach to an asymptotic value predicted by the laminar model. The measured CTE reaches 140 ppm/°C at a 103-μm layer width. In addition, the FE and laminar models predict that the blocked transverse actuation stress for the composite stack exceeds that of unconstrained SU-8.

4.6 Summary

In summary, a polymeric composite design of thermal actuators demonstrated enhanced in-plane actuation. The composite actuator (50/50 % SU-8/Si) outperforms the homogenous materials, in terms of thermal stress-strain generation and energy density. This actuator design, which embeds a high-aspect-ratio silicon microstructure, could be extended to various expandable polymers, both thermally and chemically driven, for effective in-plane actuation.

Chapter 5

Thermally Induced Strain and Stress

The compliant and highly expandable polymeric materials have been combined with stiff skeleton materials in a powerful design of thermal micro-actuators. The bond interfaces between the combined materials laterally confines the polymeric volumetric expansion but direct it predominantly in the actuation direction. A complete lateral constraint at the infinite bond width could maximize the actuation strain enhancement. However, it is not sure whether a finite bond width could garner the 'confinement effect'. The present study uses the mean-pressure method to derive close-form solutions to the thermally induced strain and stress in a bonded polymer layer between rigid interfaces. The study sheds light on the confinement effect at a finite bond width. It shows that a bond width 5 times the layer thickness of SU-8 epoxy accomplished 95% of the strain enhancement at the infinite width. In addition, the derived equations lay the theoretical foundation to understand and exploit the confinement effect in the composite design of the thermal micro-actuators.

5.1 Introduction

Material designs for extremal thermal expansions were previously developed based on metallic materials and voids [133, 134, 137]. They appeared in various complex multi-phase topologies or layouts and are specific to the considered constituent materials. The adopted metals have high stiffness but moderate thermal expansion. The metals or their combination do not deliver high thermal expansion even if embodied in the complex layout design. This limitation motivates an alternative and simple approach to material design. The approach uses extreme material combination, i.e. polymeric and skeleton materials, in a laminate design to enhance thermal strain in the actuation direction. Such integration exploits the large thermal expansion and stiffness mismatches between the polymeric and skeleton materials. It leads to a new class of powerful thermal micro-actuators [82, 83].

The new class of powerful thermal micro-actuators embeds a stiff skeleton in a thick block of a compliant and highly thermally expandable polymer. The material

bond interfaces are almost rigid to the compliant polymer. The interfaces impose lateral constraint on the polymer. Therefore, the polymeric volumetric expansion is reinforced and directed in the transverse or actuation direction. This makes the composite design exhibit a higher linear actuation strain and stiffness than the polymer alone. The adopted skeleton and polymeric materials are silicon and SU-8 epoxy respectively in this case. In addition, the silicon skeleton serve to conduct the heat, generated by an aluminium resistive heater, to the polymer, which is a thermal insulator. Experimental testing of a micro-machined device confirmed that the polymeric actuator with the embedded skeleton exhibits excellent actuation capability [82, 83].

The polymeric filling, which is confined in the meandering skeleton, to a large extent is similar in configuration to a polymeric layer sandwiched between two skeleton layers. The volumetric expansion of the bonded polymer layer is directed perpendicular to the bond interfaces, with slight lateral bulging near the free edges, because of the lateral restraint by the stiff skeleton layers. The phenomenon of directionally enhanced thermal strain is exploited to enhance electro-thermal actuation. Ideally, a bonded layer of incompressible polymer can achieve 3 times larger apparent CTE than the polymer alone [55, 82, 83, 157]. This is quite different from the case of dielectric elastomers whose stress-induced strains are suppressed by the lateral restraint [84, 116, 118].

The bond interface has an equal width as the skeleton plates, if perfect bonding is assumed. The bond or plate width affects the extent of lateral restraint on the bonded polymeric layer. For example, wide plates can impose complete lateral restraint. However, the wide plates are not desired because they occupy space and result in a long path for heat conduction. Narrow plates are preferred for compactness, in particular for a bender design that requires a low moment of inertia [78]. However, the narrow plates may compromise the directional enhancement of thermal expansion because they exert less lateral restraint and allow lateral thermal expansion for the polymeric layer. How narrow can the plates be without compromising the strain enhancement? There are no obvious answers available in literature.

So far, bi-axial lamellar models were developed to predict enhanced thermal strain for a constrained polymeric layer of infinite width [82, 83, 157]. However, the lamellar models do not predict the finite-width behavior of the constrained polymeric layer. A closed-form solution for the finite-width layer is necessary and valuable, because it not only provides insight into the thermoelastic mechanics of the bonded layer, but also enables identification of influential design parameters. In contrast, a numerical solution does not provide instantly useable formulae and a concise description. The analytical solution sheds light on the confinement effect on the thermal strain enhancement.

Due to the large thermal mismatch between the polymer and skeleton layers, there will be significant thermal stresses in the bonded polymeric layer when tem-

perature rises. The thermally induced interfacial stresses may causes delamination between the polymer and skeleton layers. They should be maintained below the interfacial bond strength to ensure reliable operation. Therefore, ability to predict the thermally induced interface stresses is also very important in the design process. The interfacial stresses in an infinitesimal thin adhesive layer between dissimilar adherends were well predicted using the lap-joint theory [20, 140, 150]. However, the lap joint theory cannot be applied to the present case where the present adherends are identical (i.e. both silicon plates) and the polymeric layer is as thick as the adherends themselves. If without taking into account this difference, the lap-joint theory may incorrectly predict zero or minimal shear stress. Therefore, an alternative stress analysis method is needed to predict the thermal stress in the rigidly bonded polymeric layer.

5.2 Outline of Mean Pressure Method

The 'mean pressure' method was developed to predict the compressive stiffness of a rigidly bonded elastic layer in seismic isolators [148, 149]. The layer is compressed under a load acting perpendicular to the layer. The bonded surfaces of the compressed layer are restrained from lateral expansion. As a result, the layer exhibits a higher apparent compressive stiffness. The mean pressure method utilized two kinematic assumptions for the bonded elastic layer under compression [44,95]: a lateral plane remains plane, and a transverse line becomes parabolic. These kinematic assumptions are also realistic for a bonded polymeric layer under thermal expansion. Therefore, the 'mean pressure' method will be extended to the thermoelastic analysis of the bonded layer.

In the subsequent derivation, we will express the basic thermoelastic equilibrium equation and constitutive equation (i.e. stress-strain relationship) in terms of the dilatation and hydrostatic pressure. Subsequently, a second-order ordinary differential equation (ODE) for the 'mean pressure' is derived and solved, leading to an analytical solutions for the thermally induced strains and stresses in the constrained polymeric layer.

5.3 Theory

Consider a polymeric strip sandwiched between two rigid plates as shown in Fig. 5.1. If the plates are rigid and do not expand during a temperature change, they will restrict lateral deformation of the bonded polymer, resulting in zero lateral displacement on the bond surfaces. When uniformly heated in the absence of external loads, the bonded strip is expected to expand predominantly in the transverse direction (i.e. along the z thickness direction) but shows slight lateral bulging. The bonded layer, under the constrained thermal expansion, is assumed to deform

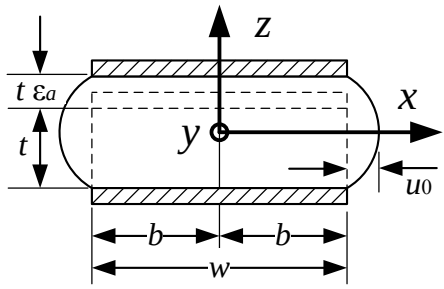

Fig. 5.1 A polymeric strip sandwiched between two rigid plates

such that a lateral plane remains plane and horizontal, and that a transverse line becomes parabolic. Mathematically, the assumed displacement field for a bonded layer with a bond width of $w = 2b$ and a thickness of t takes the form [148]:

$$\begin{aligned} u(x,y,z) &= u_0(x,y)(1-4z^2/t^2), \\ v(x,y,z) &= v_0(x,y)(1-4z^2/t^2), \\ w(x,y,z) &= w_0(z), \end{aligned} \tag{5.1}$$

in which u_0 and v_0 are lateral displacements along the mid-plane of the layer, i.e. at $z = 0$, and w_0 is the transverse displacement, which is independent of the lateral location, i.e. x and y coordinates.

In accordance to the assumed displacement field (Eq. 5.1), the strain components are

$$\begin{aligned} \epsilon_{xx} &= u_{,x} = u_{0,x}(1-4z^2/t^2), \\ \epsilon_{yy} &= v_{,y} = v_{0,y}(1-4z^2/t^2), \\ \epsilon_{zz} &= w_{,z} = w_{0,z}, \\ \gamma_{xy} &= u_{,y} + v_{,x} = (u_{0,y} + v_{0,x})(1-4z^2/t^2), \\ \gamma_{yz} &= v_{,z} + w_{,y} = -8zv_0/t^2, \\ \gamma_{zx} &= u_{,z} + w_{,x} = -8zu_0/t^2, \end{aligned} \tag{5.2}$$

in which ϵ_{xx}, ϵ_{yy}, and ϵ_{zz} are normal strains and γ_{xy}, γ_{yz}, and γ_{zx} are shear strains.

The main steps of derivation involve re-expressing the isothermal thermoelastic equations in terms of the hydrostatic pressure and displacement derivatives of the assumed displacement field (i.e. Eqs. 5.1-5.2). The isothermal thermoelastic equations are listed in the Appendix [16] for the convenience of reader.

According to Eq. A.2a, dilatation strain is related to the hydrostatic pressure, p. Substitution of Eq. 5.2 into Eq. A.2a yields

$$u_{,x} + v_{,y} = -w_{,z} - p/\kappa + 3\alpha\Delta T \tag{5.3}$$

in which α is the coefficient of linear thermal expansion, ΔT is the temperature rise, and κ is the bulk modulus.

Similarly, the constitutive equation in a stress-strain form (i.e. Eq. A.3) can be expressed in terms of hydrostatic pressure and displacement derivatives, leading to

$$\begin{aligned}
\sigma_{xx} &= -\lambda p/\kappa + 2\mu u_{,x} - 2\mu\alpha\Delta T, \\
\sigma_{yy} &= -\lambda p/\kappa + 2\mu v_{,y} - 2\mu\alpha\Delta T, \\
\sigma_{zz} &= -\lambda p/\kappa + 2\mu w_{,z} - 2\mu\alpha\Delta T, \\
\tau_{xy} &= \mu\left(u_{,y} + v_{,x}\right), \\
\tau_{yz} &= \mu\left(v_{,z} + w_{,y}\right), \\
\tau_{zx} &= \mu\left(u_{,z} + w_{,x}\right),
\end{aligned} \tag{5.4}$$

in which λ and μ are Lame elastic constants, given in Eq. A.3c.

Substituting Eq. 5.4 into the equilibrium equations (Eq. A.4) yields:

$$\begin{aligned}
u_{,xx} + u_{,yy} + u_{,zz} &= \frac{\lambda+\mu}{\mu\kappa} p_{,x}, \\
v_{,xx} + v_{,yy} + v_{,zz} &= \frac{\lambda+\mu}{\mu\kappa} p_{,y}, \\
w_{,xx} + w_{,yy} + w_{,zz} &= \frac{\lambda+\mu}{\mu\kappa} p_{,z}.
\end{aligned} \tag{5.5}$$

Differentiating the first two equations of Eq. 5.5 with respect to the lateral coordinates and combining the results containing the second-order derivatives of the pressure yield

$$\left(u_{,x} + v_{,y}\right)_{,xx} + \left(u_{,x} + v_{,y}\right)_{,yy} + \left(u_{,x} + v_{,y}\right)_{,zz} = \frac{\lambda+\mu}{\mu\kappa}\left(p_{,xx} + p_{,yy}\right) \tag{5.6}$$

This equation for isothermal expansion has a similar expression as that derived for an elastic layer under a compression load. However, the two differ in that the pressure on the right hand side of this equation is thermally induced while that of the latter is induced by an external compressive load.

In turn, the right hand side of Eq. 5.6 can be reformulated, by differentiating Eq. 5.3 twice with respect to the coordinates and using information on the assumed displacement field (Eqs. 5.1 and 5.2),

$$\begin{aligned}
\left(u_{,x} + v_{,y}\right)_{,xx} &= -p_{,xx}/\kappa, \\
\left(u_{,x} + v_{,y}\right)_{,yy} &= -p_{,yy}/\kappa, \\
\left(u_{,x} + v_{,y}\right)_{,zz} &= -\frac{8}{t^2}\left(u_{0,x} + v_{0,y}\right).
\end{aligned} \tag{5.7}$$

In the last expression above, the lateral strains on the mid-plane (i.e. $u_{0,x} + v_{0,y}$) can be expressed in terms of the mean pressure $\bar{p}$ and apparent axial strain ϵ_a in the z direction

$$u_{0,x} + v_{0,y} = \frac{3}{2}\left(-\epsilon_a - \bar{p}/\kappa + 3\alpha\Delta T\right) \tag{5.8}$$

by integrating and normalizing Eq. 5.3 with respect to the thickness t

$$\begin{aligned}
\bar{u}_{,x} =& \frac{1}{t}\int_{-t/2}^{t/2} u_{,x}dz = \frac{1}{t}\int_{-t/2}^{t/2} u_{0,x}(1-4z^2/t^2)dz = \frac{2}{3}u_{0,x},\\
\bar{v}_{,y} =& \frac{1}{t}\int_{-t/2}^{t/2} v_{,y}dz = \frac{1}{t}\int_{-t/2}^{t/2} v_{0,y}(1-4z^2/t^2)dz = \frac{2}{3}v_{0,y},\\
\bar{w}_{,z} =& \frac{1}{t}\int_{-t/2}^{t/2} w_{,z}dz = \frac{1}{t}\int_{-t/2}^{t/2} w_{0,z}dz = \frac{1}{t}\left[w\left(\frac{t}{2}\right) - w\left(-\frac{t}{2}\right)\right] = \epsilon_a,\\
\text{and } \bar{p}(x,y) =& \frac{1}{t}\int_{-t/2}^{t/2} p(x,y,z)dz.
\end{aligned} \tag{5.9}$$

The integration and normalization across the thickness form the essence of the 'mean pressure' method, which enables solution of the displacement fields using a single unknown, i.e. the 'mean pressure'.

Since the lateral strains $(u_{0,x}+v_{0,y})$ along the mid-plane are function of pressure, substituting Eqs. 5.7-5.8 into Eq. 5.6 leads to a second-order ordinary differential equation (ODE) of the mean pressure $\bar{p}$,

$$\bar{p}_{,xx} + \bar{p}_{,yy} - a^2\bar{p} = a^2\kappa\left(\epsilon_a - 3\alpha\Delta T\right) \tag{5.10}$$

where

$$a^2 = \frac{12}{t^2}\left(\frac{\mu}{\lambda+2\mu}\right).$$

This ODE bears similarity to its elastic counterpart [148], but it has the unknown 'mean pressure' as a function of thermal strain $(\alpha\Delta T)$, rather than the compressive load.

5.4 Solution for an Infinite Strip

Consider a bonded polymer strip which has a large dimension in the y-direction as compared to the the width $w = 2b$ and thickness t. The thermoelastic deformation of the strip can be solved as a two-dimensional (2D) plane-strain problem. In this case, the displacement v in the y direction vanishes, and so does the pressure gradient $p_{,y}$. As a result, Eq. 5.10 becomes

$$\bar{p}_{,xx} - a^2\bar{p} = a^2\kappa\left(\epsilon_a - 3\alpha\Delta T\right). \tag{5.11}$$

The boundary conditions relevant to this ODE will be derived in the subsequent steps.

Because $v_{,y} = 0$, Eq. 5.3 becomes

$$u_{,x} = -w_{,z} - p/\kappa + 3\alpha\Delta T. \tag{5.12}$$

Substituting Eq. 5.12 into the lateral stress given in Eq. 5.4 and following by an integration across the thickness yields the mean lateral stress in the x-direction

$$\bar{\sigma}_{xx} = -\left(\frac{\lambda + 2\mu}{\kappa}\right)\bar{p} - 2\mu\epsilon_a + 4\mu\alpha\Delta T. \tag{5.13}$$

Since the mean lateral stress at the edge is zero, i.e. $\bar{\sigma}_{xx}(x = b) = 0$, the mean pressure at the edge is obtained as

$$\bar{p}(b) = \frac{\kappa}{\lambda + 2\mu}\left[-2\mu\epsilon_a + 4\mu\alpha\Delta T\right]. \tag{5.14}$$

Solving the ODE (5.11) with this boundary condition yields the mean pressure $\bar{p}$ as

$$\bar{p}(x) = \frac{\cosh ax}{\cosh ab}\left(\frac{\kappa}{\lambda + 2\mu}\right)\left[\lambda\epsilon_a - (3\lambda + 2\mu)\alpha\Delta T\right] + \kappa\left[-\epsilon_a + 3\alpha\Delta T\right]. \tag{5.15}$$

This result shows that the mean pressure is a function of x coordinate, the isotropic thermal strain ($\alpha\Delta T$) and the axial thermal strain (ϵ_a).

5.5 Thermal Strain

Integrating and normalizing the third sub-equation of Eq. 5.4 and using the definition of the axial thermal strain (ϵ_a) in Eq. 5.9 , the mean transverse stress becomes

$$\bar{\sigma}_{zz} = -\lambda\bar{p}(x)/\kappa + 2\mu\epsilon_a - 2\mu\alpha\Delta T. \tag{5.16}$$

Since there is no external loading over the width, the transverse force over the width is zero, leading to

$$\frac{1}{2b}\int_{-b}^{b}\bar{\sigma}_{zz}dx = 0 = -\frac{\lambda}{2b\kappa}\int_{-b}^{b}\bar{p}dx + 2\mu\epsilon_a - 2\mu\alpha\Delta T. \tag{5.17}$$

Substituting Eq. 5.15 into Eq. 5.17 yields the axial thermal strain (ϵ_a) as

$$\epsilon_a = \left(\frac{3\lambda + 2\mu}{\lambda + 2\mu}\right)\chi\alpha\Delta T \tag{5.18}$$

in which

$$\chi = \left[\frac{1 - \frac{\lambda}{\lambda+2\mu}\frac{\tanh ab}{ab}}{1 - \left(\frac{\lambda}{\lambda+2\mu}\right)^2\frac{\tanh ab}{ab}}\right].$$

In the case that the bonded strip is infinitely wide, i.e. ab $\rightarrow \infty$, the axial thermal strain approaches to the following expression in terms of Poisson's ratio and Young's modulus.

$$\epsilon_a = \left(\frac{1 + \nu}{1 - \nu}\right)\alpha\Delta T.$$

This expression is identical to the one derived using the bi-axial model for the configuration with infinite widths [82, 83, 157].

In the case that the bonded strip has a very small width, i.e. ab $\rightarrow$ 0, the axial thermal strain approaches to

$$\epsilon_a = (1+\nu)\,\alpha\Delta T,$$

which is the thermal strain for an unconstrained layer with plane-strain condition.

5.6 Thermal Stress

Due to the thermal expansion mismatch with the rigid plates, the polymeric layers are subjected to thermal stresses when subjected to a uniform temperature rise.

Substituting Eq. 5.18 into Eq. 5.15 yields the mean pressure as:

$$\bar{p}(x) = \kappa\alpha\Delta T\frac{3\lambda+2\mu}{\lambda+2\mu}\left[\frac{3\lambda+6\mu}{3\lambda+2\mu} - \frac{\cosh ax}{\cosh ab} - \left(1 - \frac{\lambda}{\lambda+2\mu}\frac{\cosh ax}{\cosh ab}\right)\chi\right]. \quad (5.19a)$$

The mean pressure gradient in the x-coordinate is:

$$\bar{p}_{,x} = -a\kappa\alpha\Delta T\frac{\sinh ax}{\cosh ab}\left(\frac{3\lambda+2\mu}{\lambda+2\mu}\right)\left[1 - \frac{\lambda}{\lambda+2\mu}\chi\right]. \quad (5.19b)$$

Substituting Eq. 5.15 and Eq. 5.18 into Eq. 5.13 reduces the the mean lateral stress as

$$\bar{\sigma}_{xx} = -\alpha\Delta T(3\lambda+2\mu)\left[1 - \frac{\cosh ax}{\cosh ab}\right]\left\{1 - \frac{\lambda}{\lambda+2\mu}\chi\right\} \quad (5.20a)$$

which is compressive in the x-direction for positive temperature changes.
The maximum mean lateral stress is found for $x = 0$, with

$$\bar{\sigma}_{xx}^{\max} = -\alpha\Delta T(3\lambda+2\mu)\left[1 - \frac{\lambda}{\lambda+2\mu}\chi\right]. \quad (5.20b)$$

On the other hand, the thermally induced shear stresses can be solved by analyzing the stress equilibrium in an infinitesimal free body. This approach is similar to what [45, 46] did in deriving the shear stress induced by a compressive load on a bonded rubber layer. Gent's derivation remains valid to predict the shear stress induced in the thermally expandable polymeric layer, which is bonded between rigid plate.

The equilibrium of lateral forces in a free body of the bonded layer (see Fig. 5.2) yields

$$\frac{\partial\tau_{xz}}{\partial z} = -\frac{\partial\sigma_{xx}}{\partial x} \quad (5.21)$$

where τ_{xz} denotes the shear stress.

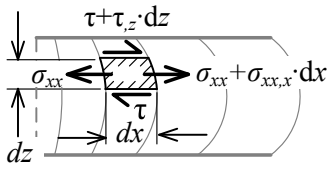

Fig. 5.2 Lateral forces acting on a free body in the bonded layer

Assuming that the shear stress on the mid-plane is assumed zero due to symmetry, Integration of Eq. 5.21 across the thickness, from the mid-plane to the top interface, yields the shear stress on the top interface as [46],

$$\bar{\tau}_{xz} = -\frac{t}{2}\frac{d\bar{\sigma}_{xx}}{dx}, \tag{5.22}$$

This equation tells neither the internal shear stress in the polymeric layer, nor spatial dependence of the shear stresses.

An alternative method of derivation is, therefore, attempted to determine the complete solution of the shear stress, together with lateral displacement u_0 along the mid-plane.

The shear stress is shown below as a function of transverse coordinate (i.e. z) by substituting the shear strain in Eq. 5.2 into $\tau_{xz} = \mu\gamma_{xz}$:

$$\tau_{xz} = -\frac{8\mu u_0}{t^2}z. \tag{5.23}$$

Substituting Eq. 5.23 and the lateral stress σ_{xx} of Eq. 5.4 into Eq. 5.21 yields

$$\frac{8\mu u_0}{t^2} = \frac{\lambda}{\kappa}p_{,x} - 2\mu u_{0,xx}(1 - 4z^2/t^2). \tag{5.24}$$

Integrating and normalizing the equation above with respect to the thickness t yields

$$u_{0,xx} - \frac{6}{t^2}u_0 = \frac{3\lambda}{4\mu\kappa}\bar{p}_{,x}. \tag{5.25}$$

Substituting the mean pressure gradient of Eq. 5.19b into Eq. 5.25 yields an ordinary differential equation for the edge lateral bulging u_0:

$$u_{0,xx} - m^2 u_0 = -an\frac{\sinh ax}{\cosh ab} \tag{5.26}$$

where

$$m^2 = \frac{6}{t^2}$$

and

$$n = \alpha\Delta T\frac{\lambda}{4\mu}\left(\frac{3\lambda + 2\mu}{\lambda + 2\mu}\right)\left[1 - \frac{\lambda}{\lambda + 2\mu}\chi\right].$$

The complete solution is

$$u_0 = u_{0h} + u_{0p} = A\cosh mx + B\sinh mx - \frac{an}{a^2 - m^2}\frac{\sinh ax}{\cosh ab}. \tag{5.27}$$

in which A and B are the unknown constants to be determined for the homogeneous solution u_{0h}, and the last term on the right-hand side is the particular solution u_{0p}.

Due to symmetry with respect to the centerline, the mean lateral displacement is zero, i.e. $u_0 = 0$ at $x = 0$. This gives $A = 0$.

Substituting $\sigma_{xx}(x = b) = 0$ into the first equation of Eq. 5.4 yields another boundary condition

$$u_{0,x}(x = b) = \alpha \Delta T \frac{3}{2} \left(\frac{3\lambda + 2\mu}{\lambda + 2\mu} \right) \left[1 - \frac{\lambda}{\lambda + 2\mu} \chi \right]. \tag{5.28}$$

Enforcing this boundary condition yields $B = 0$.

Substituting the constants A and B into Eq. 5.28, together with the definitions of m and n in Eq. 5.26, yields the solution of edge lateral bulging as

$$u_0 = \alpha \Delta T \frac{3}{2a} \frac{\sinh ax}{\cosh ab} \left(\frac{3\lambda + 2\mu}{\lambda + 2\mu} \right) \left[1 - \frac{\lambda}{\lambda + 2\mu} \chi \right]. \tag{5.29}$$

Substituting Eq. 5.29 into Eq. 5.23 yields the shear stress

$$\tau_{xz} = -\frac{12\mu}{at^2} \frac{\sinh ax}{\cosh ab} z \alpha \Delta T \left(\frac{3\lambda + 2\mu}{\lambda + 2\mu} \right) \left[1 - \frac{\lambda}{\lambda + 2\mu} \chi \right]. \tag{5.30a}$$

The maximum shear stress can be found at the edges of the top and bottom interfaces where $x = b$ and $z = \pm t/2$, such that

$$\tau_{xz}^{\max} = -\frac{6\mu}{at} \tanh ab \cdot \alpha \Delta T \left(\frac{3\lambda + 2\mu}{\lambda + 2\mu} \right) \left[1 - \frac{\lambda}{\lambda + 2\mu} \chi \right]. \tag{5.30b}$$

The derived shear stress is a spatial function of both the x- and z- coordinates, which are along the width and thickness respectively. Normalizing the shear stress leads to the following:

$$\bar{\tau}_{xz} = -\frac{ta}{2} \frac{\sinh ax}{\cosh ab} \alpha \Delta T (3\lambda + 2\mu) \left\{ 1 - \frac{\lambda}{\lambda + 2\mu} \chi \right\} \tag{5.30c}$$

It turns out to be identical to that derived by substituting the mean lateral stress of Eq. 5.20a into Eq. 5.22.

5.7 Numerical Examples and Validation

Numerical examples are use to check accuracy of the the derived analytical method. Following the numerical validation, a parametric study is performed to reveals relationships of thermally induced strains and stresses with design parameters, such as the bond width (w) and height (t). In addition, the study will also shows the dependence of the thermoelastic properties on Poisson's ratio, in addition to CTE.

The materials used in the examples are SU-8 epoxy, and an "incompressible" material, which possess the same properties as SU-8 except the Poisson's ratio. The material properties and geometric parameters are listed in Table 5.1. Numerical results using the analytical solutions are validated with those computed using finite element method (FEM). In the finite element analysis, the plane-strain layer is modeled by 2-D quadrilateral structural solid elements (PLANE42 of ANSYS) with fine meshing.

Table 5.1 Material properties and design parameters

	Units	SU-8 [37]	"Incompressible" SU-8
Young's modulus, E	GPa	3.2	3.2
Poisson's ratio, ν	1	0.33	0.49
Coef. Thermal expansion, α	ppm/°C	150	150
Layer thickness, t	μm	3	3
Layer width, w	μm	$3 \leq w \leq 60$	$3 \leq w \leq 60$

5.7.1 *Axial Strain and Lateral Displacement*

Fig. 5.3a shows that the apparent axial CTE (ϵ_a) as a function of the aspect ratio (w/t). The apparent axial CTE is normalized as the ratio of the apparent axial strain ϵ_a to the free thermal strain ($\alpha\Delta T$). A comparison between numerical solutions shows that the analytical solution according to Eq. 5.18 predicts the apparent axial CTE as accurately as finite element method. The agreement between the analytical and finite element solutions is confirmed over the range of the aspect ratio and for both the compressible and incompressible materials.

Fig. 5.4a shows that the normalized lateral bulging as a function of the aspect ratio (w/t). The normalized lateral bulging is defined as $u_0/(t\alpha\Delta T)$, i.e the ratio of the maximum lateral bulging (u_0) at the edge over the free transverse thermal expansion ($t\alpha\Delta T$). The analytical solution according to Eq. 5.29 agrees well with finite element solutions, predicting the same trends. The analytical solution provides pretty well prediction for the incompressible material. However, it shows some deviations for the compressible material with 0.33 Poisson's ratio. For example, the analytical solution for the compressible material is 8% higher at the aspect ratio of 10 than FEM solution, and it becomes 12% higher at the aspect ratio of 20.

5.7.2 *Thermally Induced Stresses*

Fig. 5.5 shows the width distribution of thermally induced stresses in a design, consisting of a rigidly bonded SU-8 strip (30-μm wide and 3-μm thick). The plotted stress distribution in this bonded layer are normalized with the thermal stress ($E\alpha\Delta T$). As shown in Fig. 5.5a, the mean lateral stress is compressive in

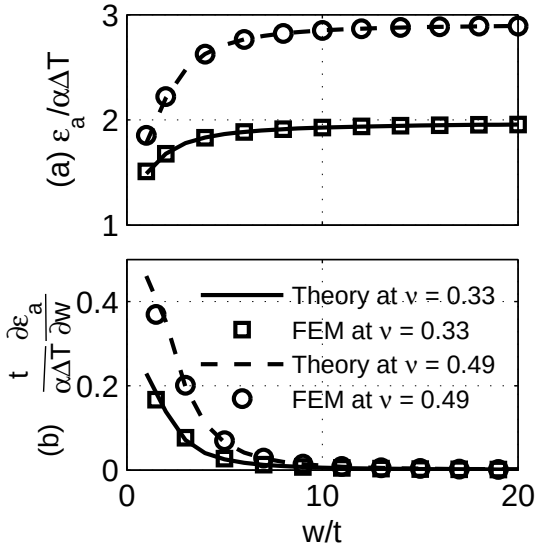

Fig. 5.3 (a) Normalized apparent axial strain and (b) its change rate with respect to the aspect ratio, for a bonded polymer layer evaluated at two different Poisson's ratios

the bonded polymer layer. It has a plateau-like trend with a maximum compressive stress at the center ($x = 0$) and a zero stress at the free edge ($x = b$). The trend is a hyperbolic cosine function of the x coordinate, according to Eq. 5.20a. Fig. 5.5b shows the spatial distribution of the thermally induced shear stress. The shear stress is zero at the center (i.e. at $x = 0$), but it increases to a maximum value at the edge (i.e. at $x = b$). The trend of the top interface shear stress at $z = t/2$ is an hyperbolic sine function following Eq. 5.30a.

In addition to spatial dependence, the thermally induced stresses depend on other factors. For example, they depend nonlinearly on the Poisson's ratio and the aspect ratio (see Fig. 5.6 and 5.7).

The 'mean-pressure' method provide accurate prediction of the thermally induced stresses at the interior of the bonded layer. This is illustrated with an example design of a layer with an aspect ratio 10. Fig 5.5 shows that the analytical method predicts the interior stresses as accurately as the finite element method. A good agreement is also shown in Fig 5.6 for the maximum lateral stress at other aspect ratios and for both the compressible and incompressible materials.

The analytical solutions of the edge stresses are given in Eq. 5.20b and Eq. 5.30b. The analytical solutions agrees in trend with finite element solutions. However, they shows discrepancies, in particularly for the compressible materials. In the example of a bonded SU-8 layer with an aspect ratio of 10, the analytical solution of the mean lateral stress at the edge is 27% lower than the finite element

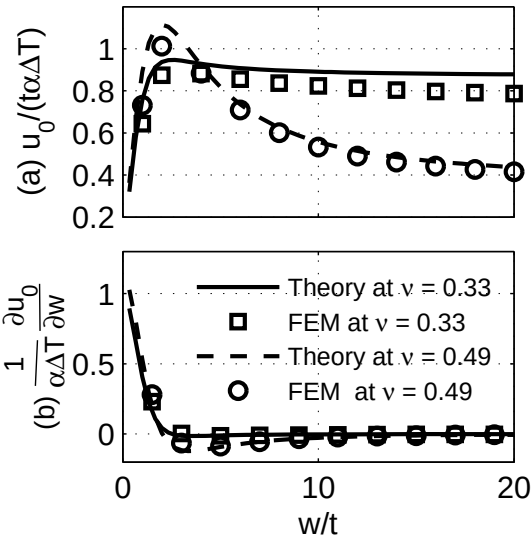

Fig. 5.4 (a) Normalized lateral displacement and (b) its change rate with respect to the aspect ratio, for a bonded polymer layer evaluated at two different Poisson's ratios.

solution, whereas the analytical solution of the interfacial shear stresss at the edge is 45% higher (see Fig. 5.5). The edge discrepancy for the interfacial shear stress are varying depending on Poisson's ratio and aspect ratio. Fig. 5.7a shows that the discrepancy for the incompressible layer is within 23%; . However, the edge discrepancy for the compressible material is larger, as much as 63% at a large aspect ratio.

The edge discrepancy is attributed to the fact that rotation happens near the edge and do not obey the kinematic assumptions used for the analytical solution (see Eq. 5.2). The displacement field in the neighborhood of the edge does not remain lateral as assumed with Eq. (1). Despite this, the assumption is adequate for predicting the stresses of the bonded layer at the interior (see Fig. 5.5).

5.8 Influences of the Aspect Ratio and Poisson's ratio

5.8.1 *Axial Strain and Lateral Displacement*

Fig. 5.3a shows that the apparent axial CTE changes nonlinearly with the aspect ratio and the Poisson's ratio, according to Eq. 5.18. The apparent axial CTE increases at a decreasing rate with the aspect ratio. The apparent axial CTE converges to finite values at a large aspect ratio. The converged CTE for the incompressible layer (with Poisson's ratio of 0.49) is almost three times higher than

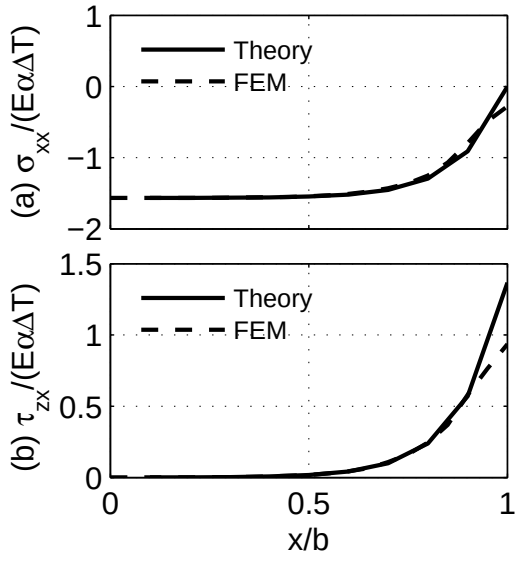

Fig. 5.5 Distribution of thermally induced stresses along the symmetric half of a 30-μm wide bonded SU-8 layer: (a) normalized lateral stress σ_{xx}; (b) normalized shear stress τ_{xy}

the free intrinsic CTE; whereas that for the compressible layer (with Poisson's ratio of 0.33) is almost twice.

Fig. 5.3b shows the normalized gradients of the axial strain, i.e. $\frac{t}{\alpha\Delta T}\frac{\partial \epsilon_a}{\partial w}$, as a function of the aspect ratio. The gradients are obtained by either differentiating the analytical equation or calcuating the finite difference of the finite element results. The gradient diminishes with the aspect ratio (w/t). The gradient for the compressible layer is smaller than that for the incompressible layer.

The thermally induced lateral bulging (u_0) is a maximum at the edge of the bonded layer while it is zero at the center. The maximum or the edge lateral bulging is a nonlinear function of geometric parameters. The edge bulging varies non-monotonically with the aspect ratio (w/t). Fig. 5.4 shows that the normalized edge bulging increases with the aspect ratio below 3. It peaks at the aspect ratio of 3. Beyond this peak aspect ratio, the normalized edge lateral bulging decreases asymptotically and converges to a smaller value. The converged value at the large aspect ratio depends on Poisson's ratio. Fig. 5.4a shows that the converged edge bulging for the compressible layer is about 2 times larger than that for the incompressible layer.

In addition, Fig. 5.4b shows the normalized rate of change of the lateral bulging, i.e. $\frac{t}{t\alpha\Delta T}\frac{\partial u_0}{\partial w}$, as a function of the aspect ratio. It is observed that the rate diminishes to zero at a large aspect ratio for both the compressible and incompressible layers. The rate for the incompressible layer dips slightly below zero at the aspect

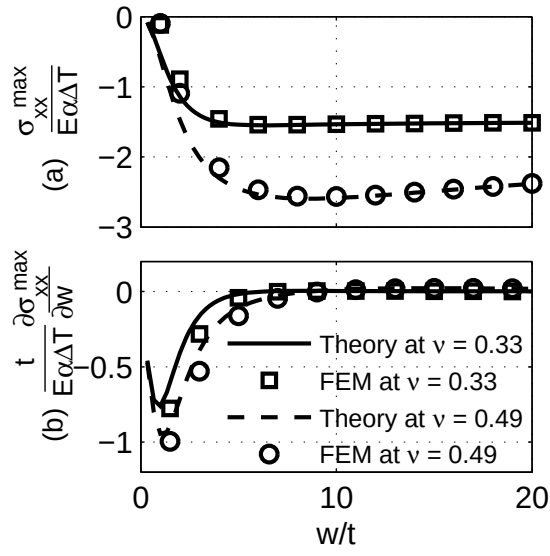

Fig. 5.6 (a) Normalized maximum lateral stress and (b) its change rate with respect to the aspect ratio, for a bonded polymer layer evaluated at two different Poisson's ratios.

ratio of about 2.

5.8.2 *Thermally Induced Stresses*

Fig. 5.6a shows that the maximum mean lateral stress as a function of the aspect ratio. The shown lateral stress is evaluated at the center of the bonded layer and it is normalized with thermal stress ($E\alpha\Delta T$). At a small aspect ratio, the center lateral stress is close to zero. However, it becomes increasingly compressive at a large aspect ratio. In short, the center lateral stress increases at decreasing rates with the aspect ratio, showing a plateau-like trend. It converges and becomes independent of the aspect ratio at a large aspect ratio. The converged center lateral stress depends on Poisson's ratio. In generally, the incompressible layer exhibits a larger compressive stresses than the compressible layer at the same aspect ratio even though both material layers have the same intrinsic Young's modulus and CTE. In addition, Fig. 5.6b shows the normalized gradient of the center lateral stress, i.e. $\frac{t}{E\alpha\Delta T}\frac{\partial \sigma_{xx}}{\partial w}$, as a function of the aspect ratio. The gradients diminishes to zero at a large aspect ratio.

Fig. 5.7 shows the maximum interface shear stress as a function of the aspect ratio. The shown interface shear stress is evaluated at the edge of the bonded layer and it is normalized with thermal stress ($E\alpha\Delta T$). The edge shear stress shows a peak at the aspect ratio about 3. Beyond this peak aspect ratio, the edge shear

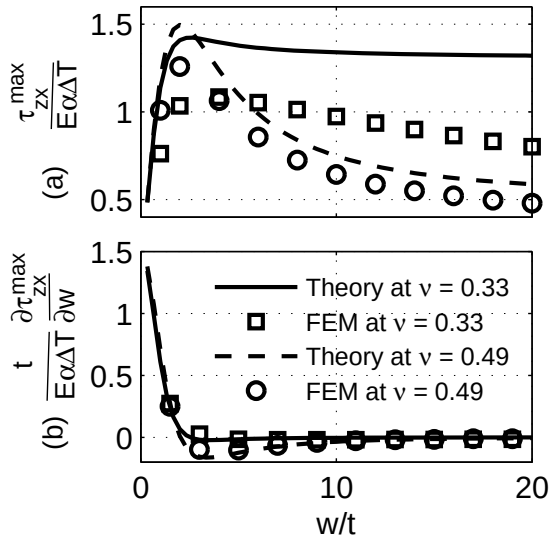

Fig. 5.7 (a) Normalized maximum shear stress and (b) its change rate with respect to the aspect ratio, for a bonded polymer layer evaluated at two different Poisson's ratios.

stress decreases with the aspect ratio. It becomes independent of the aspect ratio at a large aspect ratio. Fig. 5.7b shows the normalized gradient of the edge shear stress, i.e. $\frac{t}{E\alpha\Delta T}\frac{\partial \tau_{zx}}{\partial w}$ as a function of the aspect ratio. The gradient approach zero at a large aspect ratio. In addition, the edge shear stresses show dependence on Poisson's ratio. At aspect ratios above 3, the incompressible layer has a lower edge shear stress than the compressible layer. However, the incompressible layer shows a higher edge shear stress at a smaller aspect ratio.

5.8.3 *Confinement Widths*

In the parametric study above, all thermo-elastic responses for the bonded layer are shown dependent on the aspect ratio. They show a large rate of change at a small aspect ratio but a diminishing rate at a large aspect ratio. They converges to respective constants at a large aspect ratio. It is interesting to know at which aspect ratio or plate width the thermo-elastic responses converge to a large extent. For example, how narrow can the plates be without compromising the thermal strain enhancement?

Let us define the confinement width as the width, above which the thermally induced strain or the stress is within 5 % difference from the converged values at a large aspect ratio. The confinement widths are varying and depend on Poisson's ratio and the thermo-elastic response of interest. For example, the confinement

width for the converged axial CTE (see Fig. 5.3a) is 5 times the thickness of the compressible layer; it is 6 times the thickness of the incompressible layer. The confinement width for the converged lateral bulging (see Fig. 5.4a) is 4 times the layer thickness of the compressible layer, while it is 16 times the layer thickness of the incompressible layer. The confinement width for the converged lateral stress (see Fig. 5.6a) is about 4 times the layer thickness for both the compressible and incompressible layers. On the other hand, confinement widths for the converged shear stress (see Fig. 5.7a) are similar to those for the converged lateral displacement.

5.9 Concluding Remarks

This paper derived analytical solutions to thermally induced strains and stresses in a polymer layer bonded between two rigid interfaces. The analytical derivation is based on the 'mean pressure' method and the assumptions that lateral planes remain planar and transverse lines become parabolic when subjected to isothermal expansion. The approach leads to approximate closed-form analytical solutions for the displacement, strain and stress distributions. The close-form solutions reveals the relationship between the apparent thermo-elastic behavior with the material and design parameters for the bonded polymeric layer. The closed-form solutions lay the foundation to further evaluate and optimize the thermal micro-actuators and composite material design, which consist basically of the finite-width laminates of skeleton and polymer materials.

The close-form solutions are found in good agreement with finite element solutions at the interior parts of the bonded layer. The close-form solutions for the axial apparent strain and the lateral displacement almost exactly reproduce FEM results. However, the solutions, in particularly for the thermally induced stresses, are less accurate at the edges of the layer . The deviation is attributed to the fact that the approximate displacement field remains planar and does not allow rotation near the edge. However, this assumption is adequate for predicting the strain and stress at the interior parts of the bonded layer.

Based on the validated model, the relationships of thermoelastic behaviors are revealed being dependent on the aspect ratio and Poisson's ratio. The parametric study determines the confinement width above which the bonded SU-8 layer shows converged thermo-elastic properties. It is found that a confinement width, which is 5 times the strip thickness, could attain 95% of the maximum strain enhancement at the infinite width. A bond width larger than the confinement width could improves marginally the strain enhancement. In conclusion, a sufficiently compact design of the bonded polymeric layer could well exploit the directional enhancement for effective thermal actuation.

Chapter 6

Steady-State Thermal Analysis

This chapter [1] presents design, modeling and characterization of a novel thermal actuator design, consisting of a thermally expandable polymer and a meandering-shaped skeleton. The polymer in use is SU-8 epoxy while the skeleton is made of silicon. The design with the embedded skeleton is effective for in-plane thermal actuation, delivering the highly rectilinear displacement and stiffness. It also enhances heat transfer to the insulating polymer. Electro-thermal and thermo-elastic models are formulated to predict steady-state responses of the actuator. The electro-thermal model is obtained by straightening the meandering heat conduction path, whereas the thermo-elastic model is based on a stack of polymeric and skeleton layers. The relatively simple theoretical models capture the essence of the actuation principle, and are in good agreement with both detailed finite element simulations and experimental observations. The theoretical and experimental evaluations show that the present polymeric actuator design with a skeleton outperforms a conventional design of a polymeric actuator without a skeleton in terms of heat transfer, and thus response time, and planarity of actuation.

6.1 Introduction

Thermal actuation has advantages over other types of micro-actuation. It features compactness, a high force, a large displacement and a low driving voltage [8, 27, 64, 121]. It has a wide range of applications for both out-of-plane and in-plane motion. For example, out-of-plane thermal actuation is useful for driving ciliary conveyors [8] and optical scanners [159]; whereas in-plane thermal actuation is applied to align fibers [38], to drive optical attenuators [21] and to drive microgrippers [111]. Besides driving functional micro-devices, in-plane linear thermal actuation is also an indispensable element for an in-situ microscopic material tester with integrated load sensing. For example, arrays of V-shape actuators are used for loading a string of carbon nano tubes during tensile tests [167].

Performance of thermal actuation depends to a large extent on the expansion

[1] This chapter is based on the manuscript submitted to the Journal of Microelectromech. Syst. [79]

materials [64]. Many thermal actuators are made of silicon or metals. However, silicon and metals have relatively low coefficients of thermal expansion (CTE) and high thermal conductivities [14, 40, 42]. Consequently, they are not effective in electro-mechanical conversion. Polymers are known to have high CTE [37, 64]. There is increasing interest in using them as expansion materials. For example, large out-of-plane actuation is reported using metallic-coated polymeric bi-layers [8]; in-plane actuation using metallic-coated U-shape polymers is reported in [22]. However, polymer materials are electrical and thermal insulators. A thick polymeric layer responses slowly to heat changes, and thus leads to slow time responses. Moreover, it easily exhibits unintended out-of-plane bending, arising from internal stress gradients due to fabrication, thermal gradients across the thickness during resistive heating, or CTE mismatch between the polymeric and metallic heating layers. In addition, polymeric thermal actuators have a low stiffness as compared to their silicon or metallic counterparts. Therefore, the existing designs of polymeric thermal actuators are not ideal for in-plane actuation.

6.2 Actuator Design

For effective in-plane actuation, a novel thermal actuator design is presented in this paper. The design selects SU-8 epoxy as thermal expansion polymer, silicon as skeleton and aluminum as heater. These materials are selected because they can readily be structured using micro-machining methods and they possess the desired thermo-physical properties. In this new design, a silicon skeleton is embedded in a polymer block (see Fig. 6.1). The skeleton has a symmetric meandering shape. It could stiffen the polymer and directly polymeric thermal expansion in the in-plane longitudinal direction [78, 82]. In addition, The silicon skeleton serves to conduct heat effectively across the thick insulating polymer. A top metallic heating film, i.e. Al film, is deposited on top of the skeleton.

Actuation capability of the proposed actuator design has been evaluated in [83]. In this paper, we will present comprehensive thermal and mechanical modeling for the actuator operating at the steady state. In subsequent sections, theoretical models are developed for the actuator. Finite element modeling (FEM) and experimental characterization are included to validate the theoretical models. The steady-state evaluations and comparisons will show the advantages of the present design, in terms of the thermal conductivity, planarity of actuation strain, and magnitude of actuation stress. A parametric design study will be performed to show the influence of bond width on the apparent transverse CTE of the bonded polymeric filling.

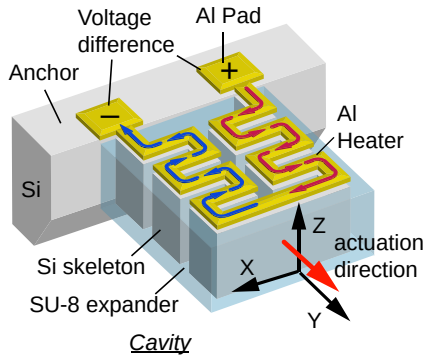

Fig. 6.1 An illustration of the thermal actuator design, consisting of polymeric encapsulant (i.e. SU-8 expander), silicon microstructure (skeleton) and a thin-film aluminum heater; the actuator resembles a cantilever, with its root anchoring to the silicon substrate and its body and tip suspended in an air cavity.

6.3 Electro-thermal Analysis

The silicon skeleton is embedded in the polymeric encapsulant (see Fig. 6.1). It provides an 'express' path for heat transfer to the latter when resistively heated using the aluminum heater. Heat diffusion from the silicon microstructure into the adjacent encapsulant is quick. This is especially true across the thickness (i.e. z direction), in which the silicon microstructure extends through the high polymer block. Note the high thermal conductivity of silicon (148 W/(mK) [14]) in comparison to SU-8 (0.2 W/(mK) [37]). A subsequent analysis will show enhanced electro-thermal behavior using the present actuator design.

6.3.1 *One-dimensional Thermal Model*

The meandering silicon microstructure has a plate-like structure with many folds along the longitudinal (y) axis . Polymer is filled in the gaps or spaces of the folds. The root of the actuator, including the silicon microstructure, is anchored to the substrate with a fixed initial temperature. When an electric potential difference is applied to the aluminum heater on top of the silicon microstructure, the entire actuator, including the polymer filling, rises in temperature. The generated heat is dissipated by heat conduction and convection. Heat conduction to the substrate is predominantly along the silicon microstructure while heat conduction across the polymer filling is minor. Heat convection is mainly through the circumferential surfaces (i.e. the top, bottom and sides) of the entire actuator. Without changing much the thermal behavior, we can unfold the meandering path of heat conduction into a straight line path (see Fig. 6.2). This geometry conversion provides a basis for one-dimensional (1-D) modeling.

The 1-D line model consists of a silicon plate, polymer cladding on two sides,

and a thin-film aluminum heater on top of the plate. The silicon plate stands vertically with respect to the wafer plane. Heat transfer and generation is along the line path. in addition, heat convection around the exact actuator is also taken into account in the line model (see Fig. 6.3). Heat convection occurs around the total circumferential surfaces of the actuator but not at the internal surfaces, which become virtually exposed due to unfolding in the line model.

In addition, the line model makes several assumptions. Firstly, it is assumed that the temperature distribution on the actuator is in the steady state. Secondly, it is assumed that a cross-section of the representative composite line has a uniform temperature. In other words, the polymeric cladding has the same temperature as the silicon plate and aluminum heater for a specific section. Thirdly, the materials, which constitute the composite actuator, are assumed to have perfect thermal contact at their interfaces. Finally, the temperature distribution is assumed to be symmetric with respect to the centerline because the actuator has a symmetric geometry (see Fig. 6.2) and the boundary conditions symmetric about the centerline.

The symmetry assumption yields an important consequence, i.e. no heat transfer transfer across the polymeric filling along the centerline. To a large extent, this ensures the assumed adiabatic condition on the internal polymeric cladding, as well as, the validity of the line model. Otherwise, the simple line model could not predict thermal behavior of the composite actuator. For example, in a bending actuator design with an embedded non-symmetric skeleton, heat transfer happens across the polymeric filling between segments of the asymmetric skeleton, consisting of a straight segment and a meandering segment [78]. Therefore, the asymmetric temperature distribution in the design could not be predicted using the simple model.

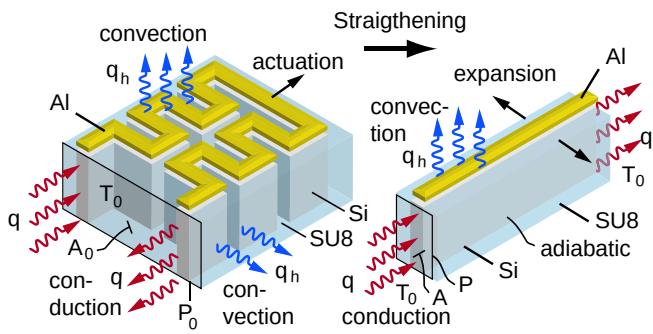

Fig. 6.2 Simplified electro-thermal model obtained by straightening the meandering heat conducting path and applying appropriate boundary conditions.

6.3.2 *Heat Transfer*

The representative line model consists of three components, i.e aluminum, silicon and SU-8, with cross section A_1, A_2, and A_3, respectively (see Fig. 6.4a). The total cross-sectional area is denoted as A. The aluminum film is very thin as compared to the silicon and SU-8 microstructures. Consequently, the aluminum section is relatively small as compared to those of silicon and epoxy.

When applying a voltage difference V, a total current I is induced and flows through the composite line with a total length L. Owing to the very low electric resistivity of aluminum, the electric current mainly flows through the aluminum section. Thus, the total electric current approximately amounts to the current through the aluminum section (see Fig. 6.4b), i.e.

$$\begin{aligned} I = I_1 + I_2 + I_3 &= \left(\frac{A_1}{\rho_1} + \frac{A_2}{\rho_2} + \frac{A_3}{\rho_3}\right)\frac{V}{L} \\ &\approx \left(\frac{A_1}{\rho_1}\right)\frac{V}{L} \end{aligned} \tag{6.1}$$

As a result of resistive heat generation in the aluminum heater (see Fig. 6.4c), the actuator rises in temperature. In turn, the temperature rise causes a proportional increase in the aluminum electric resistivity [63]:

$$\rho_1 = \rho_0 \left(1 + \beta(T - T_0)\right) \tag{6.2}$$

in which ρ_0 is the resistivity at the initial temperature T_0, and β is the temperature coefficient of resistivity (TCR).

The generated heat is conducted away through the two ends, which are assumed at the initial temperature T_0 as the substrate (see Fig. 6.2). The induced temperature rise and heat flux, is distributed non-uniformly along the length. The heat flux q conducted through a section is the sum of the component heat fluxes, i.e. q_1, q_2, q_3, through the sub-sections of aluminum, silicon and SU-8 (see Fig. 6.4d). According to Fourier's law, the heat flux is,

$$\begin{aligned} q &= q_1 + q_2 + q_3 \\ &= -\left(k_1 A_1 + k_1 A_2 + k_3 A_3\right)\frac{dT}{dx} \\ &= -kA\frac{dT}{dx} \end{aligned} \tag{6.3}$$

in which k_1, k_2 and k_3 are the thermal conductivities for aluminum, silicon and epoxy, respectively, and the effective thermal conductivity for the composite line segment is $k = \left(k_1 A_1 + k_1 A_2 + k_3 A_3\right) A^{-1}$ [93].

In addition to heat conduction, heat convection takes places at the exposed surfaces. The exposed areas A_p includes the areas at the top, bottom and sides of the actuator. However, the exposed areas do not include the internal areas of the polymeric claddings, which become exposed as a result of unfolding the meandering microstructure. The convection heat flux q_h is given as,

$$q_h = hA_p \left(T - T_\infty\right) \tag{6.4}$$

in which T denotes surface temperature; T_∞ denotes room temperature; and h denotes the heat convection coefficient as a function of surface temperature T [67].

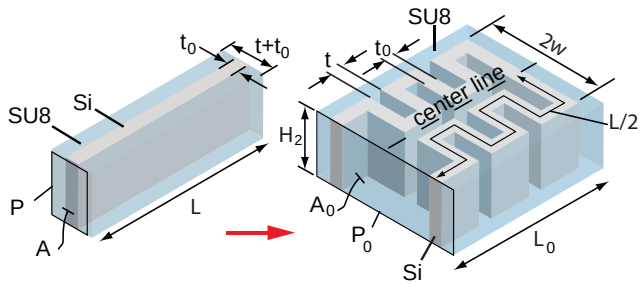

Fig. 6.3 Relationship of an effective perimeter P for the line model to the real perimeter P_0 for the entire actuator.

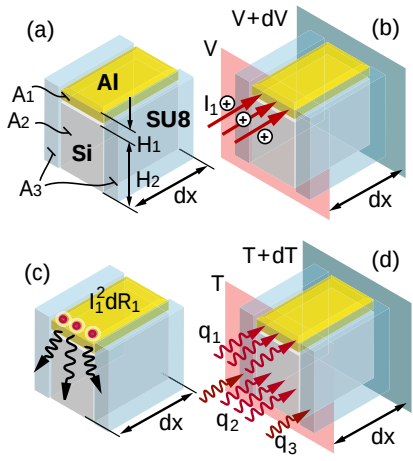

Fig. 6.4 Estimation of effective thermo-physical properties using the representative segment for the line model: (a) material components; (b) electric current flow across the cross section; (c) resistive heat generation and sectional heat transfer; (d) heat transfer along the composite conduction paths.

6.3.3 *Heat Balance*

In the steady state, heat dissipation by conduction and convection is in equilibrium with the heat generation by resistive heating [18]. Thermal equilibrium in an infinitesimal segment leads to :

$$k(T)A\frac{d^2T}{dx^2}dx - h(T)P\left(T - T_\infty\right)dx + I_1^2\frac{dR_1(T)}{dx}dx = 0 \tag{6.5}$$

in which R_1 is the resistance of the aluminum film and $dR_1/dx = \rho_1(T)/A$; P is the effective perimeter of the section such that $P = 2P_0L_0/L$ (see Fig. 6.3); P_0 is the perimeter over a section of the entire actuator; L_0 is the longitudinal length of the entire actuator and L is the heater length.

Assuming that the initial temperature T_0 is equal to room temperature T_∞, substitution of Eq. 6.1 into Eq. 6.5 leads to an ordinary differential equation (ODE):

$$\frac{d^2T}{dx^2} - m^2\left(T - T_0\right) + n^2 = 0 \tag{6.6}$$

in which

$$m^2 = \frac{h(T)P}{k(T)A}$$

$$n^2 = \frac{1}{k\rho_1(T)}\left(\frac{A_1}{A}\right)\left(\frac{V}{L}\right)^2.$$

Boundary conditions are imposed such that the temperatures at the two ends, i.e. at $x = 0$ and $x = L$, are equal to T_0.

The coefficients m^2 and n^2 are temperature dependent. Consequently, the ordinary differential equation is nonlinear and has no simple and exact solution. The nonlinear ODE can be solved as a boundary value problem using numerical methods. For example, it can be solved using a MATLAB subroutine bvp4c (based on the Simpson Method [130]) by re-casting the ODE into a state-space form.

6.3.4 *Solution for Linearized Equation*

The exact solution to the nonlinear governing equation is not readily available. However, a closed-form solution is desired to provide insight into the influence of design parameters on the electro-thermal response. For this reason, the nonlinear governing equation is linearized and solved using several assumptions. Firstly, the change in the electric resistance is assumed to be small, so that its inverse can be approximated using a linear approximation. Secondly, the heat convection coefficient of air is assumed to be independent of temperature and equal to the value at the initial temperature, i.e. $h = h_0$. Finally, the thermal conductivity of the composite is assumed to be independent of temperature and equal to the value at the initial temperature, i.e. $k = k_0$. Linearizing Eq. 6.6 yields:

$$\frac{d^2\theta}{dx^2} - m_0^2\theta = 0 \tag{6.7}$$

with

$$m_0^2 = \frac{h_0 P}{k_0 A} + \beta n_0^2 \tag{6.8}$$

$$n_0^2 = \frac{1}{k_0 \rho_0} \left(\frac{A_1}{A}\right) \left(\frac{V}{L}\right)^2 \tag{6.9}$$

$$\eta = \frac{n_0^2}{m_0^2} \tag{6.10}$$

$$\theta = (T - T_0 - \eta)\,. \tag{6.11}$$

This linear ODE has a solution [16]

$$\theta = C_1 \sinh m_0 x + C_2 \cosh m_0 x. \tag{6.12}$$

Since the two ends are fixed at the room temperature, the associated boundary conditions become:

$$\begin{aligned} \theta(x=0) &= T(x=0) - T_0 - \eta = -\eta \\ \theta(x=L) &= T(x=L) - T_0 - \eta = -\eta \end{aligned}. \tag{6.13}$$

Imposing the boundary conditions, the linear analytical solution becomes

$$\theta(x) = \eta \left(\frac{\cosh m_0 L - 1}{\sinh m_0 L}\right) \sinh m_0 x - \eta \cosh m_0 x. \tag{6.14}$$

The solution exhibits a maximum

$$\theta(x^*) = \eta \left(\frac{\cosh m_0 L - 1}{\sinh m_0 L}\right) \sinh \frac{m_0 L}{2} - \eta \cosh \frac{m_0 L}{2} \tag{6.15}$$

for

$$x^* = \frac{1}{m_0} \tanh^{-1} \left(\frac{\cosh m_0 L - 1}{\sinh m_0 L}\right) \approx \frac{L}{2}. \tag{6.16}$$

The maximum temperature T_{max} becomes

$$T_{\max} = T_0 + \eta + \theta(x^*).$$

The average temperature T_{avg} along the length is

$$T_{avg} = T_0 + \eta + \frac{\eta}{L m_0} \left[\frac{(\cosh m_0 L - 1)^2}{\sinh m_0 L} - \sinh m_0 L\right]. \tag{6.17}$$

Thus, the resistance for the entire aluminum thin-film heater can be estimated with

$$R = \frac{\rho_0 L}{A_1} \left[1 + \beta \left(T_{avg} - T_0\right)\right]. \tag{6.18}$$

This equation relates the average temperature rise to the change in the resistance, which can be measured experimentally.

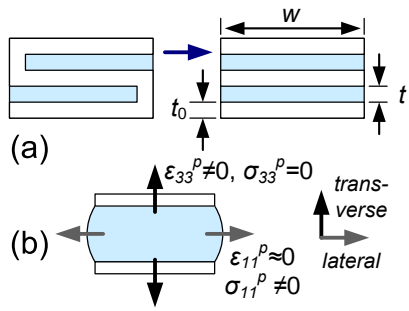

Fig. 6.5 Thermoelastic models of polymeric composite with embedded silicon microstructures: (a) the large-width meandering silicon microstructure, resembling an array of parallel silicon plates; (b) constrained thermal expansion of the polymeric layer sandwiched between the silicon layers.

6.4 Thermo-mechanical Analysis

Let us study how the embedded silicon skeleton affects thermal expansion of the polymer. Zooming into a representative unit (see Fig. 6.5) shows that the polymer filling is located and confined in the spacing between a fold of the meandering silicon microstructure . The fold consists of two plate-like segments and a single horseshoe bend that connects the two plates. A direction convention is defined here to facilitate later discussion. The plane of the plates, in other words, the sidewall, is perpendicular to the wafer plane (see Fig. 6.1) . Therefore, we define a transverse direction as perpendicular to the sidewalls, whereas a lateral direction as parallel to the sidewalls.

When heated, the polymeric filling expands and widens the spacing in each fold of the meandering microstructure. Thermo-elastic deformation of the confined polymeric filling is complex even when heated uniformly. In general, thermal expansion of the confined polymer is predominantly perpendicular to the sidewalls, which impose surface restraint. A closer look shows that the polymeric portion located at the closed end of the fold is restricted more than that located next to the opened end of the fold. The thermoelastic deformation becomes less complex in the case for a very wide fold which becomes less restrained by the horseshoe bend. In the limiting case, the polymeric filling confined in the fold is similar in configuration to a polymer sandwiched between two silicon plates (see Fig. 6.5).

Analysis of the sandwiched polymeric layer can provide insight into the confinement effect on the transverse thermal expansion (see Fig. 6.5). The bond interfaces can be assumed rigid because the silicon plates, with approximately identical thicknesses to the SU-8 filling, is approximately 40 times stiffer than SU-8 and expand 60 times less. No lateral displacement is allowed at the bonded interfaces. However, at the mid-plane away from the rigid interfaces, the bonded polymeric layer may bulge laterally. The magnitude of lateral bulging depends on the aspect ratio (r) of the bond width (w) to the layer thickness (t) of polymer. A layer with a small

aspect ratio may display substantial lateral bulging, near the free edges. However, a layer with a large aspect ratio has the lateral bulging largely suppressed. As a result of the surface restraint, the volumetric thermal expansion is concentrated in the transverse direction ($\perp$), yielding an enhanced apparent thermal strain.

In subsequent paragraphs, we shall develop an estimate to the apparent transverse thermal strain of a stack of polymer and skeleton laminas or layers. The polymeric layer is assumed to have linear isotropic elastic properties, undergoing small thermoelastic strains. A 2-D plane strain model is first developed for the bonded polymer layer with a finite width. Then, it is used to estimate thermal strain of the whole laminated composite.

6.4.1 *Finite-width Model*

Despite bonding with the rigid interfaces, a polymeric layer with a small aspect ratio (i.e. having the bond width comparable to the layer thickness) may still undergo certain lateral deformations near the free edge. The associated lateral bulging will affect the apparent transverse strain for the layer.

A plane-strain two-dimensional (2D) model is formulated to account for the lateral bulging. The 2D model assumes that the polymeric layer is made of a linear elastic isotropic material and it is bonded with rigid interfaces. In addition, this model relies on two kinematic assumptions, namely that lateral planes remain plane and the transverse lines become parabolic. These kinematic assumptions are similar to those imposed on a compressed elastic layer under transverse pressure [95,148]. In the present case, these kinematic assumptions are applied to a thermally expanded layer under a uniform temperature rise without external mechanical loading. The derivation of an approximate solution is beyond the present scope, and will be elaborated elsewhere [81]. Here, only the solution to the 2-D thermoelastic model is presented. The apparent transverse strain is a function of aspect ratio (r) and Poisson's ratio (υ), besides intrinsic CTE (α),

$$\alpha_{\perp} = \left(\frac{1+\upsilon}{1-\upsilon}\right) f(r)\alpha \tag{6.19}$$

with

$$f(r) = \frac{1 - \left(\frac{\upsilon}{1-\upsilon}\right)\frac{\tanh(r)}{r}}{1 - \left(\frac{\upsilon}{1-\upsilon}\right)^2 \frac{\tanh(r)}{r}}$$

and

$$r = \frac{w}{t}\sqrt{\frac{3}{2}\left(\frac{1-2\upsilon}{1-\upsilon}\right)}$$

The analysis confirms that the confinement effect is beneficial to thermal actuation, in contrary to the suppression in dielectric actuation using confined elastomer [84]. In the limiting case of infinite width, the function $f(r)$ approaches to 1

and the apparent transverse CTE ($\alpha_{\perp}$) becomes equal to the one derived from the bi-axial model [82].

6.4.2 *Effective Composite Thermal Expansion*

As mentioned, the polymeric actuator with a symmetric meandering skeleton is similar in configuration to a stack of polymeric and silicon layers. Therefore, the tip displacement for the former can be roughly estimated with that for the latter. An effective transverse CTE (α_c) for the stack is obtained using a law of mixtures:

$$\alpha_c = \phi\alpha_{su-8,\perp} + (1-\phi)\alpha_{si} \tag{6.20}$$

in which ϕ is the volume fraction of SU-8, $\alpha_{\perp,SU-8}$, is the apparent transverse CTE of the bonded SU-8 layer, and α_{Si} is the CTE of the bonded silicon layer. Since the apparent transverse CTE of silicon is much smaller than that of SU-8, we shall assume that the contribution of silicon thermal expansion is negligible. This leads to following, with substitution of Eq. 6.19 :

$$\alpha_c \approx \phi\alpha_{su-8,\perp} = \phi\left(\frac{1+\upsilon}{1-\upsilon}\right) f(r)\alpha \tag{6.21}$$

This equation shows that the composite CTE depends on the aspect ratio of the polymeric layer.

During resistive heating, the temperature distribution along the meandering conductor becomes non-uniform, with a hyperbolic profile according to Eq. 6.17. It leads to an average temperature rise, $(T_{avg} - T_0)$ in the polymer, and consequently an longitudinal thermal expansion, mainly contributed by the polymer. The model predict a tip displacement ΔL for the heated stack (with a length L) as below

$$\Delta L \approx L\,(T_{avg} - T_0)\,\alpha_c \tag{6.22}$$

With this, we present a simple estimation to the electro-thermo-mechanical response for the actuator.

6.5 Finite Element Analysis

The finite element software ANSYS is used to simulate performance of the proposed actuator design and to verify the theoretical models. Two sets of simulation are conducted, namely the thermo-elastic response under uniform heating, and the electro-thermal-mechanical response under steady-state resistive heating. The finite element models for thermal-elastic simulation consist of structural elements, either the two-dimensional (2-D) plane-strain elements (PLANE42) or the three-dimensional (3-D) element (SOLID45). The models for electro-thermal-mechanical simulation consists of the 3-D coupled-field elements (SOLID5).

The thermo-elastic analysis serves well to extract effective thermo-elastic properties for the actuator, by avoiding the unknown temperature distribution and the

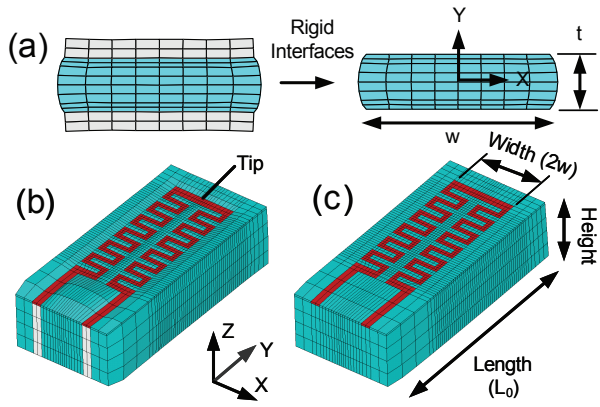

Fig. 6.6 Deformed shapes of finite element meshes (illustrative and not in exact dimensions and mesh division): (a) Model #1; (b) Model #2; (c) Model #3 (see Table 1 for detailed description).

nonlinear temperature dependent thermo-physical properties, such as electric resistivity and heat convection. The coupled analysis for resistive heating serves to predict responses of the actuator under normal operating conditions. It is more complicated and involves simulation of electric, thermal and mechanical displacement fields, simultaneously.

Three geometry models are simulated (see Fig. 6.6 and Table 6.1). The first geometry model is a 2D polymeric layer bonded between two rigid interfaces (see Fig. 6.6a). This model has the same geometry and boundary condictions as for Eq. 6.21. The second geometry model is a 3D actuator design (see Fig. 6.6b), consisting of the polymeric filling, symmetric meandering silicon skeleton and aluminum thin-film heater. The third geometry model is a 3D polymeric block with an aluminum thin-film heater on the top (see Fig. 6.6c). The third model does not have silicon skeleton embedded in it, but has the identical configuration of aluminium heater to the second model.

The first model serves to predict the apparent transverse CTE of the bonded layer under uniform heating. The second model serves to predict the actuator responses under both uniform and resistive heating. The third model serves as a reference design for comparison with the second model. The boundary and loading conditions imposed to the three models are summarized in Table 6.1. Geometry parameters for the second and third models are listed in Table 6.2.

Table 6.1 Geometry parameters for models #2 and #3

Model	Description	Element Type	Boundary Condition	Loading Condition
#1	A polymeric layer bonded between rigid interfaces (SU-8). The same configuration as for the theory in deriving Eqs. 6.19 and 6.21	PLANE42 (2D plane strain)	The layer with thickness t has its center fixed, i.e. $\{u_x, u_y\} = \{0, 0\}$ at $(x, y) = (0, 0)$, and its interfaces restrained laterally, i.e. : $\{u_x, u_y\} = \{0, \pm c\}$ at $y = \pm t/2$ where c is unknown displacement.	Uniform thermal loading ΔT = 100°C
#2	The polymeric actuator with embedded silicon microstructure and aluminum heater (SU-8/Si/Al)	SOLID45 or SOLID5 (3D structural or coupled field)	The root is fixed such that $\{u_x, u_y\} = \{0, 0\}$ and $T = T_0$ at y=0. Otherwise, the rest is free to move.	Electric loading with voltage difference across the Al heater. Mechanical loading with forces at the tip, i.e. F_y=1 at $(x, y) = (0, L_0)$. Thermal loading as in #1;
#3	A polymeric block with integrated surface aluminum heater (SU-8/Al)	As in #2	The same boundary condition as in the model #2	As in #2

Table 6.2 Geometry parameters for models #2 and #3

Parameters (μm)	Symbol	Model #2 SU8/Si/Al	Model #3 SU8/Al
Actuator length	L_0	530	530
Actuator width	$2w$	60	60
Actuator thickness	$\approx H_2$	50	50
Al. thickness	H_1	0.675	0.675
Si/SU-8 thicknesses	H_2	50/50	0/50
Si plate width	t_0	3	0
Gap between Si plates	t	3	-
Al heater length	L	5.2×10^3	5.2×10^3

Table 6.3 Material properties of solids at 300 K

Material Properties	Symbols	Unit	Si [14]	Al [40]	SU-8 [37]
Young's modulus	E	GPa	130	69	3.2
Poisson's ratio	υ		0.26	0.35	0.32
CTE	α	10^{-6}/K	2.6	23.1	150.7
Thermal conductivity	k	W/(mK)	148	237	0.2
Electric resistivity	ρ	Ω m	2E-2	3.1E-8	>1.2E10
TCR	β	1/K	–	4.1E-3	–

Table 6.4 Temperature-dependent thermal conductivity of solids [42]

Thermal conductivity (W/(mK))	Symbols	Bulk temperature (K)				
		300	400	500	600	700
Aluminium, Al	k_{al}	237	240	236	231	225
Silicon, Si	k_{si}	148	119	98.9	76.2	69.1

6.5.1 *Material properties*

The success in the modeling depends to a large extent on accurate data on material properties. This is in particularly true for electro-thermal modeling as material properties change with temperature. For example, electric resistivity, thermal conduction of solids, and thermal convection through air, are all temperature dependent. The material properties used in the present models are summarized in Table 6.3. They are based on the data available in literature [14, 37, 40, 42].

According to Table 6.4 [42], thermal conductivity of silicon decreases at a diminishing rate with temperature while that of aluminum changes slightly over the operating temperature range. Thermal conductivity of SU-8 epoxy is not directly available. It is therefore taken to be identical to that reported for other types of

epoxies [15, 18, 141]. According to Cahill and Pohl [18], the thermal conductivity for epoxy increases as a function of absolute temperature at a decreasing rate; it approaches to a constant at temperatures above 300 K . For example, the reported thermal conductivities for EPON 862 [15] and Araldite epoxy resin [141] are around 0.2 W/(mK) at temperatures equal or above 300 K.

Thermo-physical properties of air are also important in the modeling. They are strongly dependent on temperature (see Table 6.5). They affect the heat dissipation through air. At the operating temperature range, the contribution of heat radiation is insignificant as compared to heat conduction and convection [63]. The heat conduction through air (h_{cond}) is given as $h_{cond} = k_{air}/g_z$, where k_{air} denotes the thermal conductivity of air and g_z denotes the air gap beneath the actuator [59]. On the other hand, the heat convection through air (h_{conv}) depends on various thermo-physical properties and an effective diameter. It can be estimated using a dimensionless correlation formula [25] for a horizontal cylinder with diameter D,

$$Nu_D = \left\{ 0.60 + \frac{0.387 Ra_D^{1/6}}{[1 + (0.059/\,\mathrm{Pr})^{9/16}]^{8/27}} \right\}^2 \tag{6.23}$$

where $Ra_D \leq 10^{12}$. The dimensionless variables are defined as follow [67]: Rayleigh number is $Ra_D = g\gamma\,(T_s - T_\infty)\,D^3/(\nu\kappa)$, Nusselt number is $Nu_D = h_{conv}D/k_{air}$, whereas Prandtl number is $\mathrm{Pr} = \nu/\kappa$. The other symbols in the equations above are defined in Table 6.5 [66]. The effective diameter D used in the estimation is derived from the cross-sectional area A_0 and perimeter P_0 of the actuator block (see Fig. 6.4), such that $D = 4A_0/P_0$.

Other thermo-elastic properties are assumed to be temperature independent. These properties include Young's modulus, Poisson's ratio and thermal expansion coefficients. Thermo-elastic properties of silicon and aluminum at a constant temperature are obtained from literature [40]. The thermo-elastic properties of SU-8 epoxy are reported with large variation in literature, as they depend on processing parameters, testing methods and sample geometry [37]. For example, a stretched polymeric thin film manifests a CTE different from that for a confined sample in a close cylinder; even for the same thin-film sample, the in-plane CTE is different from the out-of-plane CTE [37]. In this context, SU-8 epoxy is filled between silicon plates. Therefore, its linear CTE is taken as one third of the volumetric thermal expansion, which is obtained for the confined sample.

Table 6.5 Temperature-dependent properties of air [66]

Thermophysical data of air	Symbol	Unit	Air Temperature(K)				
			300	400	500	600	700
Volumetirc thermal expansion	γ	10^{-3}/K	3.33	2.86	2.50	2.20	2.00
Kinematic viscosity	ν	10^{-6}ms^{-2}	15.9	26.4	38.8	52.7	68.1
Thermal diffusivity	κ	10^{-6}ms^{-2}	22.5	38.3	56.7	76.9	98.0
Thermal conductivity	k_{air}	10^{-3}W/(mK)	26.3	33.8	40.7	46.9	52.4
Prandtl number	Pr	10^{-3}	707	690	684	685	695
			Derived data with D=55μm				
Rayleigh number	Ra_D	10^{-6}	609	775	823	721	600
Nusselt number	Nu_D	10^{-3}	440	486	487	484	480
Convection coefficient	h_{conv}	Wm^{-2}K^{-1}	211	300	355	403	443
Conduction coefficient	h_{cond}	Wm^{-2}K^{-1}	146	188	226	261	291
Total heat transfer coeff.	h_{total}	Wm^{-2}K^{-1}	357	487	582	663	734

6.6 Characterization

To validate the theoretical and numerical modeling, experimental characterization of sample devices is performed. The sample devices (see Fig. 6.7) are fabricated using bulk silicon micro-machining and SU-8 photo-resist casting. Details of the fabrication are reported in [23, 24]. The samples are tested under either external uniform heating or integrated resistive heating. The test under uniform heating serves to show the confinement effect of varying bond widths on the apparent CTE. Samples tested have a bond width, ranging from 60 μm to 120 μm. On the other hand, the test with resistive heating serves to show the device performance under a normal operating condition.

The experiments with external heating are carried out using a temperature controllable hotplate and a microscope with a CCD camera. The displacement induced by a known temperature rise is obtained by comparing the captured image at the elevated temperature with that at the room temperature. On the other hand, the experiments with resistive heating are carried out on a probe station. A voltage difference across the heater causes a current and consequently a temperature rise and thermal expansion. The induced current is measured using an Agilent parameter analyzer, while the induced displacement is obtained by comparing the captured images before and after the electrical activation. The responses under resistive heating are more complicated because they involve an unknown temperature and are influenced by temperature-dependent properties.

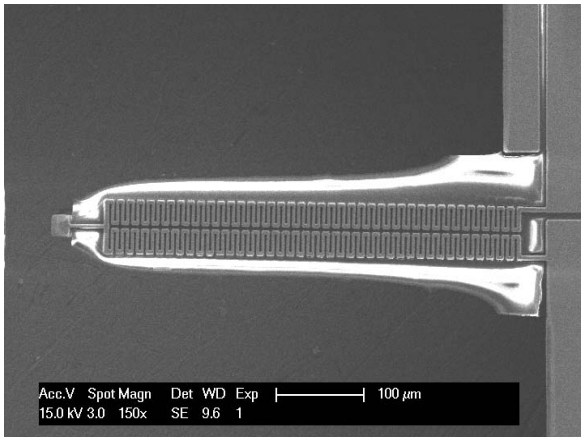

Fig. 6.7 Scanning electron micrograph of a sample device (60 μm wide)

6.7 Results and Discussion

The results and discussions are divided into three parts. The first part discusses the apparent transverse CTEs for the actuators under uniform heating. The second part discusses the temperature distribution of the actuators under resistive heating, and the third part shows electro-thermal-mechanical responses over a range of driving voltages.

6.7.1 *Uniform Heating*

The apparent CTEs for the composites are defined as the tip thermal expansion divided by the composite length and the temperature rise. They can be obtained from theoretical and numerical models, as well as, experimental measurement under uniform heating. For the first model (#1) which is a rigidly bonded SU-8 layer, the polymeric thermal expansion is substituted into Eq. 6.21 to estimate a CTE for the composite (50-50 % SU-8/Si). For the second model (#2) which is a polymeric actuator with embedded skeleton, the apparent composite CTE is estimated from the tip displacement. In experimental measurement, the apparent CTE is calculated from the measured longitudinal dimensional change ΔL.

Fig. 6.8 shows that the apparent CTEs, obtained from the various models and experiment as functions of aspect ratio. All results increase at a decreasing rate with the aspect ratio. They converge to respective levels at a large aspect ratio. However, the 2D model #1 and Eq. 6.21 predicts a higher apparent CTE than the 3-D model #2 because the model #1 assume a stack of parallel silicon plates but ignores the horseshoe bends in the model #2. The model #2 predicts the same trend of the apparent CTE as the measurement but shows some discrepancy.

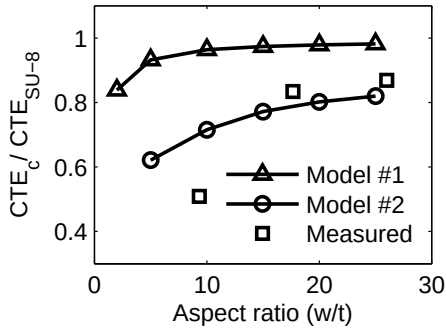

Fig. 6.8 Apparent transverse CTE as functions of the aspect ratio for the model #1, which is a polymer composite with an embedded array of rigid parallel plates, the model #2, which is a polymeric composite with an embedded meandering silicon skeleton, and for the actual device under test.

6.7.2 *Resistive Heating*

The simulations predict electro-thermo-mechanical behaviors for the actuator models (# 2 and 3) under resistive heating. The simulations are based on the theoretical (ODE) and numerical (FE) methods. In the simulations, the material properties are assumed either temperature independent (linear) as listed in Table 6.2, or temperature dependent (non-linear) as listed in Table 6.4 and 6.5. The models have the same width, i.e. a 60-μm, for the Al heater or Si skeleton (see Figs. 6.6c and 6.7). In the following discussion, simulations results for the actuator with the embedded skeleton (i.e. model # 2) are first presented before those for the polymeric block with the heating film (i.e. model #3).

For the actuator model #2, the temperature profiles along a meandering path are simulated at different driving voltages (see Fig. 6.9). The results show that the top temperature profiles on the heating film are almost identical to those on the bottom of the silicon skeleton. The temperature profiles appear to be symmetric along the path, with the two ends fixed at the room temperature and the center reaching a peak temperature. The peak temperature increases with the driving voltage. The nonlinear ODE provides temperature prediction as good as the nonlinear FEM. However, the linear ODE deviates substantially from the nonlinear simulation at a higher voltage (>1 V). The discrepancy using the linear ODE is attributed to the linear assumption that neglects the change in thermo-physical properties with respect to the temperature rise.

Fig. 6.10 shows the temperature and voltage contours induced at 1 V for model # 2. The temperature distribution is symmetric with respect to the longitudinal centerline. The tip of the actuator reaches a maximum temperature while the root remains at room temperature. The temperature contour on the top heating film is identical to that on the bottom surface of the embedded skeleton. The contour

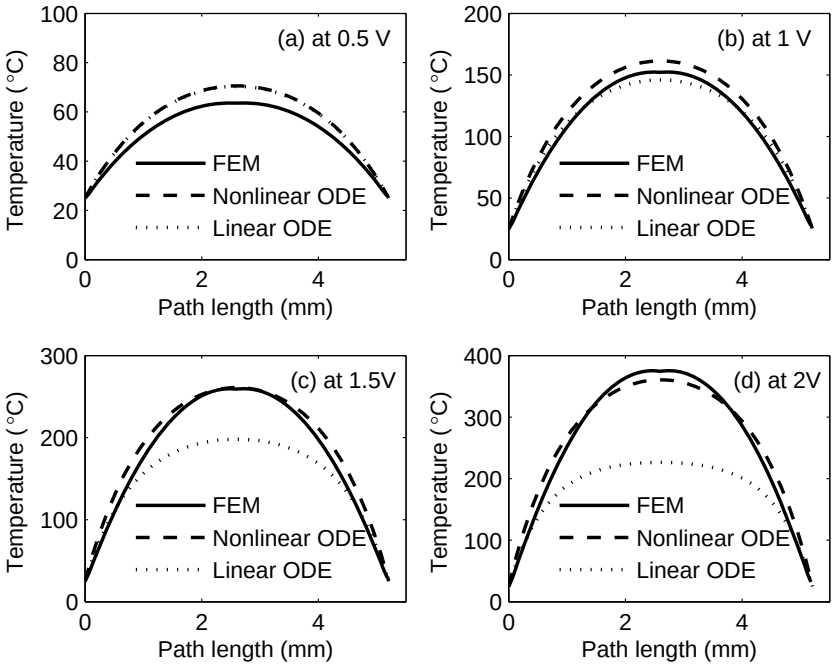

Fig. 6.9 Simulated temperature distributions along a meandering path of a polymeric composite actuator with the embedded skeleton (Model #2), including both theoretical and FEM results.

on the side shows that the temperature is almost uniform across the thickness but varying along the length. The simulated voltage field on the aluminum heater is also shown in Fig. 6.10 to be symmetric with respect to the longitudinal centerline.

Fig. 6.11 shows the displacement contours simulated at 1 V for model #2. It is found that the longitudinal displacement (u_y) increases along the length and reaches a maximum at the tip. The lateral expansion (u_x) is largely suppressed but with some lateral bulging. To a large extent, the actuation remains in-plane as observed from the vertical displacement contour (u_z). The silicon microstructure has little vertical motion when activated electro-thermally. There are small vertical displacements on the free edges of the polymer filling and at the front tip of the encapsulant, which is only restrained from one side. However, the maximum vertical expansions of the polymeric encapsulant remain less than half a micron.

For comparison, a surface-heated polymeric block (i.e. model #3) is also simulated. Finite element simulation shows that surface heating of the polymeric block leads to a substantial temperature gradient across the thickness. The surface on the top heater is hotter than the bottom surface of the insulating polymeric block, which is 50-μm thick. The temperature contour on the top differs from that on the bottom (see Fig. 6.12). Due to this gradient, the polymer block under surface

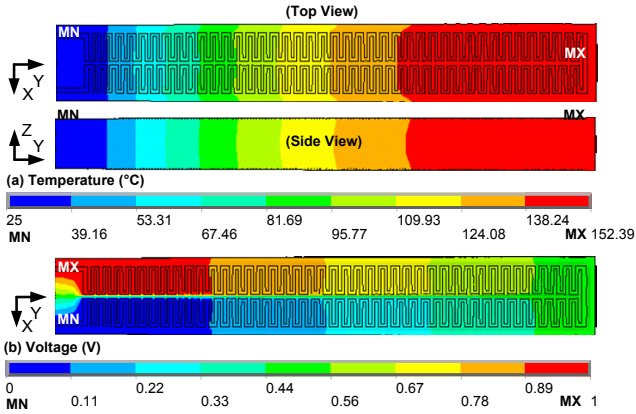

Fig. 6.10 Simulated temperature and voltage fields induced to a polymeric composite actuator with the embedded skeleton (Model #2) when resistively activated at 1 V: top, side and bottom views.

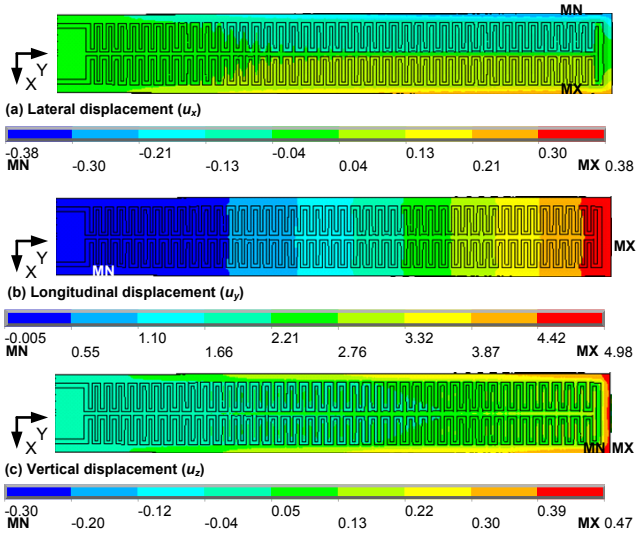

Fig. 6.11 Simulated displacement fields of a polymeric composite actuator with the embedded skeleton (Model #2) when resistively activated at 1 V: (a) lateral displacement (u_x); (b) longitudinal (or transverse) displacement (u_y) and (c) vertical displacement (u_z).

heating is subjected to a vertical motion (e.g. 1.5 μm at 1V) besides the intended longitudinal motion (see Fig. 6.13).

Fig. 6.14 shows the simulated temperature profiles induced at 1 V along meandering heat conduction paths in the polymeric block (model #3). Finite element simulation predict that the top temperature on the heater is higher than that on the bottom of the polymeric block. Both the top and bottom temperature profiles

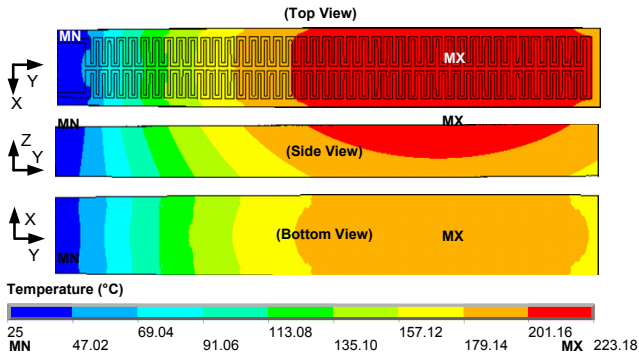

Fig. 6.12 Simulated temperature fields induced to a polymeric block (Model #3) when resistively activated at 1 V: top, side and bottom views.

appear like two 'camel humps', which have two identical peaks off the center and a 'saddle' at the center. The central saddle suggests that heat dissipation at the end tip of the polymer block is faster than at the inside. On the other hand, the non-linear ODE predicts a symmetric temperature profile of comparable magnitude as the finite element method. However, it hardly predicts the temperature difference between the top and bottom or the 'saddle' at the center.

6.7.3 *Design Comparison*

The simulated performance for the polymeric actuators with or without the embedded skeleton (i.e. models #2 and #3) are summarized in Table 6.6. The polymeric actuators without the embedded skeleton is hereafter termed as the polymer block. Both models have the identical geometry except the skeleton (see Table 6.2).

The design with embedded silicon skeleton exhibits 25 times higher stiffness in the direction of actuation. In addition, it (model # 2) has an equivalent thermal conductivity, (i.e. at 76 W/(mK)) 152 times higher than the polymer block alone (model # 3).

However, the polymeric actuator with the skeleton delivers a lower tip stroke than the polymer block when resistively heated at the same driving voltage. For example, the former delivers approximately 5 μm at 1V, in comparison to 11 μm for the latter. This is because the actuator with embedded skeleton contains 50% less the thermal expandable polymer and it is subjected to 41% less temperature rise at 1V as compared the polymer block. At the same temperature rise, the polymeric actuator with embedded skeleton could deliver as much as 77 % of the tip stroke generated by the polymer block.

The polymeric actuator with embedded skeleton has very little out-of-plane motion, coupled with the intended in-plane motion. The ratio of out-of-plane motion to in-plane motion is approximately 1% for this design under resistive heating, and it becomes 4% under uniform heating. On the the hand, the motion coupling is

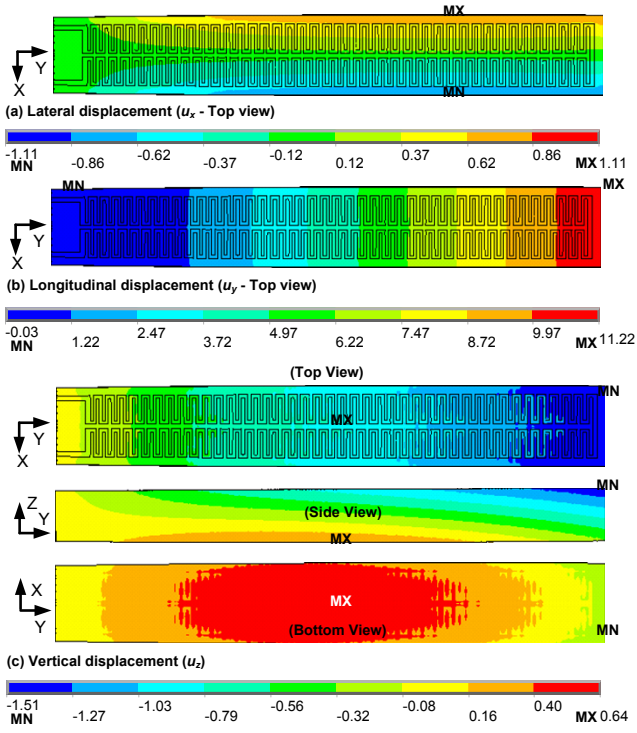

Fig. 6.13 Simulated displacement fields of a polymeric block (Model #3) when resistively activated at 1 V: (a) lateral displacement (u_x); (b) longitudinal (or transverse) displacement (u_y) and (c) vertical displacement (u_z).

very serious for the polymeric block. It is 11 % under resistive heating and becomes excessively high at 94% under uniform heating. The large out-of-plane bending happens unintendedly under the uniform heating because the polymeric block is effectively a bilayer consisting of a thin Al film on top and a thick SU-8 layer beneath.

Based on the comparison above, it is concluded that the design with embedded silicon microstructure can achieve highly in-plane actuation with large stiffness.

6.7.4 *Experimental Validation*

To validate the theoretical and numerical models under resistive heating, experiment measurements are performed using a sample device (60-μm wide and 530-μm long, see Fig. 6.7). The primary measured data includes the electric current, resistance change and tip displacement. An average temperature rise can be estimated using the measured resistance change and the temperature coefficient of resistance (TCR). The measured data is compared with the simulation results over a voltage range from 0 to 2 V. It is found that the simulation results agree well with the measurement

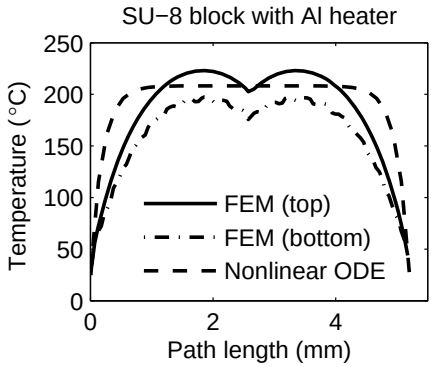

Fig. 6.14 Simulated temperature distribution along the meandering paths on the top and bottoms of a polymeric block (Model #3) when resistively heated at 1 V, including both theoretical and FEM predictions.

Table 6.6 Performance comparison based on simulation

Simulated responses	Symbols	Unit	Model #2, SU8/Si/Al	Model #3, SU8/Al
Equivalent thermal conductivity	k_{eqv}	W/(mK)	76	0.2
Electric Resistance				
at 0 V	R_0	Ω	70.4	70.4
at 1 V	R	Ω	95.4	116.4
Input power at 1 V		mW	10.5	8.6
Temperature at 1 V				
Maximum value	T_{max}	°C	152.4	223.2
Average value	T_{avg}	°C	108.6	166.5
Tip stroke at 1 V				
Lateral value	u_x	μm	0	0
Longitudinal value	u_y	μm	4.60	10.80
Vertical value	u_z	μm	0.05	1.43
Tip stroke at ΔT=100°C				
Lateral value	u_x	μm	0	0
Longitudinal value	u_y	μm	5.57	7.20
Vertical value	u_z	μm	0.23	6.74
Tip stiffness				
Lateral value	k_x	kN/m	0.38	0.15
Longitudinal value	k_y	kN/m	164.82	6.59
Vertical value	k_z	kN/m	0.17	0.07

data.

For example, Fig. 6.15a shows that the simulated electric resistance increases with voltage, like the measured resistance. Discrepancy between the simulated and measured resistance is small, but growing with the driving voltages. In particularly, the linear simulation shows growing deviations at a voltage greater than 1 V. This

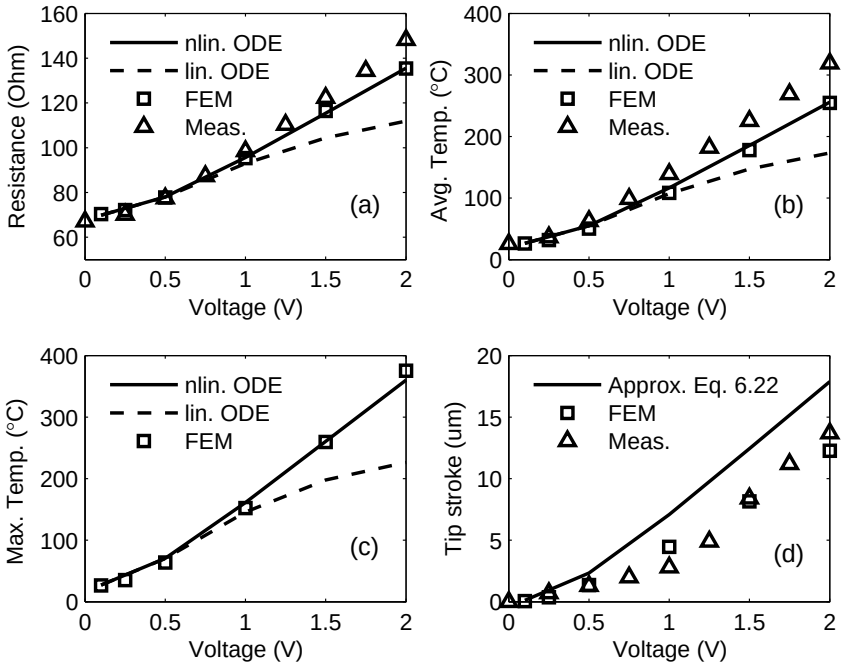

Fig. 6.15 Electro-thermal-mechanical responses as functions of driving voltage for the activated 60-*mu*m wide polymeric actuators with embedded silicon microstructures (see Fig. 6.6a): (a) electric resistance; (b) average temperature; (c) simulated maximum temperature; (d) tip displacement.

is because the assumptions of temperature-independent properties for the linear simulation do not hold at the elevated temperature. Fig. 6.15b shows that the predicted average temperature increases with the driving voltage. The trend of the average temperature is similar to that for the resistance. Maximum temperature is not available in the measurement. However, the simulation predicts (see Fig. 6.15c) that the maximum temperature increases with the driving voltage.

Fig. 6.15d shows that both the measured and simulated tip displacements increase with the driving voltage. The FEM results agree well with the measurement. However, the approximation using Eq. 6.22 over-estimates the tip displacement. Comparison between Fig. 6.15b and 6.15d shows that the FEM simulation predicts a matched tip stroke as the measurement but a smaller average temperature at the voltage range > 1 V. Therefore, this correlation suggests that the CTE values used for the simulation may be higher than the actual values, in particular that for SU-8. Therefore, material characterization is necessary to provide relevant thermo-physical data to simulation.

6.8 Conclusion

An electro-thermal model for a polymeric actuator with embedded silicon microstructure has been developed based on heat conduction and heat convection along the meandering heat path. The electro-thermal model successfully predicts the temperature distribution and is validated by finite element simulation. In addition, the thermoelastic expansion of the polymeric actuator is estimated using a stacked model of polymeric and silicon layers. This model predicts that the apparent transverse thermal strain of the polymeric layer increases with the widths of the bond interfaces. Combining the electro-thermal and thermo-elastic models yields an approximation of the actuation stroke under resistive heating. The theoretical results agree well with the FEM results and measurements.

The evaluations show that the polymeric actuator with embedded silicon microstructure could deliver highly in-plane actuation combined with relatively high stiffness. In addition, this actuator design improves tremendously the effective thermal conductivity so that it overcomes the problem of non-uniform heating, which troubles a thick insulating polymer. It is therefore concluded that the present design of thermal actuator successfully exploits the benefits of polymeric composite for effective in-plane thermal actuation. The accomplished performance cannot be achieved using a homogeneous material. The present design of thermal actuator is expected to have a wider range of applications, in particular where a large force, large displacement and high planarity are concerned.

Chapter 7

Material Selection

This chapter presents strategies of material selection for building a powerful polymeric actuator with an embedded skeleton. Various thermally expandable polymers and stiff skeleton materials are considered and combined to comprise the actuator. The material combinations are evaluated using a composite model of polymer and skeleton laminae. The evaluation shows that a polymeric lamina bonded between skeleton laminae has the stiffness and thermal expansion improved in the actuation direction. In addition, Poisson's ratio of the polymer significantly affect the actuation performance, besides its intrinsic thermal expansion and Young's modulus. Among the material under investigation, the polydimethylsiloxane-containing composites show a large thermal expansion; the composites containing liquid crystal polymer show a large stiffness; whereas, the composites containing SU-8 epoxy or nylon show high work density. On the other hand, most metals and silicon serve well as the skeleton.

7.1 Introduction

Polymers are capable to produce large thermal expansions. Therefore, they are preferred materials to constitute thermal actuators [64]. However, they are mostly insulating materials, having high electric resistivity and low thermal conductivity. The insulating properties do not allow inherent electro-thermal activation of polymers. In addition, as compared to silicon which is a common material to construct electro-thermal actuators, polymers have a low elastic modulus and may not produce high actuation stress.

Despite their shortcomings, there are still very strong incentives to use polymers as thermal expansion materials. In particular, one of the incentives is the relatively large thermal strain per unit temperature rise (i.e. the coefficient of thermal expansion (CTE)). These considerations motivate a composite design that overcomes the mentioned limitations of high-expansion polymers [8, 22, 83, 111]. A successful example of composite design is a polymeric thermal actuator with an embedded skeleton [83]. The embedded skeleton acts primarily to improves heat transfer to

thermally insulating polymer. In addition, the skeleton reinforces the relatively compliant polymer and concentrates volumetric thermal expansion of the polymer in the actuation direction. This design cleverly exploits the large stiffness and CTE mismatches between the polymer and skeleton materials for the effective thermal actuation.

The reported composite design adopts SU-8 epoxy as the expander, silicon as the skeleton, and aluminium as the thin-film heater (see Fig. 7.1). The design exhibits improved thermal conductivity as compared to SU-8 epoxy alone while maintaining excellent actuation performance [79, 83]. It is anticipated that the actuator design can be improved further by material selection and design optimization. The present paper will put focus on material selection. It will address the intriguing questions, such as, what the ideal materials are for the expander, skeleton and heater; what the ideal combination of them is. Geometry influence and the optimized proportions of material combination will be discussed in another paper on design optimization.

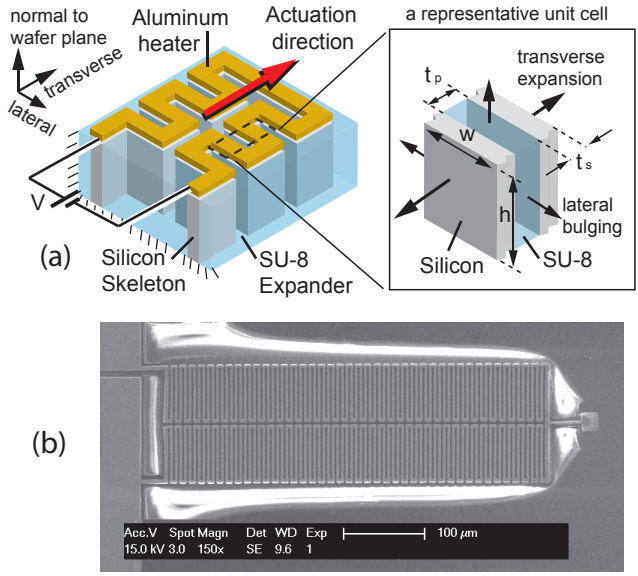

Fig. 7.1 A polymeric actuator design with an embedded silicon skeleton: (a) a schematic drawing and a sandwiched model of laminae; (b) a scanning electron micrograph of a sample device (with a total length of 500 μm and spacing gap width of 3 μm)

7.2 Material Selection

There have been a few publications studying material selection for thermal actuators. For example, Jang and Zhang [69] surveyed comprehensively thermal actuation capability of various polymers and metals, which undergo either solid thermal expansion or phase change during melting. Jonsmann and Bouwstra [71] considered solid materials, mainly metals, for application in topology optimized thermal microactuators. On the other hands, Prasanna and Spearing [120] studied material selection for thermal benders using two solid-material layers. Their work optimizes the bi-layer composite design for maximum thermally induced free-end slope, blocked moment or work density.

It is anticipated that material selection will help improving the present polymeric actuator design with the embedded skeleton. In this case, the primary concerns for material selection are to choose expansion and skeleton materials. The desired expansion materials should have high coefficients of thermal expansion (CTE) and high Young's modulus for thermal actuation. The desired skeleton materials should have high thermal diffusivity to provide quick thermal response, in addition to relatively high stiffness. A quick look at the material chart (Ashby, p. 51 [7]) suggests that polymers are suitable as thermal expanders, whereas diamond, silicon and most metals are suitable as heat conductors, which complement the insulating polymers. Their combination is anticipated to satisfy the required thermal characteristics.

Conductivity improvement of polymers with thermally conductive fillers is not new [90]. However, it is intriguing to learn how embedding the conductive microstructure does affect the thermal actuation of polymers. In general, polymeric materials possess a large CTE but a low Young's modulus. Skeleton materials, such as silicon and metals, generally, have a lower CTE but a much higher Young's modulus. The large mismatches in CTE and elastic modulus is expected to result in a complex interaction between of the two materials. A preliminary study shows a combination of SU-8 epoxy and silicon delivers better thermal actuation capability. It is interesting to investigate the room of performance improvement using other materials combinations.

7.2.1 *Scope*

There are many materials available to act as either the thermal expander or the skeleton. However, not all of them can be micro-machined into the desired shapes. In the present actuator design, the skeleton should be shaped with high-aspect-ratio trenches to hold the polymer and to have large contact surfaces with it. Conversely, the polymer needs to be filled into the trenches. The trench gap, or the polymer thickness, should be sized as small as possible to shorten the path for heat transfer and to induce the confinement effects that enhance the actuation strain and stiffness.

The shape requirement limits the skeleton materials to be those that can be

Table 7.1 List of polymer materials

Polymer names	Polymer type	Photoresist type	Exposure source	Material suppliers
SU-8 epoxy	thermoset	negative	UV	Microchem [107]
Polyimide	thermoset	negative	UV	HD Microsystems [56]
Polyimide	thermoplast	–	–	HD Microsystems [56]
BCB	thermoset	negative	UV	Dow [30]
PMMA	thermoplast	positive	E-beam, X-ray	Microchem, etc [105]
PDMS	thermoset	–	–	Dow-Corning [31], etc
PVDF	thermoplast	–	–	Arkema [4], Solvay
Nylon	thermoplast	–	–	DuPont [106], etc
Teflon PTFE	thermoplast	–	–	DuPont [33]
LCP	thermoplast	–	–	Ticona [144]

Table 7.2 List of Symbols

Symbols	Definitions
E	Young's modulus
ν	Poisson's ratio
κ	Bulk modulus, $\kappa = E/3/(1-2\nu)$
α	Linear thermal expansion coefficient
β	Volumetric thermal expansion coefficient
λ	Thermal conductivity
ρ	Density
c	Specific heat
k	Thermal diffusivity, $k = \lambda/(\rho c)$
T_m	Melting temperature
T_g	Glass transition temperature
T_d	Degradation temperature

deep etched or electroplated into deep structures, for example, silicon, aluminium, copper, gold, nickel. The process requirements generally limit the suitable polymer to be those which enable trench filling and can be patterned into a microstructure. As a result, the pool of suitable materials to build thermal microactuators becomes smaller. Examples of suitable polymers include polyimide [8], polymethylmethacrylate (PMMA), poly-dimethylsiloxane (PDMS) [17], benzocyclobutene (BCB) [54], and photo-patternable epoxies [83]. However, for a perspective and comparative view, other engineering polymers with potentially powerful thermal actuation are also included in the subsequent evaluation (see Table 7.1). These polymers include unfilled polyamide (Nylon), polyvinylidene fluoride (PVDF), Teflon polytetrafluoroethylene (PTFE) and Vecra liquid crystal polymers (LCP). The present studies will provide a glimpse, rather than an exhaustive survey, on the potentials of polymers for thermal micro-actuation.

Material properties of the selected skeleton and polymer materials are listed in

Table 7.3 List of material properties, whose symbols have been defined in Table 7.2

	E GPa	ν 1	κ^a GPa	α ppm/K	λ W/m/K	ρ g/cm^{-3}	c J/g/K	k 10^{-6}m^2/s	T_m,* T_g (T_d) °C
Si [14, 131]	130	0.28	98	2.6	124	2.33	0.702	75.8	1414
Ni [40, 41, 131]	180	0.38	186	13.4	90.7	8.90	0.445	22.9	1455
Cu [40, 41, 131]	120	0.42	138	16.4	401	8.96	0.384	116.5	1084
Al [40, 41, 131]	70	0.36	76	23.1	237	2.70	0.904	97.1	660
Au [40, 41, 131]	82	0.46	173	14.4	317	19.3	0.129	127.3	1064
SU-8 [37, 90]	3.2	0.33	5.9 [b]	150	0.23	1.2	1.0	0.19	*220
Polyimide [56, 97, 123]	2.5	0.34	2.6	20	0.33	1.42	1.09	0.21	*300
BCB [30, 65, 109]	2.9	0.34	3.0	42	0.29	1.05	2.18	0.13	*350
PMMA [49, 51, 105]	2.4-3.3	0.35-0.4	2.7-5.5	70-77	0.17	1.2	1.50	0.09	130
PDMS [29, 31, 39, 108]	2×10^{-3}	0.1-0.35	1.0 [c]	310	0.18	1.03	1.50	0.12	(200)
PVDF [4, 50, 103]	2	0.34	2.1	150	0.19	1.77	1.51	0.07	169
Nylon [48, 106]	3.3	0.41	6.1	90	0.25	1.14	1.67	0.13	211
Teflon PTFE [33, 104]	0.46	0.46	1.92	135	0.25	2.16	1.4	0.08	260
Vecra LCP [35, 47, 144, 154, 163]	10.6	(0.35)	11.7	1$\parallel$/30$\perp$	0.084	1.4	2.0	0.03	280

[a] If not specified, $\kappa = E/3/(1-2\nu)$, [b] Measured by PVT [37], [c] Measured by PVT [29]

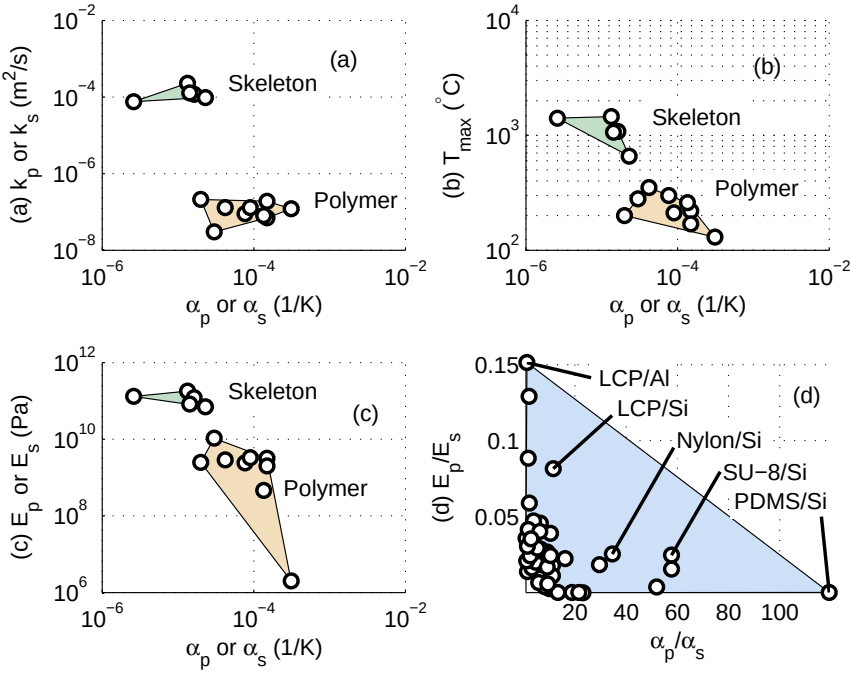

Fig. 7.2 Material chart for polymer (p) and skeleton (s) materials: (a) thermal diffusivity versus CTE; (b) maximum operating temperature (T_{max}) versus CTE; (c) Young's modulus versus CTE; (d) relative Young's modulus versus relative CTE

Table 7.3 and shown in Fig. 7.2. They are obtained from various sources. Besides handbooks and literature, some web sites like MatWeb, eFunda and GoodFellow also provide useful data. Bulk properties of silicon and metals are available from the CRC Handbook for Physics and Chemistry [14,40,41]; thin-film Young's moduli of silicon and metals are obtained from the CRC MEMS Handbook [131]. On the other hand, polymer properties are obtained from diverse web resources, including web sites of material distributors or original materials manufacturers. Polymers show property variation, dependent on their process conditions and compositions. The listed polymer properties reflect the order of magnitudes, for each polymer class, rather than the definitive value.

7.3 Theory for Laminate Composite

To guide material selection, the actual design of a polymeric actuator with an embedded skeleton is modeled using a laminated composite. A representative unit of the composite is a sandwich of polymeric lamina between two skeleton laminae (see Fig. 7.3-7.4). This sandwich model assumes that the laminae have a finite

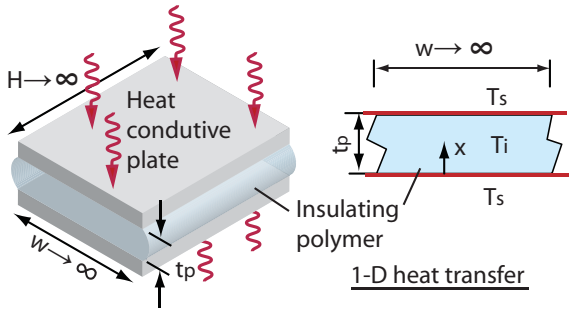

Fig. 7.3 1-D heat diffusion model

thickness but an infinite width and they are perfectly bonded to each other. The simple geometry of sandwiched laminae leads to one-dimensional (1-D) models, for which closed-form solutions can be constructed to predict thermal and thermo-elastic behavior. This could be very useful for material selection.

7.3.1 *Thermal Analysis*

We consider a 1-D laminar model to provide an estimate of the thermal response (see Fig. 7.3). This model will be used to predict how an initially cold slab thermally responses to a suddenly immersion in a hot or cold bath of constant temperature (T_s). Following the drastic change of surface temperature, an approximately one-dimensional (1-D) thermal conduction occurs in the slab, obeying

$$\frac{\partial^2 T}{\partial x^2} = \frac{1}{k}\frac{\partial T}{\partial t} \tag{7.1}$$

where k denotes the thermal diffusivity of the slab.

The solution to this 1-D heat diffusion equation yields the internal temperature (T) as a function the transverse location (x) and time (t) [155]:

$$T(x,t) = T_i + \sum\nolimits_{n=1}^{\infty} c_n \sin(\frac{n\pi x}{t_p}) \exp\left(-k(\frac{n\pi}{t_p})^2 t\right) \tag{7.2}$$

where T_i denotes initial temperature and t_p denotes thickness of the slab.

The characteristic time constant (τ_p) for heat diffusion into the slab can be approximated using the first mode time constant such that

$$\tau_{\mathrm{p}} = \frac{{t_p}^2}{k\pi^2} \tag{7.3}$$

As a result of the shortened path for heat diffusion, embedding the heat-conducting skeleton improves heat transfer to the insulating polymer.

The overall thermal responses for the laminate composite depend on effective thermal diffusivities, which are anisotropic. According to the mixture law, the

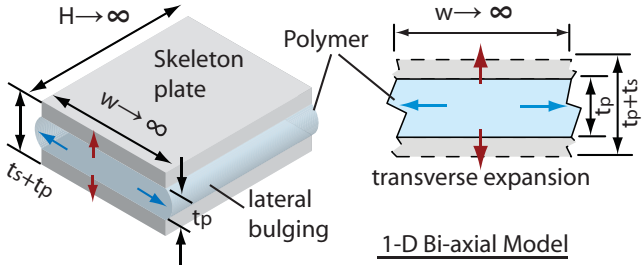

Fig. 7.4 A bi-axial thermo-mechanical model

apparent thermal diffusivities ($k_\perp$ or $k_\parallel$) in the transverse and lateral directions are functions of ϕ volume fraction of the polymer:

$$\begin{aligned} \frac{1}{k_\perp} &= \phi \frac{\rho_p c_p}{\lambda_p} + (1-\phi)\frac{\rho_s c_s}{\lambda_s} \\ k_\parallel &= \phi \frac{\lambda_p}{\rho_p c_p} + (1-\phi)\frac{\lambda_s}{\rho_s c_s} \end{aligned} \tag{7.4}$$

where the subscripts p and s denote polymer and skeleton materials, respectively; whereas, c and ρ denote the specific heat and densities, respectively.

7.3.2 *Thermo-mechanical Analysis*

Consider a lamina of expansion material sandwiched between two laminae of skeleton material (see Fig. 7.4). Material mismatches in CTE and Young's moduli cause mechanical interaction between laminae of the sandwich. The bi-axial model [83] for the sandwiched polymeric and skeleton laminae predicts transverse CTEs as:

$$\begin{aligned} \alpha_{\perp p} &= \frac{e^p_{33}}{\Delta T} = \alpha_p + \frac{2\nu_p(\alpha_p - \alpha_s)}{1-\nu_p+\gamma(1-\nu_s)} \\ \alpha_{\perp s} &= \frac{e^s_{33}}{\Delta T} = \alpha_s - \frac{2\nu_s(\alpha_p - \alpha_s)}{(1-\nu_s)+\gamma^{-1}(1-\nu_p)}, \end{aligned} \tag{7.5}$$

where $(\alpha_{\perp p})$ and $(\alpha_{\perp s})$ denotes the transverse CTEs for polymeric and skeleton laminae, respectively, and $\gamma = t_p E_p/(t_s E_s)$ is the relative stiffness between the polymeric and skeleton laminae.

In addition, the analysis yields the transverse Young's moduli for the constrained polymer $(E_{\perp p})$ and that for the constrained conductors $(E_{\perp s})$,

$$\begin{aligned} \frac{1}{E_{\perp p}} &= \frac{e^p_{33}}{\sigma^p_{33}} = \frac{1}{E_p}\left[1 - \frac{2\nu_p(\nu_p - \eta\nu_s)}{1-\nu_p+\gamma\,(1-\nu_s)}\right] \\ \frac{1}{E_{\perp s}} &= \frac{e^s_{33}}{\sigma^s_{33}} = \frac{1}{E_s}\left[1 + \frac{2\gamma\nu_s(\nu_p - \eta\nu_s)}{1-\nu_p+\gamma\,(1-\nu_s)}\right] \end{aligned} \tag{7.6}$$

where $\eta = E_p/E_s$

For a laminated composite containing ϕ volume fraction of polymer, the apparent transverse thermal expansion coefficient is

$$\alpha_{\perp} = (1-\phi)\alpha_{\perp s} + \phi\alpha_{\perp p}, \tag{7.7}$$

while the apparent transverse Young's modulus is

$$E_{\perp}^{-1} = (1-\phi)(E_{\perp s})^{-1} + \phi(E_{\perp p})^{-1}. \tag{7.8}$$

7.4 Evaluation

To start, we shall study thermo-physical properties of the individual component materials and subsequently their interaction and influences on the overall actuator performance. The following discussions are with respect to the materials under investigation, as listed in Table 7.3.

7.4.1 *Component Materials*

Characteristics of component materials are evaluated before they are combined to form laminate composites.

7.4.1.1 *Thermal Properties*

The concerned thermal properties for the components material are thermal diffusivity and the maximum operating temperature. Thermal diffusivity determines the characteristic time response, while the maximum operating temperature determines the working range using the materials.

With reference to Table 7.3 and Fig 7.2a, the selected polymers (p) show much lower thermal diffusivity (k) than the selected skeleton (s) materials. Thermal diffusivity of various selected materials is in the following range

$$0.03 < k_p < 0.21 \quad (\times 10^{-6}\mathrm{m}^2/\mathrm{s})$$
$$75.8 < k_s < 127 \quad (\times 10^{-6}\mathrm{m}^2/\mathrm{s})$$

Gold shows the highest thermal diffusivity while LCP shows the lowest. According to Eq. 7.3, thermal characteristic time is inversely proportional to thermal diffusivity. For example, an 1–μm gold lamina has a characteristic time of 0.80 ns while an 1-μm LCP lamina one has 3.37 μs. In addition, thermal characteristic time is proportional to the square of the lamina thickness (see Eq. 7.3). As a result, a thicker lamina will take a longer time to response as compared to a thinner one. For example, an 1-mm thick LCP lamina has a characteristic time of 3.37 s. Other polymers show slightly faster characteristic times but of the same order as LCP. In view of these, miniaturization and integration with heat conducting skeleton is expected to improve thermal response of the insulating polymers.

The maximum allowable temperatures of various selected solids are either limited by their melting temperature or glass transition temperature. Fig. 7.2b show the

maximum operating temperature of expansion materials in relation to their CTEs. The range of maximum operating temperature of the selected materials are given as

$$130 < T_{p,max} < 350 \quad (^{\circ}\mathrm{C})$$
$$660 < T_{s,max} < 1455 \quad (^{\circ}\mathrm{C})$$

Note that the allowable temperatures of metals may be lower than melting temperature because oxidation may happens at a lower temperature. For example, nickel oxidizes and darkens at 350 °C [121].

The maximum operating temperature of a polymer is generally lower than that of skeleton materials such as silicon and metals. This may limit the maximum thermal stress, which the polymer can deliver, despite its high CTE (see Fig 7.2b and Table 7.3).

7.4.1.2 *Thermoelastic Properties*

Characteristics of the laminate composite depend on thermoelastic parameters, such as Young's modulus, CTE, Poisson ratio and relative thickness, of both polymer and skeleton laminae. With reference to Fig 7.2c and Table 7.3, the selected polymers (p) show a relatively high CTE (α) but a much lower Young's modulus (E) in comparison to the selected skeleton (s) materials. Both types of materials show a wide variation in Poisson's ratio (ν). The thermo-elastic properties of the selected materials fall in the following ranges:

$$2 \times 10^{-3} < E_p < 10.6 \quad (\mathrm{GPa})$$
$$70 < E_s < 180 \quad (\mathrm{GPa})$$

$$20 < \alpha_p < 150 \quad (\mathrm{ppm/K})$$
$$2.6 < \alpha_s < 23.1 \quad (\mathrm{ppm/K})$$

$$0.1 < \nu_p < 0.41$$
$$0.28 < \nu_s < 0.46$$

Among the selected polymeric materials, PDMS is noted to possess the highest CTE (i.e. 310 ppm/K [31,39,108]) but the lowest Young's modulus, which is three-order lower than other engineering polymers . Therefore, an unconfined block of PDMS may not serve well to generate large actuation stress. On the other hand, the unfilled liquid crystal polymer (Vecra LCP) shows the highest Young's modulus (i.e. 10.6 GPa) among the polymers but relatively low and anisotropic CTEs, 1 ppm/K in the parallel direction and 30 ppm/K in the transverse direction. Polymers like SU-8 epoxy, nylon and PVDF display adequately high CTEs ($>$ 90 ppm/K) and remain rather stiff ($>$ 1GPa). Therefore, they could deliver much higher actuation stress than either PDMS or LCP. If they are fully confined, SU-8 epoxy and Nylon have

potential to generate high thermal stress, around 1.6-2.7 MPa/K (see Table 7.4). Therefore, these two polymers are potentially very powerful thermal expanders.

LCP and polyimide show relatively low CTEs (1-30 ppm/K), which are comparable to CTEs of metals, e.g. 23 ppm/K of Al and 16.4 ppm/K of Cu. The small CTE mismatch makes polyimide suitable for integration with metal interconnects in the 'damascene' process [1]. Likewise, it makes LCP suitable as a perfect substrate material for high-power metallic RF devices [143]. However, their low CTEs make them not very attractive as expansion material for thermal actuators.

Skeleton materials are preferred to be stiff and have as low thermal expansion as possible so as to laterally constrain thermally expandable polymer over the bond interface. However, skeleton materials, such as metals and silicon, do undergo thermal expansion. The lateral expansion will decrease the confinement effect, but the transverse expansion contributes to the total actuation, together with the polymeric expansion. In general, these skeleton materials have a smaller CTE as compared to most polymers. Metals exhibit higher CTE than silicon. Among the metals under investigation, aluminium has the highest CTE, (i.e. 23 ppm/K) but the lowest Young's modulus. Even with a moderate CTE, metals with high moduli are good at producing a large actuation stress. For examples, nickel shows a high bulk modulus of 186 GPa respectively while gold have a bulk modulus of 173 GPa. Both nickel and gold could potentially deliver the high bulk thermal stresses, around 7.5 MPa/K, if they are fully confined.

Analysis of the homogeneous materials shows that both polymers and metals outperform silicon in terms of both thermal strain and stress, though silicon is used commonly to build homogenous thermal micro-actuator.

7.4.2 *Component Interaction*

Interaction between component materials affects the apparent properties of composite. In the thermal domain, the components have weak interaction. The weak thermal interaction between the components exists due to interfacial air gaps. The air gaps cause thermal resistance and consequently deteriorate the thermal diffusivity of the composite [6]. In general, an effective thermal diffusivity is bounded within the upper and lower limits as dictated by the mixture law, i.e. Eq. 7.4. On the other hand, the maximum allowable temperature for the composite is limited by the lowest operating temperature of polymer constituent.

In the thermo-mechanical domain, the components have strong interaction. Embedding the heat-conducting skeleton in the polymer does reinforce the polymer because heat-conducting materials generally have higher elastic moduli than polymers. Bonding between polymeric/skeleton laminae results in rather stiff interfaces to restraint lateral deformation of the polymer lamina. The large CTE and stiffness mismatches could therefore lead to a strong mechanical interaction.

The subsequent study will investigate to what extent CTE and stiffness mis-

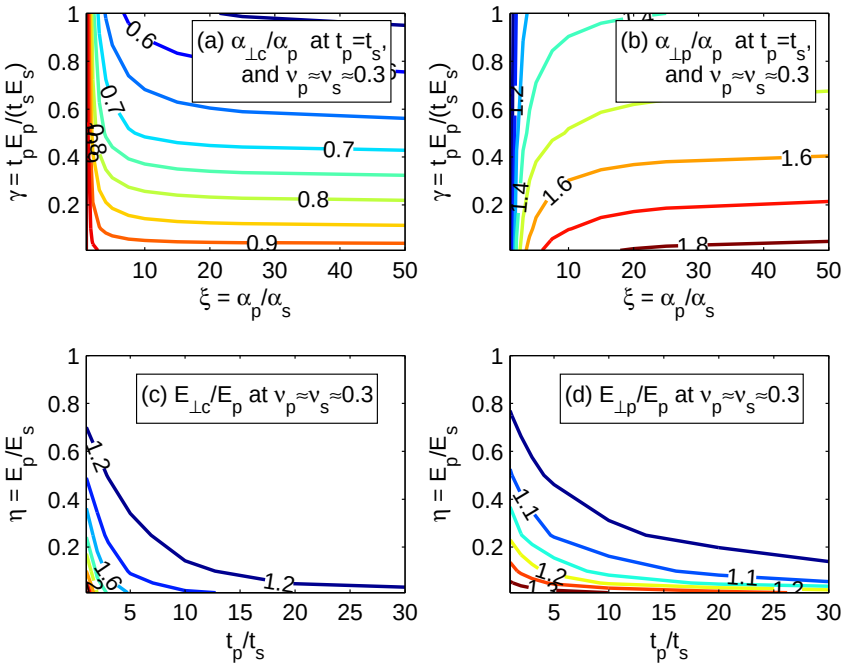

Fig. 7.5 Contour plots of enhancement factors for apparent properties as a function of CTE and stiffness mismatches: (a) apparent CTE of the composite; (b) apparent CTE of the polymeric component; (c) apparent Young's modulus of the composite; (d) apparent Young's modulus of the polymeric component

matches affect the actuation performance. For this purpose, we introduce the relative CTE (α_p/α_s) and relative lateral stiffness ($E_p t_p/E_s/t_s$). The relative CTE will be studied in the range between 1 to 100 and the relative stiffness in the range between 0.05 to 1. Such wide ranges serve to illustrate the general influences of mismatches on the actuation performance. The concerned performance indicators include the apparent transverse CTE ($\alpha_{\perp p}$) and Young's modulus ($E_{\perp p}$) of the polymer layer and the overall composite properties (i.e. $\alpha_{\perp c}$ and $E_{\perp c}$). These indictors are derived from Eqs. 7.5-7.8 by substituting the relative CTEs and Young's moduli.

In present discussion, most cases of study assume equal volume fraction of polymer and skeleton materials for the laminate composite, with an exception in the study on the influence of relative thickness (see Fig. 7.5c-d). In addition, most cases of study assume Poisson's ratio be 0.33, except in the study on the influence of Poisson's ratio (see Fig. 7.6).

The composite properties are compared with intrinsic properties for the polymer alone. This comparison leads to definition of an enhancement factor that indicates

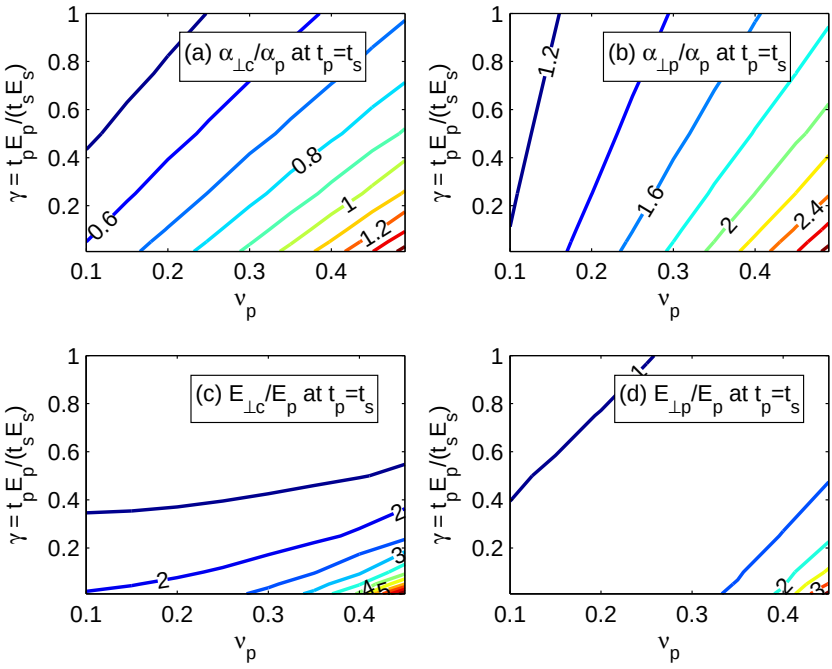

Fig. 7.6 Contour plots of enhancement factors for apparent properties as a function of stiffness mismatch and Poisson's ratio of the polymer: a) apparent CTE of the composite; (b) apparent CTE of the polymeric component; (c) apparent Young's modulus of the composite; (d) apparent Young's modulus of the polymeric component

the improvement brought by the composite design. Fig. 7.5 and Fig. 7.6 show contour plots of performance enhancement factors, at which the laminated composites bring as compared to those using the polymer alone. The plots according to Eqs. 7.5-7.6 show that the apparent transverse CTE is a function of the relative CTE and relative stiffness while the apparent Young's modulus is a function of the relative stiffness. The relative stiffness increases when the polymer lamina becomes relatively stiffer or thicker.

According to Figs. 7.5a and 7.5b with the assumed Poisson's ratio of 0.33, the laminated composite containing 50% polymer displays apparent CTE greater than 50% the CTE of polymer alone. This is attributed to the enhanced transverse CTE in the bonded polymer lamina. Volume expansion of the polymer lamina is concentrated in the transverse direction, leading to an apparent linear CTE as much as 1.8 times the CTE of polymer alone (see Fig. 7.5b). The enhancement factor for the apparent CTE increases with decreasing relative stiffness of the polymer lamina (i.e. $E_p t_p/(E_s t_s) \downarrow \Rightarrow \alpha_{\perp p}/\alpha_p, \alpha_c/\alpha_p \uparrow$)

Similarly, the laminated composite displays enhanced transverse Young's mod-

ulus (see Figs. 7.5c and 7.5d). This is a result of both reinforced polymer lamina and embedding the stiff skeleton lamina. The apparent transverse Young's modulus of the bonded polymer lamina is greater than the free polymer alone. The enhancement factor increases with an decrease in the relative stiffness ($\gamma = E_p t_p/(E_s t_s)$). In short,$\gamma \downarrow \Rightarrow E_{\perp p}/E_p, E_c/E_p \uparrow$. This means that a compliant polymer lamina will feel a stronger confinement effect, and consequently a more pronounced stiffness enhancement, than a stiff polymer lamina.

In the extreme case where the skeleton is rigid and dominates the stiffness, the non-dimensional variable γ approaches to zero, i.e.

$$\gamma = t_p E_p/2t_s E_s \to 0$$

As a result, the transverse CTEs for the bonded laminae reduce to the following:

$$\begin{aligned} \alpha_{\perp p} &= \alpha_p + \frac{2\nu_p(\alpha_p - \alpha_s)}{1-\nu_p} \\ \alpha_{\perp s} &= \alpha_s, \end{aligned} \tag{7.9}$$

while the apparent transverse Young's moduli reduce to the following:

$$\begin{aligned} E_{\perp p} &= \left[\frac{1-\nu_p}{1-\nu_p-2\nu_p^2}\right] E_p \\ E_{\perp s} &= E_s. \end{aligned} \tag{7.10}$$

In this extreme case, the lamina bonding does not affect the rigid skeleton, in terms of either apparent transverse CTE or Young's modulus. However, the rigid bonding causes the bonded polymeric lamina to show a maximum transverse CTE and Young's modulus. The enhancement factor of the maximum apparent CTE depends on CTE mismatch and Poisson's ratio of the polymeric lamina. On the other hand, enhancement factor for the Young's modulus depends solely on the Poisson's ratio of the polymeric lamina.

In the case that the skeleton is inextensible (i.e. $\alpha_c = 0$), the actual enhancement factor of CTE depends solely on Poisson's ratio of the polymer. The maximum enhancement factor is 1.8 at Poisson's ratio of 0.33. It becomes at most 3 times if the polymer is incompressible ($\nu_p = 0.5$). On the other hand, enhancement factor for Young's modulus is approximate 1.3 for a polymer with 0.3 Poisson's ratio. It becomes infinite if the polymeric lamina is incompressible, i.e. with Poisson's ratio approaching to 0.5.

Influence of Poisson's ratio on thermal actuation capability is obvious. Additional contour plots in Fig. 7.6 show that the enhancement factors of both apparent Young's modulus and CTE peak at 0.5 Poisson's ratio of the bonded polymer. This suggests that incompressible material can ideally acts as a powerful thermal expander. This motivates us to choose expansion material with reference to compressibility property, i.e. bulk moduli.

The bulk moduli listed in Table 7.4 are mostly derived from the Poisson's ratio and tensile modulus, except those for SU-8 and PDMS, which are measured using

Table 7.4 Bulk volumetric expansion

	ν 1	κ GPa	β=3α ppm/K	$\kappa\beta$ MPa/K	$\frac{1}{2}\kappa\beta^2$ J/m^3/K^2	T_m,* T_g (T_d) °C
SU-8	0.33	5.9	450	2.66	597	*220
Polyimide	0.34	2.6	60	0.16	5	*300
BCB	0.34	3.0	126	0.38	24	*350
PDMS	-	1.0	930	0.93	432	*200
PMMA	0.34	2.7-5.5	231	1.27	147	130
PVDF	0.34	2.1	450	0.95	213	169
Nylon	0.41	6.1	270	1.65	222	211
Teflon PTFE	0.46	0.46	405	0.78	157	260
Vecra LCP	(0.35)	11.7	32	0.37	6	280

the PVT method [29,37]. The selected polymers show relatively low bulk moduli as compared to the skeleton materials. Among the polymers, LCP has the highest bulk modulus. However, SU-8 and Nylon deliver among the highest bulk thermal stress and work density because they have higher CTEs than LCP. PDMS is reported to have a considerably higher bulk modulus, i.e. 1 GPa [29], as compared to its Young's modulus. A fully confined sample of PDMS is expected to exhibit high work density. However, it is not sure wether a partially confined sample of PDMS also deliver as high work density as the fully confined sample.

7.4.3 *Composite properties*

The foregoing discussions show thermo-mechanical interaction affects the apparent transverse CTE and stiffness of laminated composite. The resulting property improvement or deterioration can be gauged using the enhancement factors that compare the apparent properties to the intrinsic properties for the polymer alone. The enhancement factors are functions of the CTE and stiffness mismatches (see Fig. 7.5). In turn, the absolute properties of the laminate composite depend on both the component properties and the enhancement factors.

In the present study, polymer and skeleton materials are combined with equal volume fraction. Fig. 7.2d shows that most combinations of polymeric and skeleton materials have a relatively large stiffness mismatch and a rather large CTE mismatch. The maximum mismatches are bounded such that the relative CTE is smaller than 120 and the relative Young's modulus is smaller than 0.15. However, most material combinations are clustered in a smaller region where the relative CTE is smaller than 30 and the relative Young's modulus is smaller than 0.05. As a result of the clustering, these material combinations are subjected to a similar extent of property enhancement. Variation in the absolute composite properties reflects mainly the property variation for the various polymers. The absolute properties under evaluation includes the apparent CTE, apparent Young's modulus, thermal stress, and thermal work density.

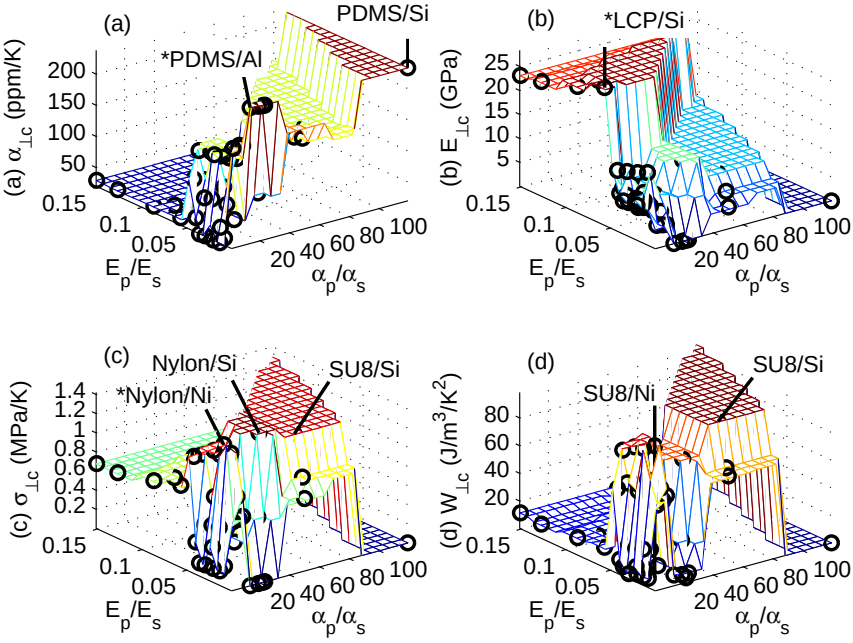

Fig. 7.7 The absolute apparent properties for various combinations of polymer and skeleton materials, with 3D meshes showing (a) the apparent CTE ($\alpha_{\perp c}$); (b) the apparent Young's modulus ($E_{\perp c}$); (c) the thermally induced stress ($\sigma_{\perp c} = \alpha_{\perp c} E_{\perp c}$); (d) the work density ($W_{\perp c} = 0.5\alpha_{\perp c}^2 E_{\perp c}$)

The property variations are plotted as three-dimensional (3-D) meshes in Fig. 7.7. Horizontal coordinates of the plots are defined with the relative CTE and Young's modulus, whereas a vertical axis indicates the absolute property. Combination of various polymeric and skeleton materials results in sparse data points scattering over the 3-D spaces without an obvious correlation to the horizontal coordinates. Meshes, linking the data points, are plotted merely to help visualizing the absolute properties. The non-smooth meshes with steps reflect the large variation in component properties.

Fig. 7.7a shows that variation in the apparent CTE with respect to material combinations. The laminated composite containing PDMS shows among the highest apparent CTE because PDMS has the highest CTE among the materials under investigation. The composites containing PDMS show large CTE and stiffness mismatches with skeleton materials. The laminated composites containing 50% PDMS have a composite CTE of at least 233 ppm/K and a slight variation. Among them, the PDMS/Al combination shows the marginally highest value, namely, 238 ppm/K, because Al contributes to more transverse thermal expansion than other skeleton

materials, such as Si.

Fig. 7.7b shows variation in the apparent Young's modulus with respect to material combinations. The LCP-containing composites display the highest apparent Young's modulus as compared to other polymer composite. This is because LCP has a relatively high Young's modulus as compared to other polymers under investigation. Among the composites containing LCP , the LCP/Ni combination gives the highest Young's modulus (28.4 GPa) because Ni is one of the stiffest skeleton materials. LCP/Si ranks second at 27.2 GPa. LCP/Al gives the lowest composite modulus (23.1 GPa).

Fig. 7.7c shows variation in the actuation stiffness with respect to material combinations. Nylon and SU-8 have rather high Young's moduli and adequately high CTEs (i.e. 3.3 GPa and 90 ppm/K for Nylon; 150 ppm/K and 3.2 GPa for SU-8). Therefore, the composites containing Nylon or SU-8 show a high value of actuation stress (at least 1.1 MPa/K) as compared to those containing other polymers. The laminated composites containing Nylon perform slightly better than those containing SU-8. For example, Nylon/Ni delivers the highest actuation stress at 1.42 MPa/K; Nylon/Si ranks second at 1.39 MPa/K. On the other hand, SU-8/Ni ranks fourth at 1.31 MPa/K after Nylon/Cu of the third place.

Thermal actuation of the composites is mainly contributed by polymeric expansion. Therefore the achievable actuation stress for the lamina composite is limited by the polymeric component, in terms of the bulk compressive thermal stress. According to Table 7.4, Nylon has a lower bulk compressive stress than SU-8, which has the highest among the materials under investigation. However, the composites containing Nylon surprisingly deliver more apparent stresses than those containing SU-8. This may be because Nylon has a Poisson's ratio closer to incompressibility and enjoys more pronounced enhancement for both the apparent CTE and Young's modulus.

Fig. 7.7d shows variation in work density with respect to material combinations. At the component level, SU-8 performs the produces the highest work density. Therefore, the composites containing SU-8 also shows among the highest work density. Among them, SU-8/Si shows the highest work density at 98.5 $kJ/m^3/K^2$ while SU-8/Ni ranks second at 96.7 $kJ/m^3/K^2$. SU-8/Al delivers the least work density at 86.6 $kJ/m^3/K^2$. On the other hand, the Nylon-containing composites also produce high work density, though slightly lower, in the range between 59.2 and 78.0 $kJ/m^3/K^2$.

7.5 Conclusion

Embedding skeleton laminae could improve heat transfer to a polymer. In addition, the embedded skeleton laminae could enhance strain and stiffness of the polymer laminae in the perpendicular direction. According to the laminate model, the strain and stiffness enhancement is more pronounced to the compliant polymer. However,

the absolute properties of the laminate composite depend to a large extent on the polymeric component. Due to the confinement effect of stiff skeleton laminae, Poisson's ratio of the polymeric laminae become an influential material property, besides CTE and Young's modulus, in affecting the actuation capabilities such as the thermal stress and work density.

Various material combinations have been considered in the the performance evaluations. Among the materials under investigation, the evaluations show that the composites based on poly-dimethyl-siloxane have among the highest thermal strains; the composites based on liquid crystal polymer exhibit among the highest actuation stiffness; Nylon-containing composites exhibit among the highest actuation stress; SU-8-containing composites deliver among the highest work density. On the other hand, most metals and silicon serve well as the skeleton.

Chapter 8

Design Optimization

This chapter presents design optimization of a polymeric actuator with an embedded skeleton. The important design parameters are identified as the bond width, layer thickness, volume fraction, and aspect ratio of the polymer component. In addition, the path length and layout of the skeleton component also affect the actuator performance. Parametric studies are conducted for several design criteria, which include maximum apparent coefficient of thermal expansion (CTE), actuator stiffness, thermally induced stress and work density. The design for maximum work density shows that 70% of SU-8 and 30% of Si comprise the optimum design. This optimum design achieves about 20% improvements for work density, apparent CTE and thermal response time, as compared to a reference design containing 50 % SU-8. In addition, it displays 2.5 times higher work density and slightly higher apparent CTE than SU-8 alone.

8.1 Introduction

Strategies of material selection have been presented to build a polymeric actuator with an embedded skeleton [80]. The study suggests that Nylon and SU-8 are powerful thermal expansion materials. SU-8 is preferred because it is photo-patternable and allows easy microfabrication. Silicon is recommended as the skeleton material because it has high thermal conductivity and high rigidity. In addition, silicon can be deep etched into a microstructure of a high aspect ratio.

The foregoing study evaluates the actuator performance using an idealized model of polymer and and skeleton laminate [80, 83]. The laminate model assumes infinite lateral dimensions but finite thickness for the laminae of polymer and skeleotn. As a result, the model does not predict significant lateral bulging in the polymeric lamina. The study based on the laminate model provide a quick evaluation for material combination on the composite level, but it pays little attention to the effect of a complex skeleton geometry. In the present study, we will focus on the geometric influences on the actuator performance.

8.2 Motivation

The main research question is whether there is room to further improve the actuator performance upon selecting the optimal material combination. This question requires us to identify relevant design parameters and investigate their influences on the actuator performance at the device level.

Geometry has substantial influences on actuator performance. For example, at the composite level, volume fraction of polymer determines the total amount of expansion material. However, this understanding needs to be refined when the composite is embodied at the device level. For example, the skeleton embedded in the actuator device has a meandering shape and finite width. This layout is different from the parallel plate-like skeletons in the laminate model. A finitely-wide meandered skeleton allows lateral bulging for the bonded polymer filling and, consequently, it leads to a lower apparent CTE than that for the infinitely wide laminated composite.

The meandering skeleton is a monolithic microstructure with horseshoe bends connecting the folds of the meanders (see Fig. 8.1). In a thermal aspect, the continuous meandering skeleton provides the sole heat conduction path to the polymer. From a mechanics point of view, the meandering skeleton reinforces the overall polymeric actuator. Due to the geometry difference, the actuator with the embedded meandering skeleton shows deviation in actuation characteristics from the laminated composite.

Geometry of the skeleton affect both thermal and thermo-mechanical behavior of the polymeric actuator with the embedded skeleton. However, at the moment, it is unclear how its geometry affects the overall thermal response? In a thermo-mechanical aspect, the polymer component is the 'muscle' that causes major thermal expansion while skeleton material provide substantial reinforcement to the polymer but little actuation. How much volume fraction of the polymer be allocated to maximize thermal actuation's capabilities? Is there an optimum volume fraction at all?

In the subsequent sections, we will attempt to provide answers to the above questions. We will first identify design goals and design parameters. Then, we will present theory and numerical methods to evaluate performance of the actuator device. In addition, we will perform a parametric study to optimize the actuator performance.

8.3 Design Optimization Problem

Generally, the overall dimensions of single-material thermal actuators are changed to improve actuator performance and to meet application requirements. For example, asymmetric U-shape thermal actuators were optimized by changing the lengths of the hot and cold arms and their width difference [58, 62, 63, 85]. In another example

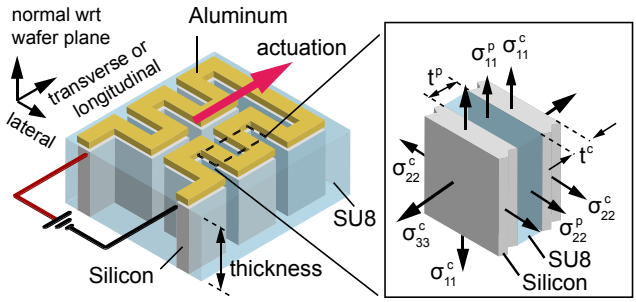

Fig. 8.1 Actuator design and representative laminates

of V-shape thermal actuators, lengths and number of the V-shape flexural beams were designed to optimize force and displacement generation [21, 86, 101]. In the design of bi-material-layer thermal benders, thickness ratio of the two layers is optimized in order to maximize the tip deflection, moment and energy [120].

In this paper, we perform design optimization of a polymeric actuator with an embedded silicon skeleton. We approach the device optimization problems as an extension of composite design [6]. Instead of changing the overall dimensions, we optimize its microscopic parameters of the composite, such as the volume fraction or lamina thickness. In the following subsections, we will identify design objectives and variables relevant to the actuator design.

8.3.1 *Design Objectives*

Depending on the field of application, thermal actuators serve various functions. For example, they may need to generate a large displacement for driving a micro-variable optical attenuator at a high frequency [21,86], a large force for driving a micro-tensile tester with small creep [167], or both large displacement and force for powerful actuation. Sometimes, actuator stiffness may need to match with that of the loaded system for maximum work transfer to the system. The mentioned applications show that the characteristics of interest to the actuator include the displacement, stiffness, force, energy transfer, and response time. These characteristics depend on geometry and material properties. Usually, the actuator performance is optimized by changing the geometry sizes or shapes.

On the other hand, performance of the actuator can also be tailored by changing the material properties. In the case that the constituent materials have been selected, the apparent material properties can be engineered by changing volume fraction of the constituents. It is anticipated that this approach provides extra room for performance improvement in addition to the classical design approach by perturbing the 'overall geometry'.

To guide composite design, the design goals at the device level has to be translated into the material level. This involves normalization of the actuation character-

istics with respect to dimensions. For example, maximization of the displacement stroke is equivalent to maximizing the apparent CTE of the composite; maximizing the stiffness is to maximize the apparent Young's modulus in the actuation direction; maximizing the actuation force is to maximize the thermally induced stress; whereas, maximizing the energy output is to maximize the work density at the material level; shortening the response time is to maximize the thermal conductivity. These translated goals help guiding and simplifying the optimization.

8.3.2 *Design Variables*

First, we identify the geometry parameters which most significantly affect the actuator performance, either thermally or mechanically.

The design variables that affect performance of the present actuator include the overall length (L_0), width (W_0) and height (H_0) of the actuator (see Fig. 8.2). If the actuator is a block of homogenous material, the actuation behaviors of the block can simply be related to the theory for a thermally expandable rod. For example, the displacement at the tip of the rod is $\Delta L_0 = \alpha_0 L \Delta T$ and the blocked force at the tip is $F = E_0 A_0 \Delta L / L_0$, where α_0 and E_0 denote coefficient of thermal expansion and Young's modulus of the homogenous material, and A_0 is the cross-sectional area such that $A_0 = W_0 H_0$. However, the present actuator design is not made of a homogeneous material. Instead, it is a composite consisting of a polymer expander, a meandering-shape skeleton, and a metal thin film. Among the three materials, metal has the least and minute volume fraction. The metallic thin film serves mainly as resistive heater. Generally, its effect on the thermo-mechanical response can be neglected. Therefore, the actuator becomes basically a bi-material composite. The actuator resembles a rod configuration with one end clamped and one end free. Using a rod model together with homogenized properties of the bi-material composite, such as the effective CTE and Young's modulus in the axial direction, can therefore provide a quick and rough estimate of the actuator performance.

The homogenized properties depend mainly on volume fraction of the bi-material laminae. In turn, volume fraction of polymer is related to thicknesses of the polymer and skeleton laminae, such that

$$\phi = \frac{t_p}{t_p + t_s}, \tag{8.1}$$

where t_p and t_s are spacing thickness of polymer and skeleton, respectively. Influence of the volume fraction on the composite properties has been discussed in the companion paper on material selection [80].

Another important design parameter that affects the homogenized properties is the finite lateral dimension of the laminae, in other words, the finite width and height. The finite-dimensioned skeleton plates, which act as rigid interfaces, do not completely suppress lateral lateral expansion of the polymer layer. This leads

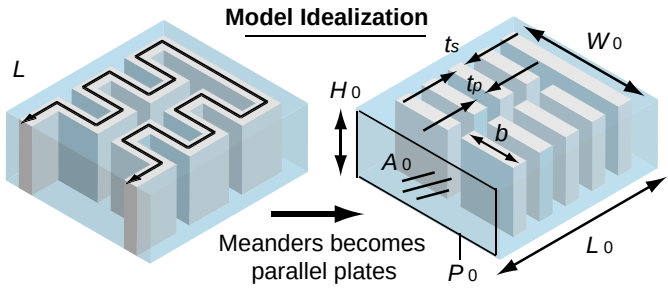

Fig. 8.2 Two skeleton layouts of similar actuation mode: (*left*) symmetric meander (*md*) and (*right*) parallel plates (*pp*)

to lateral bulging near the free edges and, consequently, less polymeric volumetric expansion is directed perpendicular to the skeleton plates. Therefore, less strain enhancement is observed from the bonded polymer layer with finite bond widths, as compared to that with infinite-wide bond widths. In the subsequent discussion of the analytical theory, we assume that the actuator is basically a two-dimensional plane design with a large height but a finite width. This reduces the thermo-elastic analysis into a plane-strain 2D problem. Thus, the only parameter left to affect the lateral bulging is thus the half-width, i.e.

$$w = W_0/2. \tag{8.2}$$

With reference to the geometry of the symmetric meandering skeleton in Fig. 8.2, the heat conduction path length L is related to the actuator length L_0, the bond width w, and the number of folds, which in turn depends on the spacing thicknesses t_p and t_s. This geometric relationship is

$$L \approx 2L_0 + 2w + \frac{2L_0 w}{t_p + t_s}. \tag{8.3}$$

It shows that the heat conduction path length depends on multiple design variables. If the actuator length (L_0) and the skeleton thickness (t_s) remain constant, an increase in the polymer spacing thickness leads to fewer folds of the meanders and therefore a shorter path length (i.e. $t_p \uparrow \Rightarrow L \downarrow$). However, if the conduction path length (L) is kept constant, an increase in the polymer spacing thickness yields a larger actuator length (i.e. $t_p \uparrow \Rightarrow L_0 \uparrow$).

8.3.3 *Impact on Thermo-physical Properties*

The free spacing (t_p) and the bonded width (w)of the polymer layers are identified as two major independent variables, whereas the actuator height (H_0) and the skeleton thickness (t_s) are set as constant. These two independent variables have influences on the actuator performance in many aspects.

First of all, t_p affects the volume fraction (ϕ) of the polymer according to Eq. 8.1. Consequently, it affects the effective thermo-physical properties of the composite as

discussed [80]. For the convenience of readers, their relationships with the volume fraction are repeated here.

The composite heat capacity reads as

$$\rho c = \phi \rho_p c_p + (1-\phi)\rho_s c_s, \tag{8.4a}$$

where ρ and c denote densities and specific heat, respectively; and the subscripts p and s denote the polymer and skeleton, respectively.

The thermal conductivities and diffusivities of the composite are anistropic. The thermal conductivities, lateral ($\lambda_\parallel$) or transverse ($\lambda_\perp$) to the path of the meandering skeleton read as

$$\begin{aligned} \frac{1}{\lambda_\perp} &= \phi \frac{1}{\lambda_p} + (1-\phi)\,\frac{1}{\lambda_s}, \\ \lambda_\parallel &= \phi \lambda_p + (1-\phi)\,\lambda_s. \end{aligned} \tag{8.4b}$$

Similarly, the lateral or transverse thermal diffisivities ($k_\parallel$ and $k_\perp$) read

$$\begin{aligned} \frac{1}{k_\perp} &= \phi \frac{\rho_p c_p}{\lambda_p} + (1-\phi)\,\frac{\rho_s c_s}{\lambda_s}, \\ k_\parallel &= \phi \frac{\lambda_p}{\rho_p c_p} + (1-\phi)\,\frac{\lambda_s}{\rho_s c_s}. \end{aligned} \tag{8.4c}$$

The lateral thermal diffusivity and conductivity are relevant to heat conduction along the meandering skeleton, whereas those transverse are relevant to heat diffusion into the polymer layer. This point will be elaborated in the theory section.

Secondly, the bond width (w) affects the cross-sectional area, $A_0 = 2wH_0$, the effective perimeter $P_0 = 2(2w + H_0)$, and the effective diameter $D = 4A_0/P_0$. Consequently, it has influences on the total heat transfer coefficient through air h, such that,

$$h = k_{air}\left(\frac{1}{\Delta z} + \frac{0.36}{D}\right), \tag{8.4d}$$

where k_{air} is the air thermal conductivity and Δz is the air gap between the actuator and the substrate [78].

Thirdly, the aspect ratio (w/t_p) determines the degree of confinement on the bonded polymer layer. In addition, t_p and w also affect the total heat conduction path length (L) and, therefore, thermal responses of the device, as well. These influences will be elaborated in the subsequent section on theory and a parametric study.

8.4 Theory for Device

To model the behavior of the actuator device with finite dimensions, we resort to simulation methods other than the bi-axial laminated model used for material selection. These methods include approximate analytical models and finite element

models. Instead of handling the actual but complex geometry, the analytical model makes use of a simplified geometry. An 1-D line model is used for transient thermal analysis while a plane-strain 2-D model is used for thermo-elastic analysis. Although the approximate models do not provide as accurate as the finite element models, they enable identification of the important design parameters and provide a quick check on performance.

The following section will present first the approximate model, followed by the finite element models.

8.4.1 *Transient Thermal Analysis*

Temperature distribution over the polymer actuator with embedded symmetric meandering skeleton can be captured using an 1-D line model (see Fig. 8.3). The 1-D line model is obtained by unfolding the heat conduction path, which is mainly the meandering skeleton, and using the effective or 'composite' thermo-physical properties along the path. The 1-D thermal model leads to the following linearized ODE for natural cooling:

$$\frac{\partial^2 T}{\partial x^2} - \frac{hP}{\lambda_{\parallel} A}(T - T_{\infty}) = \frac{1}{k_{\parallel}} \frac{\partial T}{\partial t} \tag{8.5}$$

where P is the effective perimeter for the line composite model and A is the cross-sectional area. The effective perimeter (P) is related the actuator perimeter (P_0) such that $P = 2P_0L_0/L$ [79], see Figs. 8.2 and 8.3. The cross-sectional area (A) is given by $A = H_0(t_p + t_s)$. The thermo-physical properties for the line composite are given in Eqs. 8.4a to 8.4d.

The ODE has the following transient response

$$T(x,t) = T_{\infty} + \sum\nolimits_{n=1}^{\infty} c_n \sin(\frac{n\pi x}{L}) \exp\left(-k_{\parallel}(\frac{n\pi}{L})^2 - \beta\right) t, \tag{8.6}$$

where c_n are unknown constants to be determined from the initial temperature distribution and $\beta = hPk_{\parallel}/(\lambda_{\parallel}A)$. This form of solution is obtained by solving the boundary value problem with $T(x = 0) = T(x = L) = T_{\infty}$, using the separable variable method and a transformed variable, i.e. $\theta = (T - T_{\infty})e^{\beta t}$.

The time constant for heat transfer along the heat-conducting skeleton can be approximated using the first mode time constant, such that

$$\tau_1 = \left(\frac{\pi^2 k_{\parallel}}{L^2} + \beta\right)^{-1}. \tag{8.7}$$

The above 1-D model assumes that polymer cladding on the sides of the skeleton responses almost instantaneously with the unfolded skeleton at the same cross-section. This assumption holds if the overall thermal response time for the actuator is much longer than the heat diffusion time for the insulating polymer cladding. This can be checked using the model of 'a cold slab in a hot bath', which predicts the heat diffusion time constant as [80]:

$$\tau_2 = \frac{{t_p}^2}{k_p \pi^2}, \tag{8.8}$$

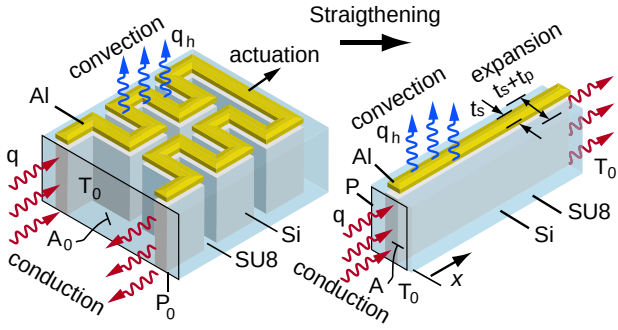

Fig. 8.3 An 1-D thermal model obtained by straightening meandering heat conduction path

where k_p is thermal diffusivity for the polymeric layer.

Comparing Eq. 8.8 with Eq. 8.7 leads to a ratio, such that

$$\frac{\tau_2}{\tau_1} = \frac{k_{\parallel}}{k_p}\left[\left(\frac{t_p}{L}\right)^2 + \frac{hPt_p{}^2}{\lambda_{\parallel}A\pi^2}\right]. \tag{8.9}$$

A small ratio will ensure that the assumption of instantaneous heat diffusion remains valid. This is usually the case because the polymeric spacing thickness (t_p) is much smaller than the conduction path length (L).

8.4.2 *Finite-width Thermo-mechanical Analysis*

The design of a polymeric actuator with an embedded meandering skeleton has a complex geometry. Therefore, the design does not lend itself to a simple thermo-mechanical analysis. To facilitate a closed-form analysis, we use a simpler, though similar, geometry. This model is a polymer actuator with embedded parallel plates of skeleton, see Fig. 8.4. The parallel plates have a similar configuration to a meandering skeleton, except without the horseshoe bends. They are expected to have a similar confinement effect on the bonded polymer. With such geometry idealization, we have a model of stacked layers of polymer and skeleton with finite widths and small thickness.

According to a biaxial model with infinite widths [83], polymer component contributes substantially to the actuation whereas the skeleton component imposes confinement. Since the skeleton material is relatively stiff and has a low CTE, it almost yields a rigid confinement on the deformation of polymer. Thus, the skeleton can be assumed as rigid. Therefore, a polymer layer bonded in a stack of parallel plates can be represented with a polymeric layer bonded between two rigid interfaces.

A rigidly bonded polymeric layer may undergo certain lateral deformations, especially near the free edge if the layer has a small bond width as compared to

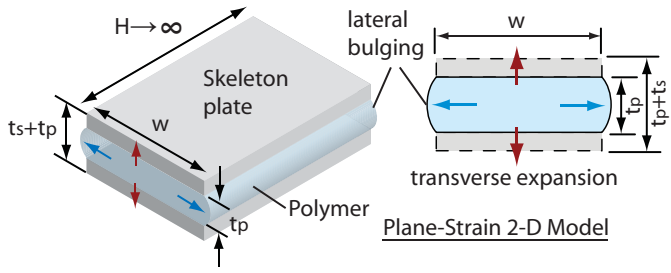

Fig. 8.4 A 2-D plane-strain thermo-mechanical model representing the stack of finite-width plates

the thickness, i.e. a small aspect ratio (w/t_p). As a result of the associated lateral bulging, less volumetric expansion is concentrated into the transverse direction, leading to less strain enhancement. A two-dimensional (2D) plane-strain model predicts that the apparent transverse strain ($\alpha_\perp$) is a function of the aspect ratio (r) and Poisson's ratio (ν), which is given by [81]:

$$\alpha_\perp = \left(\frac{1+\nu}{1-\nu}\right) f(r)\alpha, \tag{8.10}$$

with

$$f(r) = \frac{1 - \left(\frac{\nu}{1-\nu}\right)\frac{\tanh(r)}{r}}{1 - \left(\frac{\nu}{1-\nu}\right)^2 \frac{\tanh(r)}{r}}, \qquad \text{and} \qquad r = \frac{w}{t_p}\sqrt{\frac{3}{2}\left(\frac{1-2\nu}{1-\nu}\right)}.$$

Similarly, a plane-strain 2-D model for a rigidly-bonded polymer layer under compression yields for the apparent Young's modulus ($E_\perp$) [148]:

$$E_\perp = \frac{1-\nu}{1-\nu-2\nu^2}\left[1 - \left(\frac{\nu}{1-\nu}\right)^2 \frac{\tanh(r)}{r}\right] E_0. \tag{8.11}$$

Consider a composite stack of polymer and skeleton. The polymer component contributes mainly to thermal expansion and elastic flexibility. Therefore, properties of the composite can be estimated using the polymer at a volume fraction of ϕ:

$$\begin{aligned} \alpha_c &\approx \phi\alpha_\perp^p \\ E_c &\approx \phi^{-1} E_\perp^p \end{aligned} \tag{8.12}$$

With these approximations, we can also estimate the effective thermal stress and work density for the composite with finite width.

8.5 Finite Element Model

Finite element software (ANSYS) is used for performance simulation and a parametric study for the proposed actuator design. Finite element models are built

according to the actuator geometry, which includes a heater, a skeleton and a polymer. They are made of three-dimensional (3-D) structural elements (SOLID45). Two types of analyzes are conducted, namely the thermo-elastic response under uniform heating and structural response under mechanical loading. The analyzes are under various loading and boundary conditions, imposed to extract the results of interest. They lead to various effective properties, namely the apparent directional CTE, stiffness, thermally induced stress and work density.

The boundary and loading conditions are summarized in Table 8.1. The boundary and loading conditions vary according to the required property extraction. In the calculation for the effective CTE, a finite element model with a clamped-free condition is thermally loaded with a uniform temperature rise (ΔT), yielding the tip displacement (ΔL_0). In the calculation for the effective Young's modulus, the model with the clamped free condition is mechanically loaded by a tip force (ΔF), yielding the tip displacement ($\Delta L_0'$). In the calculation for the thermally induced stress, the model with a clamped-clamped condition undergoes a uniform temperature rise and yields the blocked reaction force (ΔR) at the clamped tip. On the other hand, the effective work density is estimated from the calculated effective CTE and stress.

Table 8.1 List of boundary and loading conditions

Effective Properties	Symbols	Boundary Conditions	Driving Loads	Extracted Data	Definition
Coefficient of Thermal Expansion	α_c	Clamped-Free	ΔT	ΔL_0	$\Delta L_0/L_0$
Young's modulus	E_c	Clamped-Free	ΔF	$\Delta L_0'$	$\frac{\Delta F L_0}{A_0 \Delta L_0'}$
Thermal stress	$\alpha_c E_c$	Clamped-Clamped	ΔT	ΔR	$\Delta R/A$
Work density	$\frac{1}{2}\alpha_c^2 E_c$	Mixed	–	–	$\frac{\Delta R \Delta L_0}{2AL_0}$

Table 8.2 Material properties used for simulation

Material properties	Units	Si	Al	SU-8
Young's modulus (E)	GPa	130	69	3.2
Poisson's ratio (ν)	1	0.26	0.35	0.33
Density (ρ)	10^3kg/m^3	2.33	2.7	1.5
CTE (α)	10^{-6}/K	2.6	23.1	150.7
Thermal conductivity (k)	W/m/K	148	237	0.2
Specific heat (c)	J/kg/K	702	904	1000

8.6 Parametric Study

In the subsequent study, we will evaluate and optimize the actuator design with respect to the discussed design objectives and design variables. The actuator under study is assumed to be comprised of a SU-8 expander, a silicon skeleton and an Al thin-film heater. The material properties used for simulation are summarized in Table 8.2. They are all assumed to be temperature independent.

8.6.1 *Thermal Responses*

A typical electro-thermal micro-actuator design takes times to cool from an elevated temperature to room temperature. The cooling time for the actuator decreases with shortening of the heat dissipation path. For example, a small air gap of one μm between a hot actuator and the cool substrate leads to a fast response of a few kHz. However, a large air gap leads to the diminishing thermal dissipation through air. For example, the present actuator has an air gap of around 450 μm and an extended solid conduction path of approximately 2 to 10 mm long. Therefore, it suffers from a slow thermal response of a few tens of Hz.

Could its thermal response be improved? The following studies may shed some lights on this issue. Two aspects of transient heat transfer are studied, namely heat transfer along the skeleton to the overall actuator and heat diffusion into polymer cladding.

8.6.1.1 *Cooling Time*

The polymer actuator is embedded with a heat conductive skeleton that improves heat transfer to the polymer. However, the skeleton is rather long, in the order of a few mm. The 1-D line model shows that cooling time for the device depends on the heat conduction path length L, in addition to heat convection (see Eq. 8.5 and 8.7).

At a fixed conduction path length, an increase in the spacing thickness of SU-8 relative to silicon leads to an increase in thermal response time (i. e. at $L =$ const, $\phi \uparrow \Rightarrow \tau_1 \uparrow$, see Fig. 8.5a). This is caused by a decrease in the effective thermal conductivity. However, at a fixed longitudinal space, an increase in the spacing thickness of SU-8 leads to less packing of meandering skeleton folds and therefore results in a shortened conduction path length (i. e. $L_0 = \text{const}, \phi \uparrow \Rightarrow \text{L} \downarrow$, see Fig. 8.5b). In this case, time response changes as a result of the interplay between a shortened conduction path length and a decrease of the effective thermal conductivity. The resulting trends are shown in Fig. 8.5b. At a large bond width (60 μm), the length effect dominates, leading to a decreasing trend of thermal response time with respect to volume fraction. However, at a small bond width (10 μm), the material effect dominates, leading to a increasing trend of response time with respect to volume fraction.

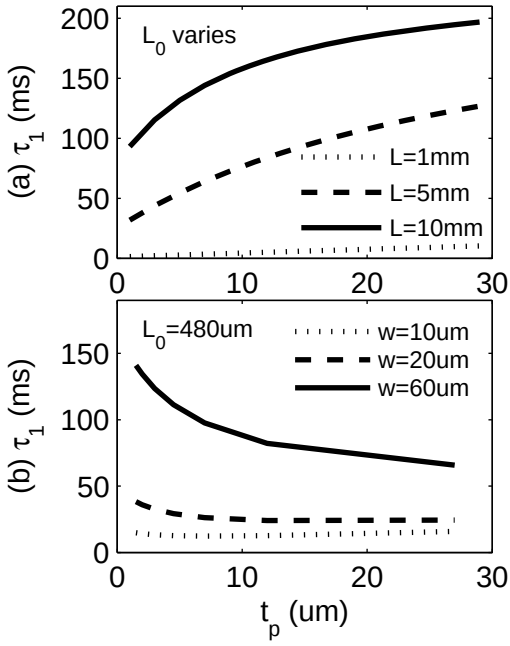

Fig. 8.5 Thermal response time (τ_1) as a function of polymeric spacing thickness (t_p): (a) at a constant heater length (L) but varying actuator length (L_0); (a) at a constant actuator length (L_0) but varying heater length (L)

8.6.1.2 *Heat Diffusion*

Upon heating through the heat-conductive skeleton, there may be a time lag for complete heating the insulating polymer even if the skeleton has reached a steady-state temperature. The 'a cold slab in a hot bath' model [80] indicates that time constant(τ_2) for heat diffusion into the polymer increases with the polymeric spacing thickness. For example, the time constant for heat diffusion is a few μs for a few μm thick polymeric cladding, but it increases to a few hundreds μs for a 30 μm thick cladding. Generally, the time constant for heat diffusion into the polymer is rather short as compared to that for heat conduction through the long skeleton, i.e. the overall response time (τ_1) for the actuator.

8.6.2 *Thermo-elastic Responses*

The width (w) and spacing thickness (t_p) of the bonded polymeric layer affect the effective thermo-mechanical properties of the actuator, such as the apparent transverse CTE (α_c) and the apparent Young's modulus (E_c). The width is proportional to the bonded surface while the spacing is proportional to the free surface. Hence,

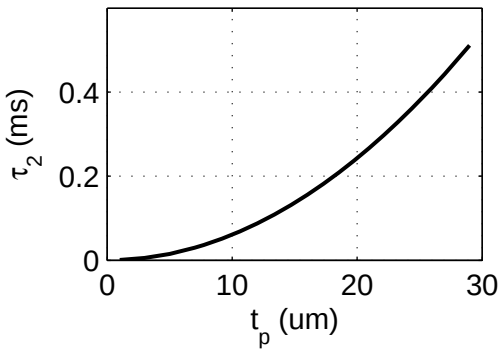

Fig. 8.6 Heat diffusion time (τ_2) as a function of polymeric spacing thickness (t_p)

the ratio (r) of the width to the spacing indicates the extent of confinement effect on the bonded polymer layer according to Eqs. 8.10 and 8.11.

8.6.2.1 *Influence of Width*

Consider a composite design containing 50-% vol. SU-8 with a constant skeleton thickness (i.e. t_s=3 μm) but varying width. The confinement effect is observed in the trend for the apparent CTE (α_c) and Young's modulus (E_c) with respect to the bond width (w). The apparent CTE increases with the bond width of the embedded meandering skeleton or parallel plates (see Fig. 8.7a). The value α_c for the composite is smaller but close to that of 100 % SU-8. On the other hand, the apparent Young's modulus E_c is enhanced at a factor of at least 2.

The trends of strain enhancement with the bond width is also observed at the other volume fraction (i.e. proportional to polymer thickness), as shown in Fig. 8.8a. Figs. 8.8 shows that the α_c, σ_c, and work density increase generally with the bond width. However, the dependence on the bond width is not very obvious for E_c (see Fig. 8.8b).

According to Eq. 8.10 and Eq. 8.11, the extent of confinement effect depends on the aspect ratio of the bond width to layer thickness of the bonded polymer. The confinement effect is more pronounced to a wide layer than a short layer. Likewise, it is more pronounced to a thin layer than a thick layer.

8.6.2.2 *Influence of Volume Fraction*

If we keep the bond width (w) constant, a change in the spacing thickness (t_p) of polymer affects the volume fraction according to geometry relationship (see Eq. 8.1). There is no doubt that the volume fraction influences the thermo-elastic performance of the actuator. An increase in the volume fraction of the polymer is expected to add 'muscle' to the actuator but decreases the confinement effect 'felt'

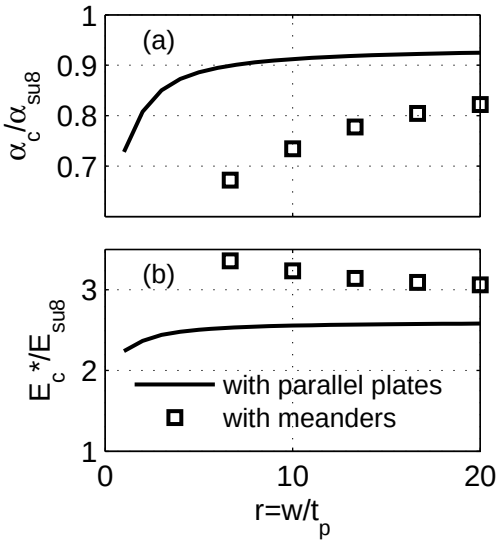

Fig. 8.7 Normalized properties as function of aspect ratio (w/t_p) at ϕ=0.5: (a) relative enhancement for the apparent CTE; (b) relative enhancemetn for the apparent Young's modulus

by the polymer. It is unclear how the interplay between 'muscle' and confinement effect on the actuator performance. Is there an optimum volume fraction that maximizes the actuator performance? The subsequent parametric study will show dependence of the apparent CTE (α_c), Young's modulus (E_c), thermal stress (σ_c) and work density on the volume fraction (ϕ).

In general, the apparent CTE (α_c) increases at a diminishing rate with respect to the volume fraction of the polymer (see Fig. 8.8a). It peaks at a volume fraction of about 0.8. Beyond the optimum volume fraction, the apparent CTE (α_c) decreases with further increase in the volume fraction because the polymer 'feel' less lateral restrain by the skeleton and its volume expansion is not concentrated in the thickness direction ('transverse direction'). The optimum volume fraction for the peak CTE depends also on the bond width and skeleton layout.

Dependence of apparent Young's modulus (E_c) on volume fraction is shown in Fig. 8.8b. It decreases monotonously with an increase in the volume fraction. This means that the less polymer content leads to a larger stiffness.

Thermal stress (σ_c) of the blocked actuator can be estimated by simply multiplying the apparent CTE (α_c) with Young's modulus (E_c). It has a combined effect from both α_c and E_c. Fig. 8.8c shows that the trends of thermal stress with respect to the volume fraction are similar to a 'flat' hump or 'plateau'. They show maxima which are rather flat with respect to the volume fraction ranging from 0.2 to 0.8. Increasing the volume fraction outside this range leads to smaller thermal stresses.

Work density defines the level of energy stored in a actuator for mechanical

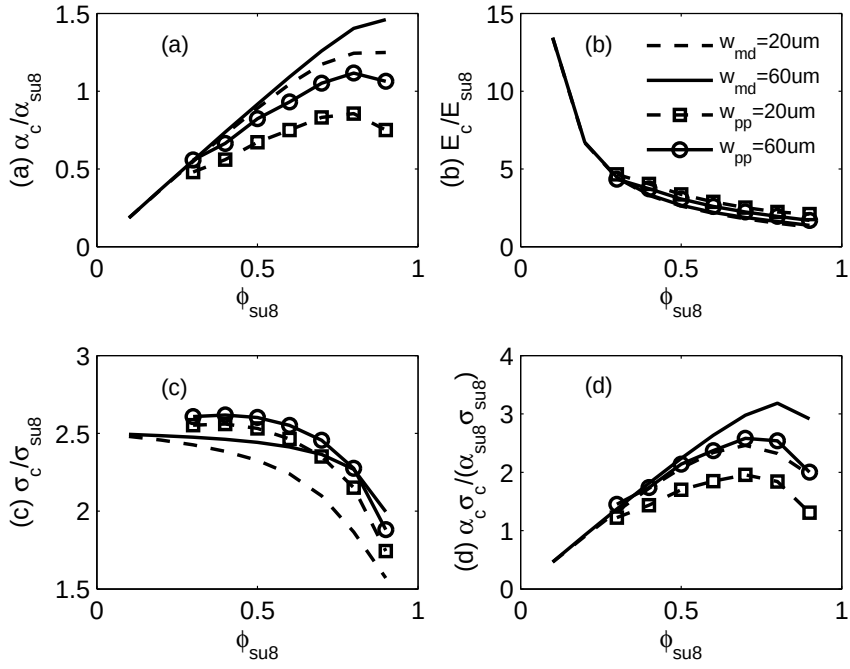

Fig. 8.8 Normalized properties as function of volume fraction for actuator designs with either meandering (*md*) skeleton or parallel plates (*pp*): relative enhancement in the actuation direction for (a) apparent CTE; (b) apparent Young's modulus; (c) thermally induced stress; (d) work density

work. In the present actuator design, work density depends significantly on the content of thermally expandable polymer. It shows similar trends to those for CTE. It basically increases with the volume fraction. It peaks at the optimum volume fraction, ranging between 0.7 and 0.8, which depends also on the bond width and skeleton layout.

8.6.2.3 *Influence of Skeleton Layout*

At the same volume fraction and bond width, the apparent properties for the composite depends also on the skeleton layout. For example, the design with the embedded meandering skeleton displays higher E_c but lower α_c than the design with the embedded parallel plates. The design with the meanders shows a decreasing trend for E_c with respect to width but an increasing trend for α_c. However, the design with the parallel plates shows an increasing trends for both E_c and α_c. This is attributed to the fact that the meandering skeleton has horseshoe bends connecting each fold and, consequently, it could exerts stiffer reinforcement and longitudinal restraint to the bonded polymer. However, both the designs approach to the same

asymptotic values at a very large width, as the influence of the horseshoe bends diminishes.

The skeleton layout does not change the trends of apparent properties with respect to the volume fraction. However, the geometry difference affects the longitudinal stiffness and consequently the magnitudes of the trends. For example, Figs. 8.8a-b show that the design with the meanders shows a lower CTE and a larger E_c than that with the parallel plates. Meanwhile, the design with the meanders shows a higher thermal stress but a lower work density at the same width and volume fraction as the latter. In addition, the skeleton layout affects on the optimum volume fraction. For example, the optimum volume fraction for maximum work energy is 0.7 for the design with the meanders but it is 0.8 for the design with the parallel plates.

8.7 A Design Case Study

After studying design trends of the actuation responses, we will use a design case to illustrate how much improvement the design optimization can offer. The composite design may need to meet multiple criteria. However, in the present case study, we restrict ourselves to a single design objective, namely maximum work density in the actuation direction.

In a preceding paper [83], we reported an actuator design consisting of SU-8 and Si laminae with 50-50% volume ratio (SU-8/Si). The reported design produces excellent actuation performance, and it produces approximately three times higher thermal stress than an unconstrained SU-8 block while maintaining considerably high thermal strain. This design is taken here as a reference design for performance comparison.

Consider a design space of 480 μm long (L_0), 50 μm high (H) and 60 μm wide ($W = 2w$). Let us explore various actuator designs that fit into the design space, using a 3 μm thick and varying length skeleton. The parametric study shows that the design for maximum energy density has an optimum volume fraction of 70-30% SU-8-Si. Table 8.3 summarizes performance comparison among the optimum design, the reference design, and the polymer alone. The comparison shows that the optimum design with 70-30% SU-8-Si improves energy density by a factor of 2.6, as compared to 2.1 for the reference design with 50-50% SU-8-Si. In addition, the optimum composite design displays enhanced apparent CTE by a factor of 1.1, in comparison to 0.8 for the reference design. However, the displayed thermal stress for the optimum design is 2.5 times higher than the thermal stress for SU-8 alone. This value is slightly lower than that obtained by the reference design, which reaches 2.6 times. Despite an increase in the insulating content of polymer, the optimum design reduces thermal response time by about 20% as compared to the reference design. This is attributed to the shortened heater length.

Table 8.3 Design comparison in terms of geometry and performance

Geometry and Performance	Units	100% SU-8	50-50% SU-8/Si	*70-30% SU-8/Si
ϕ	1	1	0.5	0.7
L_0	μm	480	480	480
$W = 2w$	μm	60	60	60
H	μm	50	50	50
t_s	μm	–	3	3
t_p	μm	480	3	7
L	mm	(6.84)	10.46	6.84
α_c	10^{-6}/K	150.7	123.9	158.4
E_c	GPa	3.2	9.80	7.1
σ_c	MPa/K	0.48	1.25	1.18
$\sigma_c\alpha_c/2$	J/m^3/K^2	36.3	77.8	93.8
τ_1	ms	(229.5)	120.9	97.7

8.8 Conclusion

We have successfully performed design optimization of a polymeric actuator with an embedded skeleton. Design parameters and objectives are identified. In the actuator design, polymeric component determines the thermal expansion but a skeleton component determines the effective thermal diffusivity and stiffness reinforcement. However, a 100% polymeric actuator design without skeleton material does not necessarily deliver better actuation than the one with less polymer. This is because strain enhancement of a polymer confined between skeleton decreases with the polymeric content. Design optimization shows that a 20-30 % of skeleton content could in fact maximize the actuation strain and work density. In addition, the skeleton content significantly improve the thermal diffusivity, and consequently, the characteristic thermal response time.

A design case for maximum work density shows that the optimum design containing 70 % SU-8 outperforms the 100% bare SU-8 in almost every aspect. In the actuation direction, the optimum design shows a 2.2 times higher effective Young's modulus, a 2.5 times higher thermal stress, a 2.6 times higher work density, and a 5% higher CTE, as compared to those for SU-8 alone. In addition, it reduces thermal response time by half. It is concluded that design optimization is a rewarding exercise in addition to material selection.

Chapter 9

A Polymeric Bender With Embedded Asymmetric Skeleton

This chapter [1] presents the design, simulation, and characterization of a new type of in-plane thermal unimorph, which utilizes a composite microstructure of SU-8 and silicon. The unimorph consist of a silicon skeleton and SU-8 photoresist, which encapsulates the silicon skeleton. The silicon skeleton is asymmetric in shape, consisting of a straight segment and a meandering segment. Gaps and surrounds of the skeleton are filled with the SU-8 polymer. Bonds between the polymer filling and the sidewalls of the silicon microstructure enhance thermal expansion and stiffness of the polymer in a transverse direction. Therefore, this unimorph design delivers excellent actuation performance. The composite actuator bends laterally when electro-thermally activated. A 530-μm long, 90-μm wide and 50μm thick micro-machined device achieves a maximum lateral displacement of 25 μm at a 1.75-V driving voltage and at 17.8-mW input power, at an average temperature below 200 °C. It has a simulated lateral stiffness of 1.2 kN/m. At 1.75 V, it is estimated to produce a 30-mN lateral blocked force that is high as compared to other micro-actuators.

9.1 Introduction

Bimetals are laminate of two metals with different coefficients of thermal expansion (CTE). The laminate is constructed by bonding the two metal layers together. When heated, bimetals deflect perpendicular to the bonding surface. They are also known as thermal bimorphs or unimorph in the literature. The concept of bimetal actuation can be extended to multilayer design or multi-morph design using non-metallic materials or semi-conductor materials. The laminate design has been miniaturized for a wide range of applications, where a large actuation range and low driving voltages are required. For example, Rietmueller and Benecke [122] fabricated bimorph actuators consisting of epitaxial silicon and gold film activated by a polysilicon heater; Ataka *et al.* [8] demonstrate large out-of-plane bending using tri-layers of high-CTE polyimide, a metallic heating film (Ni/Au/Cr) and low-CTE

[1] This chapter is based on a paper published in the Journal of Micromech. Microeng. [78]

polyimide.

Despite their successful application, the laminate design of electro-thermal micro-actuators is mostly limited to produce motion perpendicular to the wafer plane. This is because they are made of planar layers on the wafer. If in-plane motion is required, construction of the laminate design has to be rotated by 90°, becoming perpendicular to the wafer plane. This is difficult to make using micro-fabrication. Sehr *et al.* [127] have demonstrated such a rotated design, by depositing aluminium (Al) on a sidewall of a silicon vertical beam. The sidewall deposition is done at a shallow incidence angle. Successful deposition requires that the sidewall of the vertical beam is free from the shadow of neighbouring structures. As a consequence, the vertical laminate could not be packed closely to other microstructures. This makes the design and fabrication of vertical laminates more complicated than those of planar laminates.

Owing to the difficulties involved, the vertical thermal bimorph using two materials is not adopted widely for in-plane actuation. Instead, mono-material asymmetric designs are more widely adopted as in-plane thermal actuators. One type of the mono-material designs is an asymmetric design, consisting of a wide arm and a narrow arm which are parallel to each other and joined at their tips in a U shape. The asymmetric designs exploit differential heating of the asymmetric flexures to produce a lateral bending. Guckel *et al.* [53] first presented such an asymmetric design and fabricated it using nickel electroplating. Comtois and Bright [27], Pan and Hsu [114] later demonstrated them using surface micromachining of polysilicon. Recently, Nguyen *et al.* [111], Chronis and Lee [22] demonstrated designs using SU-8 epoxy and a surface metallic heating film.

Performance of these asymmetric thermal actuators depends to a large extent on expansion materials [22, 27, 53, 111, 114]. Materials of high CTE, like polymers, are preferred to produce large displacements at low operating temperatures [22, 111]. However, polymers have low elastic moduli. As a consequence, they cannot produce as much actuation force as silicon and metals. In addition, they are poor electrical and thermal conductors. To overcome the limitations of polymers while tapping their benefits, a search for alternative designs is needed. Instead of using a single material, as for the asymmetric actuators, we explore the use of multiple materials to achieve effective thermal actuation for in-plane applications. In addition, a fabrication method is developed to realize the multi-material design.

9.2 Design Concept

The proposed design acts as an in-plane thermal unimorph. It bends laterally when activated. The unimorph actuator has an asymmetric geometry and consists of multiple materials (Fig. 9.1). It primarily consists of a silicon 'skeleton' and a polymeric expansion material, which encapsulates the silicon 'skeleton'. The silicon 'skeleton' is a high-aspect-ratio microstructure with deep trenches. The silicon

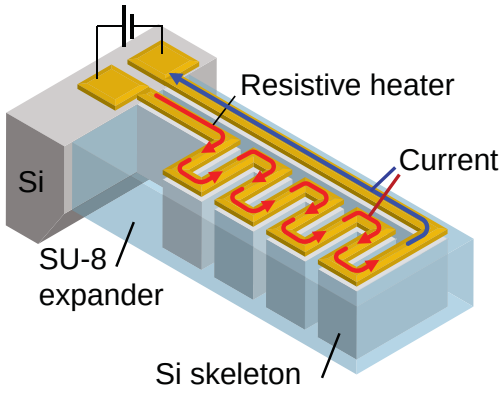

Fig. 9.1 Schematic drawing of a polymeric thermal actuator with an embedded asymmetric skeleton and an aluminium heater, showing an electric current flowing along the meandering path

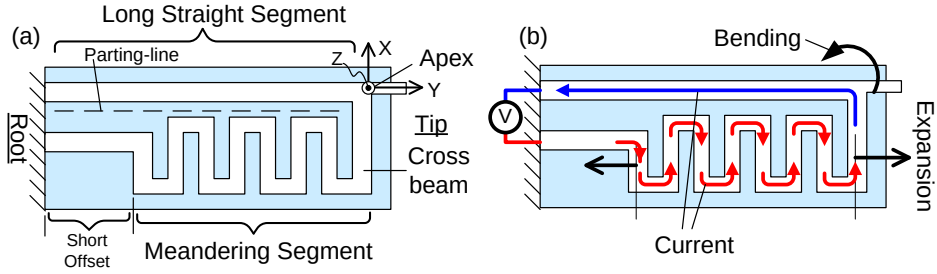

Fig. 9.2 Top layout of the multi-material asymmetric actuator: (a) definition and nomenclature of segments; (b) induced current and actuation directions under the driving voltage

skeleton is asymmetric in shape, consisting primarily of a long straight segment and a meandering segment (see Fig. 9.2). The straight segment is connected to the meandering segment at the front tip, where an apex is defined. Top of the silicon skeleton is coated with a thin film heater. The polymeric material fills the gaps and surrounds of the silicon microstructure. It is expected to have perfect bonds with sidewalls of the silicon microstructure.

Before discussing on the thermally induced motion, a convention of direction is defined in this paper with reference to Fig. 9.2a. The longitudinal or transverse direction is along the y-axis; the lateral direction is along the x-axis while the normal direction is along the z-axis. Both x- and y-axes are parallel to the wafer plane while the z-axis is normal to the wafer plane. When activated by resistive heating, polymeric filling expands in volume and is capable of opening the gaps between the meandering silicon skeleton. The polymeric expansion is predominantly in the longitudinal direction (see Fig. 9.2b) and it is higher than that for the straight silicon beam. The difference in thermal expansion pushes the straight beam through

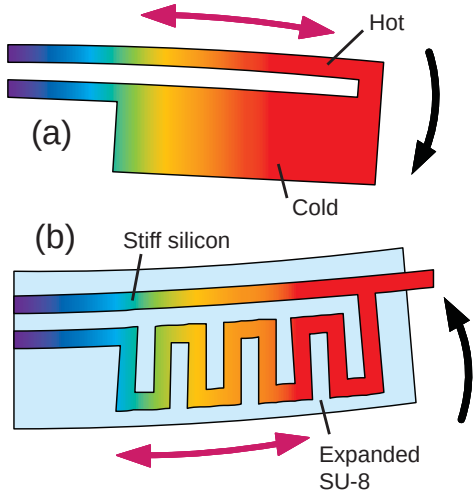

Fig. 9.3 Actuation principles based on a) differential heating of single-material asymmetric actuator; and b) heating of the layered-stack design with asymmetric geometry

a cross beam, and it is converted into a lateral bending about the z-axis.

The polymer encapsulant, together with the embedded meandering silicon segment, resembles to a stacked configuration of polymer and silicon layers. It is expected to manifest similar properties to a polymer layer filled in the gap between two silicon layers. The actuation capability of the bonded polymer is enhanced in several aspects. First, the heat transfer to and from the polymer is substantially improved by the embedded silicon. Secondly, volumetric expansion of the bonded polymer is concentrated in a transverse direction along the y-axis owing to the constraints of the bonded surfaces in the lateral direction along the x-axis. This results in a higher apparent linear CTE in the transverse direction, as compared to a free polymer. On the other hand, there remains little lateral expansion, which appears as slight bulging, at the free edges of the bonded polymer. Thirdly, the bonded polymer is reinforced by the silicon layers, resulting in a larger apparent stiffness in the transverse direction [84].

Silicon is favored here over metals as heat conductor because silicon micromachining (using deep reactive ion etching) can readily form deep trenches of high aspect ratio, for polymer filling. In the present design, photo-patternable epoxy, i.e. SU-8 photoresist, is adopted as an expansion polymer because it is easy to process and it possesses high CTE and good thermal stability, as compared to other thermal expandable materials.

The operating principle of the present design is based on differential thermal expansion between the straight segment and the meandering segment. Thus, it is very similar to the actuation principle of vertical bimetals [127]. Even at a uniform temperature rise, the present actuator design will bend laterally. The bending direction

Table 9.1 Dimensions used for geometry modeling

Geometry and dimensions	Symbol	Values (μm)
Length of a long beam minus offset	L_1	500
Length of a short offsetting beam	L_2	30
Thickness of cross beams	w_1	5
Spacing of a horseshoe bend	w_2	3
Thickness of a horseshoe bend	w_3	3
Envelope width of the meandering structures	h_1	78
Spacing between the long and short beams	h_2	15
Spacing between the straight and the meandering segments	h_3	5
Thickness of the long and short beams	t_1	5
Width of the surrounding polymeric rims	t_2	8
Layer thickness of aluminum (not shown)	z_1	0.675
Layer thickness of silicon	z_2	50
Air gap on the side of actuator	g_x	250
Air gap in front of the actuator	g_y	300
Air gap beneath the actuator	g_z	450

is towards the silicon straight beam when the actuator is heated. However, the actuation direction turns opposite if the actuator undergoes a temperature drop below the initial temperature at which the original position is. Such thermal-mechanical response to uniform heating may possibly be an advantage or a disadvantage depending on application.

The actuation principle for the present composite actuator is different from that for the single-material asymmetric actuators (see Fig. 9.3). The single-material design bends under differential heating, which induces a high temperature in a slender arm but relatively low temperature in another arm of larger width. The hot slender arm expands more than the cool arm. This principle causes a bending direction opposite to that of the newly proposed composite actuator, whose slender arm remains cool relative to the larger-width composite stack.

9.3 Finite Element Modeling

The proposed actuator design comprises of three materials: silicon, aluminum and SU-8 epoxy. It is a composite structure with a complex geometry. When activated thermally, it undergoes complex deformations, which cannot be described using a simple analytical method. Here, finite element (FE) modeling is used to evaluate performance of the new thermal actuator. The finite element software package ANSYS is used for the modeling. Two 3-D models were built for two separate analyses. A model of coupled-field elements (SOLID5) is used to simulate the electric, thermal, and mechanical fields under steady-state resistive heating. In addition, a 3D model of structural elements (SOLID45) at the room temperature is

used for estimating stiffness of the actuator under constant-force loading at the tip.

9.3.1 *Boundary Conditions and Geometry*

Fig. 9.4 shows configuration of the modeled actuator and boundary conditions imposed. The actuator model resembles an over-hanging cantilever. The actuator is clamped at the root. The rest parts of the actuator are free to move. The root temperature is fixed at a constant room temperature, i.e. 25 °C. The air in the cavity surrounding or beneath the actuator is not modeled in this context, but its effect on heat transfer either by conduction or convection can be accounted for using an effective heat transfer coefficient. The actuator is loaded either electro-

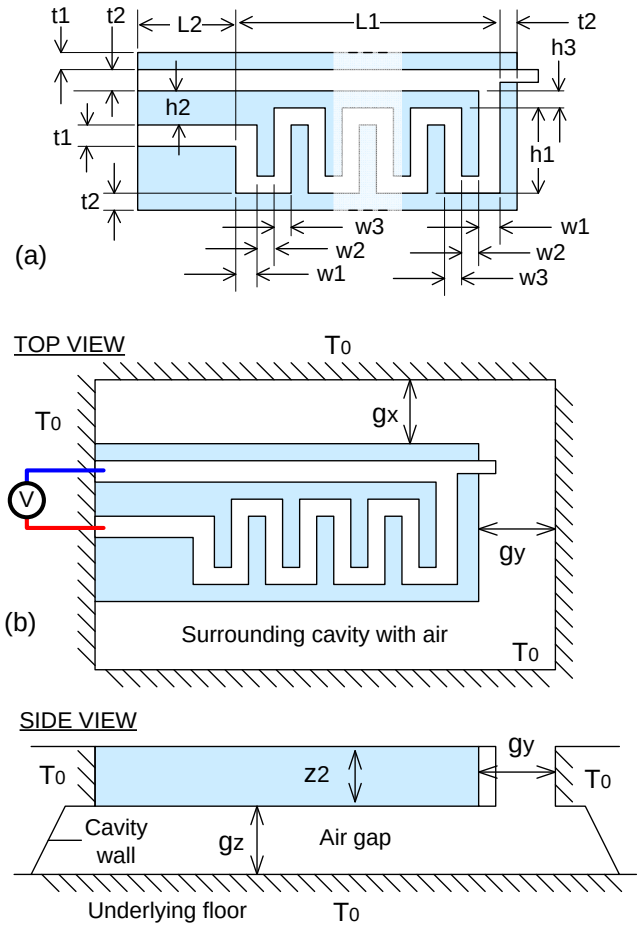

Fig. 9.4 Dimensions and boundary conditions (a) dimensions of top layout as given in Table 9.2; (b) top and side views of cavity surrounding the actuator with temperatures indicated on the boundary

thermally or mechanically. In the coupled electro-thermo-mechanical analysis, an electric potential is applied across the aluminum heater. In the mechanical analysis to estimate stiffness, three orthogonal loads are applied separately at the apex of the asymmetric composite actuator (see Fig. 9.2).

The asymmetric actuator has geometric dimensions listed in Table 9.1. The actuator consists of a 0.675-μm thick Al film, a 50-μm thick Si microstructure, and polymer encapsulant. Fig. 9.4a shows the top layout of the polymer and the aluminum heater. Beneath the heater is the silicon microstructure, which has an identical layout to the heater. The heater layout consists of three segments: a long straight segment connects to a meandering segment, which is followed by a short straight segment (see also Fig. 9.2a). The long straight segment is parallel to the short straight segment. The long straight segment is a 5-μm wide and 530-μm long. The meandering segment is 3-μm wide and it spans over 500 μm (L_1) while the short offsetting segment spans 30 μm (L_2). The meandering segment consists of many horseshoe bends, which are 78-μm long (h_1) and 3-μm wide (w_3) with a 3-μm spacing (w_2). The meandering segment connects to the other two segments, through 5-μm thick (w_1) cross beams.

9.3.2 *Material Properties*

As a preliminary study, the present modeling assumes that material properties, such as Young's modulus, thermal expansion coefficient, and thermal conductivity, are constant and temperature independent [63, 114]. However, electrical resistivity is assumed to be temperature dependent at a constant temperature coefficient of resistivity (TCR). SU-8 epoxy is very sensitive to process conditions, methods of testing, and geometry of the test sample. Consequently, SU-8 is reported to have a considerable variation in measured properties [36, 37, 57, 90]. In the present design, the SU-8 layers are predominantly confined in the trenches between neighboring silicon layers. The SU-8 layers in this configuration are very similar to a test sample confined in a close cylinder of a Pressure-Volume-Temperature (PVT) apparatus [36, 37]. They are therefore expected to exhibits bulk properties, measured from the PVT apparatus. Based on this reason, we adopted the comprehensive SU-8 properties reported by Feng and Farris [36, 37]. In the present modeling, the linear CTE is taken as one third of the bulk volumetric expansion coefficient, which is much larger than the in-plane linear CTE measured from a thin-film [36, 37]. The material properties used in the modeling are listed in Table 9.2.

9.3.3 *Heat Tranfer in Air*

There are three modes of heat transfer affecting a thermal micro-actuator immersed in air: conduction, convection and radiation. Relative importance of heat transfer modes depends on operating temperatures and dimensions of the device and cavity, in particularly the dimensions of the air gaps next the released device. Heat con-

Table 9.2 Material properties used for FE modeling

Material Properties	Unit	Si [14, 156]	Al [9, 40, 42]	SU-8 [36, 37, 57, 90]
Young's modulus, E	GPa	130	69	3.2
Poisson's ratio, ν	1	0.26	0.35	0.33
Coef. of thermal expansion	ppm/°C	2.6	23.1	150.7
Thermal conductivity	W/m/K	148	237	0.2
Electric resistivity	μm	2E-2	3.1E-8	>1.2E8
Temperature coef. of resistivity	1/°C	-	4.1E-3	-

duction in air is relatively important when the air gap distance is small, say several microns. It happens significantly over a conduction layer in a close proximity to the hot device. Heat convection plays a role in carrying heat and mass from the conduction layer to the colder ambience at a larger distance away [99]. Micro-scale heat convection in air is not zero [89], but it may be secondary as compared to heat conduction through paths like air or conducting solids. At a low operating temperature (e.g. <300 °C), micro-scale heat transfer by radiation in air is small as compared to that by conduction or convection over a wide range of dimensions [91]. Therefore, only heat conduction and convection in air is considered in the present modeling.

Based on the cavity configuration around the actuator (see Fig. 9.4), there are two major heat conduction paths in air. The first path is in plane, from the actuator to the top bounds of the cavity, at a distance of about $250 - 300$ μm (g_x or g_y); the second path is out-plane, from the actuator to the bottom of the cavity, at a distance of about 450 μm (g_z). It is approximated [59] to have a heat conduction coefficient h_{cond},

$$h_{cond} = k_{air}/\Delta z \tag{9.1}$$

where k_{air} is the air thermal conductivity of 0.027 W/m/K [67]. In this case, the effective heat transfer coefficient by air conduction ranges between $60 - 108$ W/m^2/K.

The convective heat transfer coefficient can be estimated from a limiting case for a horizontal cylinder immersed in air. In the limiting case where the horizontal cylinder becomes a very fine wire, the Nusselt number has a finite value of 0.36 for the Rayleigh number ranging between $10^{-3} - 10^{-6}$ according to Churchill and Chu [25]. The convective heat transfer coefficient is hence estimated as

$$h_{conv} = 0.36 k_{air}/D \tag{9.2}$$

where D is the diameter of the horizontal fine wire. An equivalent diameter for the actuator block is defined as $4A/P$, in which A is the cross sectional area and P is the perimeter over the section. Using the dimensions listed in Table 9.1, the equivalent diameter is calculated as 60.9 μm. Upon substituting the dimension into Eq. 9.2, the convective heat transfer coefficient is estimated to be 159.5 W/m^2/K.

Summing up the parts of conduction and convection in the surrounding air, a total heat transfer coefficient h_{total} is estimated to be

$$h_{total} = h_{cond} + h_{conv} \tag{9.3}$$

which ranges between 219 and 267 W/m^2/K.

9.4 Simulation Results

A typical coupled-field analysis of the 3-D finite element model is presented below. The analysis uses a potential difference of 1 volt, both initial and boundary temperature of 25 °C (denoted as T_0), and a total heat transfer coefficient of air (h_{total}) of 250 W/m^2/K.

Fig. 9.5a shows the electric potential distribution over the top of asymmetric actuator. A potential difference is applied across the aluminum heater and induces a current flow along it. The straight segments are shorter than the meandering segment. Therefore, a potential drop primarily takes place over the meandering segment (with reference to Fig. 9.2). There is little potential drop along the two straight segments, including the cross beam.

Fig. 9.5b and Fig. 9.5c depict the temperature distribution over the side and the top of the composite actuator. It is observed from Fig. 9.5b that the side temperature is almost uniform across the thickness, though varying along the length. This temperature distribution confirms that heat transfer across the thickness is improved, with little thermal gradient across the thick polymer layer. The top

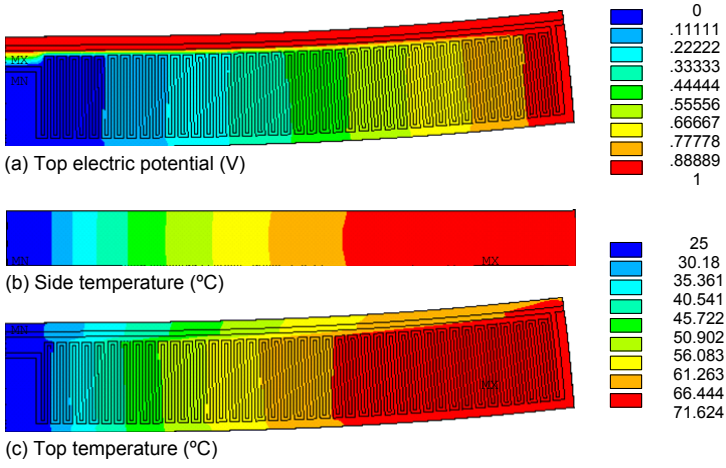

Fig. 9.5 Simulated scalar fields on which the layout of silicon microstructure (or the heater lines) are superimposed (at a 1-V driving voltage and an assumed heat transfer coefficient in air of 250 W/m^2-K): (a) electric potential on the top; (b) temperature distribution on the side; (c) temperature distribution on the top

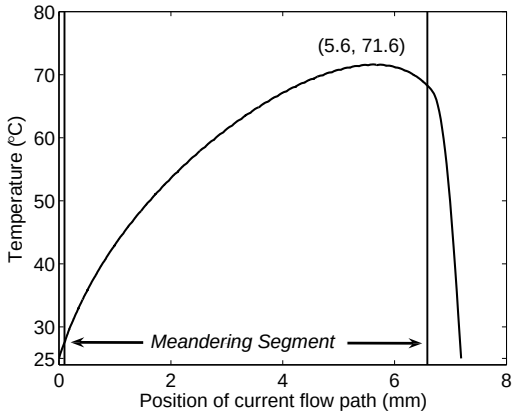

Fig. 9.6 Temperature profile along the current flow path, whose direction and segments are indicated in Fig. 9.2 (simulated at a 1-V driving voltage and an assumed heat transfer coefficient in air of 250 W/m^2-K)

temperature contour in Fig 5c shows that high temperature is developed at the meandering segment. The temperature reaches a maximum of 71.6 °C, as indicated with "MX" in Fig. 9.5c (near the cross beam).

However, the temperature along the long straight beam remains relatively low. The temperature contour at the top (Fig. 9.5c) shows that the straight beam is at a lower temperature than the meandering neighbor at the same longitudinal distance from the root. This is because the straight beam is directly connected to the heat sink at the root and it is shorter than the meander. Moving along the heat flow path on the aluminum film, temperature changes in an asymmetric profile as shown in Fig. 9.6. The temperature profile has two ends fixed at 25 °C. It rises to a maximum of 71.6 °C at a relative position of 78% over the total length of the silicon skeleton. After reaching the maximum, the temperature sharply drops along the straight beam.

Fig. 9.7 depicts the deformed shape and the corresponding displacement fields of the proposed actuator when driven at 1V. It is observed that the induced displacement is predominantly in plane. The expanded polymer opens the gaps between the silicon microstructures, contributing to longitudinal expansion of the meandering segment. The expanded meandering segment then pushes the long straight beam, resulting in a large lateral displacement as observed at the actuator tip. There is a little out-of-plane bulging observed at the free edges of the bonded polymers. Out-of-plane bulging is suppressed by the lateral constraints of the high-aspect-ratio silicon microstructure. The bulging is slightly higher on the front rim of actuator, because the polymer along the rim is only constrained on one side.

Besides the coupled-field analysis at 1 volt, displacement-field analyses under three separate concentrated loads were conducted to evaluate static stiffness at the

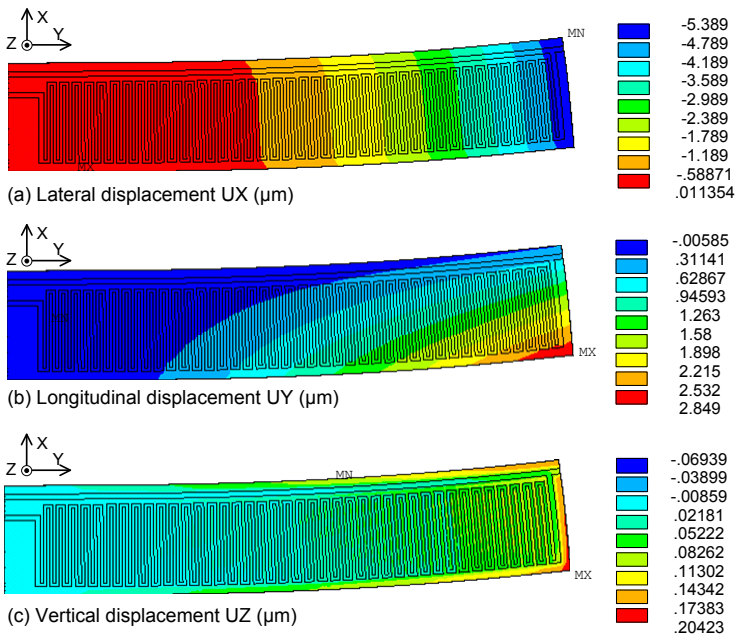

Fig. 9.7 Simulated displacements as viewed from the top (at a 1-V driving voltage and an assumed heat transfer coefficient in air of 250 W/m^2/K): (a) lateral displacement field (u_x); (b) longitudinal displacement field (u_y); (c) vertical displacement field (u_z)

apex of the actuator, see Fig. 9.2b. The simulated performance of the actuator is summarized in Table 9.3. It is observed that the actuator possesses considerable stiffness in all three directions. The transverse and out-plane stiffness is higher than the lateral stiffness, which corresponds to the actuation direction. A lateral actuation force is estimated by multiplying the lateral motion induced at 1 volt and the lateral stiffness. It turns out to be 7.3 mN, which is considered high as compared to the reported electro-thermal actuators made of polysilicon and silicon reported in [12, 101, 114].

The coupled-field analysis above is performed using a heat transfer coefficient of 250 W/m^2/K. This value is derived from a macroscopic law for heat transfer in air at a scale. However, microscopic heat transfer in air is not completely understood. A parametric study is performed here to investigate the influence of the heat transfer in air on the temperature induced to the present actuator. In this study, the driving voltage is kept at 1 V but the heat transfer coefficient in air is varying from zero to 500 W/m^2/K. Fig. 9.8a shows that the temperatures induced by resistive heating at 1V decreases with an increase in the heat transfer coefficient in air. The average induced temperature for a model with zero heat transfer in air is 9 % higher than that for a model with a heat transfer coefficient of 250 W/m^2/K. The difference in the average induced temperature increases if heat transfer in air increases. Based

Table 9.3 Simulated performance at a driving voltage of 1 V and a total heat transfer coefficient of 250 W $m^{-2}K^{-1}$.

Specifications	Unit	Values
Driving voltage	V	1
Resistance		
at $\approx$ 0 V	Ω	102.7
at 1 V	Ω	115.8
Power consumption at 1V	mW	8.6
Maximum temperature at 1V	°C	71.6
Average temperature at 1V	°C	56.9
Displacements at apex at 1V		
lateral direction, u_x	μm	5.1
transverse direction, u_y	μm	0.5
out-of-plane direction, u_z	μm	0.06
Static stiffness at apex		
lateral direction, k_x	kNm^{-1}	1.2
transverse direction, k_y	kNm^{-1}	89.3
normal direction, k_z	kNm^{-1}	4.5
Estimated lateral force at 1V	mN	6.1

on the parametric analysis above, the induced temperatures are found dependent on heat transfer coefficients in air but do not change drastically over the simulated range. This suggests that heat dissipation of the present actuator is mainly by conduction through the silicon microstructure and the polymer encapsulant to the heat sink at the root.

9.5 Fabrication

The device is fabricated using bulk micromachining of silicon and SU-8-2002 polymer filling. A sputtered aluminum film is deposited on the top of a 4-inch silicon wafer. It is then patterned using a resist mask. The resist mask is kept and used again for a later etching process. Deep reactive ion etching (DRIE) of the silicon substrate forms cavities and trenches that define the shape of the silicon microstructure, as shown in Fig. 9.9a. Afterwards, a negative photo-resist of SU-8-2002 is cast and patterned to encase the silicon structures, as shown in Fig. 9.9b. Finally, the actuator structures are released from the underlying substrate by backside etching using a nitride mask. Details of the fabrication process are reported in an accompanying paper with a focus on fabrication technology [24].

9.6 Characterization

A micro-actuator device is tested on a probe station, using a microscope and a semiconductor parameter analyzer. An electric potential difference is applied to

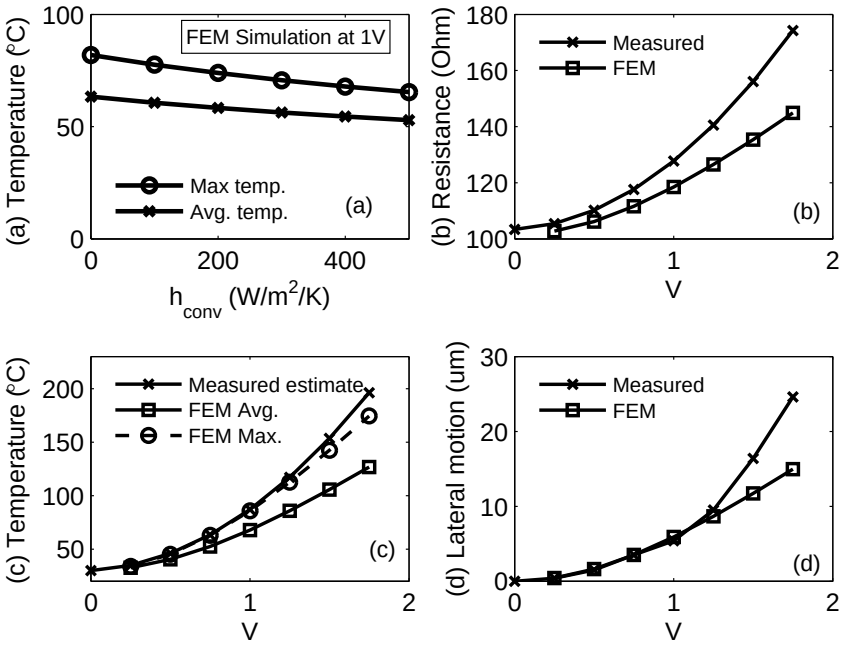

Fig. 9.8 Simulation results and measured data (with assumed h_{total}=250 W/m^2/K, if not specified): (a)average and maximum temperature induced at 1V as function of heat transfer coefficient h_{total}; (b) electric resistance as a function of voltage; (c) average and maximum temperature as a function of voltage; (d) lateral displacement as a function of voltage

contact pads of the device under test using two probes. The induced current is measured using a parameter analyzer. The consumed power and temperature rise are then derived from the measured voltage and current. Deflection of the activated device is measured in pixels using digital images, which are captured by a digital camera mounted to the microscope. Dimensions of the images pixels are measured using a reference scale of the meandering pattern, which comprises of equal silicon thickness and gap spacing of 3 μm.

Fig. 9.8b shows that electric resistance increases with voltage, as a result of resistive heating. The induced temperature rises due to resistive heating can be estimated from the resistance change using the reported temperature coefficient of resistivity (TCR) for aluminum film [9], as given in Table 9.1. The derived temperature represents an average temperature rise over the heater. Fig. 9.8c shows that it increases in a quadratic trend with the driving voltage.

The measured deflection is obtained by comparing the images before and after electrical activation. For example, Fig. 9.10 shows an image of an inactive actuator and an image of the actuator activated at 1.75 V. In the optical images, SU-8 poly-

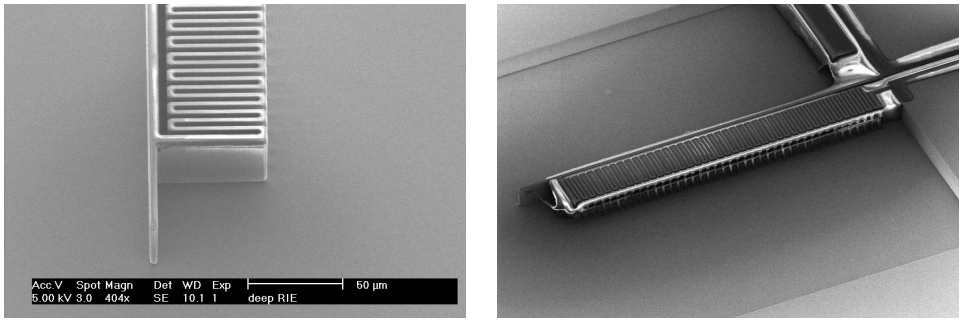

(a) (b)

Fig. 9.9 Scanning electron micrograph of devices: (a) silicon microstructure after deep reactive ion etching (DRIE); (b) SU-8 encasing the silicon microstructure

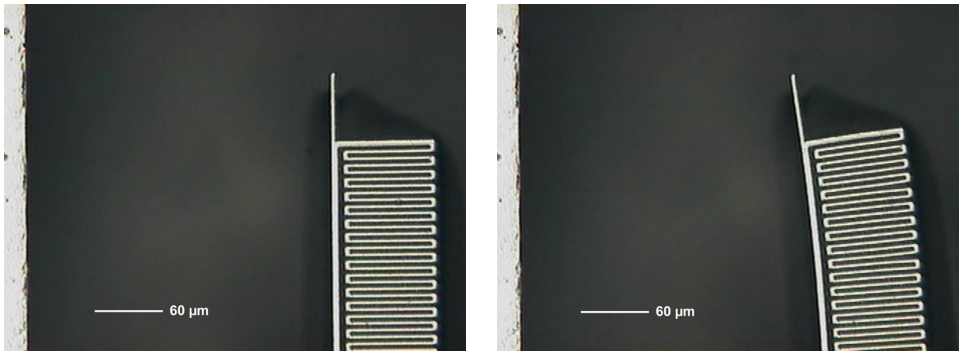

(a) (b)

Fig. 9.10 Optical images of a sample asymmetric actuator, showing a region neighboring to its tip: (a) an inactive composite unimorph; (b) an activated composite unimorph at 1.75 V

mer is hardly visible due to its transparency; whereas a aluminum heater is clearly seen. It is observed that the activated composite actuator bends leftwards (the direction towards the long straight beam). As shown in Fig. 9.8d, the measured apex displacement increases with respect to the driving voltage. The trend of displacement increment is almost quadratic, like the trend of the average temperature rise.

The asymmetric composite actuator achieves a 25-μm maximum lateral displacement at a 1.75-V driving voltage and at a 17.8-mW input power. A lateral blocked force is estimated to be 30 mN by multiplying the measured displacement at 1.75 V with the simulated stiffness. In addition, it is estimated that the large motion at 1.75 V is induced at an average temperature rise of 196 °C. Performance comparison between the present actuator design and the previous designs of comparable dimensions [101, 114] is listed in Table 9.4. The comparison table shows that the newly designed composite actuator produces a high actuation force and a high

Table 9.4 Benchmarking

	Units	U-shape PolySi [114]	V-shape Si [101]	SU8 bender with asymmetric Si skeleton
Actuator length	μm	500-750	1000	530
Actuator width	μm	7 10	200	90
Actuator height	μm	2-3	50	50
Number of actuators	[1]	1	10	1
Flexure width	μm	1-3	10	3-5
Driving voltage	V	10	12	1.75
Power consumed for actuator array	mW	20	840	18
Operating temperature	°C	< 600	< 527	<200
Actuation displacement	μm	20	12-20	25
Blocked actuation force	mN	0.003	6.7	30

displacement at a low operating temperature and a low driving voltage and power.

After the driving voltage is released, the inactive actuator cools down and restores back to its original position. Voltages higher than 2 V are to be avoided for this sample device because they are expected to heat up the actuator beyond 200 °C, which is close to the reported glass transition temperature for SU-8 around 220 °C [37]. When heated beyond the glass transition temperature, SU-8 polymer is prone to irreversible shrinkage [37], which induces a pre-stress to bend the original position of the inactive composite actuator. The shrinkage-induced bending is opposite to the normal actuation direction. It is permanent, but unintended for repeatable operation of the actuator.

Measured responses are compared with numerical results of finite element simulation. The simulation predicts similar trends of electric resistance, temperature and apex displacements, with respect to the driving voltage, see Fig. 9.10. The simulated results agree well with the measurement data at a low voltage range where resistive heating is not too high. At the low voltage range (< 1V), a slight discrepancy is observed: the simulated average temperature is slightly lower than the value estimated from the assumed TCR and the observed change in resistance, even though the simulated displacement agrees very well with the measured. This observation implies either that the polymeric CTE put into the numerical model is probably higher than true property, or that the input thermo-physical properties for thermal simulation do not well represent the true properties of the device under test. At the high voltage range (>1V), the simulation underestimates the temperature rise and induced deflection, but overestimates the induced current. This discrepancy may be attributed to decreasing thermal conductivity of silicon or nonlinear properties of SU-8 polymer over the range of elevated temperatures.

9.7 Conclusions

We have presented the design, simulation and characterization of a new type of the in-plane thermal actuator, which incorporates a composite of silicon and SU-8. The new thermal actuator acts as a unimorph, producing in-plane bending motion when electro-thermally activated. The fabricated in-plane thermal unimorph provides excellent actuation performance: a large displacement and a high stiffness at low power consumption and a low driving voltage (< 1V). A 530-μm long, 90-μm wide and 50-μm thick device demonstrates a maximum lateral displacement of 25 μm at 1.75-V driving voltage and at 17.8-mW input power, at an estimated average temperature below 200 °C.

Since its polymeric component is constrained and reinforced by a high-aspect-ratio silicon microstructure, the composite actuator possesses relatively high stiffness in the actuation direction. It is simulated to have a lateral stiffness of 1.2 kN/m. At 1.75-V driving voltage, the actuator is estimated to produce a 30-mN blocked lateral force, which is high as compared to other reported micro-actuators.

In a conclusion, a powerful electro-thermal unimorph actuator using polymeric composite is successfully demonstrated. With the improved actuation capability, the electro-thermally-activated polymeric composite unimorph can potentially be considered for a wider range of applications where energy consumption is a concern.

In this study, a preliminary numerical model is developed based on the temperature-independent properties (except the resistivity with linear temperature dependence). It provides reliable prediction for actuator performance at a low voltage range (<1 V). The prediction, however, deviates from the measurement at a high voltage range (>1 V), where the actuator is subjected to elevated temperature. In view of this, the model is to be refined with accurate inputs for temperature dependent properties.

Chapter 10

Clamped-Clamped V-shape Design

This chapter presents the design, simulation and characterization of a V-shape thermal actuator, which exploits confined SU-8 layers in a layered composite of silicon and SU-8 for effective thermal actuation. The micro-fabricated actuator (1000-μm long, 56-μm wide, 30-μm high, with a inclination angle of 15°) demonstrates a large in-plane motion (25 μm) at a 2.5-V driving voltage, consuming low power (19 mW) and operating at a relatively low temperature (177 °C). It is estimated to produce a blocked apex force of 135 mN at 2.5 V.

10.1 Introduction

V-shape silicon flexures (see Fig. 10.1a) are known to be capable of producing either a relatively large force or a relatively large displacement [121]. However, the V-shape design of a silicon flexure cannot achieve large actuation force and displacement simultaneously, which are required, for example, in optical switches [86]. Large displacement is often at the expenses of low flexural stiffness. In addition, low power consumption is desired. Present designs and technology of electro-thermal actuators based on silicon cannot completely fulfill these requirements. It motivates a search for alternative designs to overcome the shortcomings of available actuators.

Recently, polymers of high thermal expansion coefficients (CTE) have been used in a U-shape design for generating large displacements [22,111]. The concept enables thermal actuators to be driven at a lower operating temperature and at a lower power input. However, polymers are bad thermal conductors and they cannot generate as much force as a silicon actuator. In this paper, we propose a novel composite design using both polymer and silicon to improve thermal actuation and overcome the above-mentioned limitations.

10.2 V-shape Design

The present design of a V-shape thermal actuator is made of a polymeric composite with an integrated silicon microstructure, or skeleton in the other words, (see Fig.

10.1b). The skeleton has a meandering layout, which form a V-shape envelop. The skeleton is thick and has many high-aspect-ratio gaps in it. The gaps and the surrounds are filled and encased by SU-8 epoxy. Effectively, the silicon and polymeric microstructures form a layer-like composite (see Fig. 10.2).

The polymeric composite spans over a length (L) and it is bent into two equal segments at an equal angle of inclination (θ). The apex is located at the middle of the span. The two ends of the composite microstructure are anchored to the silicon substrate, while the remaining parts are released from the substrate and are free to move under thermo-elastic loads.

The top of the silicon skeleton is coated with an aluminum film, which acts as a heater. When activated electro-thermally, the V-shape polymeric composite rises in temperature. The confined polymeric layers expand and the spacing of the meandering skeleton widens . As a result, the composite of silicon and polymeric materials expands along the lengths of the two inclined segments. Owing to the restraint imposed by the anchors, the longitudinal expansion is converted into a rectilinear translation at the middle apex. The motion characteristics of the polymeric composite are similar to those of a V-shape silicon flexure (see Fig. 10.1a). However, the layer-like composite has an enhanced and higher thermal expansion than the silicon flexure.

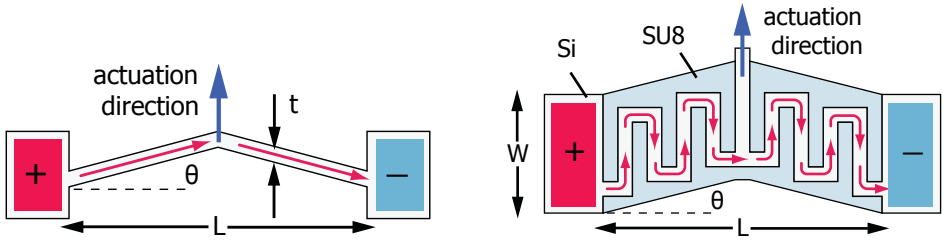

Fig. 10.1 Two V-shape actuator designs: (a) a previous design using a single material flexure; (b) the present design using the polymeric composite with an embedded meandering skeleton

10.3 Bonded Polymer Strip

Benefits of confining polymer in the meandering silicon skeleton can be illustrated using a simple model of a polymeric layer, bonded between two silicon layers. Silicon has very high Young's modulus but low CTE as compared to polymer. It can therefore assumed to be rigid and inextensible , acting as rigid bond interfaces on the polymer layer.

An unconstrained polymeric strip expands thermally in all directions. The thermo-elastic expansion is, however, restrained from lateral deformation when the

strip is bonded to the two rigid interfaces. Only a slight lateral bulging happens at the edges (see Fig. 10.2). Consequently, volumetric expansion of the polymeric strip is concentrated in the transverse direction. This leads to a higher effective linear CTE in the transverse direction ($\alpha_\perp$), which is derived below for an infinitely wide (w) strip [82]:

$$\alpha_\perp = \left(\frac{1+\nu}{1-\nu}\right)\alpha_0, \tag{10.1}$$

where α_0 is the linear CTE for an unconstrained polymeric strip and ν is the Poisson's ratio of the material constituting the polymeric strip.

Clearly, the rigid interfaces also reinforce the polymeric strip. The bonded polymer strip undergoes less transverse strain when loaded transversely. The effective transverse Young's modulus ($E_\perp$) for the infinitely wide polymeric strip is derived as:

$$E_\perp = \left(\frac{1-\nu}{1-\nu-2\nu^2}\right)E_0, \tag{10.2}$$

where E_0 is the Young's modulus for the unconstrained strip. SU-8 epoxy has the following material properties: $E_0 = 3.2$ GPa, ν =0.33 and α_0 =150.7 ppm/°C [37]. Substituting ν into Eqs. 10.1 and 10.2, the constrained SU-8 strip is found to manifest both higher effective CTE and Young's modulus in the transverse direction: $\alpha_\perp = 1.98\ \alpha_0$; $E = 1.48\ E_0$. As a result, the transverse thermal stress per unit temperature rise for the bonded SU-8 strip is derived to be 2.9 times higher than for an unconstrained SU-8 strip.

A thermo-mechanical coupling factor can be defined as the ratio of thermo-elastic energy density over the heat capacity stored in a thermal expansion material, such that

$$\eta = \frac{E\alpha^2\Delta T}{2\rho c_p} \tag{10.3}$$

where E and α denote Young's modulus and CTE of an expansion material, respectively; ρ and c_p denote the density and specific heat, respectively, while ΔT denotes a temperature rise. This coupling factor reflects the quantity of mechanical

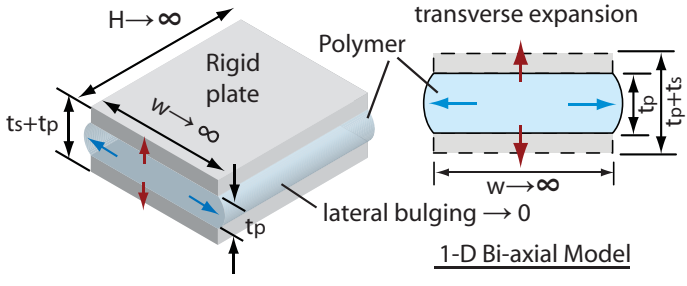

Fig. 10.2 A biaxial model for a polymeric layer sandwiched between two rigid plates

Table 10.1 Comparison of thermal expansion materials

	Symbols	Units	Al	Si	SU-8	SU-8/Si 50/50%
Young's Modulus	E	GPa	70	130	3.2	9.5
Poisson's ratio	ν	[1]	0.36	0.28	0.33	-
Coeff. Thermal Exp.	α	ppm/K	23.1	2.6	150	149
Density	ρ	kg/m^3	2700	2327	1200	1764
Specific heat	c_p	J/kg/K	904	702	1000	851
Maximum temperature	T_{max}	°C	660	1414	230	230
TM[1] coupling per degree	$\eta_{,T}$	10^{-6}/°C	7.65	0.27	30	70
Max. TM coupling [2]	η_{max}	[%]	0.486	0.037	0.615	1.44

[1] Thermo-Mechanical coupling coefficient, $\eta_{,T} = \frac{E\alpha^2}{2\rho c_p}$

[2] Maximum thermo-mechanical coupling, $\eta_{max} = \eta_{,T}(T_{max} - 25°C)$

work can be extracted from the expansion material given the input heat energy and temperature rise. Table 10.1 shows the 50% SU-8 epoxy composite with embedded silicon skeleton outperforms its constituent materials and even aluminum, in terms of the maximum thermo-mechanical coupling factor, η_{max}.

This analysis suggests that confining a thermally insulating polymer in a plate-like microstructure of high thermal conductivity and rigidity could enhance thermal actuation. Such design concept has already been embodied in a bender [78] and a linear stack [82] for in-plane bending and rectilinear actuation, respectively.

10.4 Finite Element Analysis

Performance of the V-shape polymeric composite actuator is simulated and evaluated using a finite element model (using ANSYS). The polymeric composite design modeled is 996-μm long (L), 56-μm wide (W) and 30-μm high (H) with a inclination angle of 15° (see Fig. 10.1a).

Coupled-field simulations at a 1-V driving voltage are conducted for both the V-shape polymeric composite actuator and a V-shape silicon flexure (see Fig. 10.1a). The simulations show that the polymeric composite actuator performs much better than the silicon counterpart. Performance comparison between them is summarized in Table. 10.2. The polymeric composite design provides 4.3 times more motion but consumes 5.5 times less power. The improvement in actuation does not compromise the apex stiffness, which is actually twice as good as the silicon V-shape flexure. The resistive heating at 1 V induces an average temperature rise of about 66 °C to the polymeric composite actuator, as compared to 256 °C rise to the silicon counterpart.

Horseshoe bends constitute the meandering silicon microstructure. Thus, each horseshoe bend consists of two parallel plates, which confine the polymeric filling. The plate widths of the horseshoe bends may therefore influence the actuator per-

formance. A parametric study at uniform temperature rise of 100 °C (i.e. Fig. 10.3) shows that the apex displacement changes in a range between 18 and 21 μm for polymeric composite actuators with plate widths between 10 and 60 μm. The apex motion increases at a decreasing rate with an increase in width. It peaks at a width of approximate 25 μm. Beyond this width, the apex motion decreases with a further increase in width. The trend of the apex displacement reflects the two competing consequences of increasing width, i.e. an increase in flexural rigidity of the meandering skeleton (see Fig. 10.3b) and an increase in apparent thermal strain of the confined polymer. As a result, there is an optimum plate width that leads to a maximum apex motion.

Table 10.2 Performance for V-shape actuators under resistive heating (L=996 μm, H=30 μm, θ=15°) with the same heat convection coefficients.

		Prior Design (Fig. 10.1a)	Present Design (Fig. 10.1b)
Heater/Expander		Al/Si	(Al/Si)/SU-8
Side width, W	μm	(3)	56
Al Heater length	mm	0.97	9.69
Resistance at 1V	Ω	31	170
Input power at 1V	mW	32.4	5.9
Avg. temperature at 1V	°C	256	66
Max. temperature at 1V	°C	398	82
Apex motion at 1V	μm	1.7	7.4
Translational stiffness	kN/m	2.7	5.4

10.5 Characterization

A device in accordance to the proposed actuator design is fabricated using bulk micromachining of a Silicon On Insulator (SOI) wafer and SU-8-2002 polymer filling. A negative photo-resist of SU-8-2002 is cast and patterned to encase the silicon structures, formed by Deep Reactive Ion Etching (DRIE) (see Fig. 10.4). Finally, the actuator structures are released from the underlying oxide sacrificial layer and silicon substrate by backside etching.

As shown in Fig. 10.5, the device under test is 1000-μm long, 56-μm wide, 30-μm deep, and bent at 15°. It is tested on a probe station, using a microscope and a parameter analyzer. An electric potential difference is applied to the contact pads of the device under test using two probes. The induced current is measured using the parameter analyzer. The temperature rise is derived from the relative change of electric resistance using a known temperature coefficient of resistance (4.13×10^{-3}/°C). Details of the measurement set-up are the same as [79].

The V-shape polymeric composite actuator is observed to travel in-plane and

rectilinearly for a voltage range below or equal 2.5 V. Fig. 10.6a-b show the measured in-plane displacement changes with respect to the applied voltage and the input power, respectively. The trend of the measured displacement is quadratic with respect to the driving voltage, while it is linear with respect to the input power. The apex of the V-shape actuator travels in-plane for almost 25 μm at 2.5 V, consuming 19 mW and operating at an induced temperature of 177 °C. When the actuator is driven at 3 V, out-of-plane buckling happens, with clear indication from the focus loss for the microscopic image.

Fig. 10.6c-d show the measured electric current and the derived temperature with respect to the driving voltage. The electric current is observed to increase at a decreasing rate, suggesting a resistance increase under resistive heating. The induced temperature is observed to increase with the driving voltage at an increasing rate. The derived temperature at 2.5 V is estimated to be about 177 °C, which is relatively low as compared to the reported V-shape actuators, made of either silicon or nickel [86, 121].

Fig. 10.7 shows the induced apex displacement as a function of temperature rise, activated by either uniform external heating or integrated resistive heating. During external heating, temperature on the hot chuck rather than that on the actuator is measured. Due to spatial difference in cooling, the temperature rise at the actuator is expected to be lower than that measured at the hot chuck. It therefore causes a lower apex displacement than that achieved under resistive heating at the same indicated temperature.

Although not measured directly, a blocked apex force can be estimated using a

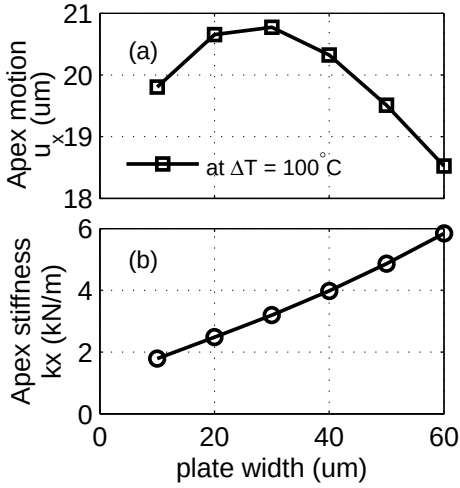

Fig. 10.3 A parametric study for the V-shape polymeric composite actuator: (a) thermally induced apex motion and (b) apex stiffness, as functions of the plate width (w)

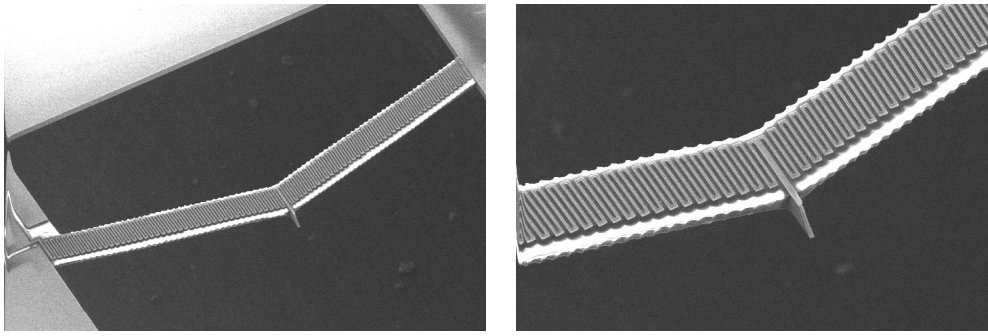

(a) (b)

Fig. 10.4 SEM micrographs of a V-shape composite actuator (a) overall view (b) zoomed-in view

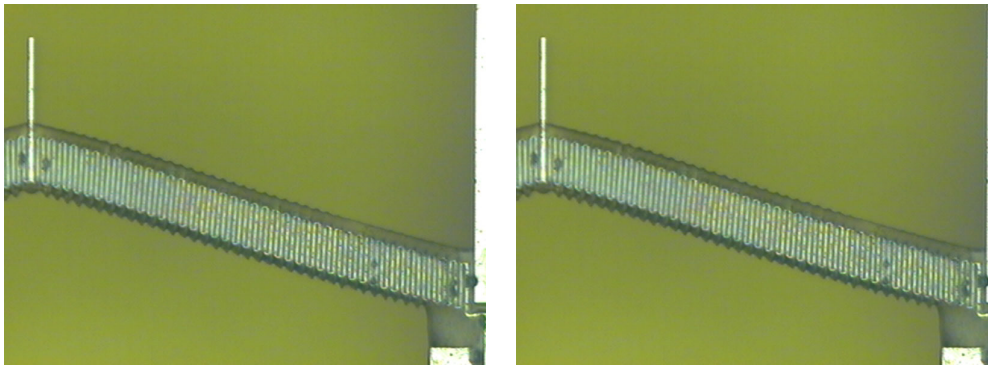

(a) (b)

Fig. 10.5 Optical images showing a half of the V-shape actuator: (a) before electrical activation (b) electric activation at 2.5 V

measured displacement and a simulated apex stiffness. At a driving voltage of 2.5 V and a corresponding input power of 19 mW, a blocked apex force is estimated to be 135 mN, which is considerably higher than that generated by the silicon flexures. This is very encouraging for applications where a large force and an adequate displacement are needed at a relatively low power input.

The blocked force increases with the temperature rise. However, beyond the glass transition temperature at 230 °C, the 'overheated' SU-8 epoxy undergoes irreversible cure shrinkage [37]. Overheating of the SU-8 expander may occur during electric activation or a releasing step by plasma etching. The cure shrinkage induces a high compressive stress that could even break the silicon skeleton at one of the two anchors, as shown in Fig. 10.8. In addition, it causes delamination between the SU-8 epoxy and silicon skeleton near the center. To avoid device failure, the SU-8 epoxy expand should not be heated beyond the glass transition temperature.

10.6 Conclusions

We have presented the design, simulation and characterization of a V-shape thermal actuator, which consist of a SU-8 epoxy expander and a silicon skeleton. The V-shape actuator features powerful thermal actuation using the silicon-confined SU-8 epoxy. However, this composite design has its silicon skeleton are clamped at both ends and its longitudinal expansion converted into an in-plane translation at the apex. However, the clamping at both ends may also cause unintended out-of-plane buckling when the longitudinal expansion becomes large at a high temperature. At the worst case, the clamping, together with cure shrinkage of the 'overheated' SU-8, causes a high blocked force that break the silicon skeleton. There is no doubt that a large blocked force can be generated using the confined polymer. However, reliability of the actuator device is at risk. Therefore, care should be taken to the SU-8 epoxy expander is not heated beyond a temperature, above which cure shrinkage happens.

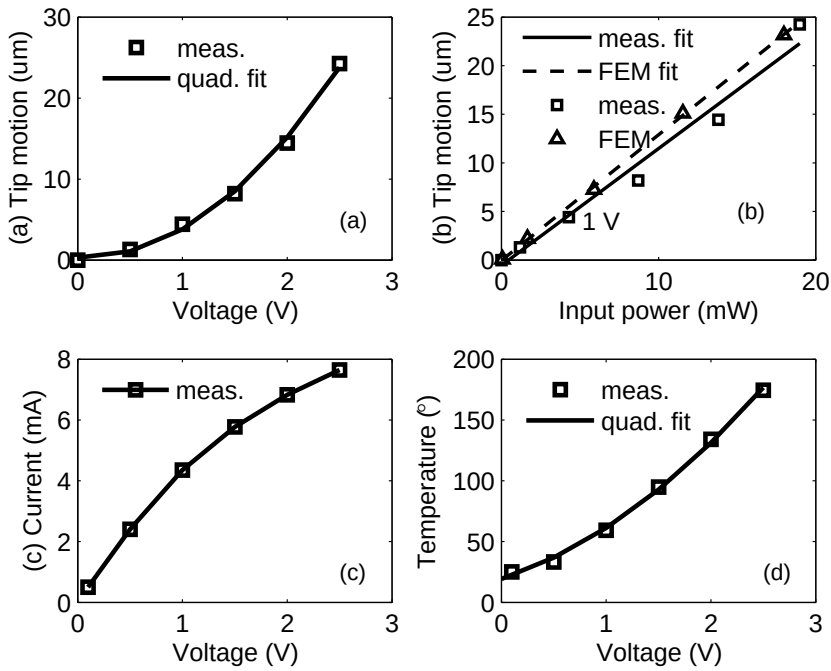

Fig. 10.6 Characterization of a V-shape polymeric composite actuator: (a) measured apex motion as a function of voltage; (b) measured and simulated apex motion as a function of input power; (c) measured current as a function of voltage; (d) derived average temperature as a function of voltage

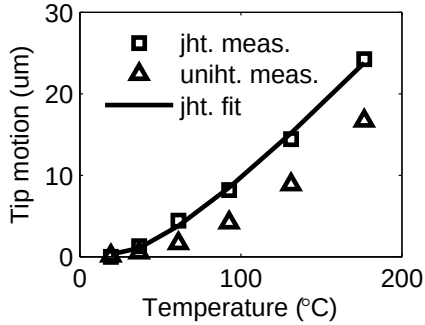

Fig. 10.7 Measured tip motion as a function of temperature, activated by either resistive heating (jht.) or uniform external heating (uniht.)

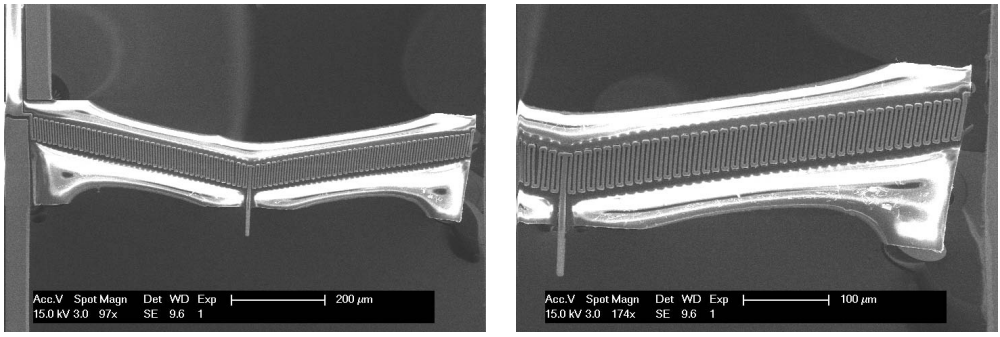

(a) (b)

Fig. 10.8 Failure mode of an overheated V-shape actuator: (a) full span (b) zoom in

Chapter 11

Conclusions

This thesis presents research efforts and results of miniaturizing polymeric 'artificial muscles' for micro-electro-mechanical systems (MEMS). The polymers considered for micro-actuation include dielectric elastomers and thermally expandable polymers. These polymers are insulating and relatively compliant. Electrodes, heat conductor or heater are integrated into them to enable electric activation. The electrodes or heater are, however, so stiff that they restrain actuation of the polymers. To effectively exploit polymers for the miniaturized actuators, confinement effects of electrodes or heaters on polymers needs to be clarified and taken into account in mechanical design of the embedded electrodes or heaters.

Confinement effects on compliant polymers are studied using both theoretical and numerical models. The confinement is found to suppress stress-induced actuation of dielectric elastomers, but it boosts strain-induced actuation of thermal expandable polymers. These understandings lead to various designs of electrode or heater for polymeric actuators. For example, dielectric elastomer micro-actuators are designed with an array of discrete and short electrodes, whereas polymeric thermal micro-actuators are designed with a meandering heat conductor.

Theoretical and numerical studies on the designs suggest that the constrained thermal expansion delivers more powerful actuation than the constrained dielectric elastomer does. In addition, fabrication of the micro-actuators using a thermally expandable polymer is more successful than that using a dielectric elastomer. Polymeric thermal micro-actuators can be built using photo-patternable polymer and a single-level microstructure of heat-conductor. However, fabrication of dielectric elastomer micro-actuator is hindered by difficulties in patterning and selective removing of dielectric elastomers. As a result, a later stage of the present research focuses mainly on the polymeric thermal actuators.

11.1 Contribution

The present research has developed a new class of polymer thermal micro-actuators with embedded heat conductors (or skeletons, in the other words). This actuator design features an adequate actuation strain, a large actuation stress, high work energy density and improved heat transfer. It outperforms many other thermal actuator designs based on either pure polymers or silicon. Therefore, the present thermal actuator could be a promising option to drive many micro-electro-mechanical systems. For example, it can be used to drive a micro-tensile tester, which requires a large actuation force.

Various layout designs of heaters and skeletons are developed for thermally expandable polymers. These include meandering skeletons of symmetric, asymmetric and V- shapes. Polymer actuators with the different skeleton layout could deliver varying characteristics of motion and force. The generated motion can be rectilinear, curvilinear, in-plane or out-of-plane.

Besides introduction of novel designs, the present research has also presented comprehensive modeling for the polymeric thermal actuators with symmetric skeletons. The modeling covers thermo-mechanical and electro-thermal aspects. For example, a bi-axial model is formulated for a sandwich of polymeric and skeleton laminae, while a finite-width plane-strain model is developed for a polymer strip bonded between rigid interfaces. In addition, a one-dimensional electro-thermal model is developed for a polymeric actuator with a symmetric meandered skeleton. These models lay the foundations for subsequent analyzes in the material selection and design optimization.

The bi-axial model accounts for thermo-mechanical interaction of the sandwiched laminae and it predicts enhanced strain and stress of the polymeric lamina in the actuation direction. The finite-width model is solved using the 'mean pressure method'. The analytical solutions for thermally induced strain and stress are in good agreement with the finite element simulation. This model shows that the enhanced thermal strain increases with the aspect ratio, i.e. the bond width to thickness of the polymeric strip. A polymeric strip with a bond width 5 times the thickness could attain 95% the maximum strain enhancement at the infinite bond width. Therefore, a sufficiently compact design is possible to achieve the strain enhancement. The electrothermal model were developed by straightening a symmetric meandering heat conduction path. The model suggests that heat transfer to polymer is effective through the heat-conducting skeleton. The study suggests that a shorter heater could accomplish a short time constant of thermal characteristics.

In the exercise of material selection, we identify the material properties, which influentially affect the thermal actuation, namely, the thermal expansion coefficient, Young's modulus and Poisson's ratio. As a result of the confinement effect of stiff skeletons, Poisson's ratio of polymers significantly affects the actuation performance. Various material combinations and performance criteria have been con-

sidered. Among the materials under investigation, PDMS-containing composites have the highest thermal strains; LCP-containing composites exhibits the highest actuation stress; Nylon-containing composites exhibit the highest actuation stress; SU-8-containing composites deliver the highest work density. On the other hand, most metals serve well as the skeleton.

In the present design of a bi-material thermal actuator,a polymeric component determines the thermal expansion but a skeleton component determines the effective thermal diffusivity and stiffness reinforcement. However, a 100% polymeric actuator design without skeleton material does not necessarily deliver better actuation than the one containing less polymer. This is because the polymeric strain enhancement caused by the skeleton confinement decreases with the polymeric content. Design optimization shows that 20-30 % of skeleton content could in fact maximize the actuation strain and work density of the polymer actuators. In addition, the skeleton content significantly improves the thermal diffusivity and, consequently, the characteristic thermal response time.

Large displacements and blocked forces were clearly witnessed from the experiments and simulations for the various actuator designs. For example, a polymeric bender with an embedded asymmetric skeleton could easily generate a 25 μm tip stroke, or equivalent to a 30 mN blocked force, at less than 2 V, less than 20 mW and below 200 °C; a 1-mm long V-shape polymer actuator with embedded skeleton could deliver 25-μm apex motion, equivalent to a 135 mN blocked apex force, at 2.5 V, consuming 19 mW and operating at 177 °C. Moreover, the thermally induced stress at a high temperature (above 220 °C) could be greater than the fracture strength of silicon. For example, the polymeric content in a V-shape actuator breaks one end of the embedded skeleton with a clamped-clamped boundary condition. Without doubts, the actuation capabilities using the integrated SU-8 expander and silicon skeleton are excellent.

11.2 Future Directions

Insights gained in the actuator development suggest that a proper material selection could further improve the actuator performance. Materials with a large bulk modulus and large volumetric thermal expansion are preferred for powerful actuation. So far, the polymeric thermal actuators are realized using a silicon skeleton and a SU-8 expander and an aluminum heater. Further work can embody other materials in the thermal actuator design. For example, nickel can be used as both the skeleton and heater simultaneously, whereas other polymers can be adopted as the expansion material.

The embedded skeleton brings beneficial confinement effects to thermal expandable polymers. In fact, the effects also applies to other passive polymers, which undergo volumetric changes in response to a stimulus. The embedded skeleton could direct volumetric expansion of thermally, hygro-thermally or even chemically

swollen materials, in a single direction with high planarity. Therefore, the directionally constrained volume expansion will yield a larger apparent linear actuation than the unconstrained expansion.

The proposed micro-actuator design using a dielectric elastomer is not realized within the period of the present research. However, the design remains promising for large-strain micro-actuation. Theoretical studies shows that actuation stiffness of the dielectric elastomer improves with the embedded electrodes. The reinforced dielectric elastomer is not prone to pull-in instability, which, in contrary, limits the actuation of an air-gap electrostatic actuator.

The challenges ahead for the proposed dielectric elastomer actuator lies with micro-fabrication technology. Micro-fabrication of a two-level copper microstructure of electrodes and interconnects has been successfully demonstrated. Further research shall address the remaining fabrication issues for dielectric elastomers. The anticipated fabrication methods should enable micro-patterning, etching and releasing the dielectric elastomers in a reliable, clean and cost-effective way. In addition, the fabrication methods are preferably compatible with integrated-circuits fabrication processes and compliant with clean-room regulations.

Demand for 'artificial muscle' is high in a wide range of microsystems, such as micro-fluidic system and micro-opto-electro-mechanical system. It is expected to provide impetus for research and development of the polymeric actuators. Further research endeavors, ranging from material research, micro-and-nano structuring, functional composite design and electro-mechanical design, will bring advance of polymeric actuator technology. Exploitation of polymeric materials will be promising and rewarding for microsystems.

Appendix A

Appendix

A.1 Thermoelastic Constitutive Equations

The total strain at each point of the heated polymer can be modeled as the sum of two parts. Assuming an linear isotropic material behavior, the first part is a uniform expansion proportional to the temperature rise ΔT. In other words, normal strains arise but no shear strains are induced thermally. The second part comprises the elastic strains induced by mechanical loading. These elastic strains are related to the stresses using the isothermal and linear elastic constitutive equations.

According to [16], the thermoelastic strain-stress relationship for isotropic and linear elastic material in Cartesian coordinate reads ,

$$\begin{aligned}
\epsilon_{xx} &= \frac{1}{E}\left[\sigma_{xx} - \nu(\sigma_{yy} + \sigma_{zz})\right] + \alpha\Delta T, \\
\epsilon_{yy} &= \frac{1}{E}\left[\sigma_{yy} - \nu(\sigma_{zz} + \sigma_{xx})\right] + \alpha\Delta T, \\
\epsilon_{zz} &= \frac{1}{E}\left[\sigma_{zz} - \nu(\sigma_{xx} + \sigma_{yy})\right] + \alpha\Delta T, \\
\epsilon_{xy} &= \frac{1}{2G}\sigma_{xy}; \epsilon_{yz} = \frac{1}{2G}\sigma_{yz}; \epsilon_{zx} = \frac{1}{2G}\sigma_{zx},
\end{aligned} \tag{A.1a}$$

where the shear modulus G is related to Young's modulus E and Poissons' ratio ν by

$$G = \frac{E}{2\,(1+\nu)}.$$

The engineering denotation above is accompanied with indices denotation ([125]) below for readers' convenient.

$$e_{ij} = \frac{1+\nu}{E}\sigma_{ij} - \frac{\nu}{E}\sigma_{kk}\delta_{ij} + \alpha\Delta T\delta_{ij} \tag{A.1b}$$

Dilatation e is the sum of strains in three orthogonal directions:

$$\begin{aligned}
e &= \epsilon_{xx} + \epsilon_{yy} + \epsilon_{zz} \\
&= \frac{1}{3\kappa}\left(\sigma_{xx} + \sigma_{yy} + \sigma_{zz}\right) + 3\alpha\Delta T,
\end{aligned} \tag{A.2a}$$

where the bulk modulus κ is related to E and ν by

$$\kappa = \frac{E}{3(1-2\nu)}.$$

The dilatation e can be related to a hydrostatic stress p, such that

$$e = \frac{-p}{\kappa} + 3\alpha\Delta T, \tag{A.2b}$$

where

$$-3p = \sigma_{xx} + \sigma_{yy} + \sigma_{zz}.$$

Inverting Eq. A.1a, the stress-strain relationships are given as:

$$\begin{aligned}
\sigma_{xx} &= \lambda e + 2\mu\epsilon_{xx} - (3\lambda + 2\mu)\alpha\Delta T,\\
\sigma_{yy} &= \lambda e + 2\mu\epsilon_{yy} - (3\lambda + 2\mu)\alpha\Delta T,\\
\sigma_{zz} &= \lambda e + 2\mu\epsilon_{zz} - (3\lambda + 2\mu)\alpha\Delta T,\\
\sigma_{xy} &= 2\mu\epsilon_{xy}; \sigma_{yz} = 2\mu\epsilon_{yz}; \sigma_{zx} = 2\mu\epsilon_{zx}.
\end{aligned} \tag{A.3a}$$

In indices notation, the stress-strain equation can be expressed as ([125]):

$$\sigma_{ij} = \lambda e_{kk}\delta_{ij} + 2\mu e_{ij} - (3\lambda + 2\mu)\alpha\Delta T\delta_{ij}. \tag{A.3b}$$

The Lame elastic constants λ and μ are related to E and ν by

$$\begin{aligned}
\lambda &= \frac{\upsilon E}{(1+\upsilon)(1-2\upsilon)},\\
\mu &= \frac{E}{2(1+\upsilon)} = G.
\end{aligned} \tag{A.3c}$$

Upon substituting the dilatation in terms of hydrostatic pressure, the stress-strain relationship for the normal strains are reduced to:

$$\begin{aligned}
\sigma_{xx} &= -\lambda p/\kappa + 2\mu\epsilon_{xx} - 2\mu\alpha\Delta T,\\
\sigma_{yy} &= -\lambda p/\kappa + 2\mu\epsilon_{yy} - 2\mu\alpha\Delta T,\\
\sigma_{zz} &= -\lambda p/\kappa + 2\mu\epsilon_{zz} - 2\mu\alpha\Delta T.
\end{aligned} \tag{A.3d}$$

A.2 Equations of Equilibrium

The equations of thermoelastic equilibrium are the same as those for isothermal elasticity since they are based on purely mechanical considerations. In rectangular Cartesian coordinate x, y, and z these equations take the form

$$\begin{aligned}
\frac{\partial\sigma_{xx}}{\partial x} + \frac{\partial\sigma_{xy}}{\partial y} + \frac{\partial\sigma_{zx}}{\partial z} + X = 0,\\
\frac{\partial\sigma_{xy}}{\partial x} + \frac{\partial\sigma_{yy}}{\partial y} + \frac{\partial\sigma_{yz}}{\partial z} + Y = 0,\\
\frac{\partial\sigma_{xz}}{\partial x} + \frac{\partial\sigma_{yz}}{\partial y} + \frac{\partial\sigma_{zz}}{\partial z} + Z = 0,
\end{aligned} \tag{A.4}$$

where X, Y, Z are body forces per volume in the three coordinates.

Bibliography

[1] Andricacos, P. C., Uzoh, C., Dukovic, J. O., Horkans, J. and Deligianni, H. (1998). Damascene copper electroplating for chip interconnections, *IBM Journal of Research and Development* **42**, 5, pp. 567–574.

[2] ANSYS Inc (2002). ANSYS element reference, Release 8.1, Tech. rep., Mason and Hanger-Silas Mason Co Inc, Canonsburg.

[3] Arias, F., Oliver, S., Xu, B., Holmlin, R. and Whitesides, G. (2001). Fabrication of metallic heat exchangers using sacrificial polymer mandrils, *Journal of Microelectromechanical Systems* **10**, 1, pp. 107–112.

[4] Arkema (2007). Kynar & Kynar flex PVDF performance characteristics & data, Arkema's Website, URL `http://www.arkema-inc.com/literature/pdf/779.pdf`.

[5] Ashby, M. (1989). Overview No. 80: On the Engineering Properties of Materials, *Acta Metall* **3**, 5, pp. 1273–1293.

[6] Ashby, M. and Brechet, Y. (2003). Designing hybrid materials. *Acta Materialia* **51**, 19, pp. 5801–5821.

[7] Ashby, M. F. (2005). *Materials Selection in Mechanical Design* (Butterworth-Heinemann).

[8] Ataka, M., Omodaka, A., Takeshima, N. and Fujita, H. (1993). Fabrication and operation of polyimide bimorph actuators for a ciliary motion system, *J. Microelectromech. Syst.* **2**, 4, pp. 146–150.

[9] Avilés, F., Ceh, O. and Oliva, A. I. (2005). Physical properties of Au and Al thin films measured by resistive heating, *Surface Review and Letters* **12**, pp. 101–106.

[10] Baker, M. (2006). Material safety data sheet of xylene (CAS #1330-20-7), Online, URL `http://www.mallbaker.com/europe/msds/default.asp`.

[11] Bar-Cohen, Y. (2002). Electroactive polymers as artificial muscles: a review. *Journal of Spacecraft and Rockets* **39**, 6, pp. 822–827.

[12] Bell, D. J., Lu, T. J., Fleck, N. A. and Spearing, S. M. (2005). MEMS actuators and sensors: observations on their performance and selection for purpose, *Journal of Micromechanics and Microengineering* **15**, 7, pp. S153–S164.

[13] Benslimane, M., Gravesen, P. and Sommer-Larsen, P. (2002). Mechanical properties of dielectric elastomer actuators with smart metallic compliant electrodes, *Proc. SPIE* **4695**, pp. 150–157.

[14] Berger, L. I. (2006). Properties of semiconductors, in D. R. Lide (ed.), *CRC Handbook of Chemistry and Physics*, internet version 87th edn. (Taylor and Francis, Boca Raton, FL.), p. 12.35.

[15] Biercuk, M. J., Llaguno, M. C., M. Radosavljevic, J. K. H., Johnson, A. T. and Fischer, J. E. (2002). Carbon nanotube composites for thermal management, *Appl.*

Phys. Lett. **80**, 15, pp. 2767–2769.

[16] Boley, B. A. and Weiner, J. H. (1960). *Theory of Thermal Stresses*, chap. 8 Summary of the formulation of thermoelastic problems (John Wiley & Sons, New York), pp. 243–271.

[17] Buma, T., Spisar, M. and O'Donnell, M. (2003). A high-frequency, 2-D array element using thermoelastic expansion in PDMS. *IEEE Trans Ultrason Ferroelectr Freq Control* **50**, 9, pp. 1161–76.

[18] Cahill, D. G. and Pohl, R. O. (1987). Thermal conductivity of amorphous solids above the plateau, *Phys. Rev. B* **35**, pp. 4067–4073.

[19] Chan-Park, M. B., Yan, Y., Neo, W. K., Zhou, W. X., Zhang, J. and Yue, C. Y. (2003). Fabrication of high aspect ratio poly (ethylene glycol)-containing microstructures by UV embossing, *Langmuir* **19**, 10, pp. 4371–4380.

[20] Chen, W. T. and Nelson, C. W. (1979). Thermal stress in bonded joints, *IBM Journal of Research and Development* **23**, 2, pp. 179–188.

[21] Chiou, J. C. and Lin, W. T. (2004). Variable optical attenutor using a thermal actuator array with dual shutters, *Optics Communications* **237**, pp. 341–350.

[22] Chronis, N. and Lee, L. P. (2005). Electrothermally activated SU-8 microgripper for single cell manipulation in solution, *J. Microelectromech. Syst.* **14**, pp. 857–863.

[23] Chu Duc, T., Lau, G. K. and Sarro, P. M. (2007). Polymeric thermal micro-actuator with embedded silicon skeleton: Part II fabrication and applications to microgrippers, Submitted to J. Microelectromech. Sys.

[24] Chu Duc, T., Lau, G. K., Wei, J. and Sarro, P. M. (2006). Silicon-polymer laterally stacked bimorph micro-gripper, in *Technical Digest of the 17th MicroMechanics Europe (MME06)* (Southampton, UK), pp. 197–200.

[25] Churchill, S. W. and Chu, H. H. S. (1975). Correlating equations for laminar and turbulent free convection from a horizontal cylinder, *International Journal of Heat and Mass Transfer* **18**, 9, pp. 1049–1053.

[26] Clariant AG (July 1997). Product datasheet of AZ9260 photoresist, Online, URL `http://www.microchemicals.eu/micro/az_9200.pdf`.

[27] Comtois, J. H. and Bright, V. M. (1997). Applications for surface-micromachined polysilicon thermal actuators and arrays, *Sensors and Actuators A* **58**, 1, pp. 19–25.

[28] Conant, R. A., Nee, J. T., Lau, K. Y. and Muller, R. (2000). A flat high-frequency scanning micromirror, *Proc. Solid-State Sensor and Actuator Workshop* , pp. 6–9.

[29] Dattelbaum, D., Jensen, J., Schwendt, A., Kober, E., Lewis, M. and Menikoff, R. (2005). A novel method for static equation-of state-development: Equation of state of a cross-linked poly (dimethylsiloxane)(PDMS) network to 10 GPa, *The Journal of Chemical Physics* **122**, p. 144903.

[30] Dow (2007). Processing procedures for CYCLOTENE 4000 series resin (immersion develop), From Dow CYCLOTENE Product Literature, URL `http://www.dow.com/cyclotene/resource/prodlit.htm`, 1995-2007.

[31] Dow-Corning (2007). Production information - information about dow corning brand silicone encapsulants, URL `http://www.dowcorning.com/DataFiles/090007c88002053c.pdf`.

[32] Dow Plastics (2007). Typical physical properties of pellethane: Thermoplastic polyurethane elastomers, Dow Website, USA, URL `http://www.dow.com/footwear/products/pellethane.htm`, 1995-2007.

[33] DuPont (2007). Teflon PTFE 7A Product Information - Granular Compression Molding Resin, Dupont Teflon Web, URL `http://www2.dupont.com/Teflon_Industrial/en_US/`.

[34] eFunda (2005). efunda engineering materials, URL `http://www.efunda.com/`

materials/materialshome/materials.cfm.

[35] eFunda (2007). Polymer material properties -unfilled liquid crystal polymer, eFunda Web, URL http://www.efunda.com/materials/polymers/properties/, Ticona Summit, NJ.

[36] Feng, R. and Farris, R. (2003). Influence of processing conditions on the thermal and mechanical properties of SU 8 negative photoresist coatings, *Journal of Micromechanics and Microengineering* **13**, 1, pp. 80–88.

[37] Feng, R. and Farris, R. J. (2002). The characterization of thermal and elastic constant for an epoxy photoresist SU8 coating, *Journal Materials Science* **27**, pp. 4793–4799.

[38] Field, L. A., Burriesci, D. L., Robrish, P. R. and Ruby, R. C. (1996). Micromachined 1x2 optical-fiber switch, *Sensors and Actuators A* **53**, pp. 311–315.

[39] Flowers, G. L., Faubion, B. D., Montague, J. L. and Switzer, S. T. (1980). Selected physical and thermal properties of various formulation of silicone potting compounds. Tech. rep., Mason and Hanger-Silas Mason Co Inc, Amarillo TX, URL http://handle.dtic.mil/100.2/ADA302639.

[40] Frederikse, H. P. R. (2006a). Elastic constants of single crystals, in D. R. Lide (ed.), *CRC Handbook of Chemistry and Physics*, internet version 87th edn. (Taylor and Francis, Boca Raton, FL.), p. 12.77.

[41] Frederikse, H. P. R. (2006b). Thermal and physical properties of pure metals, in D. R. Lide (ed.), *CRC Handbook of Chemistry and Physics*, internet version 87th edn. (Taylor and Francis, Boca Raton, FL.), pp. 12.219–220.

[42] Frederikse, H. P. R. (2006c). Thermal conductivity of metals and semiconductors as a function of temperature, in D. R. Lide (ed.), *CRC Handbook of Chemistry and Physics*, internet version 87th edn. (Taylor and Francis, Boca Raton, FL.), p. 12.219.

[43] Garra, J., Long, T., Currie, J., Schneider, T., White, R. and Paranjape, M. (2002). Dry etching of polydimethylsiloxane for microfluidic systems, *Journal of Vacuum Science & Technology A: Vacuum, Surfaces, and Films* **20**, p. 975.

[44] Gent, A. and Lindley, P. (1959). The compression of bonded rubber blocks, *Proc. Inst. Mech. Eng* **173**, 3, pp. 111–117.

[45] Gent, A. N. (1994). Compression of rubber blocks, *Rubber chemistry and technology* **67**, 3, pp. 549–558.

[46] Gent, A. N., Henry, R. L. and Roxbury, M. L. (1974). Interfacial stresses for bonded rubber blocks in compression and shear, *Journal of Applied Mechanics* **15**, 12, pp. 47–52.

[47] GoodFellow (2007). Comparative Data Tables, Available at GoodFellow Web, URL http://www.goodfellow.com/csp/active/gfHome.csp.

[48] Goodfellow (2007a). Polyamide - Nylon 6,6 - material information, Online, URL http://www.goodfellow.com/.

[49] Goodfellow (2007b). Polymethylmethacrylate (PMMA) material information, Online, URL http://www.goodfellow.com/csp/active/static/A/ME30.HTML.

[50] Goodfellow (2007c). Polyvinylidenefluoride (PVDF) - material information, Online, URL http://www.goodfellow.com/.

[51] Goods, S. (2003). Thermal Expansion and Hydration Behavior of PMMA Moulding Materials for LIGA Applications, Tech. rep., SAND2003-8000, Sandia National Labs., Albuquerque, NM (US); Sandia National Labs., Livermore, CA (US).

[52] Groves, J. *et al.* (1997). Methods of using acrylate-containing polymer blends, US Patent 5,602,202.

[53] Guckel, H., Klein, J., Christenson, T., Skrobis, K., Laudon, M. and Lovell, E. (1992). Thermo-magnetic metal flexure actuators, *5th Technical Digest. IEEE Solid-State*

Sensor and Actuator Workshop , pp. 73–75.

[54] Haasl, S., Griss, P., Sohlstrom, H., Kalvesten, E. and Stemme, G. (2004). Robust, large-deflection, in-plane thermal polymer V-shaped actuators, *17th IEEE International Conference on. Micro Electro Mechanical Systems, 2004. (MEMS)* , pp. 510–513.

[55] Han, B. and Guo, Y. (1996). Determination of an effective coefficient of thermal expansion of electronic packaging components: a whole-field approach, *IEEE Transactions on Components, Packaging, and Manufacturing Technology Part A* **19**, 2, pp. 240–247.

[56] HD Microsystems (2007). Cured film properties, Online, URL `http://www.hdmicrosystems.com/prod/cured.html`.

[57] Hexion (2005). Technical data sheet: Epon resin 8021, Online, URL `http://www.resins.com/resins/am/pdf/SC1525.pdf`, Hexion Specialty Chemicals Inc, Houston, USA.

[58] Hickey, R., Kujath, M. and Hubbard, T. (2002). Heat transfer analysis and optimization of two-beam microelectromechanical thermal actuators, *Journal of Vacuum Science & Technology A: Vacuum, Surfaces, and Films* **20**, p. 971.

[59] Hickey, R., Sameoto, D., Hubbard, T. and Kujath, M. (2003). Time and frequency response of two-arm micromachined thermal actuators, *J. Micromech. Microeng.* **13**, p. 4046.

[60] Hirano, T., Fan, L., Gao, J. and Lee, W. (1998). MEMS milliactuator for hard-disk-drive tracking servo, *Journal of Microelectromechanical Systems* **7**, 2, pp. 149–155.

[61] Hsiao, R., Yu, K., Fan, L. S., Pandhumsopom, T., Sanitini, H., Macdonald, S. A. and Robertson, N. (1997). Anisotropic Etching of a Novalak-Based Polymer at Cryogenic Temperature, *Journal of the Electrochemical Society* **144**, 3, pp. 1008–1013.

[62] Huang, Q. and Lee, N. (1999a). Analytical modeling and optimization for a laterally-driven polysilicon thermal actuator, *Microsystem Technologies* **5**, 3, pp. 133–137.

[63] Huang, Q.-A. and Lee, N. K. S. (1999b). Analysis and design of polysilicon thermal flexure actuator, *J. Micromech. Microeng.* **9**, p. 6470.

[64] Huber, J. E., Fleck, N. A. and Ashby, M. F. (1997). The selection of mechanical actuators based on performance indices, *Proc. R. Soc. Lond. A* **453**, pp. 2185–2205.

[65] Im, J., Shaffer II, E. O., Stokich Jr., T., Strandjord, A., Hetzner, J., Curphy, J., Karas, C., Meyers, G., Hawn, D., Chakrabarti, A. and Froelicher, S. (2000). On the mechanical reliability of photo-BCB-based thin film dielectric polymer for electronic packaging applications, *Journal of Electronic Packaging* **122**, 1, pp. 28–33.

[66] Incropera, F. P. and DeWitt, D. P. (1996a). Appendix A Table A.4 thermophysical properties of gases at atmospheric pressure, in *Fundamentals of Heat and Mass Transfer*, 4th edn. (John Wiley & Sons, New York), p. 839.

[67] Incropera, F. P. and DeWitt, D. P. (1996b). *Fundamentals of Heat and Mass Transfer*, chap. 9 Free convection, 4th edn. (John Wiley & Sons, New York), pp. 482–333.

[68] Ito, H. (1997). Chemical amplification resists: History and development within IBM, *IBM Journal of Research and Development* **41**, 1, pp. 69–80.

[69] Jang, B. Z. and Zhang, Z. J. (1994). Thermally-and Phase Transformation-Induced Volume Changes of Polymers for Actuator Applications, *Journal of Intelligent Material Systems and Structures* **5**, 6, p. 758.

[70] Jo, B. H., Van Lerberghe, L. M., Motsegood, K. M. and Beebe, D. J. (2000). Three-dimensional micro-channel fabrication in polydimethylsiloxane (PDMS) elastomer, *Journal of Microelectromechanical Systems* **9**, 1, pp. 76–81.

[71] Jonsmann, J. and Bouwstra, S. (2000). Material considerations for topology optimised thermal microactuators, in *Proceedings of The 14th European Conference on*

Solid-State Transducers (Eurosensors XIV) (Copenhagen, Denmark), pp. 197–200.

[72] Kim, K., Park, S., Lee, J., Manohara, H., Desta, Y., Murphy, M. and Ahn, C. (2002). Rapid replication of polymeric and metallic high aspect ratio microstructures using PDMS and LIGA technology, *Microsystem Technologies* **9**, 1, pp. 5–10.

[73] Kofod, G., Sommer-Larsen, P., Kornbluh, R. and Pelrine, R. (2003). Actuation response of polyacrylate dielectric elastomers, *Journal of Intelligent Material Systems and Structures* **14**, 12, p. 787.

[74] Kornbluh, R., Pelrine, R., Prahlad, H. and Heydt, R. (2004). Electroactive polymers: an emerging technology for MEMS, *Proceedings of SPIE* **5344**, pp. 13–27.

[75] Kouma, N., Tsuboi, O., Mizuno, Y., Okuda, H., Mi, X., Iwaki, M., Soneda, H., Ueda, S. and Sawaki, I. (2003). A multi-step DRIE process for a 128 × 128 micromirror array, *2003 IEEE/LEOS International Conference on Optical MEMS* , pp. 53–54.

[76] Kwon, S., Milanovic, V. and Lee, L. (2002). Large-displacement vertical microlens scanner with low driving voltage, *IEEE Photonics Technology Letters* **14**, 11, pp. 1572–1574.

[77] Lau, G. K., Chu Duc, T., Goosen, J. F. L., van Keulen, F. and Sarro, P. M. (2006a). Electrostatically squeezed elastomers for out-of-plane microactuation, in *CD Proceedings of the 3rd Asica-Pacific Conference of Transducers and Micro-Nano Technology APCOT,* (Daegu, Korea), paper ID 95-AT-A0238.

[78] Lau, G. K., Chu Duc, T., Goosen, J. F. L., van Keulen, F. and Sarro, P. M. (2007a). In-plane thermal unimorph using confined polymers, *J. Micromech. and Microeng.* **17**, 7, pp. S174–S183.

[79] Lau, G. K., Goosen, J. F. L., F. van Keulen, Chu Duc, T. and Sarro, P. M. (2007b). Polymeric thermal micro-actuator with embedded silicon skeleton: Part I design and steady-state analysis, Submitted to J. Microelectromech. Sys.

[80] Lau, G. K., Goosen, J. F. L. and van Keulen, F. (2007c). Material selection for polymeric thermal actuator with embedded skeleton, In preparation.

[81] Lau, G. K., Goosen, J. F. L. and van Keulen, F. (2007d). Thermoelastic behavior of a polymeric layer bonded between rigid interfaces, Submitted.

[82] Lau, G. K., Goosen, J. F. L., van Keulen, F., Chu Duc, T. and Sarro, P. M. (2006b). Electro-thermally activated polymeric stack for linear in-plane actuation, in *Proc. 5th IEEE Conference on Sensors* (Daegu, Korea), pp. 538–541.

[83] Lau, G. K., Goosen, J. F. L., van Keulen, F., Chu Duc, T. and Sarro, P. M. (2007e). A powerful polymeric thermal micro-actuator with embedded silicon microstructures, *Appl. Phys. Lett.* **90**, p. Art. 214103.

[84] Lau, G. K., Goosen, J. F. L., van Keulen, F., French, P. J. and Sarro, P. M. (2006c). Actuated elastomers with rigid vertical electrodes, *J. Micromech. Microeng* **16**, pp. S35–S44.

[85] Lee, C. and Hsu, W. (2003). Optimization of an electro-thermally and laterally driven microactuator, *Microsystem Technologies* **9**, 5, pp. 331–334.

[86] Lee, C. and Wu, C. Y. (2005). Study of electrothermal V-beam actuators and latched mechanism for optical switch, *Journal of Micromechanics and Microengineering* **15**, 1, pp. 11–19.

[87] Lee, W., Gao, J., Hirano, T., Chan, S. and Fan, L. (1997). High aspect ratio etching in polymer for microactuator applications, *Proc. SPIE* **3223**, pp. 110–117.

[88] Legtenberg, R., Groeneveld, A. W. and Elwenspoek, M. (1996). Comb-drive actuators for large displacements, *J. Micromech. Microeng* **6**, 3, pp. 320–329.

[89] Leung, A. M., Jones, J., Czyzewska, E., Chen, J. and Pascal, M. (1997). Micromachined accelerometer with no proof mass, *Electron Devices Meeting, 1997. Technical Digest., International* , pp. 899–902.

[90] Li, H., Jacob, K. and Wong, C. (2003). An improvement of thermal conductivity of underfill materials for flip-chip packages, *IEEE Transactions on Advanced Packaging* **26**, 1, pp. 25–32.

[91] Liang, X. G. and Guo, Z. Y. (2006). The scaling effect on the thermal processes at mini/microscale, *Heat Transfer Engineering* **27**, 4, pp. 30–40.

[92] Lide, D. R. (ed.) (2007). *CRC Handbook of Chemistry and Physics*, internet version 87th edn. (Taylor and Francis, Boca Raton, FL.), pp. 35, 77, 219 Sec. 12, URL `http:/www.hbcpnetbase.com`.

[93] Lin, L. and Chiao, M. (1996). Electrothermal responses of lineshape microstructures, *Sensors and Actuators A* **55**, pp. 35–41.

[94] Lindley, P. B. (1966). Load-compression relationships of rubber units, *The Journal of Strain Analysis for Engineering Design* **1**, 3, pp. 190–195.

[95] Lindley, P. B. (1979). Compression module for blocks of soft elastic material bonded to rigid end plates, *Journal of Strain Analysis* **14**, pp. 11–16.

[96] Liu, C. (2006). *Foundations of MEMS*, chap. 12 Polymer MEMS, 1st edn. (Pearson Education, Upper Saddle River, NJ), pp. 397–421.

[97] Livermore, C. and Voldman, J. (2004). Material properties database, MIT Course 6.777J/2.751J Website, URL `http://web.mit.edu/6.777/www/matprops/matprops.htm`, modified on March 19, 2004.

[98] Madden, J. D. W., Vandesteeg, N. A., Anquetil, P. A., Madden, P. G. A., Takshi, A., Pytel, R. Z., Lafontaine, S. R., Wieringa, P. A. and Hunter, I. W. (2004). Artificial muscle technology: physical principles and naval prospects, *IEEE Journal of Oceanic Engineering* **29**, 3, pp. 706–728.

[99] Mahony, J. J. (1957). Heat Transfer at Small Grashof Numbers, *Proceedings of the Royal Society of London. Series A, Mathematical and Physical Sciences* **238**, 1214, pp. 412–423.

[100] Mahorowala, A., Babich, K., Lin, Q., Medeiros, D., Petrillo, K., Simons, J., Angelopoulos, M., Sooriyakumaran, R., Hofer, D., Reynolds, G. *et al.* (2000). Transfer etching of bilayer resists in oxygen-based plasmas, *Journal of Vacuum Science & Technology A: Vacuum, Surfaces, and Films* **18**, p. 1411.

[101] Maloney, J., Schreiber, D. and DeVoe, D. (2004). Large-force electrothermal linear micromotors, *Journal of Micromechanics and Microengineering* **14**, 2, pp. 226–234.

[102] Maluf, N. (2000). *An Introduction to Microelectro-mechanical Systems Engineering*, chap. 3 processes for micromachining (Artech House, Norwood, MA), pp. 33–77.

[103] MatWeb (2007a). Arkema Kynar 1000HD PVDF, Online, URL `http://www.matweb.com/`.

[104] MatWeb (2007b). DuPont Teflon PTFE Grade 7A Granular Molding Powder, Available at MatWeb, URL `http://www.matweb.com/`, Ticona Engineering Polymers.

[105] MatWeb (2007c). Overview - acrylic, general purpose, molded, Online, URL `http://www.matweb.com/search/SpecificMaterialPrint.asp{?}bassnum=O1300`.

[106] MatWeb (2007d). Overview - Nylon 66, Unreinforced, Online, URL `http://www.matweb.com/`.

[107] MicroChem (2007). Processing guidelines for SU-8 2000 permanent epoxy negative photoresist, MicroChem Website, USA, URL `http://www.microchem.com/products/pdf/SU-82000DataSheet2000_5thru2015Ver4.pdf`.

[108] Migwi, C., Darby, M., Wostenholm, G., Yates, B., Moss, M. and Duffy, R. (1994). A method of determining the shear modulus and Poisson's ratio of polymer materials, *Journal of Materials Science* **29**, 13, pp. 3430–3432.

[109] Modafe, A., Ghalichechian, N., Powers, M., Khbeis, M. and Ghodssi, R. (2005). Embedded benzocyclobutene in silicon: An integrated fabrication process for electrical

and thermal isolation in MEMS, *Microelectronic Engineering* **82**, 2, pp. 154–167.

[110] Nguyen, N., Boellaard, E., Pham, N., Kutchoukov, V., Craciun, G. and Sarro, P. (2002). Through-wafer copper electroplating for three-dimensional interconnects, *Journal of Micromechanics and Microengineering* **12**, 4, pp. 395–399.

[111] Nguyen, N.-T., Ho, S.-S. and Low, C. L.-N. (2004). A polymeric microgripper with integrated thermal actuators, *J. Micromech. Microeng.* **14**, p. 969974.

[112] Obi, H., Yamanoi, T., Fujita, H. and Toshiyoshi, H. (2004). A vertical-comb torsion mirror with distributed gaps for suppressing in-plane instability, *IEEE/LEOS Int. Conf. on Optical MEMS and Their Applications (Optical MEMS 2004), Takamatsu, Japan* , pp. 60–61.

[113] Ono, T., Sim, D. and Esashi, M. (2000). Micro-discharge and electric breakdown in a micro-gap, *J. Micromech. Microeng* **10**, 3, pp. 445–51.

[114] Pan, C. S. and Hsu, W. (1997). An electro-thermally and laterally driven polysilicon microactuator, *Journal of Micromechanics and Microengineering* **7**, 1, pp. 7–13.

[115] Panofsky, W. K. H. and Phillips, M. (1962). *Classical Electricity and Magnetism*, chap. 6 Energy relationship and force in the electrostatic field, 2nd edn. (Addison-Wesley, Reading, MA).

[116] Pelrine, R., Kornbluh, R., Joseph, J., Heydt, R., Pei, Q. and Chiba, S. (2000a). High-field deformation of elastomeric dielectrics for actuators, *Materials Science & Engineering C* **11**, 2, pp. 89–100.

[117] Pelrine, R., Kornbluh, R., Pei, Q. and Joseph, J. (2000b). High-speed electrically actuated elastomers with strain greater than 100%, *Science* **287**, 5454, pp. 836–839.

[118] Pelrine, R. E., Kornbluh, R. D. and Joseph, J. P. (1998). Electrostriction of polymer dielectrics with compliant electrodes as a means of actuation, *Sensors and Actuators A: Physical* **64**, 1, pp. 77–85.

[119] Pimpin, A., Suzuki, Y. and Kasagi, N. (2004). Micro electrostrictive actuator with metal compliant electrodes for flow control applications, *17th IEEE International Conference on. Micro Electro Mechanical Systems* , pp. 478–481.

[120] Prasanna, S. and Spearing, S. (2007). Materials selection and design of microelectrothermal bimaterial actuators, *Journal of Microelectromechanical Systems* **16**, 2, pp. 248–259.

[121] Que, L., Park, J. S. and Gianchandani, Y. B. (2001). Bent-beam electrothermal actuators Part I: Single beam and cascaded devices, *J. Microelectromech. Syst.* **10**, pp. 247–254.

[122] Riethmuller, W. and Benecke, W. (1988). Thermally excited silicon microactuators, *IEEE Transactions on Electron Devices* **35**, 6, pp. 758–763.

[123] Rogers, J. A., Yang, Y. and Nelson, K. A. (1994). Elastic modulus and in-plane thermal diffusivity measurements in thin polyimide films using symmetry-selective real-time impulsive stimulated thermal scattering, *Applied Physics A: Materials Science & Processing* **58**, 5, pp. 523–534.

[124] Ryu, K., Wang, X., Shaikh, K. and Liu, C. (2004). A method for precision patterning of silicone elastomer and its applications, *Journal of Microelectromechanical Systems* **13**, 4, pp. 568–575.

[125] Sadd, M. (2005). *Elasticity Theory, Applications, and Numerics*, chap. 4 Material Behavior - Linear Elastic Solids (Elsevier Butterworth Heinemann), pp. 69–81.

[126] Schlaak, H. F., Jungmann, M., Matysek, M. and Lotz, P. (2005). Novel multilayer electrostatic solid state actuators with elastic dielectric, *Proc. SPIE* **5759**, pp. 121–133.

[127] Sehr, H., Evans, A., Brunnschweiler, A., Ensell, G. and Niblock, T. (2001). Fabrication and test of thermal vertical bimorph actuators for movement in the wafer

plane, *Journal of Micromechanics and Microengineering* **11**, 4, pp. 307–310.
[128] Senturia, S. D. (2001a). *Microsystem design* (Dordrecht: Kluwer).
[129] Senturia, S. D. (2001b). *Microsystem Design*, chap. 3 microfabrication (Kluwer Academic Publishers, Norwell, MA), pp. 29–77.
[130] Shampine, L. F. and J. Kierzenka, M. W. R. (2000). Solving boundary value problems for ordinary differential equations in matlab with bvp4c, Online, URL `http://www.mathworks.com/matlabcentral/`, released on August 06, 2003.
[131] Sharpe, W. N. (2002). Chapter 3 Mechanical properties of MEMS materials, in M. Gad-el-Hak (ed.), *The MEMS Handbook*, internet version edn. (CRC Press, Boca Raton, FL.).
[132] Shaw, J. M., Gelorme, J. D., LaBianca, N. C., Conley, W. E. and Holmes, S. J. (1997). Negative photoresists for optical lithography, *IBM Journal of Research and Development* **41**, 1, pp. 81–94.
[133] Sigmund, O. and Torquato, S. (1996). Composites with extremal thermal expansion coefficients, *Applied Physics Letters* **69**, 21, pp. 3203–3205.
[134] Sigmund, O. and Torquato, S. (1997). Design of materials with extreme thermal expansion using a three-phase topology optimization method, *Journal of the Mechanics and Physics of Solids* **45**, 6, pp. 1037–1067.
[135] Small, M. B. and Pearson, D. J. (1990). On-chip wiring for VLSI: status and directions, *IBM Journal of Research and Development* **34**, 6, pp. 858–867.
[136] Sommer-Larsen, P. and Kornbluh, R. (2002). Polymer actuators, *Proceeding of Actuator conference* , pp. 538–541.
[137] Steeves, C., dos Santos e Lucato, S., He, M., Antinucci, E., Hutchinson, J. and Evans, A. (2007). Concepts for structurally robust materials that combine low thermal expansion with high stiffness, *Journal of the Mechanics and Physics of Solids* **55**, 9, pp. 1803–1822.
[138] Stern, M., Palmateer, S., Horn, M., Rothschild, M., Maxwell, B. and Curtin, J. (1995). Profile control in dry development of high-aspect-ratio resist structures, *Journal of Vacuum Science & Technology B: Microelectronics and Nanometer Structures* **13**, p. 3017.
[139] Su, J., Zhang, Q., Wang, P., MacDiarmid, A. and Wynne, K. (1998). Preparation and characterization of electrostrictive polyurethane films with conductive polymer electrodes, *Polymers for Advanced Technologies* **9**, 6, pp. 317–321.
[140] Suhir, E. (1989). Interfacial Stresses in Bimetal Thermostats, *ASME Journal of Applied Mechanics* **56**, 3, pp. 595 – 600.
[141] Sundqvist, B., Sandberg, O. and Backstrom, G. (1977). The thermal properties of an epoxy resin at high pressure and temperature, *J. Phys. D* **10**, pp. 1397–1403.
[142] Thielicke, E. and Obermeier, E. (2000). Microactuators and their technologies, *Mechatronics* **10**, 4-5, pp. 431–455.
[143] Thompson, D., Tantot, O., Jallageas, H., Ponchak, G., Tentzeris, M. and Papapolymerou, J. (2004). Characterization of liquid crystal polymer (LCP) material and transmission lines on LCP substrates from 30 to 110 GHz, *IEEE Transactions on Microwave Theory and Techniques* **52**, 4, pp. 1343–1352.
[144] Ticona (2007). Datasheet Vectra A950 LCP Unfilled, Available on Ticona Web, URL `http://tools.ticona.com/tools/mcbasei/`, Ticona Engineering Polymers.
[145] Timoshenko, S. (1925). Analysis of bi-metal thermostats, *J. Opt. Soc. Am* **11**, pp. 233–255.
[146] Todd, B., Flack, W. and White, S. (1999). Thick photoresist imaging using a three wavelength exposure stepper, *SPIE Proceedings on Micromachining and Microfabrication Process* Paper number 3874-40.

[147] Toshiyoshi, H., Mita, M. and Fujita, H. (2002). A MEMS piggyback actuator for hard-disk drives, *Journal of Microelectromechanical Systems* **11**, 6, pp. 648–654.

[148] Tsai, H. C. and Lee, C. C. (1998). Compressive stiffness of elastic layers bonded between rigid plates, *Int. J. Solids. Struct.* **35**, 23, pp. 3053–3069.

[149] Tsai, H. C. and Lee, C. C. (1999). Tilting stiffness of elastic layers bonded between rigid plates, *International Journal of Solids and Structures* **36**, 17, pp. 2485–2505.

[150] Tsai, M. Y., Hsu, C. H. and Han, C. N. (2004). A note on Suhirs solution of thermal stresses for a die-substrate assembly, *Journal of Electronic Packaging* **126**, p. 115.

[151] Vinogradov, A., Su, J., Jenkins, C. and Bar-Cohen, Y. (2005). State-of-the-art developments in the field of electroactive polymers, *Materials Research* .

[152] Wang, H., Zhang, Q., Cross, L. and Sykes, A. (1993). Clamping effect on the piezoelectric properties of poly (vinylidene fluoride-trifluoroethylene) copolymer, *Ferroelectrics* **150**, 1, pp. 255–266.

[153] Wang, H., Zhang, Q., Cross, L., Ting, R., Coughlin, C. and Rittenmyer, K. (1991). The origins of electromechanical response in polyurethane elastomers, *Proceedings of the Ninth IEEE International Symposium on Applications of Ferroelectrics, 1994. ISAF'94.* , pp. 182–185.

[154] Wang, X., Engel, J. and Liu, C. (2003). Liquid crystal polymer(LCP) for MEMS: processes and applications. *Journal of Micromechanics and Microengineering* **13**, 5, pp. 628–633.

[155] Weisstein, E. W. (1999). Heat conduction equation, From MathWorld–A Wolfram Web Resource, URL `http://mathworld.wolfram.com/HeatConductionEquation.html`, 1999-2007.

[156] Wortman, J. J. and Evans, R. A. (1965). Young's modulus, shear modulus, and Poisson's ratio in Silicon and Germanium, *Journal of Applied Physics* **36**, pp. 153–156.

[157] Wu, T., Guo, Y. and Chen, W. (1993). Thermal-mechanical strain characterization for printed wiring boards, *IBM Journal of Research and Development* **37**, 5, pp. 621–634.

[158] Xia, Y. and Whitesides, G. M. (1998). Soft lithography, *Annu. Rev. Mater. Sci.* **28**, 6, p. 15384.

[159] Yang, J. P., Deng, X. C. and Chong, T. C. (2005). An electro-thermal bimorph-based microactuator for precise track-positioning of optical disk drives, *J. Micromech. Microeng.* **15**, pp. 958–965.

[160] Yeh, J., Hui, C. and Tien, N. (2000). Electrostatic model for an asymmetric combdrive, *Journal of Microelectromechanical Systems* **9**, 1, pp. 126–135.

[161] Yeh, J., Jiang, H. and Tien, N. (1999). Integrated polysilicon and DRIE bulk silicon micromachining for anelectrostatic torsional actuator, *Journal of Microelectromechanical Systems* **8**, 4, pp. 456–465.

[162] Yoon, J. B., Han, C. H., Yoon, E. and Kim, C. K. (1998). Novel two-step baking process for high-aspect-ratio photolithography with conventional positive thick photoresist, *Proc. SPIE* **3512**, pp. 316–325.

[163] Yung, K., Mei, S. and Yue, T. (2005). Pulsed UV laser ablation of a liquid crystal polymer, *The International Journal of Advanced Manufacturing Technology* **26**, 11, pp. 1231–1236.

[164] Zahn, J., Gabriel, K. and Fedder, G. (2002). A direct plasma etch approach to high aspect ratio polymermicromachining with applications in bioMEMS and CMOS-MEMS, *Proceedings of The Fifteenth IEEE International Conference on Micro Electro Mechanical Systems, 2002.* , pp. 137–140.

[165] Zhang, Q. M., Bharti, V. V. and Zhao, X. (1998). Giant electrostriction

and relaxor ferroelectric behavior in electron-irradiated poly (vinylidene fluoride-trifluoroethylene) copolymer, *Science* **280**, 5372, pp. 2101–4.

[166] Zhang, Q. M., Su, J., Kim, C. H., Ting, R. and Capps, R. (1997). An experimental investigation of electromechanical responses in a polyurethane elastomer, *Journal of Applied Physics* **81**, p. 2770.

[167] Zhu, Y., Corigliano, A. and Espinosa, H. (2006). A thermal actuator for nanoscale in situ microscopy testing: design and characterization, *J. Micromech. Microeng* **16**, pp. 242–253.

Acknowledgments

First and foremost, I would like to thank my mother and brothers for their supports and encouragement throughout all my endeavours. Thanks to my girlfriend, Sin-Yee, for her love, wisdom, inspiration, and patience while I am studying abroad for the past four years.

I would like to thank my supervisors and co-supervisor for their supports, guidance and advice throughout the course of PhD research. Thanks them for giving me the freedom to develop my own ideas. Thanks to my supervisor Fred van Keulen for his enthusiasm on the research, his creative ideas, and his critical and useful comments on my presentation and writing. Thanks to my co-supervisor Hans Goosen for coaching me on micro-fabrication technology, especially at the beginning of the project when I started without hands-on experience with micro-fabrication. Thanks to my supervisor Lina Sarro for giving me an opportunity to conduct micro-fabrication in the MEMS Lab.

I would like to thank my colleagues from the Structural Optimization and Computational Mechanics (SOCM) group: Jacqueline, Marten Jan, Koen, Andry, Gerard, Teun, Sham, Peterjan, Chiara, Bert, Caspar, Qian, Daniel, Nico, Hamed, Cadmus, and Saputra. They all together created an enjoyable and stimulating working environment. Special thanks to my fellow colleagues in the same office, Matthijs, Sham, Bert, and Cadmus for a lively environment. Beside technical discussions, their interaction, e.g. chats, 'practical jokes', games of paper ball or 'pepernoten', delights the office time. Thanks to Bert, Jeroen and Hans for their helps to translate parts of the English writing into Dutch.

I would like to thank Jan Booij for his help and expertise on computer hardware and software in the group of SOCM. Thanks to Rien van de Ruijtenbeek for arranging an advanced university license of ANSYS for me. Also, I would like to thank Marianne for her help and for arranging everything in this group. In addition, thanks to Sebastian for his help and advice on financial matter in the Department of Precision and Microsystems Engineering (PME).

Thanks to the Delft Center of Mechatronics and Microsystems (DCMM) for sponsoring my PhD research. Thanks to Inge van Marion, Marli Guffens and Marcel Tichem for arranging many interesting events and symposiums under the auspice

of DCMM.

Thanks to fellow colleagues at PME, Jo Spronck, Warner Venstra, Sanders Paalvast, and Vincent Henneken for starting the MEMS facilities in the PME Department. Thanks to Defeng for kindly lending and showing me a high-voltage amplifier, and the Keyence displacement sensor. Thanks to Kaspar Jansen for his generous help and his expert advice on polymer material testing. Thanks to Mihir Patel for his help in carrying out PVT testing. Thanks to Lingen Wang and An Xiao for their help or advice in DMA testing. Thanks to Jos van Driel, Harry Jansen and Erik Fritz for technical supports in the laboratory at the department. Thanks to Willem van Driel and Dao-Guo Yang for sharing their knowledge and theses on polymer.

In addition, I would like to thank my collaborating colleagues at the Delft Institute of Microelectronics and Submicrontechnology (DIMES). Thanks to Trinh Chu Duc, Jia Wei, Faruk Krecinic, and Mohamed Saadaoui for many discussions, many hours of working together in the clean room or measurement room, and trying out together unconventional microfabrication processes . Thanks also to other fellow colleagues at DIMES. Thanks to Jason Tian, Huseyin Sagkol, Sebastian Sosin for sharing their experiences on copper plating. Thanks to CK Yang for taking the first SEM picture for me at DIMES.

I would like to thank all technical staff of DIMES for their technical training and supports. Thanks to Tom Scholtes for the first course on chemical safety. Thanks Alex van den Bogaard and Cassan Visser for introducing me to facilities at MEMS Lab and arranging the requested instruments. Thanks to Wim van der Vlist and Ruud Klerks for their help on wafer dicing and delicate wire bonding. Thanks to Mario Laros and Charles de Boer for showing me operation of plasma etcher. Thanks to Jan Groenweg for his help in mask making. Thanks to Marco Bakker and Peter Kroon for supports in the MEMS Lab. Thanks to Hugo Schellevis for preparing wafers with sputtered metal seed. Thanks to Wim Wien for his advice on copper plating. Thanks to Henk van Zeijl for his kind help on mask templates. His generous and frequent loan of a temporary pass to Class 100 is also appreciated. Thanks to Martijn Tijssen for his help in evaporating aluminium on polymer.

Thanks to Prof. Stephen J. Picken for his kind assistance in temperature measurement using liquid crystalline polymers.

Last but not least, thanks to Kang-Shua Yeo formerly of National University of Singapore, Chin-Long Lee of UC Berkeley, YQ Fu of Cambridge University, Su Cheng formerly of MIT, Simon Tosseram of TU Eindhoven, and Jiang Lidi of Southampton University for helps in gathering literature, which is not available at Delft. Koiter collection of classical texts and literature in the department of Precision and Microsystems Engineering is also very much appreciated. The reading of literature forms a basis on which my research could extrapolate.

Gih-Keong Lau
Delft, October, 2007

List of Publications

This thesis is written to describe the research efforts and outputs of a PhD research project. The project was funded by the Delft Centre for Mechatronics and Microsystems and conducted at the Department of Precision and Microsystems Engineering, Delft University of Technology, the Netherlands. It was started on January 2004 and scheduled to be completed on December 2007. Listed below are the research contributions and publications related to this thesis, as of October 2007. The list is divided into the highlights, awards, patent, journal and refereed conference publications.

Highlights

- "Nieuwste micromotor haalt langere afstand," Delta 18 (38), 1 June 2006
- "Eureka! Artificial muscle for the robot fly," Delft Outlook, 2006 no. 2
- "A powerful polymeric thermal micro-actuator with embedded silicon microstructure," selected in the Virtual Journal of Nanoscale Science & Technology, Vol. 15(22), June 4, 2007.

Awards

- The best poster for "In-plane thermal unimorph using confined polymers", in the 17th Workshop on Micromechanics Europe (MME06), Southampton, UK, September 2006
- The best poster for "Actuated elastomers with rigid vertical electrodes", in the 16th Workshop on Micromechanics Europe (MME05), Goteberg, Sweden, September 2005

Patent

- Lau G. K., Chu Duc T. , Goosen J. F. L. (2006) "Thermische actuator," filed on 13 September 2006 at Amsterdam, Dutch Patent Application Number 2000209

Journal Publications

(1) Lau G. K., Goosen J. F. L., van Keulen F., French P. J., Sarro P. M. (2006) Actuated elastomers with rigid vertical electrodes, *Journal of Micromechanics and Microengineering* 16 (6): S35-S44
(2) Lau G. K., Chu Duc T., Goosen J. F. L., van Keulen F., Sarro P. M. (2007) In-plane thermal unimorph using confined polymers, *Journal of Micromechanics and Microengineering*, 17, S174-S183
(3) Lau G. K., Goosen J. F. L., van Keulen F., Chu Duc T., Sarro P. M. (2007) A powerful polymeric thermal micro-actuator with embedded silicon microstructure, *Applied Physics Letters*, 90, Art. 214103 (*Selected in the Virtual Journal of Nanoscale Science & Technology, Vol. 15(22), June 4, 2007)
(4) Chu Duc T., Lau G. K. and Sarro P. M. (2007) Polymer constraint effect for electro-thermal bimorph microactuators, *Applied Physics Letters*, 91, Art. 101902
(5) Lau G. K., Goosen J. F. L., van Keulen F., Chu Duc T., Sarro P. M. (2007) A polymeric thermal micro-actuator with embedded skeleton: Part I - Design and Steady-State Analysis, *Journal of Micro-electro-mechanical Systems*, submitted on Aug, 2007
(6) Chu Duc T., Lau G. K., Sarro P. M. (2007) A polymeric thermal micro-actuator with embedded skeleton Part II - Fabrication and Applications to Microgrippers, *Journal of Micro-electro-mechanical Systems*, submitted on Aug, 2007
(7) Lau G. K., Goosen J. F. L., van Keulen F. (2007) Thermoelastic behavior of a polymeric layer bonded between rigid interfaces, *submitted*, Oct 2007
(8) Lau G. K., Goosen J. F. L., van Keulen F. (2007) Design optimization for polymeric thermal micro-actuator with embedded skeleton, *submitted*, Oct 2007
(9) Lau G. K., Goosen J. F. L., van Keulen F. (2007) "Material selection for polymeric thermal micro-actuator with embedded skeleton, *submitted*, Oct 2007

Refereed Conference Publications

(1) Lau G. K., Goosen J. F. L., van Keulen F., French P. J., Sarro P. M. (2005) Actuated elastomers with rigid vertical electrodes, *Proceedings of the 16th MME MicroMechanics Europe Workshop (MME05)*, 4-6 September 2005, Goteberg, Sweden, pp. 382-385, ISBN 91 631 7553 3
(2) Lau G. K., Chu Duc T., Goosen J. F. L., van Keulen F., Sarro P. M. (2006) Electrostatically squeezed elastomers for out-of-plane microactuation, *CD Proceedings of the 3rd Asica-Pacific Conference of Transducers and Micro-Nano Technology (APCOT 2006)*, Singapore, 25-28 June 2006, Paper 95-AT-A0238. (4 pages)
(3) Lau G. K., Chu Duc T., Goosen J. F. L., van Keulen F., Sarro P.M. (2006) In-plane thermal unimorph using confined polymers, *Technical Digest of the 17th MicroMechanics Europe (MME06)*, Southampton, 3-5 September 2006,

pp. 117-120, ISBN 085432 8483

(4) Chu Duc T., Lau G. K., Wei J., Sarro P. M. (2006) Silicon-polymer laterally stacked bimorph micro-gripper, *Technical Digest of the 17th MicroMechanics Europe (MME06)*, Southampton, 3-5 September 2006, pp. 197-200 ISBN 085432 8483

(5) Lau G. K., Goosen J. F. L., van Keulen F., Chu Duc T., Sarro P.M. (2006) Electro-thermally activated polymeric stack for linear in-plane actuation, *Proceedings of the 5th IEEE Conference on Sensors*, Daegu, Korea, October 22-25, 2006, pp. 538-541, ISBN: 1-4244-0376-6

(6) Chu Duc T., Lau G. K., Wei J., Sarro P. M. (2006) Integrated silicon-polymer laterally stacked bender for sensing microgrippers, *Proceedings of the 5th IEEE Conference on Sensors*, Daegu, Korea, October 22-25, 2006, pp. 662-665, ISBN: 1-4244-0376-6

(7) Chu Duc T., Lau G. K., Wei J., Sarro P. M. (2006) 2D electro-thermal microgrippers with large clamping and rotation motion at low driving voltage, *Proceedings of the 20th IEEE International Conference on Micro Electro Mechanical Systems MEMS 2007*, Kobe, Japan Jan 21 - 25, 2007, pp. 687-690, ISBN: 1-4244-0951-9

(8) Lau G. K., Goosen J. F. L., van Keulen F. (2007) Optimization of polymeric electro-thermal micro-actuator for various criteria, *Proceedings of the 7th World Congress of Structural and Multidisciplinary Optimization*, COEX Seoul, 2125 May 2007, Korea, pp. 902-911, ISBN 978-89-959384-2-3

(9) Lau G. K., Chu Duc T., Goosen J. F. L., Sarro P. M., van Keulen F. (2007) Power efficient V-shape electro-thermal actuator using constrained SU-8, *Technical Digest of the14th International Conference on Solid-State Sensors, Actuators and Microsystems (TRANSDUCERS'07)*, Lyon, France, June 10-17 2007, (Paper ID EA0182), Lyon, Jun 10-14, 2007, pp. 287-290

(10) Krecinic F., Chu Duc T., Lau G. K., Sarro P. M. (2007) Simulation and measurement of a comb-structure silicon-polymer thermally actuated micro-gripper, *Technical digest of the 18th MicroMechanics Europe (MME07)*, 16-18 September 2007, Guimaraes, Portugal, pp. 215-218, ISBN 978-972-98603-3-1

(11) Chu Duc T. , Lau G. K., Creemer J. F. , and Sarro P. M. (2008) Electrothermal microgripper with large jaw displacement and integrated force sensors, *Proceedings of the 21th IEEE International Conference on Micro Electro Mechanical Systems MEMS 2008*, January 13-17, 2008 - Tucson, Arizona, USA, *to appear*

(12) Wei J., Chu Duc T., Lau G.K. and Sarro P.M. (2008) Novel electrothermal bimorph actuator for large out-of-plane displacement and force, *Proceedings of the 21th IEEE International Conference on Micro Electro Mechanical Systems MEMS 2008*, January 13-17, 2008 - Tucson, Arizona, USA, *to appear*

About the Author

Gih-Keong Lau was born in Muar, the state Johore of Malaysia, on 21 April 1975. He received his secondary education from Chung Hwa High School in Muar from 1988 to 1993. From 1994 to 1998, he had his tertiary education at Nanyang Technological University (NTU), Singapore. In 1998, he obtained his bachelor degree of mechanical engineering with First Class Honour. Afterwards, he further pursued a master study by research in the same university.

In 2001, he received his master degree of mechanical engineering from NTU. The title of his master thesis was "Optimal design of compliant mechanisms using topology optimization". From 2001 to 2003, he worked as a project officer and subsequently a research associate with the Centre for Mechanics of Microsystems, NTU. His research activities at NTU included mechanical design, topology optimization, and piezoelectric actuator design for hard disk drives (HDD). The research activities during the master and post-master period led to 16 international journal publications and a patent granted in Singapore.

In 2004, he embarked on his PhD research at Delft University of Technology, the Netherlands. The research project was sponsored by the Delft Centre of Mechatronics and Microsystems. His PhD research topic was on micro-actuators based on polymeric materials, which include dielectric elastomers and thermally expandable polymers. The study covered many aspects of the actuators, namely the physics, design, modelling and device fabrication. The research activities on design, modelling and polymeric material testing was carried out in the Department of Precision and Mirosystems Engineering (PME) while the device fabrication was conducted at the Delft Institute of Micro-electronics and Submicron-technology (DIMES). He had designed and developed new types of polymeric micro-actuators with tailored electrode designs. His research at Delft has resulted in this thesis, a Dutch patent application and many publications.